# Technische Universität München
## TUM School of Natural Sciences

# Aspects of Higgs phenomenology in and beyond the Standard Model

## Gabriël Abraham Koole

Vollständiger Abdruck der von der TUM School of Natural Sciences der Technischen Universität München zur Erlangung des akademischen Grades eines

**Doktors der Naturwissenschaften (Dr. rer. nat.)**

genehmigten Dissertation.

Vorsitzender: Prof. Dr. Lukas Heinrich

Prüfer der Dissertation: 1. Prof. Dr. Andreas Weiler

2. Prof. Dr. Lorenzo Tancredi

# aspects of
# HIGGS
# PHENOMENOLOGY
## *in and beyond the*
# STANDARD MODEL



Gabriël Koole

*Voor mijn ouders, David en Sophie*

MAX-PLANCK-INSTITUT
FÜR PHYSIK

# Abstract

The Higgs boson provides a unique tool to study the physics of the Standard Model, as well as to search for manifestations of physics beyond it. The first part of this thesis is devoted to precision in the Higgs sector, where we perform a phenomenological analysis of $ZZ$ production at the Large Hadron Collider (LHC) using the recently developed MiNNLO$_{\text{PS}}$ method for the matching of fixed-order QCD calculations to a parton shower. In the second part of this thesis, we explore a number of phenomenological directions to search for physics beyond the Standard Model. Within the context of the Standard Model effective field theory, we probe possible modifications of the trilinear Higgs coupling via off-shell Higgs production at the LHC, and use of a variety of non-Higgs observables to constrain dipole-type operators that modify the bottom-Higgs and charm-Higgs dynamics. Finally, we perform a sensitivity study for the high-luminosity upgrade of the LHC and other future collider options in constraining Higgs-portal interactions.

# Contents

# Chapter 1

# Introduction

A decade ago, on the 4th of July 2012, theoretical and experimental physicists gathered in the CERN auditorium for the empirical confirmation of a 48 year-old theoretical prediction: a new fundamental scalar particle with approximately the properties of the Higgs boson as predicted by the Standard Model (SM) of elementary particle physics. The implications of its discovery by the ATLAS [1] and CMS [2] collaborations at the Large Hadron Collider (LHC), in itself a tremendous success for the SM, are still being understood today. In fact, while this introduction was being written, the LHC commenced its third large round of data taking merely one day after the celebrations of the ten-year anniversary of the Higgs-boson discovery. After having undergone significant updates over the last three years to increase not only the energy of the colliding beams (reaching a world-record collision energy of 13.6 TeV) but also their intensity (aiming to obtain around 300 fb$^{-1}$ of integrated luminosity at the end of Run 3), the world's largest particle accelerator is ready for a new physics season.

In this endeavour, the Higgs boson will undoubtedly be again at the center of attention. The reasons for this are manifold, but foremost is that its discovery constitutes the first direct evidence that the Universe is pervaded by a fundamental scalar field, the Higgs field, whose profound consequences directly relate to some of most fundamental aspects of nature. Remarkably, the Higgs field has a non-vanishing expectation value in the vacuum, which plays a crucial role in explaining the origin of particle masses. Its non-zero vacuum expectation value was acquired during an electroweak (EW) phase transition in the early Universe, which could be connected with the observed matter-antimatter asymmetry. Moreover, the (in-)stability of the EW vacuum itself is related to the precise value of the measured Higgs-boson mass and possibly has far-reaching implications for cosmological models of inflation. Theoretically, the Higgs field ensures the SM to be a consistent quantum field theory as its excitations, *i.e.* the Higgs bosons, restore the perturbative unitarity of the SM that would otherwise be violated by longitudinal gauge-boson scattering. And lastly, being the only known elementary scalar field, the Higgs field could serve as a portal to other, hidden sectors possibly related to dark matter (DM). In light of this multitude of profound features, it perhaps does not come as a surprise that the theoretical path to the Higgs discovery has been one paved with Nobel Prizes.

The central theoretical principle that eventually led to the celebrated discovery at the LHC is that of a spontaneously broken symmetry. First proposed within the context

**(a)** Gluon-gluon fusion (ggF)

**(b)** Vector-boson fusion (VBF)

**(c)** Higgsstrahlung ($Vh$, $V = W, Z$)

**(d)** Associated production ($t\bar{t}h$)
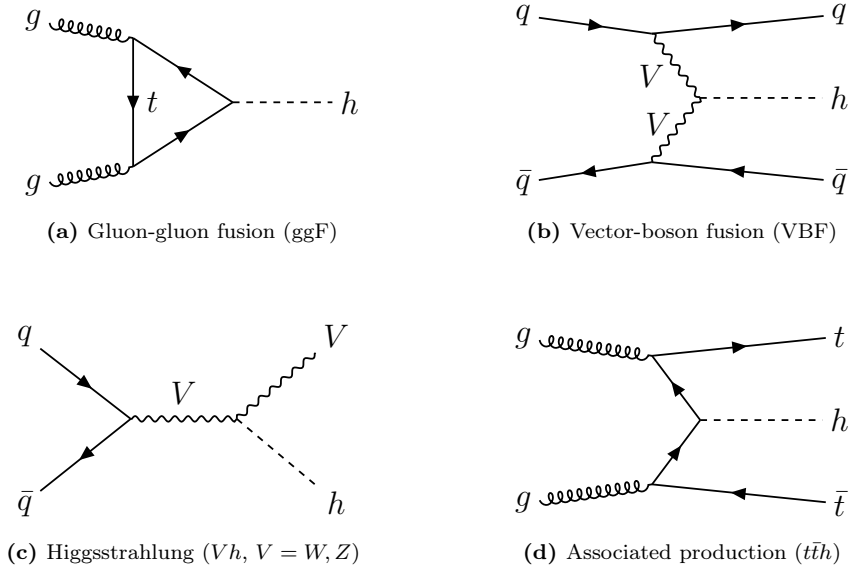
**Figure 1.1:** Examples of leading-order Feynman diagrams contributing to Higgs production at the LHC in gluon-gluon fusion (a), vector-boson fusion (b), Higgsstrahlung (c), and associated production with a top-quark pair (d).

of non-relativistic theories of superconductivity [3–5], the concept of a spontaneously broken symmetry is that of one that remains exact in the underlying dynamics but appears broken in observed phenomena as a consequence of an asymmetric vacuum. The idea was introduced into particle physics by Nambu in 1960 [6], where he hypothesized the generation of nucleon masses via the spontaneous breaking of global chiral symmetry in the strong interaction, along with the existence of an additional (almost) massless particle which he identified as the pion. Around the same time, Goldstone had conjectured that the appearance of massless spin-zero bosons is a general consequence of the spontaneous breaking of a continuous symmetry [7]. Proofs of Goldstone's theorem were derived shortly after [8], and the aforementioned massless particles became known as Goldstone bosons. However, Brout and Englert [9], Higgs [10, 11] and Guralnik, Hagen and Kibble [12], independently put forward the idea that the Goldstone theorem can be evaded for spontaneously broken *local* gauge symmetries, where the would-be Goldstone bosons are absorbed as the helicity-zero states of the vector bosons associated to the local gauge symmetry, which thereby acquire mass. This is known as the Brout-Englert-Higgs (BEH) mechanism, which furthermore predicts the existence of a new massive spin-zero particle — the Higgs boson.

The BEH mechanism however started receiving its deserved attention only after it was shown to fit beautifully into a unified theory of EW interactions [13–15] capable of making clear-cut predictions [16, 17]. Importantly, it was also shown able to generate fermion masses through their Yukawa interactions with the Higgs field. Together with the emergence of quantum chromodynamics (QCD) as a mathematically consistent theory of the strong interaction [18–22], this ushered in an era in which the SM was confirmed time after time in many different experimental measurements, culminating in

| Decay channel | $h \to b\bar{b}$ | $h \to W^+W^-$ | $h \to \tau^+\tau^-$ | $h \to ZZ$ | $h \to \gamma\gamma$ |
|---|---|---|---|---|---|
| Branching ratio | 58% | 21% | 6.3% | 2.6% | 0.23% |

**Table 1.1:** Branching ratios for the SM Higgs boson with a mass of 125 GeV. Values taken from [23].

the Higgs-boson discovery at the LHC. With it came a wealth of possible directions for further study, partially owing to the fact that the mass of the observed scalar particle with around 125 GeV turned out to be particularly fortunate for the experimental exploration of its properties, which has been one of the main goals of the physics progamme at the LHC ever since.

In Figure 1.1, we show leading-order Feynman diagrams for the four most relevant production modes of Higgs bosons at the LHC. The dominant channel is gluon-gluon fusion (ggF), which proceeds mainly through a top-quark loop and contributes roughly 90% to the total inclusive cross section. While it starts to contribute at $\mathcal{O}(\alpha_s^2)$, with $\alpha_s = g_s^2/(4\pi)$ being the strong coupling constant, it is enhanced by the large gluon luminosity at the LHC and benefits from a large top-quark Yukawa coupling. Not unimportantly, the QCD corrections to this process are also large, a point that will be discussed in detail in Chapter 4. The production mode with the second-largest cross section is vector-boson fusion (VBF), which makes up about 7% of the total cross section and has the characteristic signature of two back-to-back hard jets in the forward and backward regions of the detector. The remaining portion of the total Higgs production cross section is mostly attributed to the associated production with a vector boson ($Vh$, $V = W, Z$), *i.e.* Higgsstrahlung, and the associated production with a top-quark pair ($t\bar{t}h$). While the latter provides direct access to the top-Yukawa coupling, both contributions are smaller compared to the aforementioned production modes due to the energy burden that comes with producing a vector boson or top-quark pair in the final state.

The sensitivity of a particular channel to its corresponding Higgs signal depends not only on the Higgs production cross section, but also on the amount of non-Higgs background in the final state, the selection efficiency and the branching ratio for the specific decay mode of the Higgs. For a Higgs boson with a mass of 125 GeV, the branching ratios for the five main decay channels are given in Table 1.1. While the $h \to b\bar{b}$ channel yields the largest branching ratio, its detection is complicated by large backgrounds from multi-jet production in the dominant ggF production mode. In the case of $h \to W^+W^-$, the $W$ bosons decay either hadronically ($W \to q\bar{q}'$) or leptonically ($W \to \ell\nu_\ell$), where the sensitivity is diminished by large QCD backgrounds and the presence of neutrinos, respectively. Because of the fact that also the $h \to \tau^+\tau^-$ mode suffers from large backgrounds, the most sensitive channels are instead the $h \to ZZ$ and $h \to \gamma\gamma$ channels, despite their small branching ratios. The $ZZ$ case, where the two $Z$ bosons decay into four leptons, is often called the *golden channel* owing to its clean experimental signature and will be studied in different contexts in Chapters 4, 6 and 8. Table 1.1 nicely illustrates the point made before that, phenomenologically, we have been quite fortunate with the particular value nature has chosen for the Higgs mass as it enables us to study its properties using a wide range of production and decay
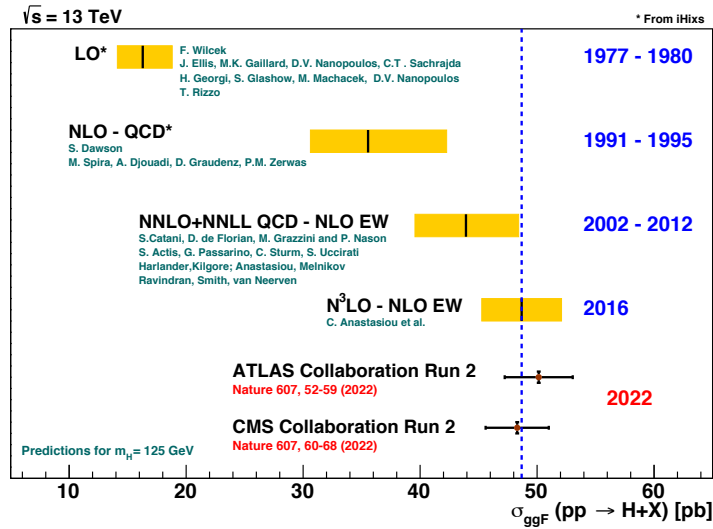
**Figure 1.2:**   Cross section for inclusive Higgs production in gluon-gluon fusion. SM predictions at 13 TeV including QCD and EW corrections at various orders are compared to ATLAS [29] and CMS [30] results using the full set Run 2 data. Figure taken from [31].

modes at the LHC.

In this regard, precision is key. The couplings of the scalar resonance to the EW gauge bosons and third-generation fermions have been tested extensively, showing agreement with those of the SM Higgs boson at the level of about $(5-20)\%$ [24, 25]. However, as nicely put in [26]: would we consider the theory of electromagnetism established if we had only verified the strength of its interaction to an accuracy of, say, 10%? Certainly not. In addition, thus far only upper limits have been achieved on its couplings to quarks and leptons of the first and second generation.[1] The experimental exploration of the Higgs sector has in that sense only just begun. However, the additional data from LHC Run 3 and the subsequently scheduled high-luminosity upgrade of the LHC (HL-LHC), together with innovative analysis techniques and accurate theoretical calculations, are expected to reduce the uncertainties on the observed Higgs-boson couplings to the level of a few percent [28].

To match the precision already currently achieved on the experimental side, but also in the future, there are essentially two broad directions for improving the accuracy of theoretical predictions. On the one hand, including more terms in the perturbative calculations of hard-scattering processes will reduce the uncertainties associated to missing higher orders. With the LHC being a hadronic machine, the dominant corrections are of QCD type. This is particularly true for Higgs production in ggF as it is purely a quantum process originating from a two-gluon initial state. Figure 1.2 shows that not only the theoretical uncertainties on the inclusive ggF cross section, displayed as yellow bands around the predicted values, are reduced by including higher-order QCD or EW corrections,[2] but also that the addition of their contributions is crucial to accurately describe the data. On the other hand, the development of novel compu-

---

[1]The first evidence for the Higgs decay into a muon pair, at the level of $3\sigma$, was presented in [27].

[2]As the NLO central value lies well outside the uncertainty bands of the LO prediction, the LO uncertainty in Figure 1.2 is significantly underestimated.

tational techniques allows us to model also more exclusive final states with improved accuracy. This is important, because studying more differential observables allows us to test the SM in more detail as one can compare not only the normalisation but also the shape of the distribution to the SM expectation.

Naturally, a lot of ongoing work aims to combine the best of both worlds by matching the best-available fixed-order QCD calculations to a parton-shower (PS) algorithm designed to simulate QCD radiation in the soft-collinear approximation. These matching frameworks are embedded in dedicated Monte-Carlo event generators to obtain hadron-level simulated events, which is crucial for comparison to experiment. This is the subject of the first part of this thesis, and a more comprehensive introduction to the topic and discussion of the relevant aspects of collider theory are provided in Chapters 2 and 3, respectively. In particular, Chapter 3 reviews some of the leading matching methods developed in the last two decades, starting from the well-known POWHEG [32, 33] framework for matching next-to-leading order (NLO) QCD calculations to a PS (*i.e.* NLO+PS), up to the recently developed MiNNLO$_{\text{PS}}$ method [34, 35] for the matching of next-to-next-to leading order (NNLO) QCD calculations to a PS (NNLO+PS). We apply MiNNLO$_{\text{PS}}$ to $ZZ$ production at the LHC in Chapter 4, obtaining NNLO+PS accurate results for the $q\bar{q} \to ZZ$ process. In addition, we construct an event generator for the loop-induced ggF channel, where we match NLO QCD accurate fixed-order results to a PS using the POWHEG method. The two implementations are then combined to perform a comprehensive phenomenological study of $ZZ$ production at the LHC.

Even though ten years of increasingly precise measurements and predictions at the LHC, in addition to the precision measurements performed by collider experiments before it [36], have thus far shown a pattern consistent with the SM picture, it is widely believed that the SM is not the end of the story. There are well-known issues, both theoretical and observational, for which the SM fails to provide a satisfactory explanation. For instance, the observed neutrino oscillations [37, 38] are in contradiction with the SM as it is not possible to generate neutrino masses in a gauge-invariant way via the BEH mechanism due to the absence of right-handed neutrinos. In addition, cosmological observations imply a DM abundance of about 26% of the total energy budget of the Universe [39], for which the SM does not provide a viable particle candidate. Moreover, the absence of antimatter in the Universe indicates additional sources that violate combined charge-conjugation and parity (CP) symmetry, beyond the amount of CP violation generated by the Kobayashi-Maskawa mechanism [40] within the SM. On the theoretical side, the SM lacks a deeper explanation for the observed pattern of particle masses, *i.e.* it does not provide any insight into the seemingly arbitrary arrangement of Yukawa couplings in the Higgs sector. Additionally, the Higgs mass itself is not protected from large quantum corrections, which causes a hierarchy problem in the presence of heavy new physics unless a large degree of fine tuning keeps the Higgs mass at the EW scale or it is stabilised by some unknown mechanism or symmetry.

It is not unlikely that most, if not all, of the major open questions mentioned above are linked in one way or the other to the Higgs boson, which therefore provides a powerful tool not only to study the physics of the SM but also to probe the landscape beyond the SM (BSM). The second part of this thesis contains, following a more detailed motivation in Chapter 5, three phenomenological studies that are directly or indirectly

related to the Higgs boson, in the presence of BSM physics.

In Chapter 6, we explore the possibility of BSM effects modifying the Higgs potential. The Higgs potential in the SM is parametrised by two parameters only: the vacuum expectation value ($v \approx 246$ GeV) of the Higgs field and the strength of the (trilinear and quartic) self-interactions of the Higgs boson, which are parametrised by the same parameter $\lambda$, given by $\lambda = m_h^2/(2v^2) \approx 0.13$ for a Higgs mass of $m_h = 125$ GeV. However, many BSM scenarios allow for deviations of the Higgs self-couplings with respect to their SM predictions [41]. Measuring or constraining $\lambda$ therefore presents a unique window into the mechanism of EW symmetry breaking in addition to providing a way to probe the existence of new physics. We study the effects of a modified trilinear Higgs coupling in the context of the SM effective field theory (SMEFT), assuming that the SM is the low-energy effective realisation of some unknown ultraviolet (UV) theory. Possible contributions from higher-dimensional SMEFT operators to the trilinear Higgs coupling are analysed in off-shell Higgs production at the LHC, where our calculation of the $gg \to h^* \to ZZ \to 4\ell$ process includes two-loop corrections to ggF Higgs production and one-loop corrections to the Higgs propagator and its decay. Employing a matrix-element based kinematic discriminant to separate the Higgs signal from the quark-antiquark annihilation and gluon continuum backgrounds, we then determine the reach of LHC Run 3 and the HL-LHC in constraining the relevant SMEFT Wilson coefficients, and compare our results to the projected indirect limits one expects to obtain from inclusive measurements of single-Higgs production processes at future LHC runs.

The SMEFT furthermore provides a consistent framework to parametrise other types of anomalous interactions, such as BSM physics modifying the bottom-Higgs and charm-Higgs dynamics. The dimension-six mixed-chirality operators within the SMEFT that can lead to modifications to the $h \to b\bar{b}$ and $h \to c\bar{c}$ partial decay widths are either of Yukawa or dipole type. Upon EW symmetry breaking, the latter type of operators induce anomalous interactions between a quark pair, one or two gluons and possibly a Higgs boson. With it come opportunities to study their effects using different Higgs and non-Higgs probes, which is the subject of Chapter 7. After a short review of the existing limits on the bottom and charm chromodipole operators from Higgs physics, we use a variety of experimental information from non-Higgs probes in order to constrain the associated Wilson coefficients. Our analysis includes collider measurements of the angular distribution of unflavoured dijet production, the invariant-mass distribution of $b$-tagged jets and the transverse-momentum spectrum of a $Z$ boson produced in association with $b$-jets, as well as measurements of flavour decays and and the neutron electric dipole moment.

We return to Higgs production in ggF in Chapter 8, where instead of including higher-dimensional SMEFT operators, we consider relevant and marginal operators of the form $|H|^2\mathcal{O}$ with $H$ the SM Higgs doublet and $\mathcal{O}$ itself a gauge-invariant operator with a mass dimension of two or lower. The possibility of sizeable Higgs-portal couplings to $|H|^2$ can be motivated by the aforementioned observed DM abundance as well the hierarchy problem of the Higgs sector. For instance, in the simplest case where $\mathcal{O} = \phi^2$ with $\phi$ being a real scalar that is a singlet under SM gauge group but odd under a $\mathbb{Z}_2$ symmetry, $\phi$ constitutes a suitable DM candidate. Furthermore, extensions of the SM where the hierarchy problem is addressed by the addition of real scalar top

partners (such as the minimal supersymmetric SM, hyperbolic Higgs or tripled top model) likewise imply Higgs-portal interactions of the form $|H|^2\mathcal{O}$. We employ the same strategy as in Chapter 6 in order to determine reach of the HL-LHC, high-energy LHC (HE-LHC) and Future Circular Collider (FCC) in constraining new physics that couples to $|H|^2$. In addition, we provide an independent analysis of the relevant Higgs-portal effects in double-Higgs production.

We conclude in Chapter 9, where we summarise our main results and comment on possible directions for future study.

This thesis is largely based on the following publications:

[42] U. Haisch and G. Koole, *Probing Higgs portals with matrix-element based kinematic discriminants in $ZZ \to 4\ell$ production*, *JHEP* **04** (2022) 166, [2201.09711].

[43] U. Haisch and G. Koole, *Off-shell Higgs production at the LHC as a probe of the trilinear Higgs coupling*, *JHEP* **02** (2022) 030, [2111.12589].

[44] L. Buonocore, G. Koole, D. Lombardi, L. Rottoli, M. Wiesemann and G. Zanderighi, *ZZ production at nNNLO+PS with MiNNLO$_{PS}$*, *JHEP* **01** (2022) 072, [2108.05337].

[45] U. Haisch and G. Koole, *Beautiful and charming chromodipole moments*, *JHEP* **09** (2021) 133, [2106.01289].

Other publications and proceedings by the author:

[46] L. Buonocore et al., *NNLO+PS with MiNNLO$_{PS}$: status and prospects*, 3, 2022. 2203.07240.

[47] R. Fleischer, R. Jaarsma and G. Koole, *Testing Lepton Flavour Universality with (Semi)-Leptonic $D_{(s)}$ Decays*, *Eur. Phys. J. C* **80** (2020) 153, [1912.08641].

# Part I

# Precision Higgs physics in the Standard Model

# Chapter 2

# Introduction & motivation

Detailed and precise predictions for scattering processes are the backbone of large parts of high-energy collider phenomenology. Combined with accurate measurements including increasingly more data, progress in this direction will allow us to test the properties and interactions of the SM particle content with unprecedented scrutiny, allowing us to further improve the sensitivity to deviations from the SM picture.

To reliably compare data to theory, we however need comprehensive simulations (performed by Monte-Carlo event generators) that model the complex final states produced in high-energy collisions. The underlying reason for this is simple: for an accurate description of a physical process we need to understand the physics at all distance or energy scales that are relevant for the process of interest. In the case of a proton-proton collider such as the LHC, the relevant distances span roughly three orders of magnitude between the size of the protons, about $10^{-15}$ m, and the hard-scattering interactions that take place on distance scales as low as or even below $10^{-18}$ m. In units of energy, accurate theory predictions for LHC cross sections should therefore include all relevant physical effects ranging from the hadronic scale of around 1 GeV up into the TeV regime. Clearly, obtaining such predictions constitutes an immensely involved task that requires carefully put together technological solutions. In fact, these problems would be unsurmountable if the underlying theory of the strong interaction, QCD, was not asymptotically free and susceptible to hard-scattering factorisation theorems — see Appendix A for more details on asymptotic freedom and other basic aspects of QCD. Before returning to the importance of having event generators that simulate collider events as accurately as possible, let us first discuss where the theoretical uncertainties arise that we aim to reduce. A more detailed account of the relevant aspects of collider theory will be provided in the next chapter.

In calculations of hadronic cross sections, hard-scattering factorisation theorems allow us to separate long-distance from short-distance behavior, thereby enabling the application of perturbative methods. For instance, in the case of inclusive Higgs production in proton-proton collisions, *i.e.* $H + X$ production where $X$ denotes any number of additional partons, the total cross section can be written as

$$\sigma \left( H + X \right) = \sum_{i,j} \int dx_1 \, f_{i/p} \left( x_1, \mu_{\mathrm{F}}^2 \right) \int dx_2 \, f_{j/p} \left( x_2, \mu_{\mathrm{F}}^2 \right) \hat{\sigma}_{ij \to H+X} \left( \hat{s}, \mu_{\mathrm{F}}^2, \mu_{\mathrm{R}}^2 \right) \\ + \mathcal{O} \left( \Lambda_{\mathrm{QCD}} / Q \right) , \tag{2.1}$$

which is valid up to power corrections of $\mathcal{O}\left(\Lambda_{\mathrm{QCD}}/Q\right)$ where $Q$ denotes the scale of the hard scattering and $\Lambda_{\mathrm{QCD}} \approx 0.2$ GeV characterises the scale at which perturbative QCD breaks down. We have furthermore defined the partonic centre-of-mass energy squared as $\hat{s} = x_1 x_2 s$ with $s$ the centre-of-mass energy of the hadrons squared, while $\mu_{\mathrm{F}}$ and $\mu_{\mathrm{R}}$ denote the factorisation and renormalisation scales, respectively. The parton densities $f_{i(j)/p}\left(x_{1(2)}, \mu_{\mathrm{F}}^2\right)$, often referred to as parton distribution functions (PDFs), describe the probability of finding the parton $i(j)$ in the proton with longitudinal momentum fraction $x_{1(2)}$. PDFs are universal and non-perturbative, meaning that the same PDFs appear in all processes (provided the same factorisation scheme is employed) and that QCD at energies near the proton mass is really a theory of the *strong* interaction. The behavior of the parton densities with respect to a changing factorisation scale $\mu_{\mathrm{F}}$[1] is governed by evolution equations such as the Dokshitzer–Gribov–Lipatov–Altarelli–Parisi (DGLAP) equations [48–50]

$$\frac{d}{d\ln\mu_{\mathrm{F}}^2} f_{i/p}\left(x, \mu_{\mathrm{F}}^2\right) = \sum_j \int_x^1 \frac{dz}{z} \frac{\alpha_s}{2\pi} P_{ij}(z) f_{j/p}\left(\frac{x}{z}, \mu_{\mathrm{F}}^2\right) , \qquad (2.2)$$

which can be viewed as the analog of the QCD $\beta$ function describing the running of $\alpha_s$ (see Appendix A). While the parton densities themselves have to be determined from experiment, their evolution (2.2) can be calculated perturbatively. Similarly to the case of the $\beta$ function, the splitting functions $P_{ij}$ appearing in (2.2) can be expanded in powers of $\alpha_s$ with the current state of the art including contributions up to the next-to-next-to-leading order (NNLO) [51, 52]. The more terms are included in the perturbative expansion of $P_{ij}$, the milder the $\mu_{\mathrm{F}}$-dependence of the ensuing cross section.

The last part of (2.1) concerns the hard-scattering interactions, often thought of as the core of the process as it usually determines its signature property (think for example of jets with high transverse momentum, di-lepton pairs or highly-virtual photons). The hard-scattering dynamics is described by the partonic cross section $\hat{\sigma}$, and takes places at energy scales $Q \gg \Lambda_{\mathrm{QCD}}$. Thanks to asymptotic freedom, we have $\alpha_s(Q) \ll 1$ and therefore $\hat{\sigma}$ is calculable with a theoretical accuracy that can be improved by including higher-order terms in its perturbative expansion

$$\hat{\sigma} = \hat{\sigma}^{\mathrm{LO}}\left(1 + \left(\frac{\alpha_s}{2\pi}\right)\delta_{\mathrm{NLO}} + \left(\frac{\alpha_s}{2\pi}\right)^2 \delta_{\mathrm{NNLO}} + \dots\right) . \qquad (2.3)$$

Here $\hat{\sigma}^{\mathrm{LO}}$ denotes the leading-order contribution and $\delta_{\mathrm{NLO}}$ and $\delta_{\mathrm{NNLO}}$ indicate the NLO and NNLO corrections, respectively. As mentioned before, $\alpha_s$ is renormalisation-scale dependent in order to deal with the UV divergences that appear beyond tree level (Appendix A). Similar to the case of the aforementioned unphysical factorisation scale, the dependence of the total cross section on the unphysical renormalisation scale decreases the more terms are included in the perturbative series for the partonic cross section (2.3). In principle, if one could include infinitely many terms in the perturbative series, the scale dependencies would compensate each other completely. Hence, varying the factorisation and renormalisation scales in the total cross section after truncating

---

[1]To be able to describe the gluons within the proton, which is especially relevant for Higgs production at the LHC, one needs to regularise the collinear divergences coming from initial-state emissions. This is done by introducing a factorisation scale $\mu_{\mathrm{F}}$ that acts as an infrared cutoff, putting the divergences in the non-perturbative PDFs — see Section 3.1.4.

the perturbative series at a given order is commonly used to estimate the theoretical uncertainties associated to missing higher-order terms. In practical applications one usually sets $\mu_{\mathrm{F}} = \mu_{\mathrm{R}} \sim Q$ with $Q$ the typical hard scale of the process — *e.g.* in the case of (2.1) one could choose the invariant mass of the Higgs — and varies the scales around this central value by a factor of two in each direction.

Thus far we have considered the simple case of fully-inclusive Higgs production, *i.e.* we did not specify anything about the final state — as indicated by the label $X$ in (2.1). However, to maximally exploit the data being harnessed at the LHC and at future colliders, it is crucial to study more exclusive observables as well. This means we are generally interested in processes with a specified number of identified additional particles or a restricted phase space for $X$, or both. These less inclusive measurements may however be affected by extra dynamics and in order to adequately describe them we will need further predictive techniques. The problem here stems from the fact that while perturbative QCD deals with partons, the final states measured in QCD processes consist of hadrons. Between the hard scattering interactions and the measured final states, the highly-energetic partons first fragment (shower) into many further partons before transitioning into hadrons. Showering and hadronisation effects are negligible for very inclusive observables since they do not significantly change the overall probability of the hard scattering. Distinguishing between partons and hadrons in the final state therefore makes little to no difference for fully-inclusive observables. In contrast, in the case of exclusive observables such as differential distributions of individual hadrons, it is crucial to account for showering and hadronisation effects. This prompts the need for dedicated computer simulations — it is the raison d'être for Monte-Carlo (MC) event generators.

MC event generators address both issues of hadron formation and the modeling of the evolution of QCD final states from short to long distances in a rather generic way. Because of their applicability to many different inclusive and exclusive observables, they have become indispensable tools for high-energy particle physics phenomenology. In Figure 2.1, we show a pictorial interpretation of the simulation of a hadron-hadron collision performed by such a MC generator. The red blob represents the hard scattering subprocess, which serves as the starting point of a PS algorithm. The PS algorithm subsequently dresses the hard partons with initial- and final-state radiation in the soft and collinear approximations, using a probabilistic Markov process. This radiation is represented by the red tree-like structure in Figure 2.1. With each of these emissions, which are ordered using a suitable ordering variable, the highly-accelerated partons are decelerated. A PS simulation is therefore typically formulated as an evolution in momentum transfer starting from a hard-scattering scale $Q \gg \Lambda_{\mathrm{QCD}}$ down to a cutoff scale $Q_0 \approx 1$ GeV where the partons become confined inside hadrons. Importantly, it includes also a non-emission probability at each iteration by introducing a so-called Sudakov form factor, resulting in a finite cross section in which large logarithmic contributions that could potentially spoil the convergence of the perturbative series are resummed to all orders in QCD. This is explained in considerably more detail in Sections 3.2 and 3.3. Finally, around energy scales of 1 GeV, the partons form color-neutral hadronic final states (represented by the light-green blobs in Figure 2.1). Since the PS predominantly generates radiation that is collinear to the original hard partons, the hadronic final state mostly consists of collimated bundles of hadrons called jets.
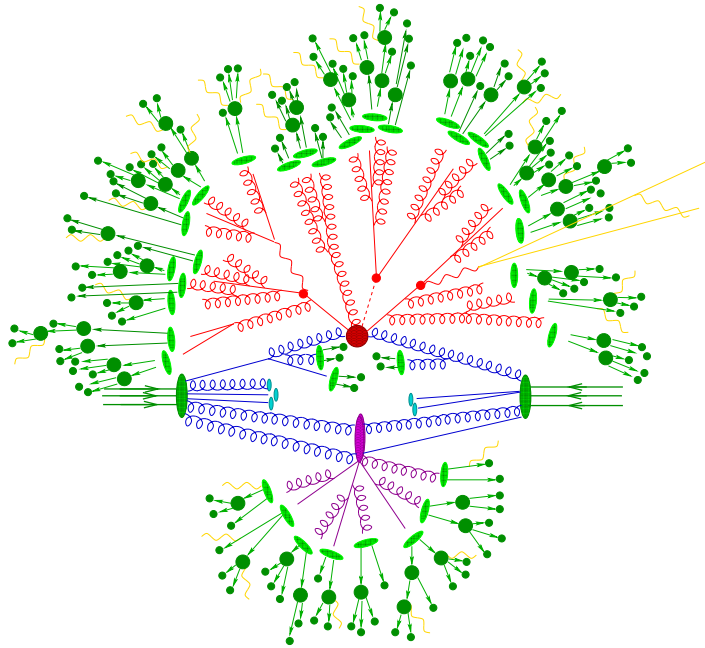
**Figure 2.1:** Pictorial interpretation of a hadron-hadron collision simulated by a MC event generator. The central red blob represents the hard collision, while the red tree-like structure around it represents QCD radiation simulated by the PS algorithm. Transitions from partons to hadrons are shown as light green blobs, while the dark green blobs indicate hadron decays. Lastly, the purple blob represents a second hard-scattering event and the yellow lines indicate soft photon radiation. Figure taken from [53].

It should at this point be clear that obtaining exclusive descriptions of hadronic collision events at the LHC is a highly non-trivial task. However, we still do not have the full picture as other effects, such as multi-parton interactions (MPI) — see *e.g.* the purple blob in Figure 2.1 — or electroweak interactions, could play a non-negligible role in experiment. They are usually labelled as part of the underlying event. Moreover, the complexity increases further if one includes higher orders in the expansion of the partonic cross section (2.3). When attempting to connect perturbative QCD calculations of the hard-scattering process beyond leading order with a PS algorithm, issues of double-counting real emissions could for instance arise. The procedure of combining fixed-order QCD calculations with a parton shower is called *matching* and plays a central role in the results presented in Chapter 4. Let us therefore give a short overview of the progress made in this direction over the last decades.

The first working proposals for the matching of NLO QCD calculations to a PS, MC@NLO [54–56] and later POWHEG [32, 33], appeared about two decades ago. The POWHEG method is described in more detail in Section 3.4.1. For multi-jet NLO+PS calculations, a method for obtaining good scale choices a priori, called Multi-scale improved NLO (MiNLO), was proposed in [57]. This method was later improved to MiNLO′ [58, 59], achieving formal NLO accuracy for colour singlet plus zero and one jet simultaneously — more details on this topic can be found in Section 3.4.2. The remarkable progress in NNLO QCD calculations[2] triggered considerable advancements

---

[2]By now all $2 \to 1$ and $2 \to 2$ colour-singlet processes are available at NNLO QCD [60–93] (see *e.g.* [94] for a review), and even first such calculations for $2 \to 3$ processes are emerging [95–98].

in the matching of NNLO QCD corrections and parton showers. The first NNLO+PS method developed was based on MiNLO′, and achieves NNLO QCD accuracy through a reweighting of MiNLO′ events. This method was successfully employed for relatively simple processes, such as Higgs production [59], Drell-Yan production [99] and associated Higgs production [100, 101], *i.e.* to processes that from a QCD point of view are just $2 \rightarrow 1$ processes. The same method was then also employed for $W^+W^-$ production, including the decay of the $W$-bosons [102]. This paper showed explicitly the limitations of the NNLO+PS method, because in practice the multi-differential reweighting can not easily be applied to more complicated processes, without making certain assumptions or approximations. About ten years ago, two more NNLO+PS methods were proposed: the UNNLOPS method, which has only been applied to Higgs [103] and Drell-Yan production [104], and the Geneva method [105, 106]. The latter was subsequently modified, as far as the interface to the shower is concerned, and applied to Drell-Yan [107], Higgsstrahlung [108], photon pair production [109], hadronic Higgs decays [110], $ZZ$ production [111], and $W\gamma$ production [112]. Recently, the Geneva method was reformulated using the transverse momentum of the colour singlet rather than the jettiness variable and applied to Drell-Yan [113].

Three years ago, the MiNNLO$_{\text{PS}}$ method was proposed [34, 35], whose underlying idea is very similar to the MiNLO′ approach. The MiNNLO$_{\text{PS}}$ method exploits the close connection to transverse-momentum resummation to include the relevant logarithmically enhanced and constant terms to reach NNLO accuracy — more details on MiNNLO$_{\text{PS}}$ are provided in Section 3.4.3. This method was first used to reproduce known results for Higgs production and Drell-Yan [34, 35] and it was applied more recently to $Z\gamma$ [114] and $W^+W^-$ production [115]. Remarkably, although it was the last NNLO+PS method to appear, MiNNLO$_{\text{PS}}$ was the first to be extended and applied to the production of a coloured final state, namely top-quark pair production [116]. In Chapter 4, we will use the MiNNLO$_{\text{PS}}$ method to obtain NNLO+PS results for $ZZ$ production, while also presenting a NLO+PS generator for the loop-induced gluon contribution. Their combination, which is dubbed nNNLO+PS, constitutes the first of its kind.

Now that we have an idea of the complexity of LHC events and the status of the tools that simulate such events, one could ask what physics insights we expect to gain from modeling these complex hadron-hadron collisions — and the elaborate final states they produce — more and more precisely. There are many answers to this question, a significant number of which are at the heart of the Higgs programme at the LHC (and possible future colliders), as was discussed in Chapter 1. Although its discovery completed the observation of the SM particle content, the Higgs has opened up many exciting avenues that remain to be fully explored. Key outstanding questions related for example to the Higgs potential (*i.e.* the nature of electroweak symmetry breaking), the Higgs mass hierarchy problem or Higgs portals to hidden sectors are the subject of ongoing research — they are studied in more detail in Part II of this thesis. However, they all have in common that not only the experimental uncertainties but also the systematics related to theoretical limitations play a crucial role in addressing them. In fact, the experimental measurements are becoming so precise that in some cases theory uncertainties could actually hinder exploiting the full potential of the LHC. Moreover, combined with the prospect of a considerable increase in statistics during the upcoming

high-luminosity phase of the LHC, this is clearly calling for a continued improvement of theory predictions.

The remainder of Part I of this thesis is structured as follows. The aim of the chapter hereafter is to explicate some of the aspects of collider theory that are most relevant for the interpretation of the precision calculations presented in Chapter 4. We will start with a discussion of the relevant aspects of perturbative QCD in Section 3.1 and resummation (Section 3.2), which leads us to a discussion of parton showers (Section 3.3), embedded in modern parton-shower MC methods in order to match them to the best-available fixed-order calculations. We will work our way up from MC frameworks designed for the matching (and merging) of NLO QCD calculations to a parton shower such as POWHEG (Section 3.4.1) and the MiNLO and MiNLO′ methods (Section 3.4.2), to the recently proposed MiNNLO$_{\rm PS}$ method (Section 3.4.3), designed for the matching of NNLO QCD calculations to parton shower, which is currently the state of the art. The MiNNLO$_{\rm PS}$ method is applied to vector-boson pair production processes in Chapter 4, presenting a comprehensive phenomenological analysis of $ZZ$ production at the LHC.

# Chapter 3

# Collider phenomenology in the precision era

## 3.1 Perturbative QCD

Short-distance quantities are perturbatively calculable in QCD thanks to asymptotic freedom, with partonic cross sections for hard-scattering reactions at hadron colliders being examples of such quantities. The collinear factorisation theorem [117] in turn disentangles these short-distance cross sections from the long-distance, non-perturbative effects, enabling the use of perturbative QCD methods to predict processes at the LHC. Here, we will discuss in some detail the anatomy of perturbative QCD computations beyond the LO, whilst introducing some of the notation[1] used in the remainder of this chapter. This section does not aim to provide a complete treatment of perturbative QCD, but rather to introduce the ingredients necessary for the interpretation of the results presented in Chapter 4. Basic aspects of QCD such as its defining Lagrangian, renormalisation and asymptotic freedom are relegated to Appendix A.

### 3.1.1 Preliminaries

The leading-order cross section for the production of an $n$-particle final state with four-momenta $p_i$ $(i = 1, \ldots, n)$ originating from two initial-state particles with four-momenta $k_1$ and $k_2$ can be written compactly as

$$\sigma^{\text{LO}} = \int d\mathbf{\Phi}_n \, \mathcal{L} \mathcal{B} \left( \mathbf{\Phi}_n \right) , \qquad (3.1)$$

where we have defined the set of variables $\mathbf{\Phi}_n = \{k_1, k_2; p_1, \ldots, p_n\}$ and $\mathcal{B} \left( \mathbf{\Phi}_n \right)$ denotes the relevant leading-order squared matrix elements

$$\mathcal{B} \left( \mathbf{\Phi}_n \right) = \left| \mathcal{M}^{(0)} \left( \mathbf{\Phi}_n \right) \right|^2 , \qquad (3.2)$$

which are assumed to include spin and colour sums and averages as well as the appropriate flux factor. In the case of hadronic collisions, the parton luminosity $\mathcal{L} = f_{i/A} \left( x_1, \mu_{\text{F}}^2 \right) f_{j/B} \left( x_2, \mu_{\text{F}}^2 \right)$ depends on the momentum-fractions of the incoming partons, defined via

$$k_1 = x_1 K_1 , \qquad k_2 = x_2 K_2 , \qquad (3.3)$$

---

[1]The notation used throughout this chapter follows closely that of [33, 34].

with $K_{1,2}$ the four-momenta of the incoming hadrons. The total cross section is obtained by integrating over the momentum fractions and phase space, *i.e.* the integral over $d\mathbf{\Phi}_n = dx_1 dx_2 d\Phi_n$ where $d\Phi_n$ is the $n$-body phase space in four dimensions,

$$
\begin{aligned}
d\Phi_n (q; p_1, \ldots, p_n) &= (2\pi)^4 \delta^4 \left( q - \sum_{i=1}^{n} p_i \right) \prod_{i=1}^{n} \frac{d^4 p_i}{(2\pi)^3} \underbrace{\delta \left( p_i^2 - m_i^2 \right) \theta \left( p_i^0 \right)}_{\delta_+ (p_i^2 - m_i^2)} \\
&= (2\pi)^4 \delta^4 \left( q - \sum_{i=1}^{n} p_i \right) \prod_{i=1}^{n} \frac{d^3 \boldsymbol{p}_i}{(2\pi)^3 2 p_i^0} ,
\end{aligned}
\tag{3.4}
$$

with $q = k_1 + k_2$.

At NLO, the generic structure of the total cross section is

$$
\sigma^{\mathrm{NLO}} = \int d\mathbf{\Phi}_n \mathcal{L} \Big[ \mathcal{B} (\mathbf{\Phi}_n) + \mathcal{V}_b (\mathbf{\Phi}_n) + \mathcal{G} (\mathbf{\Phi}_n) \Big] + \int d\mathbf{\Phi}_{n+1} \mathcal{L} \mathcal{R} (\mathbf{\Phi}_{n+1}) ,
\tag{3.5}
$$

where we have introduced $\mathbf{\Phi}_{n+1} = \{k_1, k_2; p_1, \ldots, p_{n+1}\}$ and the real and virtual corrections are denoted as $\mathcal{R} (\mathbf{\Phi}_{n+1})$ and $\mathcal{V}_b (\mathbf{\Phi}_n)$, respectively. The counterterms associated to initial-state collinear singularities in the case of hadronic initial states are contained in $\mathcal{G} (\mathbf{\Phi}_n)$.

In general, higher-order QCD calculations involve real-emission contributions and virtual-loop corrections, which foster different types of singularities. UV divergences, appearing only in virtual contributions, are removed through renormalisation (see Appendix A). Infrared (IR) divergences corresponding to the low-momentum (*soft*) and small-angle (*collinear*) limits of QCD matrix elements appear both in real and virtual corrections. They however cancel in the total cross section by virtue of the Kinoshita–Lee–Nauenberg (KLN) theorem [118, 119].[2] IR divergencies are not only important to understand the structure of events but also determine which observables are calculable within perturbative QCD.

### 3.1.2 Soft and collinear limits

To illustrate the behavior of QCD matrix elements in the soft and collinear limits, we review in some detail the simple case of $e^+ e^-$ annihilation into a quark-antiquark pair, mediated by a virtual photon. Although here the absence of hadrons in the initial state considerably simplifies the calculation[3] and we do not consider contributions mediated by a $Z$ boson, our treatment will suffice to introduce the relevant aspects of QCD in the IR regime. Initial-state radiation in the case of hadronic initial states is discussed in Section 3.1.4.

We thus consider the process $e^+ (k_2) e^- (k_1) \to q (p_1) \bar{q} (p_2)$, for which diagrams contributing at the leading and next-to-leading order in QCD are shown in Figure 3.1. The leading-order matrix element reads

$$
\mathcal{M}_{q\bar{q}} (\mathbf{\Phi}_2) = \frac{e^2 Q_q \delta_{AB}}{q^2} \left[ \overline{u} (p_1) \gamma_\mu v (p_2) \right] \left[ \overline{v} (k_2) \gamma^\mu u (k_1) \right] ,
\tag{3.6}
$$

---

[2]Except those coming from initial-state radiation in hadronic collisions because we cannot sum over degenerate states for partons in the proton, see Section 3.1.3 and 3.1.4.

[3]The PDFs in $\mathcal{L}$ could be replaced by delta functions: $f (x_a, \mu_{\mathrm{F}}^2) \to \delta (1 - x_a)$, and also $\mathcal{G} (\mathbf{\Phi}_n)$ is zero.
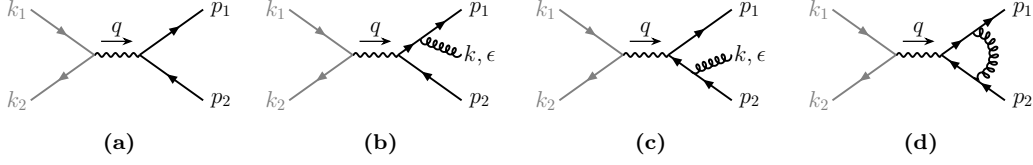
**Figure 3.1:** Schematic diagrams for $e^+(k_2)\,e^-(k_1) \to q\,(p_1)\,\bar{q}\,(p_2)$ at LO (a) and at NLO where (b) and (c) depict the real corrections and (d) shows a virtual correction.

where we defined $\mathbf{\Phi}_2 = \{q; p_1, p_2\}$ with $q = k_1 + k_2 = p_1 + p_2$, $Q_q$ is the fractional electric charge of the quarks and $\delta_{AB}$ ensures that the quark and antiquark have the same colour. The spin-averaged and colour-summed squared matrix element follows to be[4]

$$\mathcal{B}_{q\bar{q}}(\mathbf{\Phi}_2) = N_c \frac{1}{4} \left|\mathcal{M}_{q\bar{q}}(\mathbf{\Phi}_2)\right|^2 = N_c \left(e^2 Q_q\right)^2 \left(1 + \cos^2\theta\right) , \tag{3.7}$$

where $\theta$ is the centre-of-mass scattering angle of the final-state quark and $N_c = 3$ denotes the number of colours. Including the flux factor $1/(2\hat{s})$ — where $\hat{s} = q^2$ — and integrating over the two-particle phase space $d\Phi_2(q; p_1, p_2) = 1/\left(32\pi^2\right)\sin\theta\, d\theta\, d\phi$ gives the familiar parton-model total cross section for $e^+e^-$ annihiliation

$$\sigma_{q\bar{q}} = \frac{4\alpha^2\pi}{3\hat{s}} N_c Q_q^2 , \tag{3.8}$$

with $\alpha = e^2/(4\pi)$ the fine-structure constant.

The $\mathcal{O}(\alpha_s)$ correction obtained by attaching a gluon emission with four-momentum $k$ to either of the final-state quarks, *i.e.* the process $e^+(k_2)\,e^-(k_1) \to q\,(p_1)\,\bar{q}\,(p_2)\,g\,(k)$ for which the diagrams are shown in Figure 3.1 (b) and (c), corresponds to the following matrix elements

$$\mathcal{M}_{q\bar{q}g}^{(1)}(\mathbf{\Phi}_3) = g_s t^A \left[\bar{u}(p_1)\,\not{\epsilon}^*\frac{(\not{p}_1 + \not{k})}{2p_1 \cdot k}\gamma^\mu v(p_2)\right]\frac{\left(e^2 Q_q\right)^2}{q^2}\left[\bar{v}(k_2)\,\gamma_\mu u(k_1)\right] , \tag{3.9}$$

$$\mathcal{M}_{q\bar{q}g}^{(2)}(\mathbf{\Phi}_3) = -g_s t^A \left[\bar{u}(p_1)\,\gamma^\mu\frac{(\not{p}_2 + \not{k})}{2p_2 \cdot k}\not{\epsilon}^* v(p_2)\right]\frac{\left(e^2 Q_q\right)^2}{q^2}\left[\bar{v}(k_2)\,\gamma_\mu u(k_1)\right] , \tag{3.10}$$

where $\mathbf{\Phi}_3 = \{q; p_1, k, p_2\}$ with $q = k_1 + k_2 = p_1 + p_2 + k$ and $\epsilon$ is the polarisation vector of the gluon. Both matrix elements diverge when their propagators go on shell. To make the soft and collinear singular structures apparent, we write the denominators of the propagators in (3.9) and (3.10) in terms of the quark energies $E_i$ $(i = 1, 2)$, the gluon energy $\omega$ and the angle $\theta$ in the rest-frame of the virtual photon

$$2p_i \cdot k = \begin{cases} 2E_1\omega\,(1 - \cos\theta), & (i = 1) \\ 2E_2\omega\,(1 + \cos\theta), & (i = 2) \end{cases} . \tag{3.11}$$

We observe two types of singular limits: the soft-gluon limit $\omega \to 0$, where both propagators diverge, and the collinear limits $\theta \to 0$ and $\theta \to \pi$, in which either of the two propagators diverges. Importantly, the soft and collinear singular regions are insensitive to the details of the hard process, *i.e.* they are a general property of QCD matrix elements.

---

[4]Fermion masses are neglected since we are assuming a high-energy process.

**Soft limit** —— The soft limit $k \ll p_{1,2}$ (or equivalently $\omega \to 0$) is considered only for gluons since the soft limit for quarks, albeit kinematically possible for massless quarks, does not result in any divergent contributions. In the soft-gluon limit the real matrix elements in (3.9) and (3.10) simplify, adding up to

$$\mathcal{M}_{q\bar{q}g}\left(\boldsymbol{\Phi}_3\right) \underset{\text{soft}}{=\!=} g_s t^A \left[ \overline{u}\left(p_1\right) \gamma^\mu \left( \frac{p_1 \cdot \epsilon^*}{p_1 \cdot k} - \frac{p_2 \cdot \epsilon^*}{p_2 \cdot k} \right) v\left(p_2\right) \right] L_\mu \,, \qquad (3.12)$$

where we made use of the massless Dirac equations $\overline{u}\left(p_1\right) \slashed{p}_1 = 0$ and $\slashed{p}_2 v\left(p_2\right) = 0$ and the relation $\slashed{A}\slashed{B} = 2\left(A \cdot B\right) - \slashed{B}\slashed{A}$. We have furthermore introduced $L_\mu = \left(e^2 Q_q\right)^2 / q^2 \left[ \overline{v}\left(k_2\right) \gamma_\mu u\left(k_1\right) \right]$ to ease notation. Squaring (3.12) and performing the colour and polarisation sums results in a real correction which factorises into a Born piece and an eikonal factor

$$\mathcal{R}_{q\bar{q}g}\left(\boldsymbol{\Phi}_3\right) \underset{\text{soft}}{=\!=} \underbrace{\mathcal{B}_{q\bar{q}}\left(\boldsymbol{\Phi}_2\right)}_{\text{Born ME sq.}} g_s^2 C_\text{F} \underbrace{\frac{2 p_1 \cdot p_2}{\left(p_1 \cdot k\right)\left(p_2 \cdot k\right)}}_{\text{eikonal factor}} \,, \qquad (3.13)$$

where $C_\text{F} = 4/3$ is the QCD colour factor (see Appendix A). Similarly, the phase space in this limit splits into a $q\bar{q}$ piece and a radiation piece

$$d\Phi_3\left(q; p_1, k, p_2\right) \underset{\text{soft}}{=\!=} d\Phi_2\left(q; p_1, p_2\right) \times d\Phi_\text{rad}\left(k\right), \qquad d\Phi_\text{rad}\left(k\right) = \frac{d^3\boldsymbol{k}}{(2\pi)^3 2\omega} \,, \qquad (3.14)$$

which allows one to write the total cross section for $e^+\left(k_2\right) e^-\left(k_1\right) \to q\left(p_1\right) \bar{q}\left(p_2\right) g\left(k\right)$ in the soft limit as follows

$$\sigma_{q\bar{q}g} \underset{\text{soft}}{=\!=} \underbrace{\int d\Phi_2 \mathcal{B}_{q\bar{q}}\left(\boldsymbol{\Phi}_2\right)}_{\sigma_{q\bar{q}}} \times \underbrace{\int \frac{d^3\boldsymbol{k}}{(2\pi)^3 2\omega} g_s^2 C_\text{F} \frac{2 p_1 \cdot p_2}{\left(p_1 \cdot k\right)\left(p_2 \cdot k\right)}}_{\mathcal{S}} \,. \qquad (3.15)$$

One observes that in the soft limit the cross section factorises into a hard piece, indicated as $\sigma_{q\bar{q}}$, and a soft-gluon emission piece, denoted as $\mathcal{S}$. Using (3.11), the latter boils down to the following structure

$$\mathcal{S} = \frac{2\alpha_s C_\text{F}}{\pi} \int_0^\infty \frac{d\omega}{\omega} \int_0^\pi \frac{d\theta}{\sin\theta} \int_0^{2\pi} \frac{d\phi}{2\pi} \,, \qquad (3.16)$$

where $\alpha_s = g_s^2/(4\pi)$ and we have included the integration limits in the notation to make the IR divergences, for $\omega \to 0$ (soft) and for $\theta \to 0$ and $\theta \to \pi$ (collinear), explicit.

**Collinear limits** —— The limits in which the gluon becomes parallel to either the quark or the antiquark in the final state, *i.e.* $p_1 \parallel k$ and $p_2 \parallel k$ for Figure 3.1 (b) and (c), respectively, correspond to $\theta \to \{0, \pi\}$. To study the behavior of the real matrix element in the case of $\theta \to 0$ it will be convenient to use the so-called Sudakov parameterisation

$$p_1^\mu = z p^\mu + k_\perp^\mu - \frac{k_\perp^2}{z} \frac{n^\mu}{2p \cdot n} \,, \qquad k^\mu = (1-z) p^\mu - k_\perp^\mu - \frac{k_\perp^2}{1-z} \frac{n^\mu}{2p \cdot n} \,, \qquad (3.17)$$

where $p^\mu$ is a light-like ($p^2 = 0$) momentum that points in the collinear direction, $n^\mu$ is an auxiliary light-like vector and $k_\perp^\mu$ is transverse to both $p^\mu$ and $n^\mu$, *i.e.* $p \cdot k_\perp =$

$n \cdot k_\perp = 0$. We have furthermore defined the gluon's energy fraction as $z = E_1/(E_1 + \omega)$. The two-particle invariant masses follow to be

$$2p_1 \cdot k = -\frac{k_\perp^2}{z(1-z)}, \tag{3.18}$$

where the collinear limit now corresponds to $k_\perp \to 0$. We insert the parametrisation (3.17), in which we neglect the terms $\propto k_\perp, k_\perp^2$ to keep only the most singular contribution, into the real matrix element given in (3.9), square it and sum over polarisations to obtain

$$\mathcal{R}_{q\bar{q}g}(\boldsymbol{\Phi}_3) \xlongequal[\theta \to 0]{} \underbrace{\mathcal{B}_{q\bar{q}}(\boldsymbol{\Phi}_2)}_{\text{Born ME sq.}} \frac{g_s^2}{p_1 \cdot k} \underbrace{C_\mathrm{F} \frac{1+z^2}{(1-z)}}_{\hat{P}_{qq}(z)}, \tag{3.19}$$

where $\boldsymbol{\Phi}_3$ and $\boldsymbol{\Phi}_2$ are given by $\{q; p_1, k, p_2\}$ and $\{q; p_1 + k, p_2\}$, respectively, and $\hat{P}_{qq}(z)$ is the unregularised Altarelli–Parisi splitting function. Of course, in the case where the gluon is emitted from the outgoing anti-quark, in which the collinear limit corresponds to $\theta \to \pi$, one obtains an expression that is very similar to (3.19). The phase space in the collinear limit $\theta \to 0$ factorises analogously to the soft case (3.14). In the case of head-on collisions, *i.e.* in the frame where also (3.11) is valid we have explicitly that $p_1 = (E_1, 0, 0, E_1)$, $p_2 = (E_2, 0, 0, -E_2)$ and $k = \omega(1, \sin\theta\sin\phi, \sin\theta\cos\phi, \cos\theta)$. We can therefore use $k_\perp = |\boldsymbol{k}_\perp| = \omega \sin\theta$ to write the radiation phase-space element $d\Phi_{\mathrm{rad}}$ in terms of $\{z, k_\perp\}$ as follows

$$d\Phi_{\mathrm{rad}} = \frac{d^3\boldsymbol{k}}{(2\pi)^3 2\omega} = \frac{1}{8\pi^2} d\cos\theta\,\omega\,d\omega = \frac{1}{(4\pi)^2} dk_\perp^2 \frac{d\omega}{\sqrt{\omega^2 - k_\perp^2}} \approx \frac{1}{(4\pi)^2} dk_\perp^2 \frac{d\omega}{\omega}$$

$$= \frac{1}{(4\pi)^2}\left(-\frac{1}{z}\right)\frac{dz}{(1-z)} dk_\perp^2, \tag{3.20}$$

where we assumed the collinear (logarithmic) approximation in which $k_\perp^2 \ll \omega^2$. We add that imposing also the soft limit ($z^2 \to 1$) in this case further simplifies the phase-space element to

$$d\Phi_{\mathrm{rad}} = \frac{1}{(4\pi)^2}\frac{dz}{(1-z)} dk_\perp^2. \tag{3.21}$$

Combining (3.18), (3.19) and (3.20) finally allows us to write the total cross section for the process $e^+(k_2)\,e^-(k_1) \to q(p_1)\,\bar{q}(p_2)\,g(k)$ in the collinear limit $p_1 \parallel k$ as

$$\sigma_{q\bar{q}g} \xlongequal[\theta \to 0]{} \frac{\alpha_s}{2\pi} \int \frac{dk_\perp^2}{k_\perp^2} \int dz\, \hat{P}_{qq}(z) \times \underbrace{\int d\Phi_2 \mathcal{B}_{q\bar{q}}(\boldsymbol{\Phi}_2)}_{\sigma_{q\bar{q}}}. \tag{3.22}$$

We observe that, similar to the soft limit, the cross section factorises into a hard piece ($\sigma_{q\bar{q}}$) and a universal piece describing the quark-gluon splitting. The expression (3.22) contains a collinear divergence at $k_\perp \to 0$ and a soft divergence inside $P_{qq}(z)$ for $z \to 1$. However, we know that these divergences should cancel against those coming from the virtual correction — *e.g.* Figure 3.1 (d) — when combined in the total cross section, making it IR safe.

### 3.1.3 Infrared safety

Theorems such as the KLN theorem[5] state that in a theory with massless fields, suitably defined inclusive quantities are free of soft and collinear divergences: they cancel when summing over all degenerate initial and final states. To see this explicitly in the case of $e^+e^-$ annihilation, we need to calculate the virtual correction, for which a diagram is shown in Figure 3.1 (d). We will turn these divergences into something traceable using dimensional regularisation, where the phase space $d\Phi_n$ is evaluated in $d = 4 - 2\epsilon$ dimensions, i.e.

$$g_s^2 \int \frac{d^4k}{(2\pi)^4} \longrightarrow g_s^2 \mu^{2\epsilon} \int \frac{d^dk}{(2\pi)^d} \,,$$

$$d\Phi_n (q; p_1, \ldots, p_n) \longrightarrow (2\pi)^{n-d(n-1)} \delta^d \left( q - \sum_{i=1}^n p_i \right) \prod_{j=1}^n d^dp_j \delta_+ \left( p_j^2 - m_j^2 \right) , \tag{3.23}$$

where $\mu$ is the renormalisation scale, which has unit mass and is there to keep the coupling $g_s$ dimensionless for all $\epsilon$. The calculation of the real and virtual corrections in dimensional regularisation is straightforward but not very informative, so we simply give the results [121]

$$\sigma_{q\bar{q}g} = \sigma_{q\bar{q}} \times \frac{\alpha_s}{2\pi} C_F \frac{1}{\Gamma(1-\epsilon)} \left( \frac{4\pi\mu^2}{\hat{s}} \right)^\epsilon \left[ \frac{2}{\epsilon^2} + \frac{3}{\epsilon} + \frac{19}{2} - \pi^2 + \mathcal{O}(\epsilon) \right] ,$$

$$\sigma_{q\bar{q}(g)} = \sigma_{q\bar{q}} \times \frac{\alpha_s}{2\pi} C_F \frac{1}{\Gamma(1-\epsilon)} \left( \frac{4\pi\mu^2}{\hat{s}} \right)^\epsilon \left[ -\frac{2}{\epsilon^2} - \frac{3}{\epsilon} - 8 + \pi^2 + \mathcal{O}(\epsilon) \right] , \tag{3.24}$$

where $\sigma_{q\bar{q}(g)}$ denotes the virtual contribution and the strong coupling $\alpha_s$ is understood to be evaluated at the renormalisation scale $\mu$. The situation where the gluon is both soft and collinear is captured by the $1/\epsilon^2$ terms, while the cases where the gluon is either soft or collinear appear as $1/\epsilon$ poles. From (3.24) it is evident that the soft and collinear divergences cancel when combining the real and virtual contributions in the total NLO cross section, and upon taking the physical limit $\epsilon \to 0$ one obtains the simple finite result

$$\sigma_{q\bar{q}g} + \sigma_{q\bar{q}(g)} = \sigma_{q\bar{q}} \times \left( 1 + \frac{\alpha_s}{\pi} + \mathcal{O}(\alpha_s^2) \right) . \tag{3.25}$$

In fact, the KLN theorem guarantees a finite result at every order in perturbation theory. The above result (3.25) can for example be improved to NNLO QCD, by writing the total hadronic cross section $\sigma_{\text{had}}$ as

$$\sigma_{\text{had}} = \sigma_{q\bar{q}} \times \left( 1 + \left( \frac{\alpha_s}{2\pi} \right) \delta_{\text{NLO}} + \left( \frac{\alpha_s}{2\pi} \right)^2 \delta_{\text{NNLO}} + \mathcal{O}(\alpha_s^3) \right) . \tag{3.26}$$

Here, the NLO and NNLO corrections in the $\overline{\text{MS}}$ scheme[6] with renormalisation scale $\mu^2 = \hat{s}$ are given by [122, 123]

$$\delta_{\text{NLO}} = \frac{3}{2} C_F \,,$$

$$\delta_{\text{NNLO}} = \frac{1}{4} \left[ -\frac{3}{2} C_F^2 + C_F C_A \left( \frac{123}{2} - 44\zeta_3 \right) + C_F T_R n_f \left( -22 + 16\zeta_3 \right) \right] , \tag{3.27}$$

---

[5]Its quantum-electrodynamics analog is called the Bloch–Nordsieck theorem [120] and dates back to 1937.
[6]At $\mathcal{O}(\alpha_s^2)$ and higher, the coefficients $\delta_{\text{N}^n\text{LO}}$ ($n \geq 2$) generally have a $\mu^2$-dependence due to uncanceled UV divergences, i.e. they are renormalisation-scheme dependent. For the N³LO corrections, see e.g. [122].

where $C_A = 3$, $T_R = 1/2$, $n_f$ denotes the number of light quark flavours and $\zeta_3$ is shorthand notation for the Riemann zeta function $\zeta(3) \approx 1.202$.

The cancellation of IR divergences in (3.25) and (3.26) can be understood more intuitively as explained in [124] (page 550). The underlying hard process ($e^+e^- \to q\bar{q}$) takes place on very small time scales: the quark-antiquark pair is created in a time $1/\sqrt{\hat{s}}$ since the virtual photon is off-shell by an amount $q^2 = \hat{s}$. The collinear gluon emissions and virtual corrections involving soft gluons on the other hand take place over a much longer time scale and can therefore not affect the overall probability that a quark-antiquark pair was produced, but only affect the properties of the final state into which the $q\bar{q}$ system will evolve. Therefore, the only perturbative corrections that can affect the total cross section are those that have large real or virtual gluon momenta of $\mathcal{O}(\sqrt{\hat{s}})$.

As mentioned in Chapter 2, the measured final state (into which the $q\bar{q}$ system will evolve) will consist of hadrons rather than partons. Fully inclusive observables such as the total cross section unfortunately tell us nothing about the kinematic distribution of hadrons in the final state. We would therefore like to have a more exclusive description of the final state, while maintaining IR safety. To this end, let us define more precisely what is meant by an IR observable. The expectation value of an observable $\mathcal{O}(\mathbf{\Phi}_n)$ (recall $\mathbf{\Phi}_n = \{k_1, k_2; p_1, \ldots, p_n\}$) at NLO can be written as

$$\langle \mathcal{O} \rangle = \int d\mathbf{\Phi}_n \left[ \mathcal{B}(\mathbf{\Phi}_n) + \mathcal{V}_b(\mathbf{\Phi}_n) \right] \mathcal{O}(\mathbf{\Phi}_n) + \int d\mathbf{\Phi}_{n+1} \mathcal{R}(\mathbf{\Phi}_{n+1}) \mathcal{O}(\mathbf{\Phi}_{n+1}) , \quad (3.28)$$

where compared to (3.5) we have set $\mathcal{G}(\mathbf{\Phi}_n)$ to zero and removed the luminosities $\mathcal{L}$ for simplicity (*i.e.* we assumed non-hadronic initial states). The observable $\mathcal{O}$ is said to be IR (and collinear) safe if it satisfies the following criteria

$$\lim_{p_i \to 0} \mathcal{O}_{n+1}(k_1, k_2; p_1, \ldots, p_i, \ldots, p_{n+1}) = \mathcal{O}_n(k_1, k_2; p_1, \ldots, p_{i-1}, p_{i+1}, \ldots, p_n) ,$$

$$\lim_{p_i \| p_j} \mathcal{O}_{n+1}(k_1, k_2; p_1, \ldots, p_i, p_j, \ldots, p_{n+1}) = \mathcal{O}_n(k_1, k_2; p_1, \ldots, p_i + p_j, \ldots, p_n) ,$$

$$(3.29)$$

which mean that the observable should not be changed by the addition of partons in the final state that go unresolved, *i.e.* which are either soft or collinear to another parton. In the context of jets, IR safety corresponds to the jet structure being preserved when soft or collinear partons are added to the final state. The observable $\mathcal{O}$ in (3.29) — in this context often written as $\mathcal{J}$ — is then referred to as the jet or measurement function, which is defined according to a jet algorithm. The first formulation of hadronic jets was proposed for $e^+e^-$ annihilation by Sterman and Weinberg [125], but now jets are usually defined using either the $k_T$ [126, 127] or anti-$k_T$ [128] clustering algorithms, the latter of which is used in Chapter 4. The $k_T$ algorithm is briefly discussed in the context of MiNLO$'$ in Section 3.4.2. Other examples of IR-safe observables are event-shape variables such as thrust ($T$) or the $C$-parameter, defined as

$$T = \max_{\mathbf{n}} \left( \frac{\sum_i |\mathbf{p}_i \cdot \mathbf{n}|}{\sum_i |\mathbf{p}_i|} \right) , \qquad C = \frac{3}{2} \left( \frac{\sum_{i,j} |\mathbf{p}_i| |\mathbf{p}_j| \sin^2 \theta_{ij}}{\left( \sum_i |\mathbf{p}_i| \right)^2} \right) , \qquad (3.30)$$

respectively. Here, $\mathbf{p}_i$ denotes the three-momentum of particle $i$ and $\theta_{ij}$ denotes the angle between partons $i$ and $j$, with the sums running over all particles. After maximi-
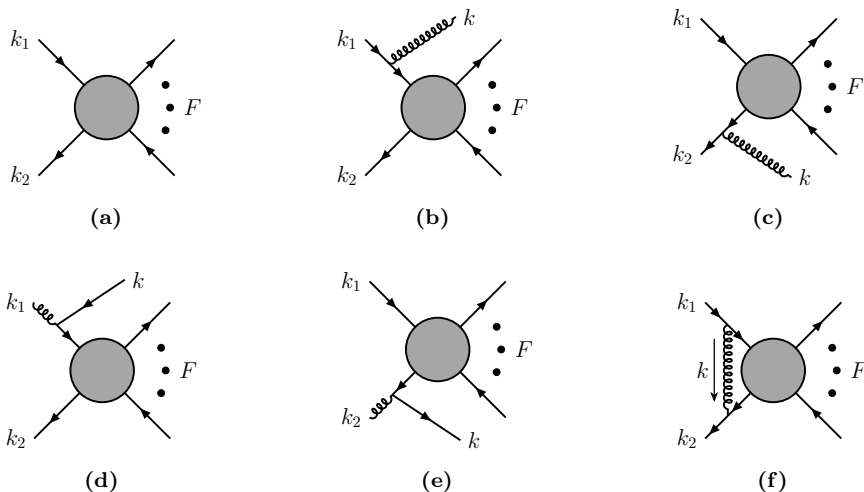
**Figure 3.2:** Schematic diagrams for the process $q\,(k_1)\,\bar{q}\,(k_2) \to F$ at LO (a) and at NLO where (b) – (e) depict real corrections while (f) shows a virtual correction. Consult the main text for further details.

sation, the unit vector $\boldsymbol{n}$ defines the thrust axis — see *e.g.* [123] and references therein for more details on event shapes in $e^+e^-$ annihilation.

### 3.1.4 Initial-state radiation

As mentioned before, the case of $e^+e^-$ annihilation provides a simple example because no QCD radiation is emitted from the initial-state leptons. Consequently, we only considered collinear limits between the final-state gluon and (anti-)quark, *i.e.* situations where the $(q \to qg)$ splitting occurs after the hard process. In this case the corresponding divergences cancel according to the KLN theorem when summing over all degenerate final states. When dealing with hadronic collisions, initial-state radiation (ISR) of soft and/or collinear gluons leads to additional divergences that do not (all) cancel against those coming from the virtual contributions.

To see this explicitly, we consider the production of a colourless $n$-particle final state $F$ through quark-antiquark annihilation, *i.e.* $q\,(k_1)\,\bar{q}\,(k_2) \to F$. Diagrams contributing at LO and NLO are shown in Figure 3.2, where we specify neither the final state $F$ nor the interaction vertex, as indicated by the grey blob. The calculation of the squared matrix elements, phase spaces and cross sections in the soft and collinear limits proceeds in a very similar fashion as for $e^+e^-$ annihilation discussed in the previous section. Instead of repeating the exercise, we will here discuss the differences between the IR limits of ISR and final-state radation (FSR). We denote the generic LO partonic cross section that follows from Figure 3.2 (a) alone as $\hat{\sigma}^{\mathrm{B}}$. Focusing on the real correction in Figure 3.2 (b) — the situation for (c) is completely analogous — we decompose the four-momentum of the gluon as $k = (1 - z)\,k_1$, with $z = E_1/(E_1 + \omega)$. Crucially, the momentum of the quark entering the hard interaction, *i.e.* after the splitting, is modified to $z k_1$. In the soft limit $\omega \ll E_i$, $(i = 1, 2)$, the partonic cross section factorises to

$$\hat{\sigma}^{\mathrm{R}}\,(k_1, k_2) \underset{\text{soft}}{=\!=} \frac{2\alpha_s C_{\mathrm{F}}}{\pi} \int \frac{d\omega}{\omega} \int \frac{d\theta}{\sin\theta} \times \hat{\sigma}^{\mathrm{B}}\,(z k_1, k_2)\,, \qquad (3.31)$$

where $\theta$ is the angle between the initial-state quark and the gluon. Taking also the small-angle (collinear) limit, we can rewrite the singular part of (3.31) in terms of $z$ and $k_\perp$ as follows

$$\frac{2\alpha_s C_F}{\pi} \int \frac{d\omega}{\omega} \int \frac{d\theta}{\sin\theta} \underset{\theta \ll 1}{=\!=} \frac{\alpha_s C_F}{\pi} \int \frac{dz}{1-z} \int \frac{dk_\perp^2}{k_\perp^2} \,, \tag{3.32}$$

where the soft and collinear divergences correspond to $z \to 1$ and $k_\perp \to 0$, respectively. In contrast to the case of FSR, the cancellation of divergences against those coming from virtual diagrams, such as the one depicted in Figure 3.2 (f), is not complete:

$$\hat{\sigma}^{\mathrm{R}} + \hat{\sigma}^{\mathrm{V}} = \frac{\alpha_s C_F}{\pi} \int \frac{dz}{1-z} \int \frac{dk_\perp^2}{k_\perp^2} \left[ \hat{\sigma}^{\mathrm{B}}\left(zk_1, k_2\right) - \hat{\sigma}^{\mathrm{B}}\left(k_1, k_2\right) \right]. \tag{3.33}$$

We observe that while the soft divergence ($z \to 1$) still cancels, the collinear one ($k_\perp \to 0$) does not, signaling that the implicit assumption of perturbative QCD being valid down to $k_\perp = 0$ is not correct. Instead of computing the real and virtual contributions explicitly in order to cancel the soft divergence, as in (3.33), it will be convenient to introduce the plus prescription

$$\int_0^1 dz \left[f\left(z\right)\right]_+ g\left(z\right) = \int_0^1 dz f\left(z\right) \left[g\left(z\right) - g\left(1\right)\right]. \tag{3.34}$$

In the collinear limit $k \parallel k_1$, where the partonic cross section factorises similar to (3.22) as follows

$$\hat{\sigma}_{qq}^{\mathrm{R+V}}\left(k_1, k_2\right) \underset{k \parallel k_1}{=\!=} \frac{\alpha_s}{2\pi} \int \frac{dk_\perp^2}{k_\perp^2} \int dz \, P_{qq}\left(z\right) \times \hat{\sigma}^{\mathrm{B}}\left(zk_1, k_2\right), \tag{3.35}$$

the soft divergence is regularised via the plus prescription for the splitting function $P_{qq}\left(z\right)$, defined as

$$P_{qq}\left(z\right) = C_F \left[\frac{1+z^2}{\left(1-z\right)}\right]_+ = C_F \left[\frac{1+z^2}{\left(1-z\right)_+} + \frac{3}{2}\delta\left(1-z\right)\right]. \tag{3.36}$$

For completeness, the explicit expressions for the remaining regularised leading-order splitting functions are given by [49]

$$\begin{aligned} P_{qg}\left(z\right) &= T_R \left[z^2 + \left(1-z\right)^2\right], \\ P_{gq}\left(z\right) &= C_F \left[\frac{1 + \left(1-z\right)^2}{z}\right], \\ P_{gg}\left(z\right) &= 2C_A \left[\frac{z}{\left(1-z\right)_+} + \frac{1-z}{z} + z\left(1-z\right)\right] + \delta\left(1-z\right)\frac{\left(11C_A - 4n_f T_R\right)}{6}. \end{aligned} \tag{3.37}$$

The NLO and NNLO corrections to (3.37) have been calculated in [129, 130] and [51, 52], respectively. The diagrams in Figure 3.2 (d) and (e), which contain initial-state splittings of the form $g \to q\bar{q}$, also contribute to the $q\left(k_1\right)\bar{q}\left(k_2\right) \to F$ process at NLO. Focusing again on the case $k \parallel k_1$ in (d), we have

$$\hat{\sigma}_{qg}^{\mathrm{R}}\left(k_1, k_2\right) \underset{k \parallel k_1}{=\!=} \frac{\alpha_s}{2\pi} \int \frac{dk_\perp^2}{k_\perp^2} \int dz \, P_{qg}\left(z\right) \times \hat{\sigma}^{\mathrm{B}}\left(zk_1, k_2\right), \tag{3.38}$$

the difference being that the splitting function $P_{qg}(z)$, defined in (3.37), does not contain a divergence at $z \to 1$, which should be the case since there is no virtual diagram to cancel it. It however still contains a collinear divergence for $k_\perp \to 0$, same as for (3.35), and these collinear divergences are not cancelled by virtual contributions.

The solution to this problem is based on collinear factorisation, which was already briefly mentioned in Chapter 2. We recall that the partonic cross section is not observable, but the total hadronic cross section is. The latter can be written as a convolution of the partonic cross section with the corresponding PDFs. The corresponding intuitive picture, called the (naive) parton model, describes the hadron at high energies as a collection of quasi-free partons (quarks and gluons), which each carry a fraction of the hadron's four-momentum. The distribution of the momentum of a hadron $H$ over its constituent partons $i$ is parametrised by parton distribution functions $f_{i/H}^{(0)}(x_i)$ that only depend on the momentum fractions $x_i$. This naive picture holds fairly well for tree-level processes, but needs some revision when considering perturbative corrections. In particular, to deal with the aforementioned initial-state collinear divergences, one introduces an arbitrary factorisation scale $\mu_{\mathrm{F}}$ and redefines the bare PDFs in such a way that the ensuing cross section is finite.

Working again in dimensional regularisation, we write the collinearly divergent integrals in (3.35) and (3.38) as follows

$$
\int_0^{\hat{s}} \frac{dk_\perp^2}{k_\perp^2} \to -\frac{1}{\Gamma(1-\epsilon)} \frac{1}{\epsilon} \left(\frac{4\pi\mu^2}{\hat{s}}\right)^\epsilon = -\frac{1}{\epsilon} + \gamma_{\mathrm{E}} - \ln(4\pi) + \ln\frac{\hat{s}}{\mu^2} + \mathcal{O}(\epsilon) , \quad (3.39)
$$

where the constant terms in the $\overline{\mathrm{MS}}$ scheme are absorbed in the $\overline{\mathrm{MS}}$ scale $\mu^2 \to \mu^2 e^{\gamma_{\mathrm{E}}}/(4\pi)$, and we have cut off the integral at $\hat{s}$ since we are considering the collinear regions. The collinear divergences, now appearing as $1/\epsilon$ poles, are absorbed in the non-perturbative PDFs via a redefinition of their bare quantities. For instance, in the case of an incoming proton with gluon radiation off one of its constituent quarks, we have [131]

$$
\begin{aligned}
f_{q/p}\left(x, \mu_{\mathrm{F}}^2\right) = & \, f_{q/p}^{(0)}(x) \\
& + \frac{\alpha_s}{2\pi} \int_x^1 \frac{dz}{z} f_{q/p}^{(0)}(z) \left[\frac{-1}{\Gamma(1-\epsilon)} \frac{1}{\epsilon} \left(\frac{4\pi\mu^2}{\mu_{\mathrm{F}}^2}\right)^\epsilon P_{qq}\left(\frac{x}{z}\right) + C_{qq}\left(\frac{x}{z}\right)\right],
\end{aligned}
$$
$$(3.40)$$

where the coefficient function $C_{qq}(x/z)$ defines the factorisation scheme, with the common choice being the $\overline{\mathrm{MS}}$ scheme, in which

$$
C_{qq}^{\overline{\mathrm{MS}}}(x) = 0 . \quad (3.41)
$$

The evolution of the parton densities with respect to a changing scale $\mu^2$ is governed by the DGLAP equation [48–50], cf. (2.2), which is a matrix in flavour space since the proton contains both gluons and quarks. Explicitly, we have

$$
\frac{d}{d\ln\mu^2} \begin{pmatrix} f_{q/p}(x, \mu^2) \\ f_{g/p}(x, \mu^2) \end{pmatrix} = \frac{\alpha_s(\mu^2)}{2\pi} \sum_{q,\bar{q}} \int_x^1 \frac{dz}{z} \begin{pmatrix} P_{qq}\left(\frac{x}{z}\right) & P_{qg}\left(\frac{x}{z}\right) \\ P_{gq}\left(\frac{x}{z}\right) & P_{gg}\left(\frac{x}{z}\right) \end{pmatrix} \begin{pmatrix} f_{q/p}(z, \mu^2) \\ f_{g/p}(z, \mu^2) \end{pmatrix},
$$
$$(3.42)$$

where the sum runs over $2n_f$ quark and anti-quark flavours. Finally, the above considerations allow us to write the total hadronic cross section up to power corrections of $\mathcal{O}(\Lambda_{\text{QCD}}/Q)$ at NLO as follows

$$\sigma^{\text{NLO}}(K_1, K_2) = \sum_{i,j} \int dx_1 f_{i/p}(x_1, \mu_{\text{F}}^2) \int dx_2 f_{j/p}(x_2, \mu_{\text{F}}^2)\, \hat{\sigma}_{ij}^{\text{NLO}}(x_1 K_1, x_2 K_2)\,,$$

(3.43)

where $K_i$ are the momenta of the incoming protons — see (3.3) — and the partonic cross sections read

$$\hat{\sigma}_{qq}^{\text{NLO}}(k_1, k_2) = \hat{\sigma}^{\text{B}}(k_1, k_2) + \frac{\alpha_s}{2\pi} \int dz\, P_{qq}(z) \ln \frac{\hat{s}}{\mu^2} \left[ \hat{\sigma}^{\text{B}}(zk_1, k_2) + \hat{\sigma}^{\text{B}}(k_1, zk_2) \right]$$
$$+ R_{qq}(k_1, k_2)\,,$$
$$\hat{\sigma}_{qg}^{\text{NLO}}(k_1, k_2) = \frac{\alpha_s}{2\pi} \int dz\, P_{qg}(z) \ln \frac{\hat{s}}{\mu^2} \hat{\sigma}^{\text{B}}(zk_1, k_2) + R_{qg}(k_1, k_2)\,,$$

(3.44)

where $R_{qq}$ and $R_{qg}$ denote the NLO pieces that are finite in the soft and collinear limits. The partonic cross sections (and hence also the total hadronic cross section) are finite since all the IR divergences ($1/\epsilon$ poles) are either cancelled or absorbed in the PDFs. Thus in general, well-defined observables should either be IR (and collinear) safe or collinearly factorisable.

## 3.2 Resummation

Fixed-order perturbative calculations of QCD processes in many cases contain logarithmic terms. For instance, we have seen that the partonic cross sections described in Section 3.1.4 — see (3.44) — contribute terms $\propto \ln(\hat{s}/\mu^2)$ to the total hadronic cross section at NLO. These terms can potentially spoil the convergence of the perturbative expansion when the combination $\alpha_s \ln(\hat{s}/\mu^2)$ becomes of order one or even larger. Their effect can however be minimised by choosing $\mu \simeq \sqrt{\hat{s}}$, which in the case of inclusive observables is sufficient as only logarithms of the form $\ln(\hat{s}/\mu^2)$ appear in their theoretical expressions. However, experimental measurements often probe only a restricted part of the full phase space, vetoing a significant part of the real emissions in the soft and collinear regions. As a result, the cancellation between the real and virtual corrections is only partial since the latter is not subject to the constraint.

Below, we will show in more detail how this incomplete cancellation leads to large logarithms to accompany each order of $\alpha_s$, but in a nutshell the problem can be understood as follows: vetoing real emissions with transverse momentum above a cutoff $k_{\text{cut}}$ will gives rise to logarithms $\alpha_s \ln^2(\mu/k_{\text{cut}})$. The virtual corrections on the other hand are not sensitive to the constraint and contain logarithms of the form $\alpha_s \ln^2(Q/\mu)$ with $Q = \sqrt{\hat{s}}$ the hard scale. Combining the two results in Sudakov logarithms of the form $\alpha_s \ln^2(Q/k_{\text{cut}})$, which become problematic when $k_{\text{cut}} \ll Q$. This observation holds in general: any observable $V$ sensitive to soft and collinear radiation, measured at some value $v$, will involve terms of the type $\alpha_s^n L^k$ with $L = \ln(Q/v)$ and $k \leq 2n$ to all $n$ orders in the perturbative expansion. Fixed-order perturbative calculations are therefore only reliable for inclusive observables or away from the soft and collinear regions

of phase space. The bulk of events is however typically in the region where $v \ll Q$, where one needs to carry out an all-order re-organisation, or *resummation*, of these logarithmically-enhanced terms in order to restore the predictivity of the perturbative treatment.

### 3.2.1 Large logarithms

The differential study of many LHC processes beyond the leading order in $\alpha_s$, *e.g.* Higgs production or Drell–Yan, is not only of phenomenological importance, but also allows for a more in-depth study of non-trivial aspects of QCD. However, similarly to case where experimental constraints on emissions in the final state induce large logarithms, differential observables are also plagued by large logarithmic terms when they are probed at scales that differ significantly from the hard scale $Q$. To see more precisely how these logarithms arise, recall that both ISR and FSR of soft-collinear gluons factorises — *cf.* (3.15) and (3.16) or (3.31) and (3.32) — resulting in contributions to the partonic cross section of the form

$$\hat{\sigma}^{\mathrm{R}} = \hat{\sigma}^{\mathrm{B}} \frac{\alpha_s C_{\mathrm{F}}}{\pi} \int \frac{d\omega}{\omega} \int \frac{dk_\perp^2}{k_\perp^2} \,. \tag{3.45}$$

Cutting the integration over $\omega$ at $\omega = k_\perp$ from below and at $\omega = Q$ from above respectively manifests the collinear and soft approximations and allows one to write the $k_\perp$-differential partonic cross section as follows

$$\frac{d\hat{\sigma}^{\mathrm{R}}}{dk_\perp^2} = \hat{\sigma}^{\mathrm{B}} \frac{\alpha_s C_{\mathrm{F}}}{\pi} \frac{1}{k_\perp^2} \int_{k_\perp}^{Q} \frac{d\omega}{\omega} = \hat{\sigma}^{\mathrm{B}} \frac{\alpha_s C_{\mathrm{F}}}{2\pi} \frac{1}{k_\perp^2} \ln \frac{Q^2}{k_\perp^2} \,. \tag{3.46}$$

Including the virtual contribution introduces a plus prescription on the singular part such that the cumulant $\hat{\Sigma}$ (or integrated contribution) is finite,

$$\frac{d\hat{\sigma}^{\mathrm{R+V}}}{dk_\perp^2} = \hat{\sigma}^{\mathrm{B}} \frac{\alpha_s C_{\mathrm{F}}}{2\pi} \left[ \frac{1}{k_\perp^2} \ln \frac{Q^2}{k_\perp^2} \right]_+ \quad \Rightarrow \quad \hat{\Sigma}\left(Q^2\right) = \frac{1}{\hat{\sigma}^{\mathrm{B}}} \int_0^{Q^2} dk_\perp^2 \frac{d\hat{\sigma}^{\mathrm{R+V}}}{dk_\perp^2} = 1 + \mathcal{O}\left(\alpha_s\right) \,, \tag{3.47}$$

where the $\mathcal{O}\left(\alpha_s\right)$ part, being free of large logarithms, will be neglected for now. Since the virtual contribution is concentrated at $k_\perp^2 = 0$, we can decompose the integral as follows

$$\hat{\Sigma}\left(Q^2\right) = \frac{1}{\hat{\sigma}^{\mathrm{B}}} \left[ \int_0^{p_{\mathrm{T}}^2} dk_\perp^2 \frac{d\hat{\sigma}^{\mathrm{R+V}}}{dk_\perp^2} + \int_{p_{\mathrm{T}}^2}^{Q^2} dk_\perp^2 \frac{d\hat{\sigma}^{\mathrm{R}}}{dk_\perp^2} \right] = \hat{\Sigma}\left(p_{\mathrm{T}}^2\right) + \frac{1}{\hat{\sigma}^{\mathrm{B}}} \int_{p_{\mathrm{T}}^2}^{Q^2} dk_\perp^2 \frac{d\hat{\sigma}^{\mathrm{R}}}{dk_\perp^2} \,, \tag{3.48}$$

where $p_{\mathrm{T}}$ is the maximally allowed total transverse momentum of the Born final state, such that

$$\hat{\Sigma}\left(p_{\mathrm{T}}^2\right) \approx 1 - \frac{\alpha_s C_{\mathrm{F}}}{2\pi} \ln^2 \frac{Q^2}{p_{\mathrm{T}}^2} \,. \tag{3.49}$$

The above result is correct in the so-called double leading logarithmic approximation (DLLA), since we only kept logarithmic terms that scale as $\alpha_s L^2$ (with $L = \ln Q^2/p_{\mathrm{T}}^2$), which become problematically large when $p_{\mathrm{T}} \ll Q$. From here, it is straightforward to

show that in the case of $n$ soft-collinear gluon emissions whose transverse momenta are strongly ordered, *i.e.*

$$k_{\perp,1} \ll k_{\perp,2} \ll \cdots \ll k_{\perp,n} \lesssim p_{\mathrm{T}} \ll Q \,, \tag{3.50}$$

we have

$$\hat{\Sigma}\left(p_{\mathrm{T}}^2\right) = \sum_{n=0}^{\infty} \frac{1}{n!} \left[ -\frac{\alpha_s C_{\mathrm{F}}}{2\pi} \ln^2 \frac{Q^2}{p_{\mathrm{T}}^2} \right]^n = \exp\left[ -\frac{\alpha_s C_{\mathrm{F}}}{2\pi} \ln^2 \frac{Q^2}{p_{\mathrm{T}}^2} \right] \,, \tag{3.51}$$

where the factor of $1/n!$ stems from the fact that gluons are indistinguishable. From (3.51), one finds the normalised differential cross section with respect to $p_{\mathrm{T}}^2$ in the DLLA as follows

$$\frac{1}{\hat{\sigma}^{\mathrm{B}}} \frac{d\hat{\sigma}}{dp_{\mathrm{T}}^2} = \frac{d}{dp_{\mathrm{T}}^2} \hat{\Sigma}\left(p_{\mathrm{T}}^2\right) = \frac{\alpha_s C_{\mathrm{F}}}{\pi} \frac{1}{p_{\mathrm{T}}^2} \ln \frac{Q^2}{p_{\mathrm{T}}^2} \exp\left[ -\frac{\alpha_s C_{\mathrm{F}}}{2\pi} \ln^2 \frac{Q^2}{p_{\mathrm{T}}^2} \right] \,. \tag{3.52}$$

Remarkably, the double leading logarithms to all orders in $\alpha_s$ have been resummed in the expression (3.52) by means of exponentiation. The exponent is called the *Sudakov form factor* [132], which encodes the probability of not emitting a gluon with a transverse momentum larger than $p_{\mathrm{T}}$. Beyond the DDLA, fixed-order perturbative descriptions of differential distributions in the small-$p_{\mathrm{T}}$ regions generally require the resummation of large logarithms of the form

$$\frac{1}{p_{\mathrm{T}}^2} \alpha_s^n \ln^m \frac{Q^2}{p_{\mathrm{T}}^2} \quad \text{with} \quad m \leq 2n - 1 \,, \tag{3.53}$$

appearing at every order in $\alpha_s$. The logarithmic accuracy of a resummed prediction is commonly defined at the level of the *logarithm* of the cumulative cross section, or, equivalently, from the argument of the exponent appearing in the Sudakov form factor in (3.52), where one refers to the dominant terms proportional to $\alpha_s^n L^{n+1}$ as leading logarithms (LL), to terms of the type $\alpha_s^n L^n$ as next-to-leading logarithms (NLL), to terms of the type $\alpha_s^n L^{n-1}$ as next-to-next-to-leading logarithms (NNLL), and so on.

One furthermore observes that the Sudakov form factor forces the cross section to tend to zero in the $p_{\mathrm{T}} \to 0$ limit, which is in fact misleading. A small value for $p_{\mathrm{T}}$ does not imply that all emitted gluons are soft, but merely that the vectorial sum of their transverse momenta is small. Contributions from multiple soft-gluon emission with $k_{\perp,i} \sim p_{\mathrm{T}}$ and $\sum_i \boldsymbol{k}_{\perp,i} = \boldsymbol{p}_{\mathrm{T}}$ are therefore relevant, but not included in the unphysically strong Sudakov suppression in (3.52). A more adequate treatment of the small-$p_{\mathrm{T}}$ distribution requires imposing the conservation of transverse momentum in multiple-gluon emission, which is usually performed in impact-parameter space.

### 3.2.2 Small-$p_{\mathrm{T}}$ resummation in impact-parameter space

It was shown in [133] that the resummation of soft-gluon effects is most naturally performed using the impact-parameter formalism, which was fully formalised by Collins, Soper and Sterman [134] in terms of perturbative coefficients. In the $b$-space method, one introduces a two-dimensional impact parameter $\boldsymbol{b}$, which is the Fourier transform of $\boldsymbol{p}_{\mathrm{T}}$, and imposes momentum conservation on the total transverse momentum of $n$ soft-gluon emissions as follows

$$\delta^2 \left( \sum_{i=1}^{n} \boldsymbol{k}_{\perp,i} - \boldsymbol{p}_{\mathrm{T}} \right) = \int \frac{d^2b}{(2\pi)^2} e^{-i\boldsymbol{b}\cdot\boldsymbol{p}_{\mathrm{T}}} \prod_{i=1}^{n} e^{i\boldsymbol{b}\cdot\boldsymbol{k}_{\perp,i}} \,, \tag{3.54}$$

allowing the resummed differential partonic cross section in (3.52) in $b$-space to be written as [135–137]

$$\frac{1}{\hat{\sigma}^{\mathrm{B}}}\frac{d\hat{\sigma}}{dp_{\mathrm{T}}^2} \simeq \frac{1}{2}\int_0^\infty b\,db\,J_0\left(bp_{\mathrm{T}}\right)\exp\left[-S\left(b,Q\right)\right]$$
$$= \frac{d}{dp_{\mathrm{T}}^2}p_{\mathrm{T}}\int_0^\infty db\,J_1\left(bp_{\mathrm{T}}\right)\exp\left[-S\left(b,Q\right)\right], \tag{3.55}$$

where in the second line we used identity $x\,J_0\left(x\right) = d\left(x\,J_1\left(x\right)\right)/dx$ relating the Bessel functions of the first kind. The exponent $\exp\left(-S\right)$ denotes the Sudakov form factor in $b$-space, which will be further discussed below. First, we write the hadronic cumulative cross section $\Sigma$, differential in the Born phase space $\mathbf{\Phi}_{\mathrm{F}}$, that follows from (3.55) by including a luminosity factor $\mathcal{L}_b$ as follows

$$\frac{d\Sigma\left(p_{\mathrm{T}}\right)}{d\mathbf{\Phi}_{\mathrm{F}}} = p_{\mathrm{T}}\int_0^\infty db\,J_1\left(bp_{\mathrm{T}}\right)\exp\left[-S\left(b,Q\right)\right]\mathcal{L}_b\left(b,Q\right), \tag{3.56}$$

where the Sudakov form factor is independent of the specific hard-scattering process, allowing us to put the derivative with respect to $\mathbf{\Phi}_{\mathrm{F}}$ in the definition of $\mathcal{L}_b$ — see (3.61). The function $S\left(b,Q\right)$ has the following integral representation

$$S\left(b,Q\right) = \int_{b_0^2/b^2}^{Q^2}\frac{dq^2}{q^2}\left[A\left(\alpha_s\left(q\right)\right)\ln\frac{Q^2}{q^2} + B\left(\alpha_s\left(q\right)\right)\right], \tag{3.57}$$

where $b_0 = 2e^{-\gamma_{\mathrm{E}}}$ and the functions $A\left(\alpha_s\right)$ and $B\left(\alpha_s\right)$ can be expanded in a perturbative series, i.e.

$$A\left(\alpha_s\right) = \sum_{i=1}^\infty \left(\frac{\alpha_s}{2\pi}\right)^i A^{(i)}, \qquad B\left(\alpha_s\right) = \sum_{i=1}^\infty \left(\frac{\alpha_s}{2\pi}\right)^i B^{(i)}. \tag{3.58}$$

The first terms in the expansions (3.58) are independent of the specific hard process, but do depend on the incoming partons. Defining $C_q = C_{\mathrm{F}}$ and $C_g = C_{\mathrm{A}}$, the explicit expressions for $A^{(i)}$ up to $i = 3$ are given by [138]

$$A_{q,g}^{(1)} = 2C_{q,g}\,,$$
$$A_{q,g}^{(2)} = 2C_{q,g}\left[C_{\mathrm{A}}\left(\frac{67}{18} - \frac{\pi^2}{6}\right) - \frac{10}{9}T_{\mathrm{R}}n_f\right],$$
$$A_{q,g}^{(3)} = 2C_{q,g}\left\{C_{\mathrm{A}}^2\left[\frac{245}{24} - \frac{67}{9}\frac{\pi^2}{6} + \frac{11}{6}\zeta_3 + \frac{11}{5}\left(\frac{\pi^2}{6}\right)^2\right] + C_{\mathrm{F}}n_f\left[-\frac{55}{24} + 2\zeta_3\right] \tag{3.59}\right.$$
$$\left. + C_{\mathrm{A}}n_f\left[-\frac{209}{108} + \frac{10}{9}\frac{\pi^2}{6} - \frac{7}{3}\zeta_3\right] + n_f^2\left[-\frac{1}{27}\right]\right\}.$$

The $B^{(i)}$ terms can be identified with the quark or gluon anomalous dimensions $\gamma_{q,g}^{(i)}$, and for $i = 1$ we have

$$B_{q,g}^{(1)} = -2\gamma_{q,g}^{(1)} = \begin{cases} -3C_{\mathrm{F}}\,, & \text{(quark)} \\ -4\pi\beta_0\,, & \text{(gluon)} \end{cases}, \tag{3.60}$$

where $\beta_0$ is defined in (A.20). Higher-order $B^{(i)}$ terms ($i \geq 2$) generally depend on the hard process — the $B^{(2)}$ terms have for instance been determined for Drell–Yan and Higgs production in [139, 140].

### 3.2.3 A prelude to MiNNLO$_{\text{PS}}$

Transverse-momentum resummation plays a central role in the MiNNLO$_{\text{PS}}$ method [34, 35], which will be discussed in more detail in Section 3.4.3. The aim of this section is to connect our discussion of small-$p_{\text{T}}$ resummation in $b$-space to MiNNLO$_{\text{PS}}$, with an emphasis on the resummation formulae upon which it is built. To this end, we proceed along the lines of Appendix E of [34] and the result of what follows will serve as the starting point of our discussion of the MiNNLO$_{\text{PS}}$ method in Section 3.4.3. We note that while the more detailed derivation presented in the main text of [34] employs transverse-momentum resummation directly in momentum space [141, 142], the result shown below is equivalent up to the accuracy required by MiNNLO$_{\text{PS}}$, as also mentioned in Appendix E of said article.

The $b$-space expression for the hadronic cumulative cross section, differential with respect the Born phase space, was already derived in the previous section — see (3.56). Very symbolically, the luminosity factor $\mathcal{L}_b$ for MiNNLO$_{\text{PS}}$ that up to NNLO includes the squared hard-virtual matrix elements $(H)$ for the production of F and the convolution of the collinear coefficient functions $(C)$ with the PDFs $(f)$ can be written as[7]

$$\mathcal{L}_b\left(b_0/b\right) \sim \sum_{a,b} \frac{d|\mathcal{M}^{\text{F}}|^2}{d\mathbf{\Phi}_{\text{F}}} \sum_{i,j} \left(C_{ia} \otimes f_i\right) \bar{H}\left(b_0/b\right) \left(C_{jb} \otimes f_j\right), \tag{3.61}$$

with $\mathcal{M}^{\text{F}}$ denoting the Born matrix element and $\bar{H}$ being identical to its momentum-space analog $H$, defined as

$$H\left(Q\right) = 1 + \left(\frac{\alpha_s\left(Q\right)}{2\pi}\right) H^{(1)} + \left(\frac{\alpha_s\left(Q\right)}{2\pi}\right)^2 H^{(2)}, \tag{3.62}$$

except for an extra term $C_{\text{F}} 16/3\pi\beta_0\zeta_3$ present in the $H^{(2)}$ terms of the latter — see [142] for more details. We have furthermore used shorthand notation for the convolution between two functions, defined as $(f \otimes g)(z) = \int_z^1 dx/x\, f(x)\, g(z/x)$. A systematic expansion of (3.57) — see e.g. [143] — in the notation of [34] is given by

$$S\left(b_0/b\right) = -Lg_1\left(\lambda_b\right) - g_2\left(\lambda_b\right) - \frac{\alpha_s}{\pi}\bar{g}_3\left(\lambda_b\right), \tag{3.63}$$

where $L = \ln\left(Qb/b_0\right)$, $\lambda_b = \alpha_s\left(Q\right)\beta_0 L$ and

$$\bar{g}_3 = g_3 + \frac{2\zeta_3\left(A^{(1)}\right)^2}{2\pi\beta_0} \frac{\lambda_b}{1 - 2\lambda_b}. \tag{3.64}$$

The coefficient functions $g_1$, $g_2$ and $g_3$, which are equivalent in momentum space and

---

[7]A more detailed and correct definition of the luminosity factor, squared hard-virtual matrix elements and collinear coefficient functions will be given in Section 3.4.3.

impact-parameter space, are given by[8]

$$
g_1\left(\lambda\right) = \frac{A^{(1)}}{\pi\beta_0}\frac{2\lambda+\ln\left(1-2\lambda\right)}{2\lambda}\,,
$$

$$
g_2\left(\lambda\right) = \frac{1}{2\pi\beta_0}\ln\left(1-2\lambda\right)B^{(1)} - \frac{A^{(2)}}{4\pi^2\beta_0^2}\frac{2\lambda+\left(1-2\lambda\right)\ln\left(1-2\lambda\right)}{1-2\lambda}
$$
$$
- A^{(1)}\frac{\beta_1}{4\pi\beta_0^3}\frac{\ln\left(1-2\lambda\right)\left(\left(2\lambda-1\right)-2\right)-4\lambda}{1-2\lambda}\,,
$$

$$
g_3\left(\lambda\right) = B^{(1)}\frac{\beta_1}{2\beta_0^2}\frac{2\lambda+\ln\left(1-2\lambda\right)}{1-2\lambda} - \frac{1}{2\pi\beta_0}\frac{\lambda}{1-2\lambda}\tilde{B}^{(2)} - \frac{A^{(3)}}{4\pi^2\beta_0^2}\frac{\lambda^2}{\left(1-2\lambda\right)^2}
$$
$$
+ A^{(2)}\frac{\beta_1}{4\pi\beta_0^3}\frac{2\lambda\left(3\lambda-1\right)+\left(4\lambda-1\right)\ln\left(1-2\lambda\right)}{\left(1-2\lambda\right)^2}
$$
$$
+ A^{(1)}\left(\frac{\lambda\left(\beta_0\beta_2\left(1-3\lambda\right)+\beta_1^2\lambda\right)}{\beta_0^4\left(1-2\lambda\right)^2}\right.
$$
$$
+ \frac{\left(1-2\lambda\right)\ln\left(1-2\lambda\right)\left(\beta_0\beta_2\left(1-2\lambda\right)+2\beta_1^2\lambda\right)}{2\beta_0^4\left(1-2\lambda\right)^2}
$$
$$
\left.+ \frac{\beta_1^2}{4\beta_0^4}\frac{\left(1-4\lambda\right)\ln^2\left(1-2\lambda\right)}{\left(1-2\lambda\right)^2}\right)\,,
$$

(3.65)

where

$$
\tilde{B}^{(2)} = B^{(2)} + 2\zeta_3\left(A^{(1)}\right)^2 + 2\pi\beta_0 H^{(1)}\,,
\tag{3.66}
$$

is indeed process-dependent and the other coefficients $A^{(i)}$ and $B^{(i)}$ have been given in (3.59) and (3.60). With the above definitions at hand, one could show that the integrand in (3.56) can be expanded around $b = b_0/p_{\mathrm{T}}$ to obtain [34, 144]

$$
\frac{d\Sigma\left(p_{\mathrm{T}}\right)}{d\boldsymbol{\Phi}_{\mathrm{F}}} \approx e^{-S\left(p_{\mathrm{T}}\right)}\left\{\mathcal{L}\left(p_{\mathrm{T}}\right)\left(1 - \frac{\zeta_3}{4}S''\left(p_{\mathrm{T}}\right)S'\left(p_{\mathrm{T}}\right) + \frac{\zeta_3}{12}S'''\left(p_{\mathrm{T}}\right)\right)\right.
$$
$$
\left.- \frac{\zeta_3}{4}\frac{\alpha_s\left(p_{\mathrm{T}}\right)}{\pi}S''\left(p_{\mathrm{T}}\right)P\otimes\mathcal{L}\left(p_{\mathrm{T}}\right)\right\} + \mathcal{O}\left(\alpha_s^3\left(Q\right)\right)\,,
$$

(3.67)

where $P$ denotes the regularised splitting function. The above result is accurate at $\mathcal{O}\left(\alpha_s^2\right)$ up to sub-leading logarithms (*i.e.* terms beyond NNLL). The terms proportional to $S''$ and $S'''$ can be absorbed into the resummation coefficients by making the following substitutions [34]

$$
B^{(2)} \rightarrow \tilde{B}^{(2)}\,,
$$
$$
H^{(2)} \rightarrow \tilde{H}^{(2)} = H^{(2)} + 2\zeta_3 A^{(1)}B^{(1)}\,,
$$
$$
C^{(2)}\left(z\right) \rightarrow \tilde{C}^{(2)}\left(z\right) = C^{(2)}\left(z\right) - 2\zeta_3 A^{(1)}P^{(0)}\left(z\right)\,.
$$

(3.68)

and by using

$$
S'''\left(p_{\mathrm{T}}\right) = 32 A^{(1)}\pi\beta_0\left(\frac{\alpha_s}{2\pi}\right)^2 + \mathcal{O}\left(\alpha_s^3\right)\,,
\tag{3.69}
$$

---

[8]The explicit expressions for the coefficients of the QCD $\beta$ function are given in (A.20).

in combination with the replacement

$$\bar{H}^{(2)} \to H^{(2)} = \bar{H}^{(2)} + \frac{8}{3}\zeta_3 A^{(1)}\pi\beta_0\,. \tag{3.70}$$

The above considerations finally allow one to write the differential cross section in $p_{\mathrm{T}}$ and $\boldsymbol{\Phi}_{\mathrm{F}}$ compactly as

$$\frac{d\Sigma\left(p_{\mathrm{T}}\right)}{d\boldsymbol{\Phi}_{\mathrm{F}}dp_{\mathrm{T}}} = \frac{d}{dp_{\mathrm{T}}}\left\{e^{-S(p_{\mathrm{T}})}\mathcal{L}\left(p_{\mathrm{T}}\right)\right\} + R_f\left(p_{\mathrm{T}}\right) + \mathcal{O}\left(\alpha_s^3\right)\,, \tag{3.71}$$

where $R_f$ contains terms that are not singular in the $p_{\mathrm{T}} \to 0$ limit. The above result (3.71) is the starting point for a derivation of the central ingredient of MiNNLO$_{\mathrm{PS}}$, the $\bar{B}$ function — see Section 3.4.3. As we will see, the MiNNLO$_{\mathrm{PS}}$ $\bar{B}$ function generates the first radiation, while the generation of the second radiation is done according to the POWHEG method discussed in Section 3.4.1. The remaining emissions are subsequently generated in a parton shower simulation, which is the subject of the next section.

## 3.3 Parton shower simulations

The analytic resummation techniques discussed in the previous section are crucial for an accurate description of spectra in regions dominated by soft and collinear QCD radiation. While for specific processes and observables analytic resummation calculations are available (NLL for most; up to N$^3$LL in some cases), a generic way of achieving resummation for any observable, at least at LL accuracy, is extremely desirable from a collider-phenomenology point of view. This is achieved by dedicated *parton shower* algorithms embedded in event-generator frameworks such as PYTHIA [145, 146], HERWIG [147, 148] and SHERPA [149, 150]. The aim of a PS algorithm is, as already mentioned in Chapter 2, to connect the perturbative and non-perturbative descriptions of hadronic collisions, thereby enabling a PS MC generator to simulate hadron-level events, which is crucial for comparison to experiment.

The starting point of any PS algorithm is the probability for a parton to split (or *branch*) into further partons. Figure 3.3 shows, schematically, the branching of a parton $a$ into partons $b$ and $c$, where $a$ is either incoming (a) or outgoing (b) with respect to the hard process, described by $\mathcal{M}_n$. While Figure 3.3 shows specifically a $g \to q\bar{q}$ splitting, the discussion here applies to any QCD splitting. Furthermore, $\theta$ denotes the angle between partons $b$ and $c$ and $\mathcal{M}_{n+1}$ is the matrix element describing the hard reaction and parton branching combined. In the collinear region, it is convenient to parametrise the phase space $\Phi_{\mathrm{rad}}$ in terms of a hardness scale $t$, the energy fraction $z$ of the emitter after the emission, and the azimuthal angle $\phi$ of splitting, which is averaged over. The differential branching probability for Figure 3.3 (b) in this region is given by[9]

$$d\mathcal{P}_{a \to bc}^{\mathrm{FSR}}\left(\Phi_{\mathrm{rad}}\right) \to d\mathcal{P}_{a \to bc}^{\mathrm{FSR}}\left(t, z\right) = \frac{dt}{t}\frac{\alpha_s(t)}{2\pi}dz\,\hat{P}_{a \to bc}\left(z\right)\,, \tag{3.72}$$

where $\hat{P}$ denotes the unregularised splitting function. The scale $t$, generally used as the ordering variable of the shower, is a key distinguishing feature of different parton

---

[9]One can easily derive it from the QCD Feynman rules — *e.g.* Figure A.1 in Appendix A — and by averaging over quark helicities and/or gluon polarisations. See for instance [122].
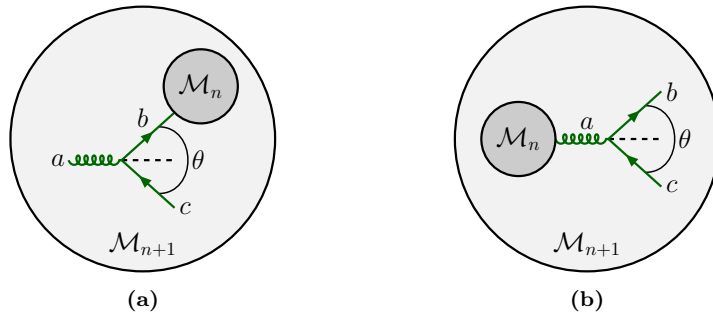
**Figure 3.3:** Parton branching of (a) incoming and (b) outgoing partons, in the case of a $g \to q\bar{q}$ splitting. See the main text for further explanations.

showers — it may for instance be chosen as the virtuality (early versions of PYTHIA, SHERPA), the energy-weighted emission angle (HERWIG) or the transverse momentum (newer versions of PYTHIA, SHERPA), provided the correct corresponding splitting kernels are employed. In the case of $g \to gg$ and $q \to qg$ splittings, the soft divergence ($z \to 1$) was previously regularised via the plus prescription for the corresponding splitting function, *cf.* (3.36) and (3.37). In the parton-shower approach, instead, the splitting function is kept unregularised and the soft integral is performed over the kinematically allowed range of $z$, *i.e.*

$$d\mathcal{P}^{\mathrm{FSR}}_{a \to bc}(t) = \frac{dt}{t} \frac{\alpha_s(t)}{2\pi} \int_{z_{\min}(t)}^{z_{\max}(t)} dz \, \hat{P}_{a \to bc}(z) \ . \tag{3.73}$$

At this point, unitarity would be violated as we have effectively removed all unresolved splittings and virtual corrections. The solution is to include a probability *not* to branch, which in the infinitesimal step $dt$ should naturally be $1 - d\mathcal{P}^{\mathrm{FSR}}_a(t)$. In the case of multiple branchings between an initial scale $t_1$ and a final lower scale $t_2$, this amounts to the following Sudakov form factor.

$$\Delta^{\mathrm{FSR}}_{a \to bc}(t_1, t_2) = \exp\left(-\int_{t_2}^{t_1} d\mathcal{P}^{\mathrm{FSR}}_{a \to bc}(t)\right) \ . \tag{3.74}$$

With each branching the scale is evolved downwards, creating a cascade of partons that evolves forwards in physical time. This so-called *forward* evolution is the basis of FSR algorithms, but in the case of ISR (*i.e.* Figure 3.3 (a)), the progression from high to low scales corresponds to a *backward* evolution in time. A crucial feature of backwards evolution in the case of ISR is that it solves the issue of matching the kinematics of the initial-state partons and the hard process. First, the PDFs are evolved to the hard scale using the DGLAP equations (2.2). Subsequently, the incoming showers are constructed backwards in time with a branching probability at each step given by

$$d\mathcal{P}^{\mathrm{ISR}}_{b/a}(t, x) = \frac{dt}{t} \frac{\alpha_s(t)}{2\pi} \int_{z_{\min}(t)}^{z_{\max}(t)} dz \hat{P}_{b/a}(z) \frac{f_a(x/z, t)}{z f_b(x, t)} \ , \tag{3.75}$$

with $z = x/x'$ defined as the ratio of momentum fractions $x^{(\prime)}$. The corresponding Sudakov form factor is similar to (3.74).

The interpretation of Sudakov form factors in terms of naive parton-branching probabilities allows one to construct a probabilistic PS algorithm suitable for computer implementation. In a nutshell, starting from (3.74) with an initial scale $Q$, the first and second emissions are found by solving the equations[10]

$$\Delta\left(Q, t_1\right) = R_1, \quad \Delta\left(t_1, t_2\right) = \frac{\Delta\left(t_1, Q\right)}{\Delta\left(t_2, Q\right)} = R_2, \dots, \tag{3.76}$$

where we eased notation by dropping the label 'FSR' for timelike branching and the sum over all possible parton splittings $a \to bc$ is implicit. Furthermore, $R_i$ denote pseudorandom numbers distributed uniformly on the interval $[0, 1]$. This process is repeated until the scale falls below an IR cutoff scale $Q_0$ of around 1 GeV.[11] Below this scale one enters the non-perturbative regime and one has to revert to hadronisation models. The result of the PS approach is a Markov chain of parton emissions, *i.e.* a parton cascade or shower, embedded in a an event generator that generates multiple emissions using the MC method. More detailed discussions of the MC implementation of PS algorithms are for instance given in [53, 122, 138, 145, 151, 152].

We add that while the above branching formalism takes collinear enhancements into account to all orders in perturbation theory, enhancements due to coherent soft-gluon emission should be incorporated as well in order to obtain a realistic picture. This leads to an ordering of successive parton emissions in terms of decreasing angles, called *angular ordering*. Shower algorithms using either emission angle ($\theta$) or transverse momentum ($p_{\mathrm{T}}$) as an ordering variable exhibit the correct angular-ordered behavior without any additional requirements on the allowed emissions [145, 153].

In order to arrive at a formula for the SMC cross section, we first define the combined splitting kernels and Sudakov form factors for emissions off an $n$-body state as $\mathcal{K}_n\left(\Phi_{\mathrm{rad}}\right)$ and $\Delta_n\left(t_1, t_2\right)$, respectively, which in the case of splittings as described in (3.72) would amount to

$$\mathcal{K}_n\left(\Phi_{\mathrm{rad}}\right) d\Phi_{\mathrm{rad}} = \sum_{\{a;b,c\}\in n} d\mathcal{P}^{\mathrm{FSR}}_{a\to bc},$$

$$\Delta_n\left(t_1, t_2\right) = \prod_{\{a;b,c\}\in n} \Delta^{\mathrm{FSR}}_{a\to bc}\left(t_1, t_2\right). \tag{3.77}$$

This yields the radiation pattern up to the first emission, given by the SMC, as

$$d\sigma_{\mathrm{SMC}}\left(\mathbf{\Phi}_{\mathrm{FJ}}\right) = d\mathbf{\Phi}_{\mathrm{F}} B\left(\mathbf{\Phi}_{\mathrm{F}}\right)\left\{\Delta_n\left(Q, Q_0\right) + \int_{Q_0}^{Q} d\Phi_{\mathrm{rad}} \mathcal{K}_n\left(\Phi_{\mathrm{rad}}\right)\Delta_n\left(Q, t\right)\right\}, \tag{3.78}$$

where we have included the luminosity factor in the definition of the Born contribution, *i.e.* $B\left(\mathbf{\Phi}_{\mathrm{F}}\right) = \mathcal{L}\left(\mathbf{\Phi}_{\mathrm{F}}\right)\mathcal{B}\left(\mathbf{\Phi}_{\mathrm{F}}\right)$, to ease notation. Subsequent radiation is modeled by iterating the terms in the curly brackets in an appropriate fashion.

The PS method, as described above, provides only an approximation of the higher-order real corrections in soft and collinear approximations, and estimates the contributions from higher-order virtual corrections through unitarity conditions. As a result,

---

[10]The Sudakov form factors in (3.76) contain integrated splitting kernels, which are often not known analytically. The PS therefore solves these equations numerically using the the so-called (Sudakov) veto algorithm — consult *e.g.* [145] for more details.

[11]Typically of a few $\Lambda_{\mathrm{QCD}}$, for instance in Chapter 4 a cutoff of 0.89 GeV is used.

the parton shower by construction fails to account for any higher-order effects impacting on the total cross section, and is typically not suited to describe the more complicated pattern of hard emissions. Hence, these regions are best described in fixed-order perturbation theory including the full matrix elements. However, the PS does provide a much better description of emissions in the soft and collinear regions of phase space, by resumming the associated large logarithms via its Sudakov form factor. Logically, a lot of ongoing work aims to combine the best of both worlds, by matching the best-available fixed-order calculations with the all-order resummation of the PS, embedded in MC event generators. However, some intricacies arise when attempting to match fixed-order perturbative calculations beyond the leading order in QCD with the all-order PS approach, and some of the frameworks developed for precisely that purpose are discussed in the coming sections.

## 3.4 Matching and merging

Because of their flexibility in generating exclusive event samples, parton-shower MC (SMC) event generators have become invaluable for both theorists and experimentalists. In their simplest form, SMCs start from a LO description of the hard process, and subsequently dress the hard partons with soft-collinear radiation as simulated by the PS (*i.e.* LO+PS). Over the last two decades, the central goal in the development of SMCs has been to improve upon this simple picture. The first advancements were made in the direction of merging LO multi-jet matrix elements of different jet multiplicities with a PS, including pioneering work by groups such as Catani, Krauss, Kuhn and Webber (CKKW) [154] — for a detailed comparison of different LO merging schemes, see *e.g.* [155].

Whilst describing experimental data acceptably well, the LO multi-jet merging approach can never reach formal NLO accuracy since it does not include virtual corrections. Full NLO QCD computations are however known to perform better at describing hard emissions and total emission rates compared to LO SMCs. Therefore, methods that aim to match full NLO QCD matrix elements to a PS appeared shortly after, with the foremost examples being the MC@NLO method, developed in [54–56], and the Powheg method [32, 33]. The goal of any NLO+PS approach is to achieve NLO accuracy for inclusive observables, such as the total emission rate, while maintaining the (leading) logarithmic accuracy of the PS. This demands that the hardest emission is generated exactly, such that it exhibits the correct behavior also away from the soft and collinear regions, while integrated quantities maintain NLO accuracy also in the soft and collinear regions. Naturally, the next step forward was to merge NLO+PS matched simulations for multi-jet cross sections — see *e.g.* [53] and references therein. A generalisation of the CKKW method to NLO, MiNLO, was proposed in [57] in order to obtain good scale choices in an NLO multi-jet computation a priori. MiNLO was later improved to MiNLO′ [58, 59], achieving NLO accuracy for both F and FJ, where F is a colour-singlet final state and J denotes one jet.

However, in some cases where the NLO corrections are still large, as is for example the case in Higgs-boson production, the inclusion of the full NNLO QCD corrections is mandatory for an accurate description of events and reliable scale uncertainties. Moreover, the impressively small uncertainties on the experimental side, which for most LHC

|  | **F** | **FJ** | **FJJ** | **F($\geq$3J)** |
|---|---|---|---|---|
| POWHEG | NLO | LO | PS | PS |
| MiNLO′ | NLO | NLO | LO | PS |
| MiNNLO$_{PS}$ | NNLO | NLO | LO | PS |

**Table 3.1:** Formal accuracies for the inclusive production of a system F of colour-singlet particles in association with a (non-)zero number of jets J, achieved by the matching frameworks MiNLO′ and MiNNLO$_{PS}$, compared to a NLO+PS F+0-jet implementation in POWHEG.

production processes today are at the order of a few percent [156],[12] further motivate the construction of event generators in which NNLO QCD computations are matched to a PS. As mentioned in Chapter 2, the first NNLO+PS method achieved NNLO QCD accuracy through a reweighting of MiNLO′ events [59, 99–102]. Since then, three more NNLO+PS methods have been proposed: the UNNLOPS method [157, 158], the GENEVA method [105, 106],[13] and the MiNNLO$_{PS}$ method [34, 35, 114]. The latter is used in the next Chapter to obtain NNLO+PS accurate results for $ZZ$ production, and combined with a NLO+PS implementation of the loop-induced ggF contribution within the POWHEG framework. Therefore, we first discuss the POWHEG method in the section hereafter, before turning our attention to MiNLO$^{(\prime)}$ and MiNNLO$_{PS}$ in Sections 3.4.2 and 3.4.3, respectively. A brief comparison of the accuracies reached by these methods for different jet multiplicities is provided in Table 3.1.

### 3.4.1 The POWHEG method

The challenge of matching full NLO matrix elements to parton showers is essentially that of avoiding double-counting real emissions, as the shower approximates them already. Here, we introduce a solution to this issue as provided by the POWHEG (Positive Weight Hardest Emission Generator) method, proposed in [32]. We aim to provide a synoptic explanation of the method, and refer the reader to [33] for a detailed and comprehensive review. The general strategy is, as the name suggests, to generate the hardest (*e.g.* highest $p_T$) emission first, before feeding the event to a SMC generator to generate subsequent softer radiation. To this end, a crucial role is played by the ordering variable for the shower. Transverse-momentum ordered showers always generate the hardest emission first, which POWHEG then replaces with the exact result. For showers ordered in the emission angle, this is not always the case and one needs to revert to so-called truncated showers to restore soft coherence. Below, we discuss the general formalism of POWHEG.

We start with the SMC approximation of the cross section for the production of a colourless final state F, up to the first emission, given in (3.78) and write the corre-

---

[12]These uncertainties are expected to improve further in the coming years, especially after the high-luminosity upgrade of the LHC.
[13]Recently, the GENEVA method was reformulated using the transverse momentum of the colour singlet rather than the jettiness variable and applied to Drell-Yan [113].

sponding expression for the expectation value of an IR-safe observable as

$$\langle \mathcal{O} \rangle_{\text{SMC}} = \int d\boldsymbol{\Phi}_{\text{F}} B\left(\boldsymbol{\Phi}_{\text{F}}\right) \left\{ \Delta_n\left(Q, Q_0\right) \mathcal{O}\left(\boldsymbol{\Phi}_{\text{F}}\right) \right.$$
$$\left. + \int_{Q_0}^{Q} d\Phi_{\text{rad}} \mathcal{K}_n\left(\Phi_{\text{rad}}\right) \Delta_n\left(Q, t\right) \mathcal{O}\left(\boldsymbol{\Phi}_{\text{F}}, \Phi_{\text{rad}}\right) \right\}, \tag{3.79}$$

which, after expanding the expression up to $\alpha_s$, reads

$$\langle \mathcal{O} \rangle_{\text{SMC}} = \int d\boldsymbol{\Phi}_{\text{F}} B\left(\boldsymbol{\Phi}_{\text{F}}\right) \left\{ \mathcal{O}\left(\boldsymbol{\Phi}_{\text{F}}\right) \right.$$
$$\left. + \int d\Phi_{\text{rad}} \mathcal{K}_n\left(\Phi_{\text{rad}}\right) \left[ \mathcal{O}\left(\boldsymbol{\Phi}_{\text{F}}, \Phi_{\text{rad}}\right) - \mathcal{O}\left(\boldsymbol{\Phi}_{\text{F}}\right) \right] + \mathcal{O}\left(\alpha_s^2\right) \right\}, \tag{3.80}$$

where the integration limits $\{Q_0, Q\}$ are omitted for clarity. The full NLO QCD analog[14] can be written as

$$\langle \mathcal{O} \rangle = \int d\boldsymbol{\Phi}_{\text{F}} \left[ B\left(\boldsymbol{\Phi}_{\text{F}}\right) + V_b\left(\boldsymbol{\Phi}_{\text{F}}\right) \right] \mathcal{O}\left(\boldsymbol{\Phi}_{\text{F}}\right) + \int d\boldsymbol{\Phi}_{\text{FJ}} R\left(\boldsymbol{\Phi}_{\text{FJ}}\right) \mathcal{O}\left(\boldsymbol{\Phi}_{\text{FJ}}\right), \tag{3.81}$$

where we used the subscript $b$ to indicate that $V$ is IR divergent (but UV finite) and similar to the Born case we have included the luminosity factors for the real and virtual corrections also in the definition of the corresponding contributions, *i.e.* $R\left(\boldsymbol{\Phi}_{\text{FJ}}\right) = \mathcal{L}\left(\boldsymbol{\Phi}_{\text{FJ}}\right) \mathcal{R}\left(\boldsymbol{\Phi}_{\text{FJ}}\right)$ and $V_b\left(\boldsymbol{\Phi}_{\text{F}}\right) = \mathcal{L}\left(\boldsymbol{\Phi}_{\text{F}}\right) \mathcal{V}_b\left(\boldsymbol{\Phi}_{\text{F}}\right)$, to ease notation. The IR divergences from the real and virtual contributions in (3.81) cancel upon integration when combined in inclusive observables. However, from a numerical point of view it is preferable to cancel them prior to integration. The *subtraction* method is one way to achieve this. In the subtraction method, one parametrises the full real-emission phase space $\boldsymbol{\Phi}_{\text{FJ}}$, similarly the SMC case, in terms of the underlying Born ($\boldsymbol{\Phi}_{\text{F}}$) and radiation ($\Phi_{\text{rad}}$) phase spaces. Here we will simply assume the mapping

$$\{\boldsymbol{\Phi}_{\text{FJ}}\} \Rightarrow \{\boldsymbol{\Phi}_{\text{F}}, \Phi_{\text{rad}}\}. \tag{3.82}$$

One furthermore includes a set of real counterterms $C\left(\boldsymbol{\Phi}_{\text{F}}, \Phi_{\text{rad}}\right)$, and reorganises the integrals in (3.81) into the form

$$\langle \mathcal{O} \rangle = \int d\boldsymbol{\Phi}_{\text{F}} \left[ B\left(\boldsymbol{\Phi}_{\text{F}}\right) + V\left(\boldsymbol{\Phi}_{\text{F}}\right) \right] \mathcal{O}\left(\boldsymbol{\Phi}_{\text{F}}\right)$$
$$+ \int d\boldsymbol{\Phi}_{\text{F}} d\Phi_{\text{rad}} \left[ R\left(\boldsymbol{\Phi}_{\text{F}}, \Phi_{\text{rad}}\right) \mathcal{O}\left(\boldsymbol{\Phi}_{\text{F}}, \Phi_{\text{rad}}\right) - C\left(\boldsymbol{\Phi}_{\text{F}}, \Phi_{\text{rad}}\right) \mathcal{O}\left(\boldsymbol{\Phi}_{\text{F}}\right) \right], \tag{3.83}$$

where

$$V\left(\boldsymbol{\Phi}_{\text{F}}\right) = V_b\left(\boldsymbol{\Phi}_{\text{F}}\right) + \int d\Phi_{\text{rad}} C\left(\boldsymbol{\Phi}_{\text{F}}, \Phi_{\text{rad}}\right). \tag{3.84}$$

By a suitable choice of the counterterms $C\left(\boldsymbol{\Phi}_{\text{F}}, \Phi_{\text{rad}}\right)$, the integral of the radiation variables in $V\left(\boldsymbol{\Phi}_{\text{F}}\right)$ can be performed analytically. A detailed discussion of subtraction schemes such as Frixione, Kunszt and Signer (FKS) subtraction [159, 160] and Catani

---

[14]Here we neglect the counterterms $\mathcal{G}\left(\boldsymbol{\Phi}_{\text{F}}\right)$ associated with initial-state collinear singularities to keep the discussion illustrative, see [33] for the more detailed expressions.

– 41 –

and Seymour (CS) subtraction [161], in the context of POWHEG, is given in [33]. Furthermore, in (3.83) the soft and collinear divergences in $R\left(\mathbf{\Phi}_{\mathrm{F}}, \Phi_{\mathrm{rad}}\right)$ cancel because in the soft or collinear limit $\mathcal{O}\left(\mathbf{\Phi}_{\mathrm{F}}, \Phi_{\mathrm{rad}}\right) = \mathcal{O}\left(\mathbf{\Phi}_{\mathrm{F}}\right)$ (IR safety), and $C\left(\mathbf{\Phi}_{\mathrm{F}}, \Phi_{\mathrm{rad}}\right)$ has the same singularity structure as $R\left(\mathbf{\Phi}_{\mathrm{F}}, \Phi_{\mathrm{rad}}\right)$.

The characteristic step of POWHEG is then to define the function

$$\bar{B}_{\mathrm{pwg}}\left(\mathbf{\Phi}_{\mathrm{F}}\right) = B\left(\mathbf{\Phi}_{\mathrm{F}}\right) + V\left(\mathbf{\Phi}_{\mathrm{F}}\right) + \int d\Phi_{\mathrm{rad}}\Big[R\left(\mathbf{\Phi}_{\mathrm{F}}, \Phi_{\mathrm{rad}}\right) - C\left(\mathbf{\Phi}_{\mathrm{F}}, \Phi_{\mathrm{rad}}\right)\Big], \qquad (3.85)$$

which can be viewed as describing the Born-level configurations, modified by a local K-factor, defined as $R\left(\mathbf{\Phi}_{\mathrm{F}}, \Phi_{\mathrm{rad}}\right)/B\left(\mathbf{\Phi}_{\mathrm{F}}\right)$. One furthermore introduces the POWHEG Sudakov form factor

$$\Delta_{\mathrm{pwg}}\left(\mathbf{\Phi}_{\mathrm{F}}, p_{\mathrm{T}}\right) = \exp\left[-\int d\Phi_{\mathrm{rad}}\frac{R\left(\mathbf{\Phi}_{\mathrm{F}}, \Phi_{\mathrm{rad}}\right)}{B\left(\mathbf{\Phi}_{\mathrm{F}}\right)}\theta\big(k_{\mathrm{T}}\left(\mathbf{\Phi}_{\mathrm{F}}, \Phi_{\mathrm{rad}}\right) - p_{\mathrm{T}}\big)\right], \qquad (3.86)$$

where $k_{\mathrm{T}}\left(\mathbf{\Phi}_{\mathrm{F}}, \Phi_{\mathrm{rad}}\right)$ describes the transverse momentum of the emitted particle. The expected value of $\mathcal{O}$ in (3.83), which is accurate at the NLO in QCD, upon using the definition of $\bar{B}_{\mathrm{pwg}}\left(\mathbf{\Phi}_{\mathrm{F}}\right)$ in (3.85), takes the form

$$\begin{aligned}\langle\mathcal{O}\rangle = &\int d\mathbf{\Phi}_{\mathrm{F}}\bar{B}_{\mathrm{pwg}}\left(\mathbf{\Phi}_{\mathrm{F}}\right)\mathcal{O}\left(\mathbf{\Phi}_{\mathrm{F}}\right) \\ &+ \int d\mathbf{\Phi}_{\mathrm{F}}d\Phi_{\mathrm{rad}}R\left(\mathbf{\Phi}_{\mathrm{F}}, \Phi_{\mathrm{rad}}\right)\Big[\mathcal{O}\left(\mathbf{\Phi}_{\mathrm{F}}, \Phi_{\mathrm{rad}}\right) - \mathcal{O}\left(\mathbf{\Phi}_{\mathrm{F}}\right)\Big].\end{aligned} \qquad (3.87)$$

By comparing (3.87) to the SMC approximation (3.80), one observes that NLO accuracy is achieved (schematically) via the replacements $B\left(\mathbf{\Phi}_{\mathrm{F}}\right) \to \bar{B}_{\mathrm{pwg}}\left(\mathbf{\Phi}_{\mathrm{F}}\right)$ and $B\left(\mathbf{\Phi}_{\mathrm{F}}\right)\mathcal{K}_n\left(\Phi_{\mathrm{rad}}\right) \to R\left(\mathbf{\Phi}_{\mathrm{F}}, \Phi_{\mathrm{rad}}\right)$. Therefore, by combining the $\bar{B}_{\mathrm{pwg}}\left(\mathbf{\Phi}_{\mathrm{F}}\right)$ terms in (3.85) with the first-order correct SMC radiation pattern (3.80), one obtains a simulation which is correct to the first order in $\alpha_s$ for both the inclusive cross section and for the emission of the hardest parton. The corresponding POWHEG differential cross section for the generation of the hardest event is then given by

$$d\sigma = d\mathbf{\Phi}_{\mathrm{F}}\bar{B}_{\mathrm{pwg}}\left(\mathbf{\Phi}_{\mathrm{F}}\right)\left\{\Delta_{\mathrm{pwg}}\left(\mathbf{\Phi}_{\mathrm{F}}, p_{\mathrm{T}}^{\mathrm{min}}\right) + \Delta_{\mathrm{pwg}}\left(\mathbf{\Phi}_{\mathrm{F}}, k_{\mathrm{T}}\right)\frac{R\left(\mathbf{\Phi}_{\mathrm{F}}, \Phi_{\mathrm{rad}}\right)}{B\left(\mathbf{\Phi}_{\mathrm{F}}\right)}d\Phi_{\mathrm{rad}}\right\}, \qquad (3.88)$$

where we have dropped the argument $\left(\mathbf{\Phi}_{\mathrm{F}}, \Phi_{\mathrm{rad}}\right)$ of $k_{\mathrm{T}}$ for brevity. The cross section (3.88) has the following properties [33]:

✓ At large $k_{\mathrm{T}}$ it coincides with the exact NLO cross section up to NNLO terms.

✓ It reproduces NLO-accurate expectation values of IR-safe observables and thus also its integral around the small $k_{\mathrm{T}}$ region has NLO accuracy.

✓ At small $k_{\mathrm{T}}$ it performs as good as SMC generators, meaning it preserves the (leading) logarithmic accuracy of the PS.

Finally, the POWHEG result for the all-order emission probability follows to be

$$\begin{aligned}\langle\mathcal{O}\rangle_{\mathrm{pwg}} = \int d\mathbf{\Phi}_{\mathrm{F}}\bar{B}_{\mathrm{pwg}}\left(\mathbf{\Phi}_{\mathrm{F}}\right)\Bigg\{&\Delta_{\mathrm{pwg}}\left(\mathbf{\Phi}_{\mathrm{F}}, p_{\mathrm{T}}^{\mathrm{min}}\right)\mathcal{O}\left(\mathbf{\Phi}_{\mathrm{F}}\right) \\ &+ \int d\Phi_{\mathrm{rad}}\Delta_{\mathrm{pwg}}\left(\mathbf{\Phi}_{\mathrm{F}}, k_{\mathrm{T}}\right)\frac{R\left(\mathbf{\Phi}_{\mathrm{F}}, \Phi_{\mathrm{rad}}\right)}{B\left(\mathbf{\Phi}_{\mathrm{F}}\right)}\theta\big(k_{\mathrm{T}} - p_{\mathrm{T}}^{\mathrm{min}}\big)\mathcal{O}\left(\mathbf{\Phi}_{\mathrm{F}}, \Phi_{\mathrm{rad}}\right)\Bigg\}.\end{aligned} \qquad (3.89)$$

We add that the discussion presented here is a simplified explanation of the Powheg method. In particular, one should keep track of different flavour structures, which always give rise to different events, and one generally distinguishes between contributions to the real cross section that are either singular or finite in the small-$p_{\mathrm{T}}$ region, *i.e.* $R\left(\boldsymbol{\Phi}_{\mathrm{F}}, \boldsymbol{\Phi}_{\mathrm{rad}}\right) = R_s\left(\boldsymbol{\Phi}_{\mathrm{F}}, \boldsymbol{\Phi}_{\mathrm{rad}}\right) + R_f\left(\boldsymbol{\Phi}_{\mathrm{F}}, \boldsymbol{\Phi}_{\mathrm{rad}}\right)$. The first point could be addressed by including a sum over the different Born flavour structures, while the second issue is solved by replacing $R\left(\boldsymbol{\Phi}_{\mathrm{F}}, \boldsymbol{\Phi}_{\mathrm{rad}}\right)$ by $R_s\left(\boldsymbol{\Phi}_{\mathrm{F}}, \boldsymbol{\Phi}_{\mathrm{rad}}\right)$ everywhere in (3.89) and adding a term $\int d\boldsymbol{\Phi}_{\mathrm{FJ}} R_f\left(\boldsymbol{\Phi}_{\mathrm{FJ}}\right)$ to it. The expression corresponding to (3.89) in full generality is given in equation (4.20) of [33].

### 3.4.2 MiNLO and MiNLO′

While Powheg provides a general formalism for matching NLO matrix elements to a PS based on the subtraction method, attempts to merge LO multi-jet matrix elements to parton showers generally rely on phase-space *slicing* methods. Essentially, the underlying idea of such merging methods is to decompose the emission phase space into a hard regime and a soft regime, which are associated with the production of a hard jet and its evolution, respectively. The hard regime is described by the full matrix elements, while the soft regime is left to the PS and the separation between the two is parametrised by a jet resolution criterion $Q_{\mathrm{cut}}$, which is typically related to the transverse momentum. Naively, one could think that from a formal-accuracy point of view it is desirable to choose $Q_{\mathrm{cut}}$ as low as possible, *i.e.* near the cutoff scale of the PS (around 1 GeV). However, as we have seen before, this could induce large logarithms of the form $\ln Q/Q_{\mathrm{cut}}$ with $Q$ the hard scale. Therefore, an adequate procedure for choosing the unphysical scales — as we will see, the renormalisation and factorisation scales are closely related — is crucial in multi-jet calculations. At LO, the CKKW method provides such a procedure for obtaining good scale choices *a priori*, where $Q_{\mathrm{cut}}$ is indeed chosen as the $k_{\mathrm{T}}$-jet measure from the $k_{\mathrm{T}}$ (or Durham) jet algorithm [126, 127].

The MiNLO method, proposed in [57], can most easily be understood as the NLO extension of the CKKW procedure, including Sudakov weights to suppress large logarithms. It is therefore particularly useful in the context of interfacing NLO calculations to a PS, for example in the context of Powheg, leading to a considerable improvement in reliability near the Sudakov regions. Thus, using Powheg in combination with MiNLO extends the validity of an NLO computation with jets in the final state in regions where jets become unresolved. The formal accuracy of MiNLO was further investigated in [58], finding that by including also the NNLL coefficients in the resummation formula, formal NLO accuracy both for F and FJ is achieved simultaneously, a method which was dubbed MiNLO′. Moreover, the authors found that via a simple reweighting procedure, an NNLO+PS generator can be constructed from MiNLO′, constituting the first of its kind. This set the stage for the development of the MiNNLO$_{\mathrm{PS}}$ method, which will be discussed in detail in the next section.

The general idea of MiNLO is thus to adopt the CKKW formalism to NLO to obtain good scale choices a priori in a multi-jet NLO computation. The MiNLO procedure for the production of a generic colourless final state F in association with $n$ jets is characterised by the following steps [57, 154]:

■ **Use the $k_{\mathrm{T}}$-clustering algorithm to reconstruct the most-likely branch-**

**ing history.** One defines a test variable $y_{\tilde{ij}} = 2\min\left\{E_i^2, E_j^2\right\}(1 - \cos\theta_{ij})/Q^2$, where $E_{i(j)}$ is the energy of the particle $i(j)$, $\theta_{ij}$ the angle between the momenta of objects $i$ and $j$, and $Q$ the hard scale. The test variable $y_{\tilde{ij}}$ is then compared to the jet resolution variable $y_{\mathrm{cut}}$ to determine wether $i$ and $j$ are resolved ($y_{\tilde{ij}} > y_{\mathrm{cut}}$) or not resolved ($y_{\tilde{ij}} < y_{\mathrm{cut}}$). In the latter case, the pair is clustered with a combined four-momentum of $p_{\tilde{ij}} = p_i + p_j$, provided the clustering is consistent with the flavour structure. This process is repeated recursively until the minimum value is above $y_{\mathrm{cut}}$, creating a tree-like branching (or fake parton-shower emission) history. The remaining system of particles is called the *primary system*, to which the scale $Q$ is assigned.

- **At each splitting, evaluate $\alpha_s$ at the nodal scale (local $p_{\mathrm{T}}$) of the splitting.** During the clustering of the event, the respective flavours and momenta define a splitting kernel and the corresponding kinematics at each vertex, or node, $i$ ($i = 1, \ldots, n$) within the branching history, from which the nodal scales $q_i$ are determined, which are identified with the local relative transverse momentum value ($p_{\mathrm{T},i}$) at which the clustering has taken place. The branching history thus leads to a sequence of scales, $q_1 < q_2 < \ldots < q_{n-1} < q_n$. The strong couplings associated with each node are evaluated at the corresponding nodal scale, *i.e.* $\alpha_s(\mu_i) = \alpha_s(K_{\mathrm{R}} q_i)$, where $K_{\mathrm{R}}$ is a normalisation factor that can be used to probe scale variations. One furthermore sets $q_1 = Q_{\mathrm{cut}}$.

- **Set $\mu_{\mathrm{R}}$ in the virtual corrections to the geometric average of the nodal scales and $\mu_{\mathrm{F}}$ to the softest scale.** We have $n$ strong coupling constants evaluated at different nodal scales, and $m$ couplings associated with the primary system, which are evaluated at $\mu_Q = K_{\mathrm{R}} Q$. The $\mu_{\mathrm{R}}$-dependence of the virtual corrections is then chosen as the geometrical average $\bar{\mu}_{\mathrm{R}} = \left[(\mu_Q)^m \prod_{i=1}^n \mu_i\right]^{\frac{1}{m+n}}$. The factorization scale $\mu_{\mathrm{F}}$ is assigned the scale $K_{\mathrm{F}} q_1$, where $K_F$ is a normalisation factor for the factorization scale.

- **Include Sudakov form factors for Born and virtual terms, and for real terms after first branching.** For each internal line within the branching history one includes a Sudakov weight, which is given by $\Delta(Q_{\mathrm{cut}}, q_i)/\Delta(Q_{\mathrm{cut}}, q_j)$ between nodes $i$ and $j$, where $q_j < q_i$ and the Sudakov form factor is defined in (3.90). External lines that join at the first node, *i.e.* at scale $q_1$, will be associated with a Sudakov factor of $\Delta(Q_{\mathrm{cut}}, q_1) = 1$ since $q_1 = Q_{\mathrm{cut}}$.

- **Subtract the NLO bit that resides in the CKKW Sudakov of the Born.** The Sudakov form factors included in the previous step induce higher-order effects, of which some are already accounted for by the NLO calculation. They should therefore be compensated for to avoid double-counting. This is done by modifying the Born term by a factor which subtracts the first order in the $\alpha_s$-expansion of the analytic Sudakov form factors. The explicit form of this factor can be read off from (3.92).

The scale choices are now connected with the inclusion of Sudakov form factors, obtaining smooth CKKW behavior in the singular regions for processes with multiple scales — hence the name Multi-scale Improved NLO. The MiNLO$^{(\prime)}$ Sudakov form

factor is defined as

$$\Delta\left(p_{\mathrm{T}}, Q\right)=\exp\left[-\tilde{S}\left(p_{\mathrm{T}}, Q\right)\right], \tag{3.90}$$

with

$$\tilde{S}\left(p_{\mathrm{T}}, Q\right) \equiv \tilde{S}\left(p_{\mathrm{T}}\right)=2\int_{p_{\mathrm{T}}}^{Q} \frac{dq}{q}\left[A\big(\alpha_s\left(q\right)\big)\ln\frac{Q^2}{q^2}+B\big(\alpha_s\left(q\right)\big)\right]. \tag{3.91}$$

The functions $A$ and $B$ have a perturbative expansion in terms of constant coefficients, as shown in (3.58), with the explicit expressions for the coefficients $A^{(1-3)}$ and $B^{(1)}$ given in (3.59) and (3.60), respectively. The expansion of the Sudakov form factor to the first order in $\alpha_s$ is given by

$$\begin{aligned}\Delta\left(p_{\mathrm{T}}, Q\right) &= 1+\Delta^{(1)}\left(p_{\mathrm{T}}, Q\right)+\mathcal{O}\left(\alpha_s^2\right)\\ &= 1-\frac{\alpha_s\left(p_{\mathrm{T}}\right)}{2\pi}\underbrace{\left(\frac{1}{2}A^{(1)}\ln^2\frac{Q^2}{p_{\mathrm{T}}^2}+B^{(1)}\ln\frac{Q^2}{p_{\mathrm{T}}^2}\right)}_{\equiv[\tilde{S}(p_{\mathrm{T}})]^{(1)}}+\mathcal{O}\left(\alpha_s^2\right).\end{aligned} \tag{3.92}$$

In MiNLO, only the coefficients $A^{(1)}$, $A^{(2)}$, and $B^{(1)}$ are used in the expansion of the Sudakov form factor. However, by a careful investigation of the accuracy of the procedure, the authors of [58] found that by including the $B^{(2)}$ coefficient and setting the scale of the power of $\alpha_s$ entering the virtual corrections ($\bar{\mu}_{\mathrm{R}}$), $\Delta^{(1)}$ and the real corrections equal to $p_{\mathrm{T}}$, spurious $\alpha_s^{3/2}$ terms are avoided and full NLO accuracy is maintained also for the F+0-jet configuration.

In practice, the improvement that MiNLO′ provides in the context of POWHEG could be summarised by considering the $\bar{B}$ function of the latter — *cf.* (3.85) — for a colourless final state F in association with one jet J,

$$\bar{B}_{\mathrm{pwg}}\left(\boldsymbol{\Phi}_{\mathrm{FJ}}\right)=\frac{\alpha_s\left(\mu_{\mathrm{R}}\right)}{2\pi}\left\{B\left(\boldsymbol{\Phi}_{\mathrm{FJ}}\right)+\frac{\alpha_s}{2\pi}\left[V\left(\boldsymbol{\Phi}_{\mathrm{FJ}}, \mu_{\mathrm{R}}\right)+\int d\Phi_{\mathrm{rad}}R\left(\boldsymbol{\Phi}_{\mathrm{FJ}}, \Phi_{\mathrm{rad}}\right)\right]\right\}, \tag{3.93}$$

where the subtraction terms are not written explicitly, and modifying it in the following way

$$\begin{aligned}\bar{B}_{\mathrm{MiNLO'}}\left(\boldsymbol{\Phi}_{\mathrm{FJ}}\right)=\frac{\alpha_s\left(p_{\mathrm{T}}\right)}{2\pi}\Bigg\{&e^{-\tilde{S}(p_{\mathrm{T}})}\left[B\left(\boldsymbol{\Phi}_{\mathrm{FJ}}\right)\left(1+\frac{\alpha_s\left(p_{\mathrm{T}}\right)}{2\pi}\left[\tilde{S}\left(p_{\mathrm{T}}\right)\right]^{(1)}\right)\right.\\ &\left.+\frac{\alpha_s}{2\pi}V\left(\boldsymbol{\Phi}_{\mathrm{FJ}}, \bar{\mu}_{\mathrm{R}}\right)\right]+\frac{\alpha_s}{2\pi}\int d\Phi_{\mathrm{rad}}R\left(\boldsymbol{\Phi}_{\mathrm{FJ}}, \Phi_{\mathrm{rad}}\right)e^{-\tilde{S}(p_{\mathrm{T}})}\Bigg\},\end{aligned} \tag{3.94}$$

where $\bar{\mu}_{\mathrm{R}}=\mu_{\mathrm{F}}=p_{\mathrm{T}}$ and the strong couplings multiplying the real and virtual corrections are also evaluated at $p_{\mathrm{T}}$, with $p_{\mathrm{T}}$ being the transverse momentum of F. Below, we will absorb the powers of $\alpha_s$ that appear in (3.94) into the contributions $B$, $V$ and $R$ for brevity, after which $\bar{B}_{\mathrm{MiNLO'}}$ takes the simple form

$$\begin{aligned}\bar{B}_{\mathrm{MiNLO'}}\left(\boldsymbol{\Phi}_{\mathrm{FJ}}\right)=e^{-\tilde{S}(p_{\mathrm{T}})}&\left[B\left(\boldsymbol{\Phi}_{\mathrm{FJ}}\right)\left(1+\frac{\alpha_s\left(p_{\mathrm{T}}\right)}{2\pi}\left[\tilde{S}\left(p_{\mathrm{T}}\right)\right]^{(1)}\right)+V\left(\boldsymbol{\Phi}_{\mathrm{FJ}}\right)\right]\\ &+\int d\Phi_{\mathrm{rad}}R\left(\boldsymbol{\Phi}_{\mathrm{FJ}}, \Phi_{\mathrm{rad}}\right)e^{-\tilde{S}(p_{\mathrm{T}})}.\end{aligned} \tag{3.95}$$

Finally, the MINLO′ formula for an arbitrary IR-safe observable $\mathcal{O}$, embedded in the POWHEG method follows to be [34]

$$
\langle \mathcal{O} \rangle_{\text{MINLO}'} = \int d\boldsymbol{\Phi}_{\text{FJ}} \int d\Phi_{\text{rad}} \bar{B}_{\text{MINLO}'} \left(\boldsymbol{\Phi}_{\text{FJ}}\right) \left[ \Delta_{\text{pwg}} \left(\boldsymbol{\Phi}_{\text{FJ}}, p_{\text{T}}^{\min}\right) \mathcal{O} \left(\boldsymbol{\Phi}_{\text{FJ}}\right) \right.
$$
$$
\left. + \Delta_{\text{pwg}} \left(\boldsymbol{\Phi}_{\text{FJ}}, k_{\text{T}}\right) \frac{R\left(\boldsymbol{\Phi}_{\text{FJ}}, \Phi_{\text{rad}}\right)}{B\left(\boldsymbol{\Phi}_{\text{FJ}}\right)} \mathcal{O}\left(\boldsymbol{\Phi}_{\text{FJ}}, \Phi_{\text{rad}}\right) \right], \tag{3.96}
$$

where we have omitted the factor $\theta\left(k_{\text{T}} - p_{\text{T}}^{\min}\right)$ to ease notation and $k_{\text{T}}$ now corresponds to the transverse momentum of the secondary emission, associated with the radiation phase space $\Phi_{\text{rad}}$. It will be convenient to expand (3.96) in $\alpha_s$, which yields

$$
\langle \mathcal{O} \rangle_{\text{MINLO}'} = \int d\boldsymbol{\Phi}_{\text{FJ}} \left\{ e^{-\tilde{S}(p_{\text{T}})} \left[ B\left(\boldsymbol{\Phi}_{\text{FJ}}\right) \left(1 + \frac{\alpha_s\left(p_{\text{T}}\right)}{2\pi} \left[\tilde{S}\left(p_{\text{T}}\right)\right]^{(1)}\right) + V\left(\boldsymbol{\Phi}_{\text{FJ}}\right) \right] \right.
$$
$$
\left. + \int d\Phi_{\text{rad}} e^{-\tilde{S}(p_{\text{T}})} R\left(\boldsymbol{\Phi}_{\text{FJ}}, \Phi_{\text{rad}}\right) \mathcal{O}\left(\boldsymbol{\Phi}_{\text{FJ}}, \Phi_{\text{rad}}\right) \right\} + \mathcal{O}\left(\alpha_s^3\right), \tag{3.97}
$$

up to terms that are of N³LO. We emphasize that the result of the MINLO′ procedure, *i.e.* the merging of F and FJ, is achieved without introducing an unphysical merging scale ad hoc — such a scale formally spoils the NLO accuracy of merged samples in some regions of phase space [162]. It was further argued in [58] that it is not only possible to improve MINLO′ to higher jet multiplicities,[15] but that it can also straightforwardly be turned into an NNLO+PS generator through a reweighting procedure. However, this constitutes a multi-dimensional reweighting in the Born phase space which is numerically highly demanding, especially for more complicated processes or when aiming for high precision. Therefore, already from a computational point of view, it is highly desirable to construct a NNLO+PS generator that includes the NNLO QCD corrections directly during event generation. In the next section, we discuss the method that addresses this issue called MINNLO$_{\text{PS}}$.

### 3.4.3 The MINNLO$_{\text{PS}}$ method

In this section, we discuss the method already anticipated in Section 3.2.3 and the previous section: MINNLO$_{\text{PS}}$. The MINNLO$_{\text{PS}}$ method is designed for the matching of NNLO QCD calculations to a PS without any computationally intensive reweighting procedure. It has been formulated in [34], optimised for $2 \to 1$ processes in [35] and later extended to generic colour-singlet processes in [114] and to heavy-quark pair production in [116].

Before we detail some of its technicalities, let us first give a brief outline of the method. MINNLO$_{\text{PS}}$ includes NNLO corrections in the event generation of a system F of colour-singlet particles, and involves essentially three steps: in the first one (Step I) F is generated in association with one light parton at NLO according to the POWHEG method, inclusively over the radiation of a second light parton. The second step (Step II) characterises the MINNLO$_{\text{PS}}$ approach, and it corrects the limit in

---

[15] The MINLO′ procedure was extended numerically to higher jet multiplicities in [163], where in particular the case of Higgs production in association with up to two jets was worked out.

which the light partons become unresolved by supplementing the appropriate Sudakov form factor and higher-order terms, such that the simulation remains finite as well as NNLO accurate for inclusive F production. In the third step (Step III), the kinematics of the second radiated parton (accounted for inclusively in Step I) is generated through the Powheg method to preserve the NLO accuracy of the F+1-jet cross section, and subsequent radiation is included through the parton shower. In these three steps all emissions are appropriately ordered (when using a $p_T$-ordered shower) and the applied Sudakov matches the leading logarithms resummed by the PS. Thus, the MiNNLO$_{PS}$ approach preserves the (LL) accuracy of the PS.

We now discuss in more detail the anatomy of MiNNLO$_{PS}$, starting, as promised, from the transverse-momentum resummation formula given in (3.71). Adopting the notation of [34],[16] the cross section for the production of a generic colour-singlet system F of invariant mass $Q$ and transverse momentum $p_T$ in hadronic collisions, differential in $p_T$ and $\mathbf{\Phi}_F$, reads

$$\frac{d\sigma}{d\mathbf{\Phi}_F dp_T} = \frac{d}{dp_T}\left\{e^{-\tilde{S}(p_T)}\mathcal{L}\left(\mathbf{\Phi}_F, p_T\right)\right\} + R_f\left(\mathbf{\Phi}_F, p_T\right), \qquad (3.98)$$

where $R_f\left(\mathbf{\Phi}_F, p_T\right)$ denotes the terms that are non-singular in the small-$p_T$ limit and the function $\tilde{S}\left(p_T\right)$, defined in (3.91), in the case of MiNNLO$_{PS}$ includes the following perturbative coefficients

$$
\begin{aligned}
A\left(\alpha_s\right) &= \left(\frac{\alpha_s}{2\pi}\right)A^{(1)} + \left(\frac{\alpha_s}{2\pi}\right)^2 A^{(2)} + \left(\frac{\alpha_s}{2\pi}\right)^3 A^{(3)}, \\
\tilde{B}\left(\alpha_s\right) &= \left(\frac{\alpha_s}{2\pi}\right)B^{(1)} + \left(\frac{\alpha_s}{2\pi}\right)^2 \tilde{B}^{(2)},
\end{aligned}
\qquad (3.99)
$$

where $\tilde{B}^{(2)}$ is defined in (3.66). The explicit expressions for the coefficients $A^{(1-3)}$ and $B^{(1)}$ are given in (3.59) and (3.60), respectively, while $B^{(2)}$ for Drell–Yan and Higgs production can for instance be found in Appendix B of [34]. The luminosity factor $\mathcal{L}\left(\mathbf{\Phi}_F, p_T\right)$ in (3.98) for the first emission with momentum $k_{T,1}$ is given by [34]

$$
\begin{aligned}
\mathcal{L}\left(\mathbf{\Phi}_F, k_{T,1}\right) = \sum_{c,c'}\frac{d|\mathcal{M}^F\left(\mathbf{\Phi}_F\right)|^2}{d\mathbf{\Phi}_F}\sum_{i,j}\Bigg\{ &\left(\tilde{C}_{ci}^{[a]}\otimes f_i^{[a]}\right)\tilde{H}\left(k_{T,1}\right)\left(\tilde{C}_{c'j}^{[b]}\otimes f_j^{[b]}\right) \\
+ &\left(G_{ci}^{[a]}\otimes f_i^{[a]}\right)\tilde{H}\left(k_{T,1}\right)\left(G_{c'j}^{[b]}\otimes f_j^{[b]}\right)\Bigg\},
\end{aligned}
\qquad (3.100)
$$

where $\mathcal{M}^F$ denotes the Born matrix element and the labels $a$ and $b$ indicate the initial-state legs. The squared hard-virtual matrix elements $H$, related to $\tilde{H}$ in (3.68), are evaluated at the scale $k_{T,1}$ instead of $Q$, in line with the MiNLO$'$ procedure, *i.e.* we have

$$H(Q) \to H\left(k_{T,1}\right) = \frac{\alpha_s\left(k_{T,1}\right)}{2\pi}H^{(1)} + \left(\frac{\alpha_s\left(k_{T,1}\right)}{2\pi}\right)^2 H^{(2)} + \dots \qquad (3.101)$$

The coefficient functions $C$ and $G$ appearing in (3.100), which respectively deal with initial-state collinear singularities for quarks and gluons, admit the following perturba-

---

[16]Compared to (3.71), the cumulative cross section $\Sigma$ is denoted as $\sigma$ and $S \to \tilde{S}$ to emphasize that it contains the coefficient $\tilde{B}^{(2)}$, defined in (3.66).

tive expansions

$$
\begin{aligned}
C^{[a/b]}(z) &= \delta(1-z) + \frac{\alpha_s(k_{\mathrm{T},1})}{2\pi}C^{(1)}(z) + \left(\frac{\alpha_s(k_{\mathrm{T},1})}{2\pi}\right)^2 C^{(2)}(z) + \dots , \\
G^{[a/b]}(z) &= \frac{\alpha_s(k_{\mathrm{T},1})}{2\pi}G^{(1)}(z) + \dots ,
\end{aligned}
\tag{3.102}
$$

where $\tilde{C}$ is related to $C$ in (3.68). We add that the definitions presented above derive from the momentum-space formulation of $p_{\mathrm{T}}$-resummation presented in [142], which includes corrections up to N$^3$LL and NNLO. The result of said formulation, restricted to the single-radiation case with momentum $k_{\mathrm{T},1}$, presented in a more compact form in [34], is the starting point for MiNNLO$_{\mathrm{PS}}$ shown in (3.98). It also contains the regularised splitting kernels $P(z)$ upon integration over $p_{\mathrm{T}}$, given by

$$
P(z) = P^{(0)}(z) + \frac{\alpha_s(k_{\mathrm{T},i})}{2\pi}P^{(1)}(z) + \left(\frac{\alpha_s(k_{\mathrm{T},i})}{2\pi}\right)^2 P^{(2)}(z) + \dots
\tag{3.103}
$$

In order to make contact with the MiNLO$'$ procedure, we emphasize that $\mathbf{\Phi}_{\mathrm{F}}$ on the left-hand side of (3.98) is defined via the projection of $\mathbf{\Phi}_{\mathrm{FJ}}$ and $\mathbf{\Phi}_{\mathrm{FJJ}}$ onto $\mathbf{\Phi}_{\mathrm{F}}$, which in [34] is denoted as $\mathbf{\Phi}_{\mathrm{F,res}}$ with the label "res" to indicate that the projection depends on how the recoil of F is defined in the resummation approach. We then notice that integrating the MiNLO$'$ result in (3.97) for an observable of the type $\mathcal{O}(\Phi) = \delta(\mathbf{\Phi}_{\mathrm{F,res}} - \mathbf{\Phi}_{\mathrm{F}})\delta(p_{\mathrm{T}}(\Phi) - p_{\mathrm{T}})$, where $\Phi = \mathbf{\Phi}_{\mathrm{FJ}}$ or $\Phi = \mathbf{\Phi}_{\mathrm{FJJ}}$, results in the following differential cross section [34]

$$
\begin{aligned}
\frac{d\sigma}{d\mathbf{\Phi}_{\mathrm{F}}dp_{\mathrm{T}}} = e^{-\tilde{S}(p_{\mathrm{T}})}\Bigg\{ &\frac{\alpha_s(p_{\mathrm{T}})}{2\pi}\left[\frac{d\sigma_{\mathrm{FJ}}}{d\mathbf{\Phi}_{\mathrm{F}}dp_{\mathrm{T}}}\right]^{(1)}\left(1 + \frac{\alpha_s(p_{\mathrm{T}})}{2\pi}\left[\tilde{S}(p_{\mathrm{T}})\right]^{(1)}\right) \\
&+ \left(\frac{\alpha_s(p_{\mathrm{T}})}{2\pi}\right)^2\left[\frac{d\sigma_{\mathrm{FJ}}}{d\mathbf{\Phi}_{\mathrm{F}}dp_{\mathrm{T}}}\right]^{(2)}\Bigg\},
\end{aligned}
\tag{3.104}
$$

where $[X]^{(i)}$ denotes the coefficient of the $i^{\mathrm{th}}$ term in the perturbative expansion of the quantity $X$. To demonstrate the connection to the $p_{\mathrm{T}}$-resummation formula in (3.98), we cast the latter into the form

$$
\frac{d\sigma}{d\mathbf{\Phi}_{\mathrm{F}}dp_{\mathrm{T}}} = e^{-\tilde{S}(p_{\mathrm{T}})}\left\{D(p_{\mathrm{T}}) + \frac{R_f(p_{\mathrm{T}})}{e^{-\tilde{S}(p_{\mathrm{T}})}}\right\},
\tag{3.105}
$$

with

$$
D(p_{\mathrm{T}}) \equiv \frac{d\mathcal{L}(p_{\mathrm{T}})}{dp_{\mathrm{T}}} - \frac{d\tilde{S}(p_{\mathrm{T}})}{dp_{\mathrm{T}}}.
\tag{3.106}
$$

One could show that expanding (3.105) in $\alpha_s$ and keeping all terms up to $\mathcal{O}(\alpha_s^2)$ yields precisely the MiNLO$'$ result shown in (3.104). The above considerations furthermore expose what is needed to reach NNLO accuracy for the fully differential cross section for F, obtained upon integration over $p_{\mathrm{T}}$. To see this more clearly, we estimate the size of each contribution to the total integral of (3.105) between the IR scale $\Lambda$ and $Q$ to be (see Appendix C of [58] for a derivation) of order

$$
\int_{\Lambda}^{Q} dp_{\mathrm{T}}\frac{1}{p_{\mathrm{T}}}\alpha_s^m(p_{\mathrm{T}})\ln\frac{Q}{p_{\mathrm{T}}}e^{-\tilde{S}(p_{\mathrm{T}})} \approx \mathcal{O}\left(\alpha_s^{m-\frac{n+1}{2}}(Q)\right).
\tag{3.107}
$$

Then, in order for the integral to be NLO accurate, one thus has to include all terms up to order $\alpha_s^2$ — which agrees with (3.104). Moreover, NNLO accuracy is reached upon inclusion of all terms of up to order $\alpha_s^3$, *i.e.*

$$
\begin{aligned}
\frac{d\sigma}{d\mathbf{\Phi}_{\text{F}}dp_{\text{T}}} =\, & e^{-\tilde{S}(p_{\text{T}})}\Bigg\{ \frac{\alpha_s\left(p_{\text{T}}\right)}{2\pi}\left[\frac{d\sigma_{\text{FJ}}}{d\mathbf{\Phi}_{\text{F}}dp_{\text{T}}}\right]^{(1)}\left(1+\frac{\alpha_s\left(p_{\text{T}}\right)}{2\pi}\left[\tilde{S}\left(p_{\text{T}}\right)\right]^{(1)}\right) \\
& +\left(\frac{\alpha_s\left(p_{\text{T}}\right)}{2\pi}\right)^2\left[\frac{d\sigma_{\text{FJ}}}{d\mathbf{\Phi}_{\text{F}}dp_{\text{T}}}\right]^{(2)}+\left(\frac{\alpha_s\left(p_{\text{T}}\right)}{2\pi}\right)^3\left(D\left(p_{\text{T}}\right)-\frac{\alpha_s\left(p_{\text{T}}\right)}{2\pi}\left[D\left(p_{\text{T}}\right)\right]^{(1)} \right.\\
& \left. -\left(\frac{\alpha_s\left(p_{\text{T}}\right)}{2\pi}\right)^2\left[D\left(p_{\text{T}}\right)\right]^{(2)}\right)F^{\text{corr}}\left(\mathbf{\Phi}_{\text{FJ}}\right)+R_f\text{-terms of }\mathcal{O}\left(\alpha_s^3\right)\Bigg\},
\end{aligned}
\tag{3.108}
$$

where the regular $(R_f)$ terms of $\mathcal{O}\left(\alpha_s^3\right)$ can safely be neglected as they do not produce NNLO contributions upon integration over $p_{\text{T}}$ — essentially because they do not contain the $1/p_{\text{T}}$ factor in (3.107). Note also that one could either truncate the third term in (3.108) at the third order [34]

$$
D\left(p_{\text{T}}\right)-\frac{\alpha_s\left(p_{\text{T}}\right)}{2\pi}\left[D\left(p_{\text{T}}\right)\right]^{(1)}-\left(\frac{\alpha_s\left(p_{\text{T}}\right)}{2\pi}\right)^2\left[D\left(p_{\text{T}}\right)\right]^{(2)}=\left(\frac{\alpha_s\left(p_{\text{T}}\right)}{2\pi}\right)^3\left[D\left(p_{\text{T}}\right)\right]^{(3)}+\mathcal{O}(\alpha_s^4),
\tag{3.109}
$$

or keep the terms of $\mathcal{O}(\alpha_s^4)$ and higher [35], which are beyond accuracy, in order to preserve the total derivative in (3.105). We employ the latter option in Chapter 4. Finally, $F^{\text{corr}}$ in (3.108) determines the appropriate function to spread the NNLO corrections in the FJ phase space, which is necessary to include those corrections in the context of an FJ Powheg calculation — see Section 3 of [34] for details. As described in Step III above, the generation of the second radiation is done according the the Powheg method,[17] after which one obtains the master formula for the MiNNLO$_{\text{PS}}$ method

$$
\begin{aligned}
\frac{d\sigma}{d\mathbf{\Phi}_{\text{FJ}}} =\, & \bar{B}_{\text{MiNNLO}_{\text{PS}}}\left(\mathbf{\Phi}_{\text{FJ}}\right)\Bigg\{ \Delta_{\text{pwg}}\left(\mathbf{\Phi}_{\text{FJ}},p_{\text{T}}^{\text{min}}\right)\mathcal{O}\left(\mathbf{\Phi}_{\text{FJ}}\right) \\
& +\Delta_{\text{pwg}}\left(\mathbf{\Phi}_{\text{FJ}},k_{\text{T}}\right)\frac{R\left(\mathbf{\Phi}_{\text{FJ}},\Phi_{\text{rad}}\right)}{B\left(\mathbf{\Phi}_{\text{FJ}}\right)}\mathcal{O}\left(\mathbf{\Phi}_{\text{FJ}},\Phi_{\text{rad}}\right)\Bigg\},
\end{aligned}
\tag{3.110}
$$

where $\Delta_{\text{pwg}}$ is the Powheg Sudakov form factor, $\mathbf{\Phi}_{\text{FJ}}$ is the phase space of the FJ system, $\Phi_{\text{rad}}$ and $k_{\text{T}}$ are the phase space and the transverse momentum of the second radiation, respectively, and $B\left(\mathbf{\Phi}_{\text{FJ}}\right)$ and $R\left(\mathbf{\Phi}_{\text{FJ}},\Phi_{\text{rad}}\right)$ denote the squared tree-level matrix elements for FJ and FJJ production, respectively. The MiNNLO$_{\text{PS}}$ $\bar{B}$ function

---

[17]In Chapter 4, a default cutoff of $p_{\text{T}}^{\text{min}}=\Lambda_{\text{pwg}}=\sqrt{0.8}\,\text{GeV}$ is used

is given by

$$
\begin{aligned}
\bar{B}_{\text{MiNNLO}_{\text{PS}}}\left(\boldsymbol{\Phi}_{\text{FJ}}\right) = e^{-\tilde{S}(p_{\text{T}})} \Bigg\{ & \frac{\alpha_s\left(p_{\text{T}}\right)}{2\pi}\left[\frac{d\sigma_{\text{FJ}}}{d\boldsymbol{\Phi}_{\text{F}}\,dp_{\text{T}}}\right]^{(1)} \left(1 + \frac{\alpha_s\left(p_{\text{T}}\right)}{2\pi}\left[\tilde{S}\left(p_{\text{T}}\right)\right]^{(1)}\right) \\
& + \left(\frac{\alpha_s\left(p_{\text{T}}\right)}{2\pi}\right)^2\left[\frac{d\sigma_{\text{FJ}}}{d\boldsymbol{\Phi}_{\text{F}}\,dp_{\text{T}}}\right]^{(2)} + F^{\text{corr}}\left(\boldsymbol{\Phi}_{\text{FJ}}\right)\Bigg[D\left(p_{\text{T}}\right) \\
& - \frac{\alpha_s\left(p_{\text{T}}\right)}{2\pi}\left[D\left(p_{\text{T}}\right)\right]^{(1)} - \left(\frac{\alpha_s\left(p_{\text{T}}\right)}{2\pi}\right)^2\left[D\left(p_{\text{T}}\right)\right]^{(2)}\Bigg]\Bigg\},
\end{aligned}
\tag{3.111}
$$

which contains the same contributions to generate the first emission (and inclusively the second emission) as in a standard FJ POWHEG calculation, described in Step I above, but it is modified according to the MiNNLO$_{\text{PS}}$ procedure in order to reach NNLO accuracy for inclusive F production, as discussed in Step II above. Note that in the MiNNLO$_{\text{PS}}$ approach the renormalisation and factorisation scales are evaluated, similarly to MiNLO$'$, as $\mu_{\text{R}} \sim \mu_{\text{F}} \sim p_{\text{T}}$, where $p_{\text{T}}$ is the transverse momentum of F and regular contributions at order $\alpha_s^3\left(p_{\text{T}}\right)$ are, as mentioned, of subleading nature.

We summarise our discussion of MiNNLO$_{\text{PS}}$ by reminding the reader that the benefits of the MiNNLO$_{\text{PS}}$ approach reside in the following features:

- ✓ It provides the possibility to include NNLO corrections on-the-fly, without the need of any a-posteriori reweighting. This considerably reduces the computational costs for obtaining NNLO+PS accurate results.

- ✓ Since it is based on the MiNLO$'$ method for obtaining good scale-choices a priori, it is not necessary to introduce a merging scale or unphysical boundaries to partition the phase space into different regions according to the number of resolved emissions.

- ✓ When using a $p_{\text{T}}$-ordered shower, the matching performed by MiNNLO$_{\text{PS}}$ preserves the logarithmic accuracy of the parton shower, which is in general far from trivial.

By now, MiNNLO$_{\text{PS}}$ has been applied to the production of colour-singlet systems such as $Z\gamma$ [114, 164], $W^+W^-$ [115], $ZZ$ [44], $VH$ including the $h \to b\bar{b}$ decay at NNLO+PS [165, 166]. It was furthermore extended to deal with the production of massive coloured final states in [116, 167], where it was applied to top-quark pair production, which was the first NNLO+PS result for LHC processes with coulored final states. In the next chapter, we present the aforementioned application of the MiNNLO$_{\text{PS}}$ method to $ZZ$ production, in combination with a NLO+PS computation for the loop-induced ggF channel that opens up at NNLO.

# Chapter 4

# $ZZ$ production at nNNLO+PS with MiNNLO$_{\text{PS}}$

Proton-proton collisions in which a pair of vector bosons is produced provide some of the most relevant signatures in precision measurements, which have evolved to one of the cornerstones of the rich physics programme at the LHC. The accurate determination of production rates and distributions provides a valuable path towards the observation of deviations from the predictions made by the SM of particle physics. Observing or constraining anomalous interactions among SM particles is one of the central goals of such analyses.

Through diboson signatures, the couplings among three vector bosons (triple-gauge couplings) are directly accessible, which are altered in various BSM theories. Therefore, the observation of small deviations from the expected rates or shapes of distributions would be a clear sign of new physics. Similarly, measurements at high transverse momentum of some of the particles produced in diboson processes provide constraints on the mass range of possible heavy $Z'$ bosons. Apart from that, vector-boson pair final states constitute an irreducible background to on- and off-shell Higgs cross-section measurements, when the Higgs boson decays to four leptons. These measurements are important for the extraction of the Higgs couplings and for constraints on the Higgs width [168–178]. Furthermore, modern fits of parton distribution functions (PDFs) have started to include more and more LHC data. For instance NNPDF3.1 [179] already includes top-pair production and the transverse momentum of the Drell-Yan pair. Upcoming fits will also include direct photon, dijet and single top production. It is clear that a further step would be the inclusion of diboson production and other processes with more final-state particles such as three jets, provided the accuracy of theory predictions, both at the level of higher-order QCD and electroweak corrections, is sufficient. It is therefore crucial to have theoretical predictions for vector-boson production processes at the best possible accuracy.

While the cross section for $ZZ$ production is smaller than the ones for $W^{\pm}Z$ or $W^+W^-$ production, experimentally the decay to four charged leptons provides the cleanest signature of the massive diboson processes, since the final state does not involve any missing transverse momentum. Accordingly, experimental measurements already reach a remarkable level of precision. In particular, both ATLAS and CMS collaborations have performed measurements of the $ZZ$ production cross sections at

5.02 TeV [180], 7 TeV [181–185], 8 TeV [184–190] and 13 TeV [190–195] and used these measurements to test the SM and constrain triple-gauge couplings.

The first NLO QCD corrections to $Z$-boson pair production started to appear about thirty years ago [196–200]. NLO QCD calculations were later consistently matched with fully exclusive PS MC programs using the Powheg [201, 202] or MC@NLOmethod [203]. EW effects at NLO were also computed first in the on-shell approximation [204, 205] and later keeping off-shell and spin-correlation effects [206, 207]. The combination of NLO QCD and NLO EW corrections was presented in [208] and recently also their matching to parton showers was performed [209]. Likewise, in the case of polarized $Z$ bosons NLO QCD and NLO EW corrections have been combined very recently [210]. NNLO QCD corrections have been computed for on-shell [79, 81] and off-shell $ZZ$ production [80, 82], and their combination with NLO EW effects was presented in [211]. The loop-induced $gg \to ZZ$ process starts contributing only at $\mathcal{O}(\alpha_s^2)$, but it is enhanced by the gluon PDF. Since higher-order corrections to this process can be formulated as a gauge-invariant set of contributions and their impact was expected to be important, NLO QCD corrections to $gg \to ZZ$ production have also been computed in the recent years [172, 212–214]. The leading order matching of the loop-induced ggF process was presented in [215], while NLO+PS predictions were first obtained neglecting the quark channels [216] and very recently also including the full NLO QCD corrections with quark-gluon and quark-antiquark channels and the Higgs resonance [217].

The remarkable progress in NNLO QCD calculations triggered considerable advancements in the matching of NNLO QCD corrections and parton showers, as detailed in Chapter 2 and Section 3.4. In this chapter, we employ the MiNNLO$_{PS}$ method to include NNLO QCD corrections for $ZZ$ production in the Powheg framework. Additionally, we present a NLO+PS Powheg calculation for the loop-induced $gg \to ZZ$ process. When combined, these predictions, dubbed nNNLO+PS, become the most advanced theoretical predictions for $ZZ$ production at the LHC, since they include the highest perturbative accuracy in QCD available to date. Spin correlations, interferences and off-shell effects are included by considering all contributions to the four-lepton final state. Moreover, the matching to the parton shower renders it possible to achieve a fully exclusive description at the level of hadronic events. In the future, the NNLO+PS predictions of our MiNNLO$_{PS}$ $ZZ$ generator could be compared to those recently obtained in the Geneva framework [111]. In Section 4.1, we discuss in detail the calculation and implementation of the MiNNLO$_{PS}$ method for the $q\bar{q}$-initiated process and the Powheg implementation for the loop-induced $gg$-initiated process. We also show how to avoid that the two-loop amplitudes, whose numerical evaluation is very time-consuming, slow down our code in a considerable way. Our phenomenological results for both cross sections and distributions in $ZZ$ production are discussed in Section 4.2, where we present a comparison between showered, fixed-order, and analytically resummed results at high accuracy for various observables as well as a comparison of our nNNLO+PS predictions to recent LHC data from CMS. A summary is presented in Section 4.3.
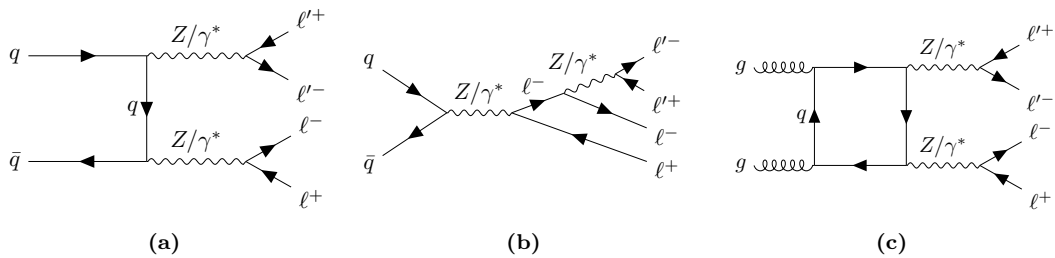
**Figure 4.1:** Sample Feynman diagrams for $ZZ$ production with four charged leptons in the final state. Panels (a) and (b): tree-level diagrams of the quark annihilation ($q\bar{q}$) channel; Panel (c): loop-induced diagram in the ggF ($gg$) channel.

## 4.1 Outline of the calculation

### 4.1.1 Description of the process

We study the process

$$pp \to \ell^+\ell^-\ell^{(\prime)+}\ell^{(\prime)-} \tag{4.1}$$

for any combination of charged leptons $\ell, \ell' \in \{e, \mu, \tau\}$. While at the matrix-element level our calculation is based on the different-flavour channel $\ell \neq \ell'$, at the event-generation level arbitrary combinations of charged leptons can be considered, both with different flavours $\ell \neq \ell'$ and with same flavours $\ell = \ell'$ (in the latter case interference effects when exchanging the charged leptons, which are typically at the $(1-2)\%$ level [80], are neglected). Moreover, lepton masses are included via reshuffling of the momenta in the event generation. For simplicity and without loss of generality we consider only the process $pp \to e^+e^-\mu^+\mu^-$ here, which we will refer to as $ZZ$ production in the following. By including all resonant and non-resonant topologies leading to this process, off-shell effects, interferences and spin correlations are taken into account. Sample diagrams are shown in Figure 4.1 and they include:

(a) tree-level double-resonant $t$-channel $ZZ$ production in the $q\bar{q}$ channel;

(b) tree-level single-resonant $s$-channel Drell–Yan topologies in the $q\bar{q}$ channel;

(c) loop-induced $ZZ$ production in the $gg$ channel.

The loop-induced $gg$ contribution, including also the single-resonant Higgs mediated diagrams, proceeds through a quark loop and enters the cross section at $\mathcal{O}(\alpha_s^2)$, *i.e.* it is part of the NNLO QCD corrections. Since this contribution is enhanced by the large gluon-gluon luminosity at LHC energies, it yields a relatively large fraction of the NNLO corrections [83, 84]. Moreover, it is known that at NLO QCD [212, 214], *i.e.* $\mathcal{O}(\alpha_s^3)$, its relative correction is very sizable (about a factor of two). It is likely that these corrections constitute the most significant contribution to $ZZ$ production at $\mathcal{O}(\alpha_s^3)$, since the $\mathcal{O}(\alpha_s^3)$ corrections to the $q\bar{q}$ channel are not expected to be of the same size as those at the previous order.

We include the most accurate currently available information in QCD perturbation theory for both the $q\bar{q}$-initiated and the loop-induced $gg$-initiated process, and match them consistently with a parton shower. Thus, we calculate NNLO+PS predictions

in the $q\bar{q}$ channel by means of the MINNLO_PS method [34, 35, 114] and NLO+PS predictions in the loop-induced $gg$ channel using the POWHEG approach [32, 33, 218]. Full top-quark mass effects are included everywhere, except for the two-loop amplitudes. For the $q\bar{q}$ channel they are expected to be small in the relevant phase-space regions, while for the loop-induced $gg$ contribution we have included them approximately via reweighting in the two-loop correction (*cf.* Section 4.1.3). We stress that to avoid any overlap, our MINNLO_PS implementation of the NNLO+PS calculation in the $q\bar{q}$ channel does not include the loop-induced $gg$-initiated contribution. In this way, all loop-induced $gg$ contributions are correctly accounted for when combining the former with our NLO+PS predictions for the $gg$ channel. Our ensuing result is dubbed as nNNLO+PS, as the NLO corrections to the loop-induced ggF contribution are of $\mathcal{O}(\alpha_s^3)$. These corrections are separately gauge-invariant and constitute the most significant $N^3$LO corrections, as pointed out before.

## 4.1.2 MINNLO_PS for $q\bar{q} \to ZZ$ production

In this section we present the implementation of a NNLO+PS generator for $ZZ$ production in the $q\bar{q}$ channel by means of the MINNLO_PS method. The MINNLO_PS method is described in detail in Section 3.4.3. In the following we provide some information on our implementation of a MINNLO_PS generator for $ZZ$ production in the $q\bar{q}$ channel within the POWHEG-BOX-RES framework [219]. Our NLO+PS generator for the loop-induced $gg$ channel is discussed in the next section. We stress that, while we distinguish these processes as $q\bar{q}$ and $gg$, in their higher-order corrections of course all the relevant partonic initial states are consistently included, with the exception of the $gg$ loop-induced partonic channel in the NNLO corrections to the $q\bar{q}$ process, since this contribution is already accounted for by our NLO+PS generator for the loop-induced $gg$ channel.

Since no implementation for $ZZ$+jet production was available in POWHEG-BOX to date, the first step was to implement this process in the POWHEG-BOX-RES framework. We have implemented all relevant flavour channels and, in addition, adapted the routine `build_resonance_histories` of POWHEG-BOX-RES such that it is capable of automatically constructing the correct resonance histories. The tree-level single and double real matrix elements for $e^+e^-\mu^+\mu^-+1, 2$-jet production and the one-loop amplitude for $e^+e^-\mu^+\mu^-+1$-jet production are evaluated through OPENLOOPS [220–222].

In a second step, we have employed the MINNLO_PS method to obtain NNLO+PS predictions for $ZZ$ production in the $q\bar{q}$ channel. In particular, we made use of the implementation of the MINNLO_PS method that was developed and applied to $Z\gamma$ production in [114]. The respective tree-level and one-loop $q\bar{q} \to e^+e^-\mu^+\mu^-$ amplitudes are also evaluated through OPENLOOPS, while the two-loop helicity amplitudes have been obtained by extending the interface to MATRIX [223] developed in [114] to $ZZ$ production. The evaluation of the two-loop coefficients in this implementation relies on the code VVAMP [224] and is based on the calculation of [225].

As discussed in [115] for $W^+W^-$ production, the evaluation of the two-loop helicity amplitudes for massive diboson processes is particularly demanding from a computational point of view. In [115] this problem was circumvented by constructing a set of interpolation grids for the two-loop coefficients that achieves their fast on-the-fly

evaluation. In this work we pursue a different strategy: we exploit the possibility of reweighting the events at the generation level (*i.e.* stage 4 in POWHEG-BOX) to include the two-loop contribution. In combination with a suitable caching system of the two-loop amplitude that we implemented this allows us to omit the evaluation of the two-loop contribution entirely in the calculation up to stage 4, where it needs to be evaluated only once per event.[1] To be more precise, we have implemented a new flag (`run_mode`), which is accessible from the POWHEG input file, and allows the user to switch between four different ways of running the code. Either the full calculation is performed including the two-loop contributions throughout (`run_mode 1`), or one completely drops the NNLO corrections provided by MiNNLO$_{\text{PS}}$, specifically the terms $\left(D - D^{(1)} - D^{(2)}\right) \times F^{\text{corr}}$ in (3.111), thus effectively reproducing MiNLO$'$ predictions (`run_mode 2`). Alternatively, the evaluation of two-loop amplitude can be omitted only in the grid setup, *i.e.* stage 1 in POWHEG-BOX, (`run_mode 3`), or completely (`run_mode 4`). For all results presented in this manuscript we run the code with the last option `run_mode 4`, *i.e.* without evaluating the computationally expensive two-loop amplitude. In this way, also the generation of the events is faster. However, once an event has been accepted, it is reweighted such that the two-loop contribution is included by resetting the `run_mode` keyword in the event reweight information of the POWHEG input file.

As a result the two-loop amplitude is evaluated only once for each event, considerably improving the efficiency of the code. Moreover, following the same logic we can also compute MiNLO$'$ weights in parallel to the generation of MiNNLO$_{\text{PS}}$ ones using the appropriate setting for `run_mode` in the event reweight information. We have first validated our implementation in an inclusive setup, requiring only a suitable $Z$-mass window for the opposite-charge same-flavour dilepton pairs. Here we compared the inclusive cross section at the Les Houches event (LHE) level obtained at stage 4 with the one computed at stage 2 when including the two-loop contribution, finding excellent agreement. Another very robust cross-check of the reweighting procedure is provided by the comparison of the MiNLO$'$ results obtained directly or through reweighting, which also agree perfectly. Our calculation involves the evaluation of several convolutions with the PDFs, for which we employ HOPPET [226]. The evaluation of the polylogarithms entering the collinear coefficient functions is done through the HPLOG package [227].

Finally, let us summarise some of the most relevant (non-standard) settings that we have used to produce NNLO+PS accurate $ZZ$ events in the $q\bar{q}$ channel. For more detailed information on those settings we refer to [35, 116]. To avoid spurious contributions from higher-order logarithmic terms at large $p_{\text{T}}$, we replace the logarithm $L = \ln Q/p_{\text{T}}$, where we set $Q = m_{4\ell}$, with a modified logarithm $\tilde{L}$ which is identical to $L$ below $p_{\text{T}} = Q/2$ and smoothly vanishes at $p_{\text{T}}$ equal or larger than $Q$ [116]. As far as the renormalization and factorization scales are concerned, we use the standard MiNNLO$_{\text{PS}}$ scale setting at small $p_{\text{T}}$ [35],

$$\mu_{\text{R}} = K_{\text{R}} \, Q \, e^{-\tilde{L}}, \qquad \mu_{\text{F}} = K_{\text{F}} \, Q \, e^{-\tilde{L}}, \tag{4.2}$$

---

[1]Note that in order for the caching to work properly and not having to reevaluate the two-loop amplitude for every scale variation in the event reweighting, we have set the parameter `rwl_group_events 1` in the input file, which ensures that the events are reweighted one-by-one instead of in batches.

where $K_{\mathrm{R,F}}$ are scale variation parameters varied between $1/2$ and $2$. In the NLO $ZZ$+jet cross section at large $p_{\mathrm{T}}$ the scale setting is changed to [35]

$$\mu_{\mathrm{R}} = K_{\mathrm{R}}\, p_{\mathrm{T}}\,, \qquad \mu_{\mathrm{F}} = K_{\mathrm{F}}\, p_{\mathrm{T}}\,, \tag{4.3}$$

by activating the option `largeptscales 1`. The Landau singularity is regulated by freezing the strong coupling and the PDFs for scales below $0.8\,\mathrm{GeV}$. Finally, as recommended for processes with jets in the final state, we turn on the option `doublefsr 1` of the POWHEG-BOX, see [228] for details. For the parton-shower we have used the standard settings, also for the recoil scheme (namely a global recoil scheme for initial state radiation, with `SpaceShower:dipoleRecoil 0`).

### 4.1.3   NLO+PS for $gg \to ZZ$ production

As discussed before, the leading-order contribution to the loop-induced ggF process enters the $ZZ$ cross section at $\mathcal{O}(\alpha_s^2)$. Thus, it constitutes a NNLO correction relative to the LO part of the $q\bar{q}$ channel, but it is significantly enhanced by the large gluon-gluon luminosities. It is therefore mandatory to include also the NLO corrections to the loop-induced ggF contribution in any precision study of $ZZ$ production that compares theory and data.

We have implemented a NLO+PS generator for loop-induced $ZZ$ production in the $gg$ channel within the POWHEG-BOX-RES framework. Note that in addition to continuum $ZZ$ production as shown in Figure 4.1 (c) we also include the contribution mediated by a Higgs boson (or a single $Z$ boson). The calculation of these loop-induced processes is effectively of similar complexity as a NNLO calculation, as far as the amplitude evaluation is concerned. Despite that, the matching to the parton shower through the POWHEG method, which is essentially automated in POWHEG-BOX-RES, can be applied to loop-induced processes as well, without any further conceptual issues. However such an NLO calculation requires the evaluation of both one-loop and two-loop helicity amplitudes and the process at hand is numerically substantially more demanding than a tree-level one, since the evaluation time of the one-loop and two-loop amplitudes is much slower and the stability of the one-loop matrix elements with one emitted real parton is challenged in the IR regions. To cope with these numerical issues, we have implemented and exploited a number of handles within POWHEG-BOX-RES, which will be discussed below.

For the implementation in POWHEG-BOX-RES, we have specified the relevant flavour channels and hard-coded also the resonance channels of the process, as the automatic determination of the latter via the already mentioned routine `build_resonance_histor ies` is not available yet for loop-induced processes. At NLO, all relevant partonic channels, namely $gg$, $gq$, $qg$, $q\bar{q}$ and the charge-conjugated ones, are included. To unambiguously define the NLO corrections to the loop-induced ggF process for each of those initial states, we follow the approach introduced in [214] and include all diagrams that involve a closed fermion loop with at least one vector boson attached. The one-loop amplitudes with zero and one jet are evaluated through OPENLOOPS [220–222]. For this purpose, we have adapted the OPENLOOPS interface in POWHEG-BOX-RES developed in [229] to deal with loop-induced processes. As a cross-check, we have also interfaced RECOLA to POWHEG-BOX-RES and found full agreement for all one-loop
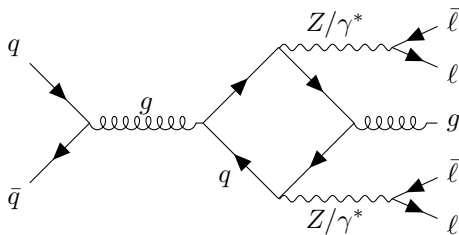
**Figure 4.2:** Sample Feynman diagram for a $q\bar{q}$-initiated regular contribution to the loop-induced $gg$ channel at $\mathcal{O}(\alpha_s^3)$.

amplitudes. For the two-loop helicity $gg \to \ell^+\ell^-\ell^{(\prime)+}\ell^{(\prime)-}$ amplitudes we exploit their implementation within MATRIX [223], which is based on the evaluation of the two-loop coefficients through VVAMP [225] from their calculation in [230]. To this end, we have extended the interface of POWHEG-BOX-RES to MATRIX developed in [114] to include the $gg \to \ell^+\ell^-\ell^{(\prime)+}\ell^{(\prime)-}$ two-loop amplitudes. Also here the evaluation of the two-loop coefficients through VVAMP is very slow, lasting from a few seconds to several tens of seconds. Since this leads to a severe bottleneck in the calculation and especially in the event generation, we have implemented a caching system for the two-loop corrections and we include them only through event reweighting. This is very similar in spirit to the way the two-loop hard function is included in the MiNNLO$_{\text{PS}}$ generator in the $q\bar{q}$ channel, as described in the previous section. Our calculation includes the full top-quark mass effects, except for the two-loop $gg \to \ell^+\ell^-\ell^{(\prime)+}\ell^{(\prime)-}$ amplitudes, where they are not known to date.[2] Instead, we follow the same approach as [214] and include them approximately through a reweighting of the massless two-loop amplitude with the ratio of the one-loop result including massive loops to the one with only massless loops. Since here we are interested in the $ZZ$ signal region, such reweighting is expected to work extremely well. In fact, [217] recently confirmed that using an asymptotic expansion in the top-quark mass leads to practically identical results as using such reweighting, as long as one sticks to the validity range of the expansion itself.

Very recently, [217] presented a completely independent NLO+PS generator for loop-induced $ZZ$ production in the $gg$ channel within the POWHEG-BOX-RES framework. We have compared our calculation to theirs both at the level of individual phase-space points and of the integrated cross sections, and we have found perfect agreement when applying the same approximation for the two-loop virtual corrections.[3] Since, although developed independently, the two calculations are essentially interchangeable (both developed in POWHEG-BOX-RES using OPENLOOPS and VVAMP), we advocate that it is equivalent to use either code and combine the results subsequently with our MiNNLO$_{\text{PS}}$ generator in the $q\bar{q}$ channel to obtain nNNLO+PS accurate results.

To better control the numerical stability of the calculation we have implemented settings similar to those reported in [217]: in particular we apply small ($0.5\,\text{GeV}$) generation cuts on the transverse momentum of the four-lepton system and of each $Z$ boson. Moreover, we exploit the stability system of OPENLOOPS and set the parameter `stability_kill2 0.01` to remove the remaining unstable points. We have further

---

[2]For the case of on-shell $gg \to ZZ$ production the full top-quark mass dependence was recently calculated in [231, 232].

[3]We would like to thank the authors of [217] for providing the `gg4l` code and in particular Jonas Lindert for very helpful correspondence.

modified the code in such a way that, whenever the real-emission contribution is set to zero by one of the previous stability checks, also the respective counter terms are set to zero. Finally, we use `withdamp 0` in order not to split the real cross section into a singular and a remnant contribution as the considerably small value of the latter leads to numerical issues when generating events. The same is true for the regular contribution that contains only the $q\bar{q}$ channel (see Figure 4.2 for a sample diagram): after verifying that it is completely negligible, we have turned it off for all results obtained in this paper.

Since in the upcoming section we study phenomenological results for the full $pp \to e^+e^-\mu^+\mu^-$ process, we show some plots for the loop-induced $gg$ channel separately in Figure 4.3, both at LO and at NLO. The settings and inputs that we use here correspond to those introduced in Section 4.2.1 in the inclusive setup (`setup-inclusive`) with just a $Z$-mass window applied between $60\,\text{GeV}$ and $120\,\text{GeV}$. The renormalization and factorization scales are set to $\mu_{\text{R}} = \mu_{\text{F}} = \sqrt{m_{4\ell}^2 + p_{\text{T},4\ell}^2}$, where $m_{4\ell}$ and $p_{\text{T},4\ell}$ are the invariant mass and the transverse momentum of the four-lepton system, respectively. Furthermore, the uncertainty bands are obtained through a standard seven-point scale variation, and we employ the PYTHIA8 parton shower [146] with the A14 tune [233] (see Section 4.2.1 for further details) to obtain the showered results presented in Figure 4.3. For the genuine NLO-accurate quantities shown in Figure 4.3, namely $m_{4\ell}$ and the rapidity of the four-lepton system ($y_{4\ell}$), we find results that are completely in line with the findings of previous fixed-order calculations [212, 214], which is expected since shower effects are negligible for those observables, as one can see from the LHE results. In particular, NLO corrections are sizable and increase the value of the inclusive cross section by almost a factor of two, with scale uncertainties at the level of 10-15%. In certain phase-space regions, like in the tail of the $m_{4\ell}$ distribution, the NLO corrections can even become significantly larger than a factor of two. However, in those regions the relative impact of the loop-induced $gg$ contribution is reduced. When looking at the transverse-momentum spectrum of the four-lepton system ($p_{\text{T},4\ell}$) and of the leading jet ($p_{\text{T},j_1}$) in Figure 4.3, the importance of matching to the parton shower becomes clear:[4] at LO only the parton shower fills those distributions and at NLO it still provides a substantial correction. In fact, in a fixed-order calculation both observables would diverge, and therefore be unphysical, at small transverse momenta. It is interesting to notice that the LO+PS result is actually higher than the NLO+PS one in the intermediate $p_{\text{T},4\ell}$ region before it falls off steeply. This region is completely filled by the shower, whose starting scale by default is set to $m_{4\ell}$ in the LO calculation. The fact that $m_{4\ell}$ is on average relatively large explains why the shower fills the spectrum even at such high transverse momenta.

---

[4]Note that, compared to the LO+PS results quoted for $gg \to ZZ$, predictions at higher accuracy in the presence of an additional radiated jet, possibly including zero- and one-jet merging, have been presented in [234–236].
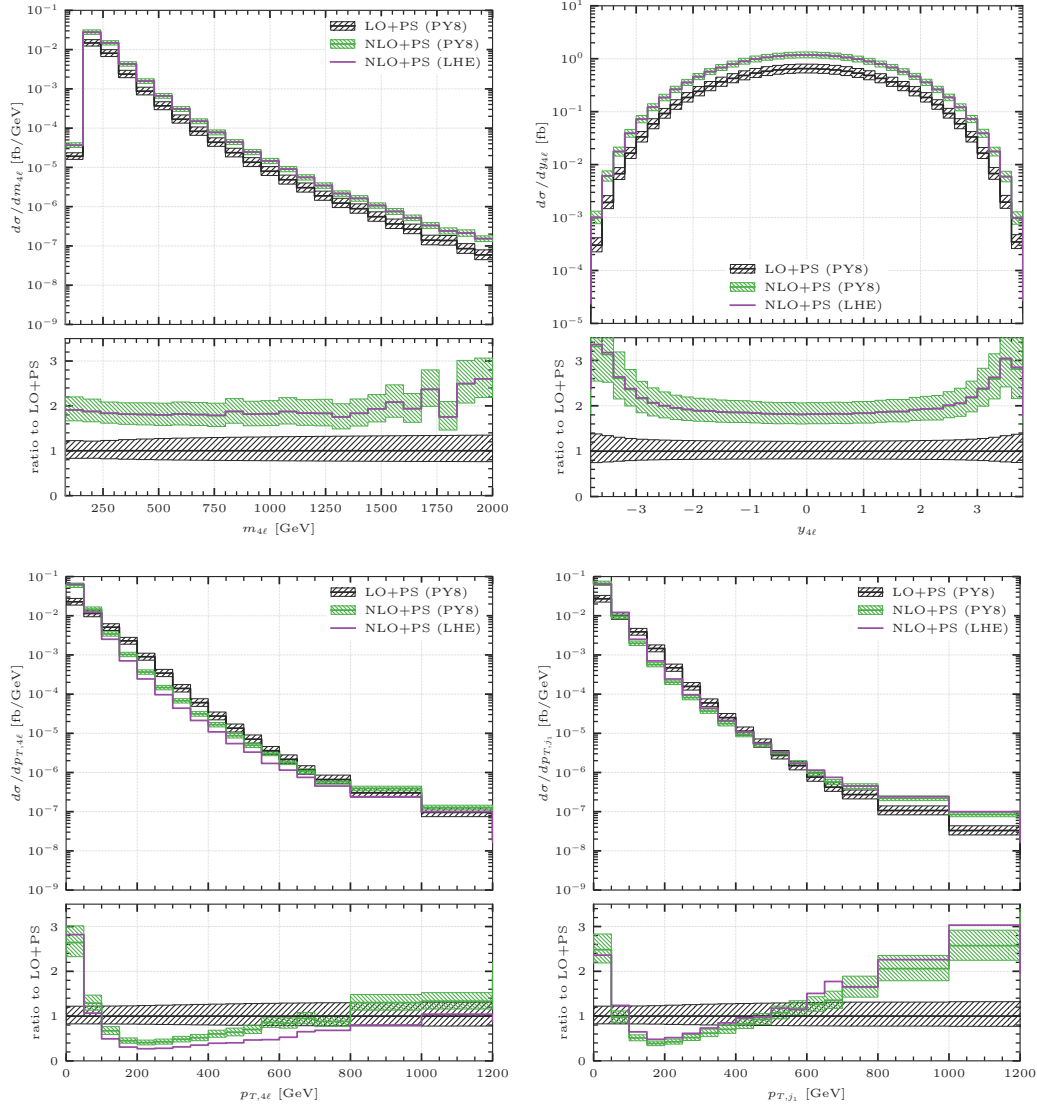
**Figure 4.3:** Predictions for $ZZ$ production in the loop-induced $gg$ channel at LO+PS and NLO+PS. For reference also the LHE-level central result at NLO is plotted. Shown are the distributions in the invariant mass, rapidity and transverse momentum of the four-lepton system, and in the transverse momentum of the leading jet.

## 4.2 Phenomenological results

In this section we present phenomenological results for the process $pp \to e^+e^-\mu^+\mu^-$. After discussing our setup in Section 4.2.1, we compare our MINNLO$_\text{PS}$ predictions for integrated cross sections (Section 4.2.2) and at the differential level against fixed-order predictions at NNLO accuracy and MINLO′ results (Section 4.2.3), and against experimental data from the CMS experiment [195] (Section 4.2.3.2).

### 4.2.1 Input parameters and setup

We consider proton–proton collisions at the LHC with a center-of-mass energy of 13 TeV and present predictions for $pp \to e^+e^-\mu^+\mu^-$ production. We use the complex-mass scheme [237] throughout and set the EW inputs to their PDG [23] values: $G_F = 1.16639 \times 10^{-5}$ GeV$^{-2}$, $m_W = 80.385$ GeV, $\Gamma_W = 2.0854$ GeV, $m_Z = 91.1876$ GeV, $\Gamma_Z = 2.4952$ GeV, $m_h = 125$ GeV and $\Gamma_h = 0.00407$ GeV. We set the on-shell top-quark mass to $m_t = 173.2$ GeV, and $\Gamma_t = 1.347878$ GeV is used. We determine the other EW parameters in the $G_\mu$ scheme with the EW coupling $\alpha_{G_\mu} = \sqrt{2}/\pi G_\mu |(m_W^2 - i\Gamma_W m_W)\sin^2\theta_W|$ and the EW mixing angle $\cos^2\theta_W = (m_W^2 - i\Gamma_W m_W)/(m_Z^2 - i\Gamma_Z m_Z)$. We use the NNPDF3.1 [179] NNLO set with $\alpha_s = 0.118$ via the LHAPDF interface [238] for all our predictions. For MINLO′ and MINNLO$_\text{PS}$, the PDFs are read by LHAPDF and evolved internally by HOPPET [226] as described in [34]. The central factorization and renormalization scales are set as discussed in Section 4.1.2 for the MINNLO$_\text{PS}$ $ZZ$ generator in the $q\bar{q}$ channel and as given in Section 4.1.3 for the loop-induced $gg$ channel. Scale uncertainties are estimated by varying $\mu_\text{F}$ and $\mu_\text{R}$ around their central value by a factor of two in each direction, while keeping the minimal and maximal values with the constraint $0.5 \leq \mu_\text{R}/\mu_\text{F} \leq 2$.

By combining the MINNLO$_\text{PS}$ $q\bar{q}$ results and loop-induced $gg$ results at (N)LO+PS, we obtain predictions for $ZZ$ production at (n)NNLO accuracy matched to parton showers. For all (n)NNLO+PS predictions presented in this work we make use of the PYTHIA8 parton shower [146] with the A14 tune [233] (`py8tune 21` in the input card). To validate our calculation and to show where shower effects are crucial, we compare (n)NNLO+PS predictions obtained with MINNLO$_\text{PS}$ and (n)NNLO fixed-order predictions obtained with MATRIX [223]. Additionally, we consider the inclusion of NLO EW effects. In the MATRIX predictions we set $\mu_\text{R} = \mu_\text{F} = m_{4\ell}$, and we construct the scale-uncertainty bands with the same canonical seven-point scale variation used for our MINLO′ and MINNLO$_\text{PS}$ results.

Moreover, we compare our predictions with recent results from the CMS collabora-

| | setup-inclusive | setup-fiducial |
|---|---|---|
| $Z$-mass window | $60\,\text{GeV} < m_{Z_1}, m_{Z_2} < 120\,\text{GeV}$ | $60\,\text{GeV} < m_{Z_1}, m_{Z_2} < 120\,\text{GeV}$ |
| lepton cuts | $m_{\ell^+\ell^-} > 4\,\text{GeV}$ | $p_{\text{T},\ell_1} > 20\,\text{GeV}, \quad p_{\text{T},\ell_2} > 10\,\text{GeV},$ $p_{\text{T},\ell_{3,4}} > 5\,\text{GeV}, \quad |\eta_\ell| < 2.5,$ $m_{\ell^+\ell^-} > 4\,\text{GeV}$ |

**Table 4.1:** Inclusive and fiducial cuts used to the define the `setup-inclusive` and `setup-fiducial` phase space regions [195]. See text for more details.

tion [195] within the fiducial volume defined in Table 4.1, denoted as `setup-fiducial`. Note that the reconstructed $Z$ bosons $Z_1$ and $Z_2$ are identified by selecting the opposite-sign same-flavour (OSSF) lepton pair with an invariant mass closest to the $Z$-boson mass as $Z_1$ and identifying the remaining OSSF lepton pair with $Z_2$. Since here we only consider the different-flavour channel ($e^+e^-\mu^+\mu^-$), the two $Z$ bosons are unambiguously reconstructed and this procedure only selects which lepton pair is called $Z_1$ and which $Z_2$. Note that in the different-flavour channel the additional $m_{\ell^+\ell^-} > 4\,\mathrm{GeV}$ cut in Table 4.1 has no effect. Besides the fiducial setup, we also consider an inclusive setup (dubbed `setup-inclusive`), where we only require a $Z$-mass window between $60\,\mathrm{GeV}$ and $120\,\mathrm{GeV}$ for the two resonances.

In order to provide the most realistic comparison to experimental data, our final predictions include effects from hadronization and multi-particle interactions (MPI). We also include QED showering effects as provided by Pythia8. In order to prevent charged resonances to radiate photons and photons to branch into lepton- or quark-pairs, we set the two flags `TimeShower:QEDshowerByOther` and `TimeShower:QEDshower ByGamma` to `off`. Finally, we define dressed leptons by adding to the four-momentum of a lepton the four-momenta of all photons within a distance $\Delta R_{\gamma\ell} = \sqrt{\Delta\phi_{\gamma\ell}^2 + \Delta\eta_{\gamma\ell}^2} <$ 0.1.

### 4.2.2 Integrated cross sections

We start the discussion of our results by first considering integrated cross sections. In Table 4.2 we report predictions both in the inclusive and in the fiducial setup introduced above for various perturbative calculations. Specifically, we consider MiNLO′ predictions, and a number of predictions including NNLO corrections, both at fixed order and matched to parton showers through MiNNLO$_{PS}$: besides the complete NNLO predictions (that include the LO loop-induced $gg$ contribution), we provide the NNLO corrections to the $q\bar{q}$ channel (dubbed NNLO$_{q\bar{q}}$) and nNNLO cross sections (as defined before). For completeness, we also quote nNNLO predictions combined with NLO EW corrections, computed at fixed-order with Matrix, either using an additive or multiplicative scheme. In the latter predictions we also take into account the photon-induced contribution at LO and beyond.[5] In order to compare our predictions to fixed-order results, all MiNNLO$_{PS}$ (and MiNLO′) results of Table 4.2 are obtained at parton level, without including hadronization, MPI or photon radiation effects. We have checked explicitly that those effects have a negligible impact on the integrated cross sections.

The MiNNLO$_{PS}$ prediction and the NNLO result are in excellent agreement with each other both in the inclusive and in the fiducial setup. The perturbative uncertainty at (n)NNLO(+PS) is at the $(2-3)\%$ level. In particular, despite the fact that the loop-induced $gg$ process at LO (NLO) contributes only about $(6-8)\%$ $\big((10-15)\%\big)$ to the NNLO (nNNLO) cross section, the uncertainties of the (n)NNLO results are dominated by the gluon-initiated contribution. The NLO correction for the loop-induced $gg$ channel is particularly sizable, almost doubling the LO contribution entering at $\alpha_s^2$, as discussed in Section 4.1.3. Accordingly, the nNNLO central prediction is not included in the NNLO uncertainty band.

---

[5]We used the `NNPDF31_nnlo_as_0118_luxqed` [239–241] PDF set to compute fixed-order predictions which include EW corrections, and verified that the (n)NNLO prediction is modified at the few permille level with respect to the prediction obtained with `NNPDF31_nnlo_as_0118`.

| $\sigma(pp \to e^+e^-\mu^+\mu^-)$ [fb] | setup-inclusive | setup-fiducial |
|---|---|---|
| NLO (MATRIX) | $32.50(1)^{+1.9\%}_{-1.6\%}$ | $16.49(1)^{+1.9\%}_{-1.6\%}$ |
| MiNLO$'$ | $31.42(3)^{+6.3\%}_{-5.0\%}$ | $16.38(2)^{+6.0\%}_{-5.0\%}$ |
| NNLO$_{q\bar{q}}$ (MATRIX) | $34.42(4)^{+1.0\%}_{-1.0\%}$ | $17.45(3)^{+1.0\%}_{-1.0\%}$ |
| NNLO (MATRIX) | $36.57(4)^{+2.4\%}_{-2.1\%}$ | $18.84(3)^{+2.5\%}_{-2.1\%}$ |
| nNNLO (MATRIX) | $38.31(4)^{+2.2\%}_{-2.0\%}$ | $19.96(3)^{+2.6\%}_{-2.3\%}$ |
| nNNLO+NLO$_{\text{EW}}$ (MATRIX) | $36.43(7)^{+2.6\%}_{-2.4\%}$ | $19.00(4)^{+2.7\%}_{-2.4\%}$ |
| nNNLO×NLO$_{\text{EW}}$ (MATRIX) | $35.63(7)^{+2.5\%}_{-2.3\%}$ | $18.58(4)^{+2.6\%}_{-2.3\%}$ |
| NNLO$_{q\bar{q}}$+PS (MiNNLO$_{\text{PS}}$) | $34.36(3)^{+0.8\%}_{-1.0\%}$ | $17.45(3)^{+0.9\%}_{-1.0\%}$ |
| NNLO+PS (MiNNLO$_{\text{PS}}$) | $36.50(3)^{+1.9\%}_{-2.0\%}$ | $18.90(3)^{+2.5\%}_{-2.0\%}$ |
| nNNLO+PS (MiNNLO$_{\text{PS}}$) | $38.35(3)^{+2.1\%}_{-2.0\%}$ | $20.04(3)^{+2.5\%}_{-2.0\%}$ |
| Extracted from CMS 13 TeV | $39.4 \pm 0.7_{\text{(stat)}}$ $\pm 1.1_{\text{(syst)}} \pm 0.9_{\text{(theo)}} \pm 0.7_{\text{(lumi)}}$ | $20.3 \pm 0.4_{\text{(stat)}}$ $\pm 0.6_{\text{(syst)}} \pm 0.4_{\text{(lumi)}}$ |

**Table 4.2:** Integrated cross sections at various perturbative orders in both the `setup-inclusive` and `setup-fiducial` region. In brackets we report the statistical uncertainties, while scale uncertainties are reported in percentages. We also report the inclusive and fiducial cross sections measured by the CMS experiment in [195]. Since the measured inclusive cross section corresponds to on-shell $pp \to ZZ$ production, we have multiplied the measured cross section by a branching fraction of $\text{BR}(Z \to \ell^+\ell^-) = 0.03366$, as quoted in [195], for each $Z$ boson and by a factor of two to compare with our predictions for $pp \to e^+e^-\mu^+\mu^-$ production. For the measured fiducial cross section the CMS analysis includes both different-flavour ($e^+e^-\mu^+\mu^-$) and same-flavour ($e^+e^-e^+e^-$, $\mu^+\mu^-\mu^+\mu^-$) decay channels of the two $Z$ bosons. We have therefore divided the measured fiducial cross section by a factor of two to compare with our $pp \to e^+e^-\mu^+\mu^-$ predictions.

The MiNLO$'$ result is $(8-10)\%$ smaller than the MiNNLO$_{\text{PS}}$ result. Its uncertainty band, which is considerably larger than the MiNNLO$_{\text{PS}}$ one, does not contain the central (n)NNLO+PS prediction, because scale variations cannot account for the additional loop-induced $gg$ process entering at NNLO. We also note that the MiNLO$'$ uncertainty band is larger than the NLO one, and it includes the NLO result. On the contrary, the NLO uncertainty band is very small and neither MiNLO$'$ nor the NNLO central results lie inside it.

Notwithstanding the excellent agreement between the nNNLO(+PS) result and the fiducial cross section measured by CMS, the theoretical predictions should be supplemented with EW corrections. Their inclusion, using either an additive or multiplicative scheme [211], has a non-negligible impact on the nNNLO result and reduces the cross section by about $(4-6)\%$ in the fiducial region, slightly deteriorating the agreement with the experimental measurement. We note that EW effects include photon-initiated processes. These have a negligible impact in the fiducial setup, where the leading lepton has a transverse momentum larger than 20 GeV, and all leptons have a transverse momentum larger than 5 GeV. On the contrary, in the inclusive setup, without a minimal transverse momentum, the photon-initiated contribution features a collinear divergence. To avoid this divergence, the CMS analysis [195] imposed a transverse momentum cut of 5 GeV on the leptons in the evaluation of the photon-induced component. With this cut, they showed that the photon-induced contribution is less than

1% of the total cross section. For this reason, we set the photon-induced component to zero for the nNNLO+NLO$_{\text{EW}}$ and nNNLO×NLO$_{\text{EW}}$ results in the inclusive case.

### 4.2.3 Differential distributions

In this section we present our results for differential distributions. We start by comparing the nNNLO+PS predictions obtained with MiNNLO$_{\text{PS}}$ against MiNLO$'$ and fixed-order nNNLO predictions in the `setup-inclusive`, and subsequently move to consider the `setup-fiducial` and we compare our MiNNLO$_{\text{PS}}$ predictions at nNNLO+PS with the data collected and analyzed by the CMS experiment [195].

#### 4.2.3.1 Comparison against theoretical predictions

In Figure 4.4 we compare nNNLO+PS predictions for MiNNLO$_{\text{PS}}$ with MiNLO$'$ and nNNLO predictions at fixed order for four different distributions which are non-zero at LO. In particular, we consider the invariant mass of the $e^+e^-$ pair ($m_{e^+e^-}$), the invariant mass ($m_{4\ell}$) and the rapidity of the diboson system ($y_{4\ell}$), and the rapidity ($y_{Z_1}$) of the $Z$ boson whose invariant mass is closer to $m_Z$. We remind the reader that both the MiNNLO$_{\text{PS}}$ and the MiNLO$'$ predictions are obtained at parton level, without including hadronization, MPI or photon radiation effects. We observe a very good agreement between the nNNLO+PS and the nNNLO predictions, both for the central values and for the scale-variation bands. The latter are at the few-percent level across the whole range shown in the plots, becoming larger (about $\pm 5\%$) at high $m_{4\ell}$. Minor differences are visible in the tails of the distributions, in particular at large $m_{4\ell}$, where the nNNLO-accurate MiNNLO$_{\text{PS}}$ and fixed-order predictions however still overlap. Indeed, in the large invariant-mass region scale choices and terms beyond accuracy become increasingly important, as it was recently pointed out for $W^+W^-$ production in [115] and extensively discussed for $t\bar{t}$ production [242, 243]. The MiNLO$'$ result is in all cases about $(15-20)\%$ smaller than the nNNLO results, which provides mostly flat corrections to the distributions under consideration, increasing slightly only at large $m_{4\ell}$. We stress that the relatively flat QCD corrections are a feature of the chosen distributions (in the inclusive setup) that does not apply in general, as we shall see below. Although the MiNLO$'$ uncertainty is a factor of 3 larger than the MiNNLO$_{\text{PS}}$ and nNNLO ones, the MiNLO$'$ predictions do not overlap with the nNNLO-accurate results. This is not unexpected since a large part of the difference is caused by the loop-induced $gg$ contribution. Since the latter is missing in the MiNLO$'$ predictions, the MiNLO$'$ scale variation can not account for this new production process, which instead enters the nNNLO results. From the second ratio panel we can appreciate the effect of the loop-induced $gg$ contribution both at LO (comparing NNLO+PS to NNLO$_{q\bar{q}}$+PS) and at NLO (comparing nNNLO+PS to NNLO$_{q\bar{q}}$+PS). It is clear from the plots that due to the gluon flux the impact of the loop-induced $gg$ process is more prominent in certain phase-space regions. The LO (NLO) corrections, which inclusively amount to $(6-8)\%$ $\big((10-15)\%\big)$ as pointed out before, contribute more significantly in the bulk region of the distributions, i.e. at the $Z$ resonance in $m_{e^+e^-}$ as well as for small $m_{4\ell}$ and central rapidities.

In Figure 4.5 we show the same comparison for the transverse momentum of the $\mu^+\mu^-$ pair ($p_{\text{T},\mu^+\mu^-}$) and the transverse momentum of the leading jet ($p_{\text{T},j_1}$) above
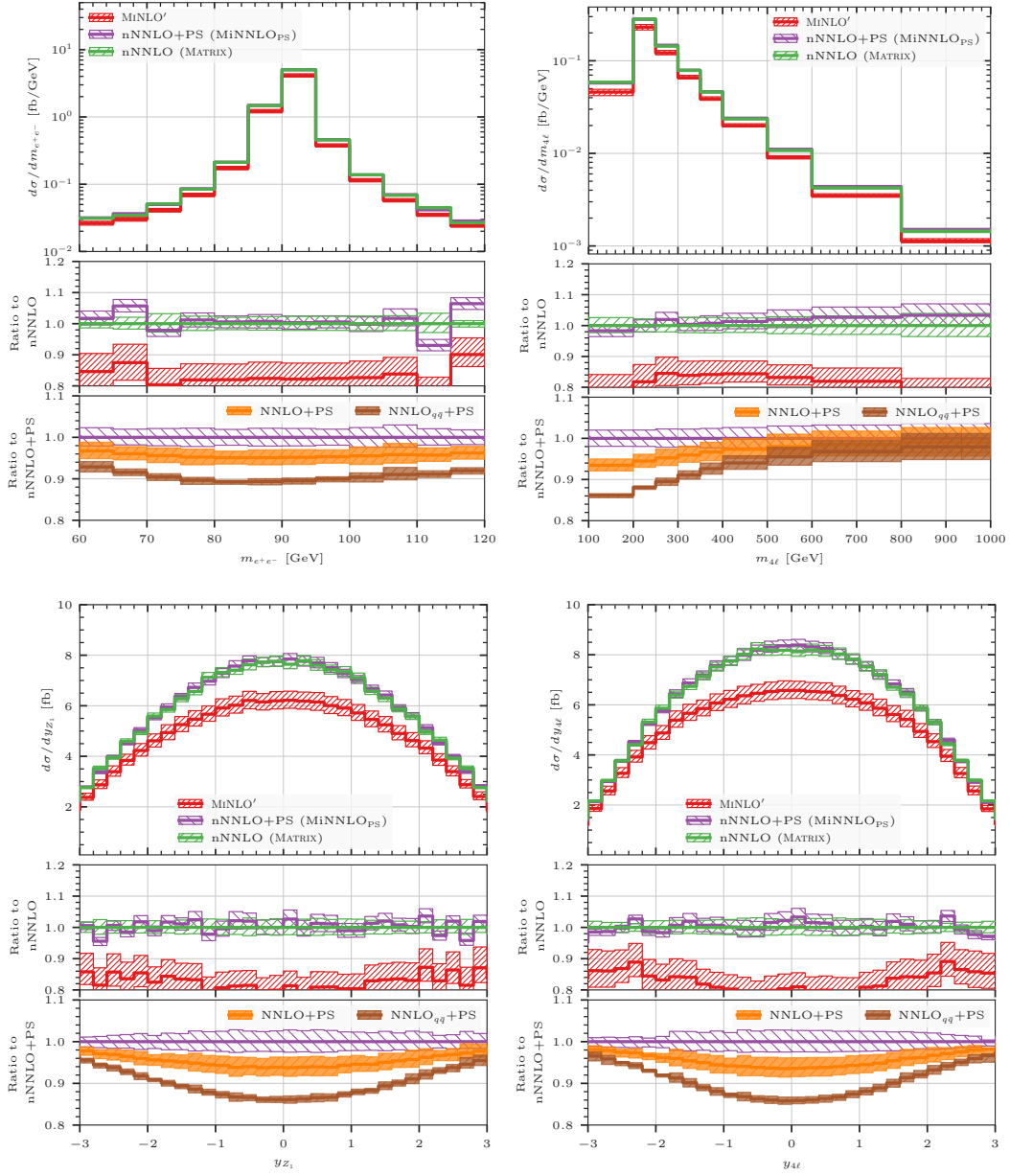
**Figure 4.4:** Comparison between selected distributions computed with MATRIX, MiNNLO_PS and MiNLO′. Upper panel: invariant mass of the $e^+e^-$ pair (left) and of the $ZZ$ pair (right); lower panel: rapidity of $Z_1$ (left) and of the $ZZ$ pair (right).
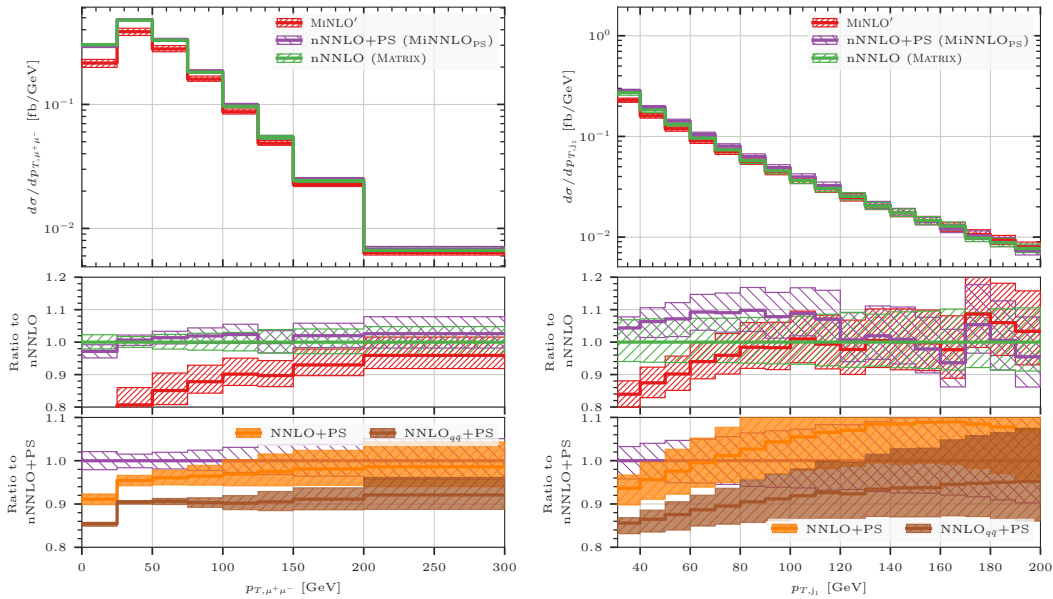
**Figure 4.5:** Same as Figure 4.4, for the transverse momentum of the $\mu^+\mu^-$ pair (left) and of the leading jet (right).

30 GeV. The latter was constructed using the anti-$k_{\text{T}}$ algorithm [128] with a jet radius of $R = 0.4$ as implemented in FASTJET [244]. While $p_{\text{T},\mu^+\mu^-}$ is already defined at LO, $p_{\text{T},j_1}$ receives its first contribution only at NLO and its accuracy is thus effectively reduced by one perturbative order. The MiNNLO$_{\text{PS}}$ and the nNNLO results for $p_{T,\mu^+\mu^-}$ are in good agreement with each other in the whole range shown here. The MiNLO$'$ result is more than 20% smaller at low values of the transverse momentum, while it agrees with the other two predictions at large values of $p_{\text{T},\mu^+\mu^-}$. Hence, this distribution shows that in general QCD corrections are not uniformly distributed in phase space. By and large, the three predictions for the transverse momentum of the leading jet display a good agreement, especially in the tail of the distribution. The level of agreement between nNNLO and MiNNLO$_{\text{PS}}$ is expected as both predictions are effectively nNLO accurate at large $p_{\text{T},j_1}$. The residual scale uncertainties are at the $(5-10)\%$ level and they are larger than those in the other distributions, which is a direct consequence of the lower accuracy of the predictions for this distribution. Looking at the effect of loop-induced $gg$ contribution in the second ratio panel, we observe a rather peculiar behaviour with the nNNLO+PS corrections being negative with respect to NNLO+PS for $p_{\text{T},j_1} \gtrsim 80$ GeV. However, this is completely in line with the results presented in Figure 4.3 and it is a consequence of the fact that the NNLO+PS predictions include only a LO+PS calculation for the loop-induced $gg$ process, which is not expected to describe the high $p_{\text{T},j_1}$ range as it is filled entirely by the parton shower, which has no accuracy in this region. This further underlines the need for including NLO corrections to the loop-induced $gg$ process. Indeed, after including the NLO corrections, the loop-induced $gg$ contribution reduces to 5% (and less) at high $p_{\text{T},j_1}$ (comparing nNNLO to NNLO$_{q\bar{q}}$+PS), which is more reasonable.

In Figure 4.6 we show an analogous comparison for the transverse-momentum spectrum of the electron ($p_{\text{T},e^-}$) and of the leading lepton ($p_{\text{T},\ell_1}$). For the $p_{\text{T},e^-}$ distribution we observe excellent agreement over the whole range between the MiNNLO$_{\text{PS}}$ and
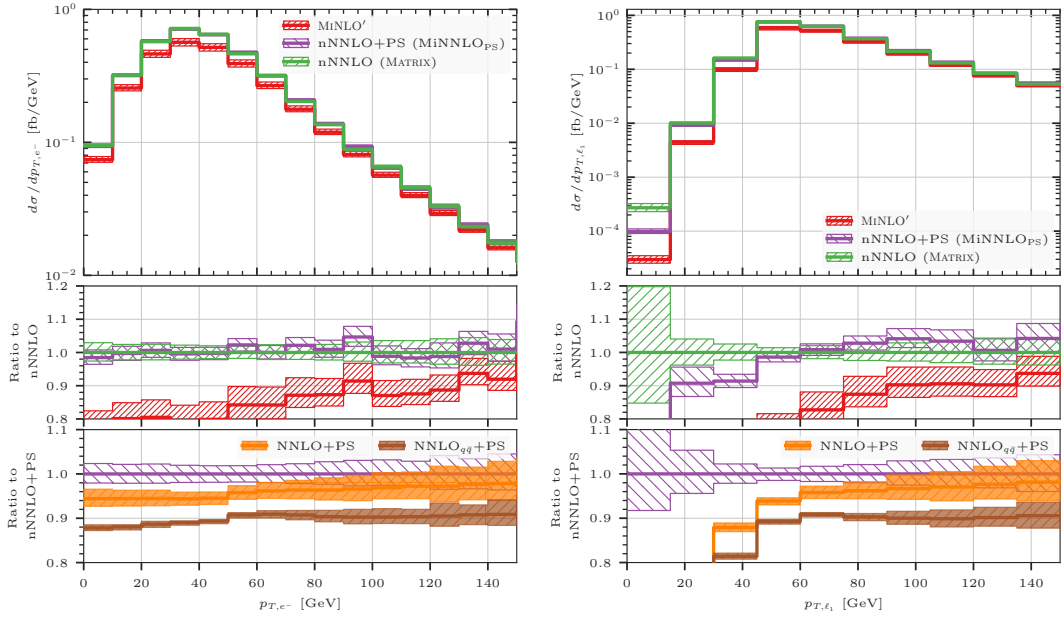
**Figure 4.6:** Same as Figure 4.4, for the transverse momentum of the electron (left) and of the leading lepton (right).

the nNNLO results, which is fully expected since this distribution should be affected very mildly by resummation/shower effects. We have explicitly checked that a similar level of agreement is obtained when considering the same comparison at NNLO$_{q\bar{q}}$ accuracy, as opposed to the GENEVA calculation in [111], where differences between the GENEVA and fixed-order results are observed for $p_{\text{T},e^-} > 40$ GeV. When comparing the MINNLO$_{\text{PS}}$ and the MINLO′ predictions for the $p_{\text{T},e^-}$ spectrum we observe that the effect of both the NNLO$_{q\bar{q}}$ corrections and the loop-induced $gg$ contribution is particularly pronounced in the bulk region of the distribution, where the MINLO′ result is more than 20% smaller than the nNNLO result. On the other hand, the transverse momentum of the leading lepton is subject to shower effects, especially at low $p_{\text{T},\ell_1}$, and indeed we observe a difference between the MATRIX results and the MINNLO$_{\text{PS}}$ predictions below 40 GeV, which become increasingly larger the more steeply the distribution falls when $p_{\text{T},\ell_1}$ approaches zero. Above this value, the shower effects are less pronounced and the two predictions are in good agreement. By comparing the nNNLO+PS predictions to the NNLO+PS and NNLO$_{q\bar{q}}$+PS results we can see that the impact of the loop-induced $gg$ contribution is particularly relevant below 40 GeV, and it is also predominantly responsible for the relatively large shower effects that we observe. In fact, we have checked that for the NNLO$_{q\bar{q}}$+PS result the relative impact of the shower is smaller than for the NLO+PS result in the $gg$ channel, which is expected considering the higher perturbative accuracy (and thereby logarithmic terms) already included at fixed order in the $q\bar{q}$ channel.

Finally, in Figure 4.7 we show predictions for the transverse momentum of the diboson pair ($p_{\text{T},4\ell}$). In this case, we also show the NNLO+N$^3$LL result obtained with MATRIX+RADISH [245], which interfaces MATRIX [223] to the RADISH resummation formalism [141, 142], using $\mu_{\text{R}} = \mu_{\text{F}} = m_{4\ell}$ and $Q_{\text{res}} = m_{4\ell}/2$ for the resummation scale. Since MATRIX+RADISH does not include the contribution stemming from the loop-
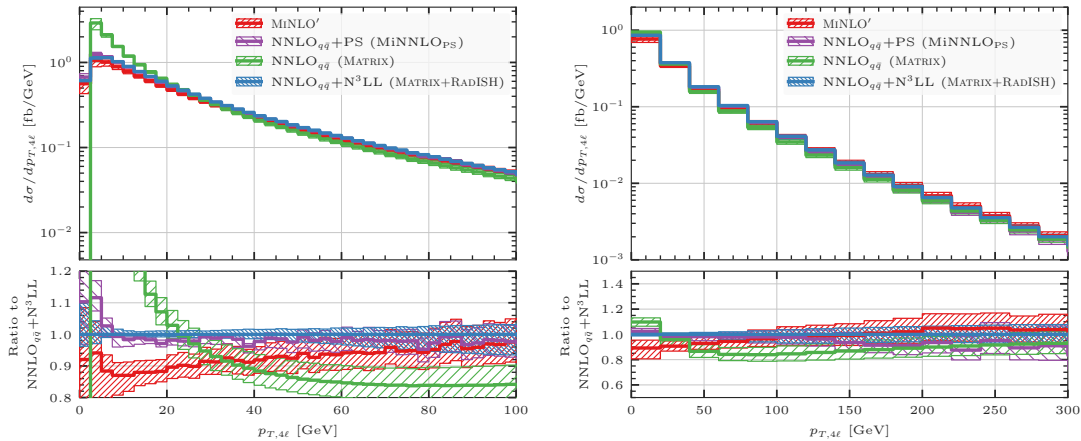
**Figure 4.7:** Same as Figure 4.4, for the transverse momentum of the $ZZ$ pair for two different ranges of $p_{T,4\ell}$. In both plots, we also show the NNLO+N$^3$LL result computed with Matrix+RadISH [245].

induced $gg$ channel, we perform this comparison by considering only the $q\bar{q}$-initiated process, *i.e.* at the NNLO$_{q\bar{q}}$(+PS) level. At small values of the $ZZ$ transverse momentum we observe an excellent agreement between the NNLO+N$^3$LL and the MiNNLO$_{PS}$ result, especially considering the lower accuracy of the parton shower in that region; MiNNLO$_{PS}$ is between 5% and 8% larger than the NNLO+N$^3$LL prediction below 10 GeV and has a larger uncertainty band reflecting its lower accuracy. On the other hand, the MiNLO$'$ result is $\mathcal{O}(10\%)$ smaller than the NNLO+N$^3$LL and the MiNNLO$_{PS}$ predictions and its uncertainty band does not overlap with either of the more accurate results below 40 GeV. Fixed-order calculations actually lead to unphysical results in the small-$p_{T,4\ell}$ region due to large logarithmic corrections, which need to be resummed to all orders. Indeed, the NNLO result diverges at low transverse momentum, and its prediction differs significantly from the ones including resummation effects. At larger values of $p_{T,4\ell}$ the NNLO result is instead in agreement with the NNLO+N$^3$LL, MiNLO$'$ and MiNNLO$_{PS}$ predictions, as one may expect since all of them have the same formal accuracy in the tail of the distribution.

In conclusion, we observe overall a very good agreement between MiNNLO$_{PS}$, fixed-order, and analytically resummed results across a variety of distributions, which provides a robust validation of our calculation. The MiNLO$'$ result, despite the considerably larger uncertainty bands, rarely overlaps with the (n)NNLO(+PS) predictions, thus highlighting the importance of higher-order corrections to this process. Moreover, certain observables require the resummation of large logarithmic contributions, which renders the matching to the parton shower mandatory.

### 4.2.3.2 Comparison against data

In this section we compare our MiNNLO$_{PS}$ predictions at nNNLO+PS to the CMS measurement presented in [195] in the `setup-fiducial` defined in Table 4.1. We have generated the events and estimated the theoretical uncertainties as described in Section 4.2.1. We note that in order to compare against data our predictions include MPI and hadronization effects, as well as QED corrections in the shower approximation.

The comparison between MiNNLO$_{PS}$ predictions and experimental data is pre-

sented in Figure 4.8. Altogether, we show predictions for six observables: the invariant mass and the transverse momentum of the diboson pair ($m_{4\ell}$ and $p_{\text{T},4\ell}$), the sum of the four individual transverse-momentum distributions of each final-state lepton (which corresponds to the average of the lepton transverse-momentum distributions), the sum of the two distributions of the transverse momentum of the reconstructed $Z$ bosons (which analogously corresponds to the average of the $Z$ transverse-momentum distributions), and the separation between the two $Z$ bosons in the azimuthal angle ($\Delta\phi_{Z_1,Z_2}$) and in the $\eta$–$\phi$ plane ($\Delta R_{Z_1,Z_2}$). In all cases, except for $\Delta\phi_{Z_1,Z_2}$ that has a kinematical endpoint at $\Delta\phi = \pi$, the last bin shown in the figures also includes the contribution of the overflow.

By and large, we observe a quite remarkable agreement between our predictions and the experimental data. The invariant mass is well described at low $m_{4\ell}$, but there is a tendency of the data to undershoot the prediction at large $m_{4\ell}$, with the last bin being almost two standard deviations away. In this region EW corrections are known to be important and they are only partly included here through the QED shower. Below, we discuss how the inclusion of the NLO EW corrections at fixed order improves the agreement with data in this region. The transverse-momentum distribution of the $ZZ$ pair is also well described, except for a two-sigma deviation in the last bin, with a remarkable agreement for $p_{\text{T},4\ell}$ values below $\sim 100\,\text{GeV}$, where the all-order corrections provided by the shower are particularly important. The two averaged distributions of $p_{\text{T},\ell_i}$ and $p_{\text{T},Z_i}$ also compare very well to MINNLO$_{\text{PS}}$, with deviations in the tail of the distributions only. In the last bins the experimental data are about two standard deviations away from the theoretical predictions, which can again be related to the missing EW corrections, as discussed below. The $\Delta\phi_{Z_1,Z_2}$ and the $\Delta R_{Z_1,Z_2}$ distributions are also very well described by MINNLO$_{\text{PS}}$, with the data fluctuating (within one sigma, except for one bin with a two-sigma deviation) around the central theoretical prediction across the whole plotted range.

The comparison at the level of integrated cross section in Section 4.2.2 showed that the inclusion of NLO EW effects has a small, but non-negligible impact in the fiducial setup. Since in our comparison with data we include QED effects via parton-shower matching, one may wonder whether the proper inclusion of NLO EW effects in a MC context, see *e.g.* [209, 246], would further improve the agreement with the data, especially in the tails of distributions where EW logarithms are important. A possible way to assess the impact of the EW corrections beyond the parton shower approximation is to apply to the MINNLO$_{\text{PS}}$ predictions a differential $K$-factor correction for the NLO EW corrections that is computed at fixed order accuracy.

We have done this exercise turning off the QED shower in the MINNLO$_{\text{PS}}$ predictions to avoid double counting. The central rescaled prediction is shown in the lower ratio panels in Figure 4.8. We adopt as our default a factor $K^{(\times)}_{\text{NLOEW}}$, defined using the multiplicative scheme nNNLO$\times$NLO$_{\text{EW}}$ [211], which includes an estimate of mixed higher-order corrections, divided by the nNNLO result. Note that for distributions starting at NLO QCD we do not perform this additional comparison, since one would need to compute the EW corrections to the $ZZ$+1-jet process. We find that the inclusion of NLO EW corrections within this approximation improves the agreement with the experimental data for the tails of the $m_{4\ell}$ and the averaged $p_{\text{T},Z_i}$ distributions, where the effects of Sudakov logarithms are expected to be visible. For the averaged
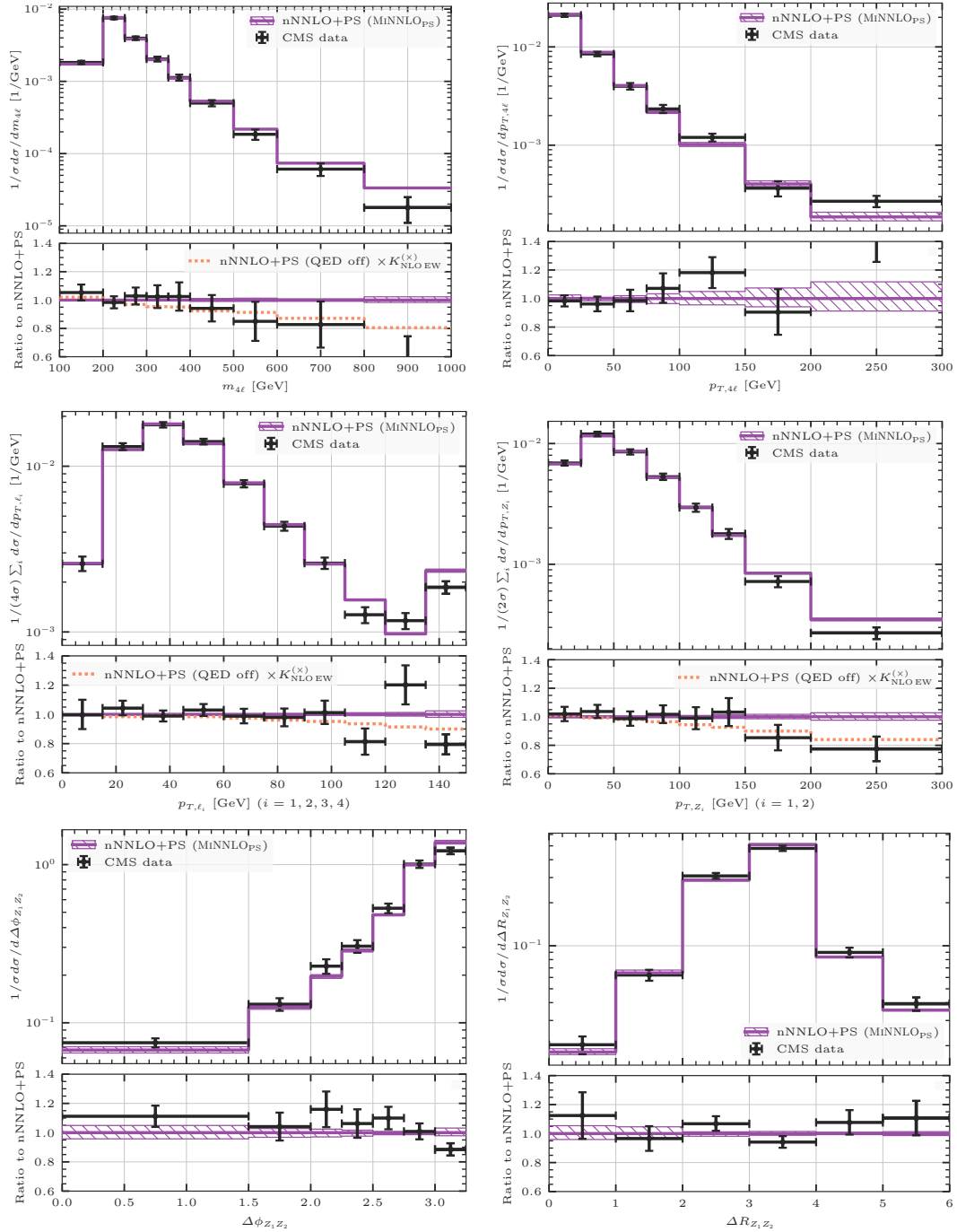
**Figure 4.8:** Comparison between the MiNNLO_PS predictions and the CMS data of [195] based on a 137 fb$^{-1}$ 13 TeV analysis for various observables. The MiNNLO_PS predictions include hadronization and MPI effects, as well as QED effects as provided by the Pythia8 parton shower. See text for more details.

$p_{\mathrm{T},\ell_i}$ distribution their impact is a bit milder, also because the distribution extends to lower values, and there is no significant improvement compared to data. Furthermore, we would like to add some comments on the effects of the QED shower below the $m_{4\ell} \sim 2\, m_Z$ threshold (where QED effects are expected to be sizable) in light of its limited accuracy. First of all, we verified that its effect is below 10% in the first bin of the $m_{4\ell}$ distribution in Figure 4.8, but it can become as large as 35% when considering the `setup-inclusive` for the same bin instead. Moreover, we notice from Figure 4.8 that the approximation of the QED shower in that region is in good agreement with the result including NLO EW effects. This is not unexpected, because logarithmic contributions due to EW Sudakov effects are small in that region and the first emission is the most relevant one for dressed leptons. We note that a full inclusion of NLO EW effects in our MINNLO_PS predictions with a complete and consistent matching to QCD and QED, is left for future work.

## 4.3 Summary

Let us summarise our main results for *Z*-boson pair production at the LHC. We have matched NNLO QCD predictions for the $q\bar{q}$-initiated process to parton showers using the MINNLO_PS method, and furthermore included the loop-induced $gg$-initiated process, which contributes at $\mathcal{O}(\alpha_s^2)$, in the POWHEG-BOX-RES framework at NLO QCD accuracy matched to parton showers. When combined, the ensuing nNNLO+PS results constitute the most accurate theoretical predictions for this process to date.

We have performed an extensive comparison of our MINNLO_PS predictions against (n)NNLO fixed-order results and the analytic resummation in the transverse momentum of the four-lepton system. We found excellent agreement with fixed-order predictions in phase-space regions where shower effects are expected to be small. As expected, for distributions that have a singularity at fixed order the MINNLO_PS predictions feature the appropriate Sudakov damping close to the singularity and yield physical results. In particular, the comparison to the NNLO+N³LL $p_{\mathrm{T},4\ell}$ spectrum showed quite a remarkable agreement. Moreover, we have shown that MINNLO_PS corrections are at the level of $(15-20)\%$ with respect to MINLO′, and that the matching to the parton shower is crucial for observables sensitive to soft-gluon effects. It is interesting to notice that we do not observe the mild tension in the $p_{\mathrm{T},e^-}$ distribution observed in [111] when comparing NNLO$_{q\bar{q}}$+PS to fixed-order predictions, which motivates a more comprehensive comparison between GENEVA and MINNLO_PS predictions in the future.

We have compared our nNNLO+PS predictions against 13 TeV CMS data of [195] and found excellent agreement both at the level of production rates and shapes of kinematical distributions, with nNNLO+PS predictions and CMS data agreeing on almost all bins within one sigma. In the few bins where the differences are at the two-sigma level we have shown that the inclusion of NLO EW corrections removes those differences in most instances. Our final results have missing higher-order uncertainties that are of the order of 2% both for inclusive and fiducial cross sections. These uncertainties[6]

---

[6]We note that we consider here only uncertainties associated to scale variation. In particular we have omitted PDF uncertainties, those related to missing interference effects in the case of identical leptons in the final state, and those intrinsic to the approximations in the event simulation (*e.g.* related to the QED shower).

are of similar size as the current precision of experimental results, which will further decrease in the future. It is then clear that theoretical predictions with an accuracy comparable to that of the results presented in this work are mandatory to fully exploit $ZZ$ cross section measurements at the LHC. This is particularly the case when using $ZZ$ production data for off-shell Higgs cross section measurements in the $h \to 4\ell$ channel to put bounds on the Higgs-boson width, or when constraining the coefficients of effective-field-theory operators or anomalous triple-gauge couplings. It is interesting to note that, even though the loop-induced $gg$ contribution is only about 10% of the total cross section, its uncertainty dominates our final predictions. It is unlikely that a three-loop calculation for this process will become available in the near future. Still, the theoretical precision can be further improved if one imposes fiducial cuts that suppress the loop-induced ggF contribution. For instance, when requiring a large invariant mass of the lepton system or when considering high-$p_{\mathrm{T}}$ leptons, as done in BSM searches, the ggF contribution becomes less important since the gluon PDFs decrease strongly at large $x$ values. On the other hand, electroweak effects become more important in these regions. The approximate combination considered here, which already increases the agreement with the experimental data in the high-energy tails, needs to be improved by combining highest-order QCD and QED corrections consistently in parton-shower simulations in the future.

Since the evaluation of the two-loop contributions is numerically highly demanding, we made full use of the reweighting facility of POWHEG and introduced the possibility to evaluate the two-loop contributions only at the very end of the event generation, considerably speeding up the calculation. The code used for our simulations will be publicly available within POWHEG-BOX-RES.[7] We are confident that this will be valuable for upcoming experimental measurements of $ZZ$ production at the LHC, which require an accurate and fully exclusive simulation of hadron-level events, including all-order, non-perturbative, and QED effects.

---

[7] https://powhegbox.mib.infn.it/

# Part II

# Higgs physics beyond the Standard Model

# Chapter 5

# Introduction & motivation

The observed resonance around 125 GeV at the LHC [1, 2] with approximately the properties of the SM Higgs boson not only provides a wealth of possibilities to study the SM in detail, but also provides a unique tool for searches of manifestations of new physics, *i.e.* physics beyond the SM. Without any direct discoveries of new BSM states at the LHC, in addition to an absence of statistically significant global deviations from the SM predictions, an effective-field-theory (EFT) paradigm has emerged in which effects of possible BSM physics can be studied systematically using existing collider measurements while reserving the possibility to remain agnostic about the specific UV completion of the theory. In fact, it could very well be that the lack of significant deviations from the SM picture is mostly due to a large degree of decoupling between the SM physics around the EW scale and the BSM dynamics at much higher energy scales, motivating the use of EFTs to search for physics beyond the SM indirectly.

At the heart of any EFT approach lies the concept of decoupling [247], or the idea that the physics at very small distances should in general not affect the dynamics on much larger scales, up to a certain accuracy. In situations with a sufficient degree of decoupling, *i.e.* with sufficiently separated scales, one can use the ratio of these scales as an expansion parameter to obtain an effective description of the physics at the macroscopic level rather than having to consider the full microscopic theory that underlies it. This is very useful in particle physics, in particular in the search of BSM dynamics where the potential BSM states are too heavy to be produced on shell. Such heavy new particles can still contribute to low-energy scattering processes by appearing as virtual intermediate states in tree-level or loop-level diagrams. Recall that in quantum field theory, scattering amplitudes are expressed in terms of correlation functions which exhibit non-analytic behavior (*i.e.* poles and branch cuts) when the kinematics allow for internal propagators $\propto 1/(p^2 - m^2 + i\epsilon)$ to go on shell ($p^2 = m^2$). However, when a virtual particle with mass $M$ is too heavy to be produced on shell ($p^2 \ll M^2$), its contributions to the amplitude are purely analytic and can therefore be Taylor expanded, *e.g.* the tree-level internal propagators for such heavy intermediate states can be written as

$$\frac{1}{p^2 - M^2} = -\frac{1}{M^2} \left\{ 1 + \frac{p^2}{M^2} + \mathcal{O}\left(\frac{p^4}{M^4}\right) \right\} . \tag{5.1}$$

The expanded non-local correlation functions will thus resemble an infinite set (or tower) of local operators that consist purely of light fields.

In fact, the expansion in terms of local operators can already be achieved at the level of the Lagrangian, after *integrating out* the heavy degrees of freedom (*i.e.* those associated to the scale $M$) from the generating functional of correlation functions. The result is an EFT that includes in addition to the original low-energy Lagrangian a series of local operators, built purely out of (products of) light degrees of freedom and derivatives, that obey the symmetries of the low-energy theory such as Lorentz or gauge invariance. They are accompanied by Wilson coefficients parametrising the short-distance physics. This constitutes a so-called top-down EFT approach as it starts from a specific theory in the UV and integrates out the heavy fields to obtain a low-energy effective description. The projection or matching of the UV model onto the EFT framework fixes the EFT parameters (*i.e.* the Wilson coefficients), which can be done using perturbation theory when the UV completion is weakly-coupled.

It is also possible to define the EFT dynamics without knowing a priori the exact details of the underlying theory. Starting at a low (accessible) energy scale, one augments the low-energy Lagrangian by a set of higher-dimensional local operators, assembled from the low-energy degrees of freedom. The additional operators must respect the symmetries of the low-energy theory, and are suppressed by a cutoff scale $\Lambda$ that resembles the mass $M$ in (5.1). The associated Wilson coefficients have to determined by experiment. Such bottom-up EFT approaches are powerful tools because they provide a systematic way of classifying BSM scenarios in a rather model-independent fashion.

The SMEFT [248–250] is an example of such a bottom-up EFT, where the SM is viewed as the low-energy realisation of some unknown UV-complete theory. It will be used throughout Chapters 6 and 7. In the SMEFT, the renormalisable SM Lagrangian is extended by a series of higher-dimensional operators invariant under the SM gauge group $SU(3)_c \times SU(2)_L \times U(1)_Y$, in the following way

$$\mathcal{L}_{\text{SMEFT}} = \mathcal{L}_{\text{SM}} + \sum_{n=5}^{\infty} \sum_i \frac{c_i^{(n)}}{\Lambda^{n-4}} \mathcal{O}_i^{(n)} \,, \tag{5.2}$$

where $\mathcal{O}_i^{(n)}$ denote the local operators with mass dimension $n \geq 5$ and $c_i^{(n)}$ are their corresponding dimensionless Wilson coefficients which are suppressed by powers of the cutoff scale $\Lambda$. The idea is that extensions to the SM will involve particles that are at least heavier than then measured Higgs vacuum expectation value ($v \approx 246$ GeV), and the SMEFT constructed in this way is a consistent IR limit of such extensions, only limited by the assumptions that $\Lambda > v$ and the existence of a SM-like Higgs doublet (see *e.g.* [250] for a more detailed discussion). We add that the scale $\Lambda$ in (5.2) for Wilson coefficients with a magnitude of one does not necessarily correspond to the mass $M$ of a heavy particle that has been integrated out, but will rather be a combination of $M$ and its coupling constant in the UV. Moreover, if the operators are expected to be SM-coupling- and/or loop-suppressed, it will be more useful to adopt a different normalisation (*cf.* (6.9) or the discussion in Section 7.3).

At the dimension-five level, the SMEFT adds merely one operator to the SM Lagrangian, which violations lepton-number conservation [251] but allows for the generation of neutrino masses. Chapters 6 and 7 of this thesis are however rely on the SMEFT at dimension six, for which the first complete and non-redundant operator basis was presented in [249]. While efforts are being made to obtain a general fit of the many

dimension-six SMEFT operators, *e.g.* 63 in the case of [249], to the available experimental data (see for example [252, 253] for some recent results), requiring absolute model-independence can in practice impede the extraction of meaningful results due to the large number of free parameters in the fit. In Chapters 6 and 7 we will therefore consider only a subset of the full dimension-six operator basis, the choices of which we will further motivate in the relevant sections.

Also the in Chapter 1 mentioned hierarchy problem of the Higgs sector can be understood from an EFT perspective. A nice intuitive explanation, adopted from [254], is based on the same dimensional analysis that leads to the suppression of higher-dimensional operators. The $\Lambda$-suppression in (5.2) follows immediately from the requirement of a dimensionless action in a four-dimensional spacetime and could explain the fact that so far any significant effects due to higher-dimensional operators have escaped detection. Applying the same logic to the only dimension-two operator in the Lagrangian, the Higgs mass, then yields an enhancement by two powers of $\Lambda$, *i.e.*

$$c\,\Lambda^2 |H|^2\,, \tag{5.3}$$

where $c$ is a numerical coefficient and $H$ the SM Higgs doublet. Since we have measured the Higgs mass to be $m_h = 125$ GeV and therefore $\mu^2 = m_h^2/2 = (89 \text{ GeV})^2$ in the SM, it follows that when new dynamics is suppressed by a large cutoff scale, for instance in a Grand Unified Theory (GUT) associated with a scale $\Lambda_{\text{GUT}} \sim 10^{16}$ GeV, an enormous hierarchy appears as

$$\frac{\mu^2}{\Lambda_{\text{GUT}}^2} = \frac{(89 \text{ GeV})^2}{(10^{16} \text{ GeV})^2} \sim 10^{-28}\,. \tag{5.4}$$

The unnaturally small ratio in (5.4) is what reflects the hierarchy problem in this context, which boils down to the issue that by virtue of the same dimensional analysis that requires the higher-dimensional operators to be suppressed by powers of the scale of heavy new physics, we would expect a Higgs mass that is different from the observed value by many orders of magnitude. The problem moreover manifests itself beyond tree level, when heavy states perturb the Higgs mass via loop contributions to its self-energy, which exhibit a strong sensitivity to $\Lambda$. This is most easily made explicit using a cutoff-based regularistation scheme where the suppression scale $\Lambda$ enters as the regulator of the (quadratic) UV divergences, but holds also when using a mass-independent regularisation scheme like dimensional regularistation. It follows that a miraculous cancellation has to occur within the renormalisation procedure in order to correctly predict the Higgs mass around the EW scale, and hence the hierarchy or naturalness problem is phrased in terms of a fine-tuning issue.

Assuming the SM to be valid up to a cutoff scale $\Lambda$, the degree of tuning can be understood more quantitatively as follows. The SM particle with the largest coupling to the Higgs is the top quark, which at one loop generates a correction to the Higgs mass of

$$\delta\mu^2 = -\frac{3y_t^2 \Lambda^2}{8\pi^2}|H|^2\,, \tag{5.5}$$

where $y_t = \sqrt{2}m_t/v$ denotes the top-Yukawa coupling constant. We can quantify the

fine-tuning of the Higgs mass as follows

$$\Delta = \left| \frac{\delta\mu^2}{\mu^2} \right| = \left| \frac{3y_t^2 \Lambda^2}{8\pi^2} \frac{1}{\mu^2} \right| \approx \begin{cases} 1\,, & \Lambda = 500 \text{ GeV} \\ 4\,, & \Lambda = 1 \text{ TeV} \\ 100\,, & \Lambda = 5 \text{ TeV} \end{cases} \,. \tag{5.6}$$

Thus, to have a degree of tuning at the order of one requires new physics at the TeV scale. Solutions to the hierarchy problem that have received a lot of attention include supersymmetric models and composite-Higgs models, where the dimension-two Higgs mass term is either protected by a new symmetry or even absent (see *e.g.* [254, 255] for extensive reviews of such scenarios).

Instead of considering a specific theory implementation, one can adopt a more bottom-up approach and ask how we can probe a large class of possible solutions from a phenomenological point of view (as done in [256]). An appealing possibility is to focus on theories where the large top-quark corrections to the Higgs are cancelled by the addition of neutral (*i.e.* uncharged under the SM group) scalar top partners, achieving so-called *neutral naturalness*. This motivates us to look in Chapter 8 for generic Higgs-portal interactions of the form

$$c_\phi |H|^2 \phi^2 \,, \tag{5.7}$$

where $\phi$ is a real scalar that is a singlet under the SM gauge group. Notice that the aforementioned cancellation requirement fixes the coefficient to $|c_\phi| = 2N_c/\sqrt{N_r}\, y_t^2$ with $N_c = 3$ the number of colours and $N_r$ the number of scalar top partners, assuming the scalar partners to be approximately degenerate in mass.

The remainder of Part II of this thesis is structured as follows. In Chapter 6, we study modifications of the trilinear Higgs coupling within the context of the SMEFT. After a discussion of the mechanism of electroweak symmetry breaking (EWSB) in the SM (Section 6.1.1) and in the presence of dimension-six operators in the SMEFT (Section 6.1.2), we analyse in Section 6.2 the sensitivity to such operators in off-shell Higgs production at the LHC. We compare our results to projections of future single-Higgs cross-section measurements in Section 6.3 and provide a summary and outlook in Section 6.4. Subsequently, in Chapter 7 we turn our attention to the SMEFT dimension-six operators that lead to modifications of the bottom-Higgs and charm-Higgs dynamics. We provide a short review of the limits on these operators that were previously obtained in Higgs physics (Section 7.1), after which in Section 7.2 we analyse a variety of non-Higgs observables to constrain the associated Wilson coefficients. A discussion of our results in provided in Section 7.3. Finally, in Chapter 8 we study Higgs-portal couplings to $|H|^2$. Motivated the connections DM and models of neutral naturalness (*cf.* Section 8.1), we perform a sensitivity study for the HL-LHC, high-energy LHC (HE-LHC) and Future Circular Collider (FCC) to Higgs-portal interactions contributing to off-shell Higgs production in the $ZZ \to 4\ell$ decay channel (Section 8.2) and finish with a discussion of our results in Section 8.3.

# Chapter 6

# The trilinear Higgs coupling

In the pursuit of observing or constraining deviations from the SM picture, measuring the couplings of the Higgs boson to the other bosons, fermions and itself lies at the heart of the physics programme at the LHC. The couplings of the scalar resonance to EW gauge bosons and third-generation fermions have been tested extensively, showing agreement with those of the SM Higgs boson at the level of $(5 - 20)\%$ [24, 25]. The strength of these couplings will be further scrutinised at the high-luminosity option of the LHC and possible future colliders. In contrast to the couplings of the Higgs boson to EW gauge bosons and third-generation fermions, the Higgs couplings to light matter fields and its self-interactions are largely unexplored at present (*cf.* for example [257] for an overview).

In this chapter, we study possible modifications of the trilinear Higgs self-interaction originating from local dimension-six operators within the SMEFT. First, in Section 6.1 we provide a brief review of the mechanism of EWSB in the SM, introduce the effective interactions that are relevant for the computations performed in Section 6.2 and show explicitly how they modify the trilinear Higgs coupling. In Section 6.2, we investigate the LHC Run 3 and the HL-LHC sensitivity to these modifications from off-shell Higgs production in the ggF channel, considering decays to four charged leptons, *i.e.* $h^* \to ZZ \to 4\ell$. Within the context of the SMEFT, we study the effects of a modified trilinear Higgs coupling through a shape analysis of differential distributions. We compare our results to the limits one expects to obtain from inclusive single-Higgs production cross-section measurements at future LHC runs in Section 6.3. Finally, we provide a brief summary and outlook in Section 6.4.

## 6.1 Electroweak symmetry breaking

### 6.1.1 Standard Model

In the SM, the minimal realisation of electroweak symmetry is achieved by introducing one complex Higgs doublet field. The renormalisability of the SM requires its Lagrangian density, and thus also the terms that describe the potential energy associated to the Higgs field, to have a mass dimension of four. From there, it follows that the most general form of the Higgs potential in the SM is given by

$$V_{\mathrm{SM}} = -\mu^2 H^\dagger H + \lambda \left( H^\dagger H \right)^2 , \qquad (6.1)$$

where the Higgs field $H$ is a weak isospin doublet, defined as

$$H = \begin{pmatrix} H^+ \\ H^0 \end{pmatrix} . \tag{6.2}$$

Notice that the SM Higgs potential (6.1) is fully parametrised by the two parameters $\mu$ and $\lambda$, which have a mass dimension of one and zero, respectively. The vacuum, which corresponds to the ground state of the potential (*i.e.* the configuration with minimum energy), is found by minimising (6.1). This will give rise to the notion of a vacuum expectation value (VEV) for the Higgs field as a combination of $\mu$ and $\lambda$. In order for the potential to be bounded from below we must require $\lambda > 0$, after which we are left with two possibilities depending on the sign of $\mu^2$. For $\mu^2 < 0$, the potential has a simple parabolic shape with a minimum located at zero, while for $\mu^2 > 0$, minimising (6.1) gives rise to an infinite number of degenerate minima

$$\langle H^\dagger H \rangle \equiv \frac{v^2}{2} = \frac{\mu^2}{2\lambda} , \tag{6.3}$$

where the Higgs VEV, denoted as $v$, is the value of $H$ that minimises the potential. Any choice for $v$ will spontaneously break the $SU(2)_L \times U(1)_Y$ electroweak symmetry and hence generate masses for the weak gauge bosons. This is often referred to as the Brout–Englert–Higgs mechanism [9–11]. Since the photon should remain massless, only the neutral component of $H$ should acquire a non-zero VEV. Hence, without loss of generality,[1] we choose the the vacuum state of the Higgs field as

$$\langle H \rangle = \frac{1}{\sqrt{2}} \begin{pmatrix} 0 \\ v \end{pmatrix} . \tag{6.4}$$

After EWSB, we can expand the Higgs field about its VEV in order to study the fluctuations around this new minimum. To this end, we introduce the following reparametrisation of the Higgs field

$$H = U^{-1}(\xi) \begin{pmatrix} 0 \\ (v+h)/\sqrt{2} \end{pmatrix} , \quad \text{with} \quad U(\xi) = \exp\left( -\frac{i}{v} \sum_i \tau_i \xi^i \right) , \tag{6.5}$$

where $\tau_i$ denote the three $SU(2)_L$ generators and $\xi^i$ and $h$ are four real scalar fields, which all of course have a vacuum expectation value of zero. One could expect the three phase fields $\xi^i$ to be the massless Goldstone bosons as postulated by the Goldstone theorem [7, 8] for any spontaneously-broken continuous symmetry. However, in a theory where these would-be Goldstone bosons have the same quantum numbers as the long-range vector fields, these modes instead provide the extra longitudinal degrees of freedom needed to turn the massless gauge bosons into massive particles. This is most easily understood by performing a gauge transformation[2] in such a way that the physical Higgs field $h$ is the only remaining dynamical field entering the Higgs doublet, *i.e.*

$$H \to \frac{1}{\sqrt{2}} \begin{pmatrix} 0 \\ v+h \end{pmatrix} , \tag{6.6}$$

---

[1] We can always make a $SU(2)_L$ rotation such that the only $H^0$-component of $H$ acquires a real VEV.
[2] See for instance [122] for the explicit transformations.

which is called unitary gauge. In this gauge the Lagrangian becomes simply that of a massive gauge boson and it is therefore often said that in unitary gauge, the would-be Goldstone boson is *eaten* by the gauge boson via the Higgs mechanism. By plugging (6.6) into the scalar potential in (6.1) and using the definition of the Higgs VEV given in (6.3), one obtains the following SM Higgs potential after EWSB

$$V_{\text{SM}} = \frac{m_h^2}{2} h^2 + v \lambda h^3 + \frac{\lambda}{4} h^4 \, , \tag{6.7}$$

where we have omitted constant terms and identified the Higgs mass as $m_h = \sqrt{2 \lambda v^2}$. Notice that in the SM the trilinear and the quartic Higgs self-couplings are described by the same parameter $\lambda$.

### 6.1.2   Dimension-six SMEFT

To allow for a model-independent analysis, we work in the framework of the SMEFT to parametrise the possible BSM physics entering the trilinear Higgs coupling. We consider only the subset of dimension-six CP-even operators in the so-called Strongly Interacting Light Higgs (SILH) basis [258] that are build purely from SM Higgs doublets $H$ and derivatives:

$$\mathcal{O}_6 = -\lambda |H|^6 \, , \qquad \mathcal{O}_H = \frac{1}{2} \left( \partial_\mu |H|^2 \right)^2 , \qquad \mathcal{O}_T = \frac{1}{2} \left( H^\dagger \overset{\leftrightarrow}{D}_\mu H \right)^2 , \tag{6.8}$$

where we have used the short-hand notation $H^\dagger \overset{\leftrightarrow}{D}_\mu H = H^\dagger D_\mu H - (D_\mu H)^\dagger H$. We thus implicitly assume that the couplings of the Higgs boson to EW gauge boson and fermions are SM-like and focus our attention on the self-interactions contained in (6.17). Note that the redundant operators $\mathcal{O}_R = |H|^2 |D_\mu H|^2$ and $\mathcal{O}_D = |D^2 H|^2$ do not appear in (6.8) as they can be removed in the full SILH basis via an appropriate redefinition of the Higgs field or equivalently its equations of motion [259]. Furthermore, as the operator $\mathcal{O}_T$ does not modify the trilinear Higgs coupling and is moreover severely constrained through measurements of the $\rho$ parameter describing the degree of custodial symmetry violation [23], it is irrelevant for the purpose of this work.

Within these restrictions, it is sufficient to supplement the SM Lagrangian with the effective operators $\mathcal{O}_6$ and $\mathcal{O}_H$ only, resulting in the following effective Lagrangian

$$\mathcal{L} = \mathcal{L}_{\text{SM}} + \sum_{i=6,H} \frac{\bar{c}_i}{v^2} \mathcal{O}_i \, , \tag{6.9}$$

where $\bar{c}_i$ are Wilson coefficients understood to be evaluated at the EW scale, *i.e.* $\mu = \mathcal{O}(v)$. Including the operator $\mathcal{O}_6$ in the Higgs potential results in the following form before EWSB

$$V_{\text{SMEFT}} = -\mu^2 H^\dagger H + \tilde{\lambda} \left( H^\dagger H \right)^2 + \frac{\lambda \bar{c}_6}{v^2} \left( H^\dagger H \right)^3 \, , \tag{6.10}$$

where we have used the notation $\tilde{\lambda}$ to distinguish it from the SM coupling $\lambda$. By minimising the potential, we find the following relation for VEV of the Higgs field

$$\langle H^\dagger H \rangle \equiv \frac{v^2}{2} = \frac{2\mu^2}{3\bar{c}_6 \lambda + 4\tilde{\lambda}} \, , \tag{6.11}$$

where one observes that the SM result (6.3) is retrieved by setting $\bar{c}_6$ to zero and $\tilde{\lambda} \to \lambda$, as should be the case. We proceed along the lines of the SM case and apply the EWSB procedure by substituting $H$ with its expansion around the VEV in unitary gauge. This yields, neglecting terms of $\mathcal{O}\left(h^5\right)$ and higher, in the broken phase

$$V_{\text{SMEFT}} = \frac{v^2}{2}\left(3\bar{c}_6\lambda + 2\tilde{\lambda}\right)\hat{h}^2 + \left(\tilde{\lambda} + \frac{5}{2}\bar{c}_6\lambda\right)v\hat{h}^3 + \frac{1}{4}\left(\tilde{\lambda} + \frac{15}{2}\bar{c}_6\lambda\right)\hat{h}^4 \,, \qquad (6.12)$$

where we have written $\hat{h}$ to indicate that our result is not yet canonically normalised, as will be explained below. The Higgs mass can be read off from the first term in (6.12), which in turn provides the following definition for $\tilde{\lambda}$

$$\tilde{\lambda} = \frac{m_h^2}{2v^2} - \frac{3}{2}\bar{c}_6\lambda = \lambda\left(1 - \frac{3}{2}\bar{c}_6\right) \,, \qquad (6.13)$$

where we have used the SM relation $\lambda = m_h^2/(2v^2)$. The above consideration allow us to write the potential (6.12) in the following simple form

$$V_{\text{SMEFT}} = \frac{m_h^2}{2}\hat{h}^2 + \lambda\left(1 + \bar{c}_6\right)v\hat{h}^3 + \frac{\lambda}{4}\left(1 + 6\bar{c}_6\right)\hat{h}^4 \,. \qquad (6.14)$$

The last step is to perform the canonical normalisation, which is necessary to have a well-defined propagator for the physical Higgs field $h$.[3] The dimension-six operator $\mathcal{O}_H$ contributes to the kinetic term of the Higgs field, which together with the SM term yields a factor of $(1 + \bar{c}_H)$ multiplying the kinetic term for $\hat{h}$. The kinetic term for the canonically normalised physical Higgs field $h$ is then obtained via the simple rescaling

$$\hat{h} \to h = \left(1 + \bar{c}_H\right)^{\frac{1}{2}}\hat{h} \,. \qquad (6.15)$$

The effect of $\mathcal{O}_H$ therefore represents a universal shift of all couplings of the Higgs boson. Hence, the trilinear and quartic self-couplings of the physical Higgs field $h$ including effects of both $\mathcal{O}_6$ and $\mathcal{O}_H$ are given by

$$\mathcal{L} \supset -\lambda\left(1 + \bar{c}_6 - \frac{3}{2}\bar{c}_H\right)v h^3 - \frac{\lambda}{4}\left(1 + 6\bar{c}_6 - 2\bar{c}_H\right)h^4 \,. \qquad (6.16)$$

## 6.2 Off-shell Higgs production as a probe of the trilinear Higgs coupling

As shown in Section 6.1.1, the trilinear and quartic couplings of the physical Higgs field $h$ in the SM are parametrised by the scalar potential

$$V_{\text{SM}} = \frac{m_h^2}{2}h^2 + \lambda v h^3 + \frac{\kappa}{4}h^4 \,, \qquad (6.17)$$

where $m_h \simeq 125\,\text{GeV}$ and $v \simeq 246\,\text{GeV}$ are the Higgs mass and VEV, respectively, and the trilinear ($\lambda$) and quartic ($\kappa$) Higgs couplings obey the relation

$$\lambda = \kappa = \frac{m_h^2}{2v^2} \simeq 0.13 \,. \qquad (6.18)$$

---

[3]The canonical rescaling corresponds to a finite wave-function renormalisation which ensures that the residuum of the Higgs propagator is one [260].

The SM potential is thus fully determined by only two parameters, namely $v$ and $\lambda$. However, many BSM scenarios allow for deviations of the Higgs self-couplings with respect to their SM predictions (a comprehensive collection of such theories can be found in the white paper [41]) and, consequently, could imply a departure from the SM relation (6.18). Measuring or constraining the Higgs self-couplings is therefore essential to our understanding of the mechanism of EWSB and furthermore provides a way to probe the existence of new physics.

The aforementioned relatively loose constraints on the Higgs self-interactions are due to the smallness of the cross sections of double-Higgs and triple-Higgs production, the go-to observables for testing the Higgs potential because of their direct sensitivity to trilinear and quartic Higgs couplings. As the triple-Higgs cross section is $\mathcal{O}(0.1\,\text{fb})$ for $pp$ collisions at a centre-of-mass energy of $\sqrt{s} = 14\,\text{TeV}$ even at the end of HL-LHC, having an integrated luminosity of $3\,\text{ab}^{-1}$ at hand, the quartic Higgs coupling will remain unexplored (cf. [261–270] for the prospects to determine the quartic Higgs coupling at future colliders). The HL-LHC prospects for double-Higgs production are considerably better but still remain challenging as the cross section is $\mathcal{O}(33\,\text{fb})$ in $pp$ collisions at $\sqrt{s} = 14\,\text{TeV}$. As a result, only $\mathcal{O}(1)$ determinations of the trilinear Higgs coupling from double-Higgs production seem to be possible at the LHC — see [271, 272] for the latest prospect studies by ATLAS and CMS. With this in mind, other methods of constraining the trilinear Higgs coupling have been proposed in recent years. The indirect approach first outlined in [273], where the sensitivity to the trilinear Higgs coupling arises from loop corrections to the process $e^+e^- \to Zh$, was later extended to the Higgs production and decay modes relevant at the LHC [274–279], at lepton colliders [280, 281] and to EW precision observables [282, 283].

Analyses of the constraints on the trilinear Higgs coupling including indirect probes have been presented in [277, 284–286] and recently also by ATLAS and CMS [24, 287–289]. Generally, the direct constraints on $\lambda$ obtained through double-Higgs production were shown to furnish the most stringent bounds, but indirect constraints from single-Higgs production processes have the potential to be competitive or could fulfil at least a complementary role. As already pointed out in the works [257, 275, 276], including measurements of differential distributions of single-Higgs processes could turn out to be crucial due to their non-trivial dependence on $\lambda$. This point was further investigated in the article [277], where it was found that the associated production of the Higgs together with a EW gauge boson ($Vh$) or a top-antitop pair ($t\bar{t}h$) provide additional sensitivity to $\lambda$ at the differential level.

In this section, we examine the constraints on the trilinear Higgs coupling that originate from off-shell Higgs production in proton-proton ($pp$) collisions. BSM effects entering the trilinear Higgs coupling are parametrised within the SMEFT as discussed in Section 6.1.2, which, upon EWSB and canonical normalisation of the Higgs kinetic term, can be summarised as $\big(cf.\ (6.16)\big)$

$$\mathcal{L} \supset -\lambda c_3 v h^3\,, \tag{6.19}$$

where

$$c_3 = 1 + \bar{c}_6 - \frac{3}{2}\bar{c}_H\,. \tag{6.20}$$

Notice that while the sensitivity to the Higgs trilinear coupling in the process $gg \to h^* \to ZZ \to 4\ell$ arises through NLO EW corrections, the Wilson coefficient $\bar{c}_H$ appears already at the Born level as it not only modifies the Higgs trilinear coupling, but also causes a universal shift of all couplings of the Higgs boson. We therefore include $\bar{c}_H$ at LO in our numerical analysis (Section 6.2.2), while parametrising the NLO corrections involving insertions of the Higgs trilinear coupling (Section 6.2.1) solely via the Wilson coefficient $\bar{c}_6$. Including $\bar{c}_H$ also at NLO would require taking into account all SM NLO EW effects, but this has a negligible effect on the extraction of $\bar{c}_6$ [277, 281]. Effects coming from higher-dimensional pure Higgs operators such as $\mathcal{O}_8 = -\lambda \bar{c}_8/v^4 \, |H|^4$ are not considered, but could in principle be implemented by shifting the correction factor in (6.20) in an appropriate manner, for example by $2\bar{c}_8$ in the case of $\mathcal{O}_8$.

### 6.2.1 Description of the $gg \to h^* \to ZZ$ calculation

In this section we describe the calculation of the $\mathcal{O}(\lambda)$ corrections to the process $gg \to h^* \to ZZ$ that arise in the context of (6.9). The corrections associated to insertions of the operator $\mathcal{O}_6$ are illustrated in Figure 6.1. They fall into three classes: (i) corrections to ggF Higgs production, (ii) corrections to the Higgs propagator and (iii) corrections to the Higgs decay. In the following, we will discuss separately each of these three ingredients as well as their implementation in our MC code.

#### 6.2.1.1 Higgs production

The $\mathcal{O}(\lambda)$ corrections to ggF Higgs production receive contributions from both two-loop topologies (see the upper Feynman diagram in Figure 6.1) as well as from the wave-function renormalisation of the Higgs boson field. The relevant renormalised vertex that describes the process $g(p_1) + g(p_2) \to h(p_1 + p_2)$ can be written as [278]

$$\hat{\Gamma}^{\mu\nu}_{ggh}(p_1, p_2) = -\frac{\alpha_s \delta^{a_1 a_2}}{\pi v} \left( \eta^{\mu\nu} p_1 \cdot p_2 - p_1^\nu p_2^\mu \right) \left[ \frac{\delta Z_h}{2} \mathcal{F}_1 + \frac{\lambda \bar{c}_6}{(4\pi)^2} \mathcal{F}_2 \right], \qquad (6.21)$$

where $a_1$ and $a_2$ are colour indices and $\eta^{\mu\nu} = \text{diag}(1, -1, -1, -1)$ is the Minkowski metric. In addition,

$$\delta Z_h = N_h \bar{c}_6 (\bar{c}_6 + 2), \qquad N_h = \frac{\lambda}{(4\pi)^2} \left( 9 - 2\sqrt{3}\pi \right) \simeq -1.54 \cdot 10^{-3}, \qquad (6.22)$$

is the one-loop correction to the Higgs boson wave function associated to insertions of the operator $\mathcal{O}_6$ [274, 275] and

$$\mathcal{F}_1 = \frac{m_t^2}{m_h^2} \left[ 2 - \left( m_h^2 - 4m_t^2 \right) C_0 \left( \hat{s}, 0, 0, m_t^2, m_t^2, m_t^2 \right) \right], \qquad (6.23)$$

represents the one-loop triangle diagram with internal top quarks and $m_t$ is the top-quark mass. Here $\hat{s} = 2p_1 \cdot p_2$ and the $C_0$ function denotes a three-point Passarino–Veltman scalar integral for which our definition follows the conventions used in the `LoopTools` package [290]. The non-factorisable two-loop form factor $\mathcal{F}_2$ has been calculated analytically in [275, 278] using the method of asymptotic expansions, which in this case is valid up to energies $\sqrt{\hat{s}} \simeq m_t$. To cover the full off-shell range of interest up
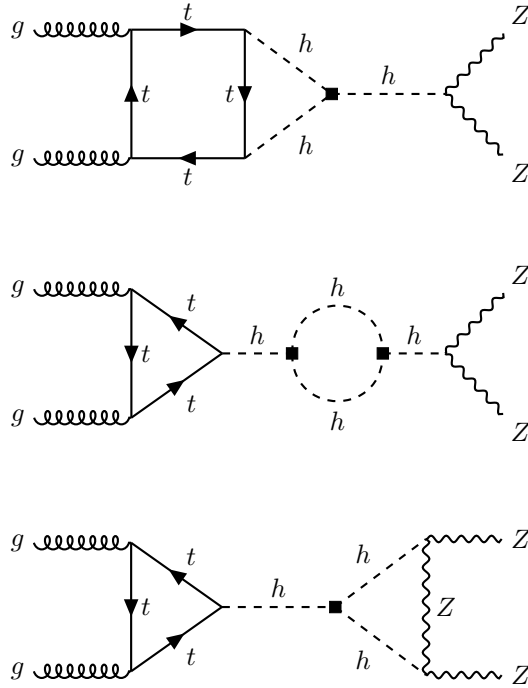
**Figure 6.1:** Representative Feynman diagrams that lead to a $\mathcal{O}(\lambda)$ correction to the process $gg \to h^* \to ZZ$. The black boxes denote insertions of the operator $\mathcal{O}_6$ introduced in (6.8). Consult the main text for further details.

to $\sqrt{\hat{s}} = 1\,\text{TeV}$, we employ the numerical results for the non-factorisable two-loop form factor $\mathcal{F}_2$ presented in [267, 268] in our numerical analysis performed in Section 6.2.2.

#### 6.2.1.2  Higgs propagator

The Higgs propagator also receives corrections from insertions of the operator $\mathcal{O}_6$ (see the centre graph in Figure 6.1). The resulting renormalised contribution to the self-energy of the Higgs takes the form

$$\hat{\Sigma}(\hat{s}) = \Sigma(\hat{s}) + \left(\hat{s} - m_h^2\right) \delta Z_h - \delta m_h^2 \,, \tag{6.24}$$

where the one-loop corrections to the Higgs wave function has already been given in (6.22) and the bare Higgs self-energy and the mass counterterm in the on-shell scheme are given by the following expressions

$$\Sigma(\hat{s}) = \frac{\lambda \bar{c}_6}{(4\pi)^2} \left(\bar{c}_6 + 2\right) 9 m_h^2 B_0\!\left(\hat{s}, m_h^2, m_h^2\right) \,,$$

$$\delta m_h^2 = \frac{\lambda \bar{c}_6}{(4\pi)^2} \left(\bar{c}_6 + 2\right) 9 m_h^2 B_0\!\left(m_h^2, m_h^2, m_h^2\right) \,. \tag{6.25}$$

Here the $B_0$ functions are two-point Passarino-Veltman scalar integrals defined as in [290].

### 6.2.1.3 Higgs decay

The full $\mathcal{O}(\lambda)$ correction to the Higgs decay $h \to ZZ$ receives a two-loop contribution (see the lower diagram in Figure 6.1) as well as a counterterm contribution involving Higgs wave-function renormalisation. In the notation of [276], the relevant renormalised vertex describing the $h(p_1 + p_2) \to Z(p_1)Z(p_2)$ transition reads

$$\hat{\Gamma}_{hZZ}^{\mu\nu}(p_1, p_2) = \frac{2m_Z^2}{v}\left[\eta^{\mu\nu}\mathcal{G}_1 + p_1^\nu p_2^\mu \mathcal{G}_2\right] , \tag{6.26}$$

where $m_Z$ denotes the $Z$-boson mass. The $\mathcal{O}(\lambda)$ corrections to the one-loop form factors $\mathcal{G}_1$ and $\mathcal{G}_2$ are given by

$$\mathcal{G}_1 = \frac{\delta Z_h}{2} - \frac{\lambda\bar{c}_6}{(4\pi)^2}\left\{12\left[m_Z^2 C_0\big((p_1+p_2)^2, p_1^2, p_2^2, m_h^2, m_h^2, m_Z^2\big)\right.\right.$$

$$\left.\left. - C_{00}\big((p_1+p_2)^2, p_1^2, p_2^2, m_h^2, m_h^2, m_Z^2\big)\right] + 3B_0\big((p_1+p_2)^2, m_h^2, m_h^2\big)\right\} ,$$

$$\mathcal{G}_2 = \frac{\lambda\bar{c}_6}{(4\pi)^2}12\left[C_1\big((p_1+p_2)^2, p_1^2, p_2^2, m_h^2, m_h^2, m_Z^2\big)\right.$$

$$\left. + C_{11}\big((p_1+p_2)^2, p_1^2, p_2^2, m_h^2, m_h^2, m_Z^2\big) + C_{12}\big((p_1+p_2)^2, p_1^2, p_2^2, m_h^2, m_h^2, m_Z^2\big)\right] ,$$

<div align="right">(6.27)</div>

and the tensor coefficients $C_1$, $C_{00}$ and $C_{11}$ of the three-point Passarino-Veltman integrals are defined as in the publications [276, 290].

### 6.2.1.4 MC implementation

The three different types of $\mathcal{O}(\lambda)$ corrections affect not only the overall size of the $gg \to h^* \to ZZ \to 4\ell$ cross section, but also modify the shape of kinematic distributions such as the four-lepton invariant mass $m_{4\ell}$. In order to be able to predict $gg \to h^* \to ZZ \to 4\ell$ we have implemented the $\bar{c}_6$ corrections arising from ggF Higgs production, the Higgs propagator and the Higgs decay to $Z$ bosons into version 8.0 of MCFM [291]. Our implementation includes all contributions up to $\mathcal{O}(\lambda^2)$ that arise from squaring the full $gg \to h^* \to ZZ$ matrix element (ME) which comprises both the BSM graphs depicted in Figure 6.1 as well as the LO SM Feynman diagram shown on the left-hand side of Figure 6.2. We also note that the contribution to the wave-function renormalisation constant (6.22) coming from the propagator corrections at $\mathcal{O}(\lambda)$ exactly cancels against those of the vertices when combined to obtain the full BSM contribution to the off-shell $gg \to h^* \to ZZ$ amplitude. This cancellation is expected since in the considered process the Higgs propagates on an internal line. It can be explicitly seen by comparing the $\delta Z_h$ part of (8.3), which contributes as $(-\delta Z_h)$ times the LO SM amplitude since it is part of the second-order correction in the geometric series expansion of the propagator, with the $\delta Z_h$-dependent parts of the vertex contributions in (6.21) and (6.27), which each gives a contribution proportional to $\delta Z_h/2$ times the LO SM amplitude. Notice that as a result of this cancellation the only $\mathcal{O}(\lambda)$ contributions quadratic in the Wilson coefficient $\bar{c}_6$ arise from (6.25) with the bare self-energy $\Sigma(\hat{s})$ being the only $\hat{s}$-dependent correction of this type.
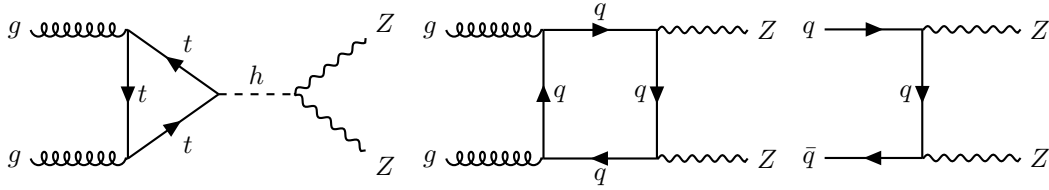
**Figure 6.2:** SM contributions to $pp \to ZZ$. The left, centre and right Feynman diagram represents a LO contribution to the $gg \to h^* \to ZZ$, $gg \to ZZ$ and $q\bar{q} \to ZZ$ channel, respectively. In the case of the left graph there are also contributions involving bottom quarks. These diagrams are included in our analysis. See the text for additional details.

## 6.2.2 Numerical analysis

In this section, we study the impact of the $\mathcal{O}(\lambda)$ corrections to the $gg \to h^* \to ZZ \to 4\ell$ process on the $m_{4\ell}$ spectrum and a ME kinematic discriminant to be defined later. Following a brief discussion of the impact of QCD corrections, these results are then used to perform a sensitivity study of the two-dimensional constraints on the Wilson coefficients $\bar{c}_6$ and $\bar{c}_H$ that can be obtained at LHC Run 3 and the HL-LHC from measurements of $pp \to ZZ \to 4\ell$. The bounds from Higgs off-shell measurements are compared to the limits that are expected to arise from a combination of inclusive single-Higgs measurements at the end of LHC Run 3 as well as the HL-LHC era in the next section.

### 6.2.2.1 Modifications of differential distributions

In Figure 6.3 we show $m_{4\ell}$ distributions for the Higgs channel alone (left panel) and for the Higgs channel, the gluon continuum background and their interference combined (right panel) at LO in QCD. An example of a one-loop Feynman diagram that contributes to the SM $gg \to ZZ$ background is shown in the centre of Figure 6.2. We restrict ourselves to the off-shell region by considering a mass window of $220\,\text{GeV} < m_{4\ell} < 1000\,\text{GeV}$. The leptons ($\ell = e, \mu$) are required to be measured in the pseudorapidity range $|\eta_\ell| < 2.5$ and the lepton with the highest transverse momentum ($p_T$) must satisfy $p_{T,\ell_1} > 20\,\text{GeV}$ while the second, third and fourth lepton in $p_T$ order is required to obey $p_{T,\ell_2} > 15\,\text{GeV}$, $p_{T,\ell_3} > 10\,\text{GeV}$ and $p_{T,\ell_4} > 6\,\text{GeV}$, respectively. The lepton pair with the mass closest to the $Z$-boson mass is referred to as the leading dilepton pair and its invariant mass is required to be within $50\,\text{GeV} < m_{12} < 106\,\text{GeV}$, while the subleading lepton pair must be in the range of $50\,\text{GeV} < m_{34} < 115\,\text{GeV}$. Similar cuts are employed in the ATLAS and CMS analyses [292–298]. The input parameters used throughout our work are given by $G_F = 1/(\sqrt{2}v^2) = 1.16639 \cdot 10^{-5}\,\text{GeV}^{-2}$, $m_Z = 91.1876\,\text{GeV}$, $m_h = 125\,\text{GeV}$ and $m_t = 173\,\text{GeV}$. The shown spectra assume $pp$ collisions at $\sqrt{s} = 14\,\text{TeV}$ and employ `NNPDF40_nlo_as_01180` parton distribution functions (PDFs) [299] with the renormalisation and factorisation scales $\mu_R$ and $\mu_F$ dynamically, *i.e.* for each event, set to $m_{4\ell}$. Our predictions include both the different-flavour (*i.e.* $e^+e^-\mu^+\mu^-$) and the same-flavour (*i.e.* $2e^+2e^-$ and $2\mu^+2\mu^-$) decay channels of the two $Z$ bosons.

Two features of the distributions shown on the left-hand side of Figure 6.3 deserve a further discussion. First, below the two-Higgs production threshold at $m_{4\ell} = 2m_h$ the
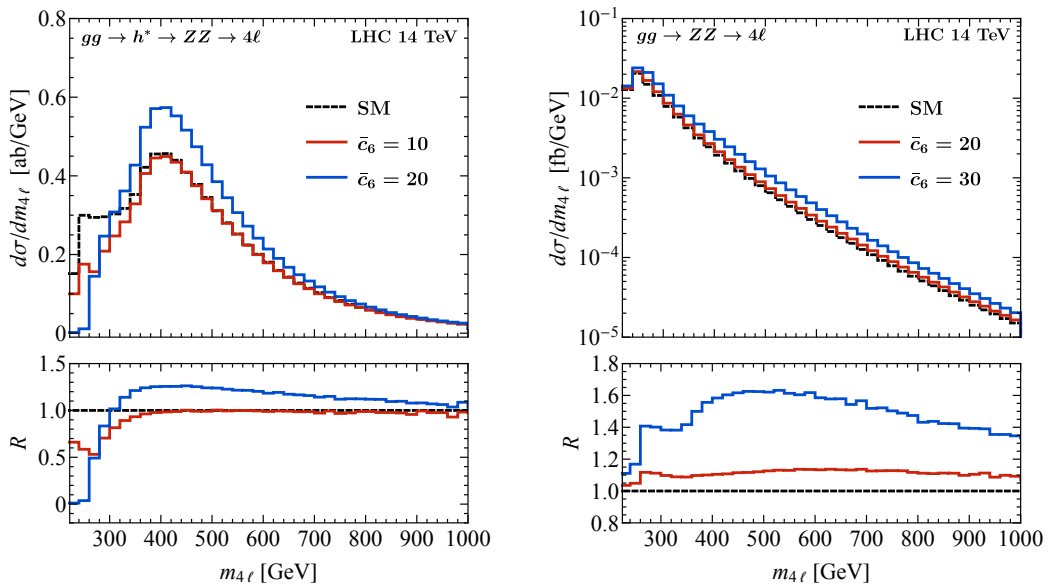
**Figure 6.3:** Left: $m_{4\ell}$ distributions for the Higgs signal in the SM (dashed black) and including the $\mathcal{O}(\lambda)$ corrections calculated in Section 6.2.1 assuming $\bar{c}_6 = 10$ (solid red) and $\bar{c}_6 = 20$ (solid blue). Right: $m_{4\ell}$ spectra including the Higgs signal, the continuum background and their interference in the SM (dashed black). The results for the two BSM scenarios corresponding to $\bar{c}_6 = 20$ (solid red) and $\bar{c}_6 = 30$ (solid blue) are also displayed. All distributions are obtained at LO in QCD assuming $pp$ collisions at $\sqrt{s} = 14\,\text{TeV}$. The lower panels show the ratios between the distributions and the corresponding SM predictions. Consult the main text for further details.

BSM $gg \to h^* \to ZZ \to 4\ell$ spectra are both visibly smaller that the SM prediction. This feature can be understood by noting that for sufficiently large values of the Wilson coefficient $\bar{c}_6$ the terms (6.25) provide the dominant $\mathcal{O}(\lambda)$ corrections. In fact, the Higgs propagator corrections necessarily reduce the real part of $gg \to h^* \to ZZ \to 4\ell$ amplitude for $m_{4\ell} < 2m_h$, and this destructive interference can be so pronounced that the BSM contribution almost exactly cancels the SM contribution. Second, above the two-Higgs production threshold the bare Higgs self-energy $\Sigma(\hat{s})$ develops an imaginary part because both internal Higgs lines in the propagator correction (see the centre graph in Figure 6.1) can go on their mass shell. As a result the BSM $gg \to h^* \to ZZ \to 4\ell$ spectra can be larger than the SM prediction for $m_{4\ell} > 2m_h$. Notice that the two aforementioned features are clearly visible in the case of the BSM distribution corresponding to $\bar{c}_6 = 20$, while for $\bar{c}_6 = 10$ the spectrum is not enhanced above the two-Higgs production threshold because the $\mathcal{O}(\lambda)$ corrections to Higgs production and decay (see the upper and lower graph in Figure 6.1) are numerically relevant in this case and tend to cancel the effect of the Higgs propagator.

Our results for the $gg \to ZZ \to 4\ell$ distributions including the Higgs signal, the continuum background and their interference are displayed in the right panel of Figure 6.3. In the vicinity of the two-Higgs production threshold $m_{4\ell} = 2m_h$ one observes a plateau-like structure in both BSM spectra. This feature arise from the combination of the modified Higgs signal and the interference of the BSM signal with the continuum SM background. This atypical shape change provides a genuine probe of loop corrections to the Higgs propagator involving light virtual particles. Such corrections

arise in the case at hand from the insertions of the operator $\mathcal{O}_6$ but they can also appear in ultraviolet (UV) complete models of BSM physics (see for instance [300–303]). Both BSM spectra also show an enhancement in the $m_{4\ell}$ tail. Notice that the observed shape change is qualitatively different from the relative modifications that arise from tree-level insertions of dimension-six SMEFT operators which typically show a roughly quadratic growth with $m_{4\ell}$ (see for example [301, 304]). Similar statements apply to the case when the SM Higgs boson width is rescaled in such a way that the $pp \to h^* \to ZZ \to 4\ell$ cross section close to the Higgs peak is unchanged [168, 169, 305]. See Appendix B for a detailed discussion.

We have seen that the inclusion of the $\mathcal{O}(\lambda)$ corrections to the $pp \to h^* \to ZZ \to 4\ell$ amplitude associated to insertions of the SMEFT operator $\mathcal{O}_6$ lead to phenomenologically relevant kinematic features in the $m_{4\ell}$ distribution. The analysis sensitivity to the Higgs channel, especially in the off-peak region, has been shown to benefit considerably from the use of ME-based kinematic discriminants (see for instance [169, 292–298, 306–308]) to separate the $gg \to h^* \to ZZ \to 4\ell$ signal from the main SM background coming from $ZZ$ production in $q\bar{q}$-annihilation. A relevant Feynman diagram that contributes to the $q\bar{q} \to ZZ$ background at LO in QCD is displayed on the right in Figure 6.2. Being sensitive not only to $m_{4\ell}$ but to another seven variables such as the invariant masses of the two opposite-sign lepton pairs (for details consult [306–308]), the ME-based discriminants fully exploit the event kinematics. In practice, the ME-based discriminants are often embedded in a multivariate discriminant based on a boosted decision tree (BDT) algorithm, but as it turns out in the case of the four-lepton final state the sensitivity of the BDT analysis improves only very little with respect to the ME-based discriminant alone (for example in the case of the analysis [293] the improvement amounts to a mere 2%). In the following, we restrict ourselves to an approach with only a ME-based discriminant, which we define as follows [293, 294, 296, 298]

$$D_S = \log_{10}\left(\frac{P_h}{P_{gg} + c \cdot P_{q\bar{q}}}\right). \tag{6.28}$$

Here $P_h$ denotes the squared ME for the $gg \to h^* \to ZZ \to 4\ell$ process, $P_{gg}$ is the squared ME for all $gg$-initiated channels (including the Higgs channel, the continuum background and their interference) and $P_{q\bar{q}}$ is the squared ME for the $q\bar{q} \to ZZ \to 4\ell$ process. Following the publications [293, 294, 296, 298] the constant $c$ is set to 0.1 to balance the $q\bar{q}$- and $gg$-initiated contributions. We add that in the SM more than 99% of the $pp \to ZZ \to 4\ell$ cross section fall into the range of $-4.5 < D_S < 0.5$ [293]. The kinematic discriminant (6.28) thus presents a null test for BSM models that lead to events with $D_S < -4.5$ or $D_S > 0.5$.

To illustrate the discriminating power of the variable $D_S$ we show in the left panel of Figure 6.4 the normalised SM distributions at LO in QCD for the three contributions corresponding to the MEs that enter (6.28). The discriminant $D_S$, which is calculated for every event in the simulation, is implemented in MCFM which uses the $gg$-initiated MEs provided in [169]. One observes that the distribution corresponding to $q\bar{q} \to ZZ \to 4\ell$ peaks at $D_S \simeq -3$, while the $gg \to h^* \to ZZ \to 4\ell$ spectrum is shifted to higher $D_S$ featuring a maximum at around $D_S \simeq -0.5$. An enhancement of the $gg \to h^* \to ZZ \to 4\ell$ amplitude in the off-shell region will hence lead to a $D_S$ distribution of the full $pp \to ZZ \to 4\ell$ process that is shifted to the right compared to the SM
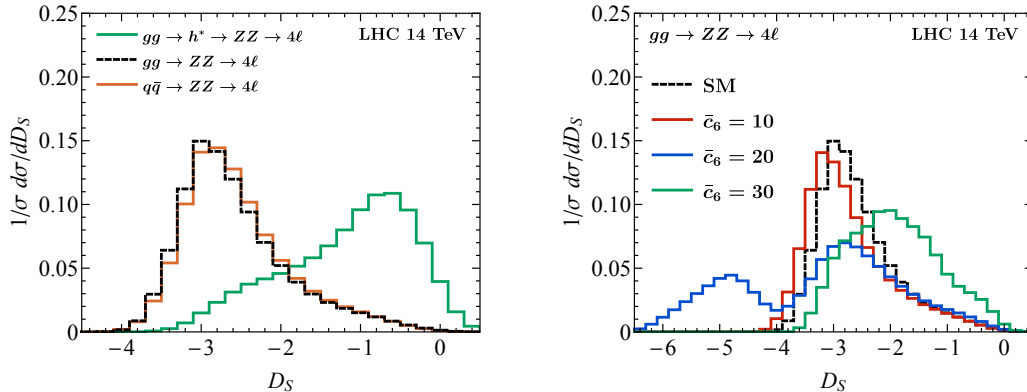
**Figure 6.4:** Left: Normalised $D_S$ distributions in the SM for the Higgs signal (solid green), all $gg$-initiated channels combined (dashed black) and the $q\bar{q}$-initiated background (solid orange). Right: Normalised $D_S$ distributions for the $gg$-initiated contributions in the SM (dashed black) and for $\bar{c}_6 = 10$ (solid red), $\bar{c}_6 = 20$ (solid blue) and $\bar{c}_6 = 30$ (solid green). See the main text for further explanations.

spectrum. For BSM scenarios that predict an enhancement in the tail of the $m_{4\ell}$ distribution, one thus expects to find an excess of events for $D_S \gtrsim -1$. As discussed in Appendix B, this is precisely what happens if the Higgs boson couplings and its total decay width are modified according to (B.1).

In the case of the $\mathcal{O}(\lambda)$ corrections to off-shell Higgs production resulting from the insertions of the SMEFT operator $\mathcal{O}_6$, the modifications of the normalised $D_S$ distributions are more intricate. For the full $gg \rightarrow ZZ \rightarrow 4\ell$ contribution this is shown on the right-hand side of Figure 6.4. One observes that in the case of $\bar{c}_6 = 10$ the BSM spectrum is shifted to lower values compared to the SM result. This is a simple consequence of the fact that for $\bar{c}_6 = 10$ the $gg \rightarrow h^* \rightarrow ZZ \rightarrow 4\ell$ amplitude and therefore $P_h$ in (6.28) is reduced for $m_{4\ell}$ values below the two-Higgs production threshold (*cf.* the left panel in Figure 6.3). For $\bar{c}_6 = 20$ one instead sees that the $D_S$ distribution has two maxima: one at $D_S \simeq -5$ and another one at $D_S \simeq -3$. The peak at $D_S \simeq -5$ ($D_S \simeq -3$) is associated to kinematic configurations that lead to a reduction (an enhancement) of $P_h$ for $m_{4\ell} < 2m_h$ ($m_{4\ell} > 2m_h$) — see again the left plot in Figure 6.3. Finally, for $\bar{c}_6 = 30$ the BSM contributions always enhance $P_h$ and hence the $D_S$ distribution is shifted to larger values. Notice that the sharp cut-off of the SM distribution at $D_S \simeq -3.5$, makes (6.28) more sensitive to kinematic configurations that reduce $P_h$ rather than enhance it. In fact, this feature turns out to be the key element that allows to set powerful constraints on BSM scenarios with $\bar{c}_6 \neq 0$ by means of the ME-based discriminant $D_S$.

#### 6.2.2.2 Impact of QCD corrections

In the following we discuss the possible impact of higher-order QCD corrections to the $pp \rightarrow ZZ \rightarrow 4\ell$ cross section differential in the ME-based kinematic distribution introduced in (6.28). In fact, as the ggF contribution to $pp \rightarrow ZZ \rightarrow 4\ell$ is loop-induced (see the centre graph in Figure 6.2), it enters the $ZZ$ production cross section

at $\mathcal{O}(\alpha_s^2)$, *i.e.* at the next-to-next-to-leading order (NNLO) in QCD. State-of-the-art predictions for four-lepton production at the LHC, obtained at NNLO in QCD [79–81, 214] and matched to parton shower [44, 217], are reaching an impressive accuracy of $\mathcal{O}(2\%)$ for inclusive cross sections and $\mathcal{O}(5\%)$ in the case of differential distributions.

While a precision phenomenological study of $ZZ$ production a la [44, 79–81, 172, 212, 214, 217] including the $\mathcal{O}(\lambda)$ corrections associated to the insertions of $\mathcal{O}_6$ is beyond the scope of this work, we wish to assess at least approximately the impact of higher-order QCD corrections on our analysis, in particular the effects on the $D_S$ spectra. To this purpose we proceed in the following way. We first calculate for each production channel the so-called $K$-factor defined as the ratio between the fiducial cross section at a given order in QCD and the corresponding LO QCD prediction. In the case of the $gg$-initiated contribution we employ the results of the recent work [44], where one of us reported NLO QCD corrections to the corresponding four-lepton invariant mass spectrum (see Figure 2 of that article). One observes that the ratio between the NLO and LO ggF predictions is essentially flat in the region of interest for this work, *i.e.* for values of the invariant mass within $220\,\mathrm{GeV} < m_{4\ell} < 1000\,\mathrm{GeV}$. By averaging over the ratio of the NLO and LO $m_{4\ell}$ spectra within the aforementioned $m_{4\ell}$ window we find $K_{gg}^{\mathrm{NLO}} = 1.83$, which is in line with the previous works [172, 212, 214]. In the case of the $q\bar{q}$-initiated contribution we utilise the LO and NNLO QCD results obtained in [214] using MATRIX [223]. The relevant $K$-factor again turns out to be basically flat in $m_{4\ell}$, with a central value of $K_{q\bar{q}}^{\mathrm{NNLO}} = 1.55$, which is in accordance with [79].

The aforementioned $K$-factors are listed in Table 6.1, along with the scale uncertainties in each production channel at the relevant order in QCD. They are then used to obtain a QCD-improved prediction for the $D_S$ distributions, in the following way:

$$\left( \frac{d\sigma(pp \to ZZ \to 4\ell)}{dD_S} \right)_{\mathrm{improved}} = K_{gg}^{\mathrm{NLO}} \left( \frac{d\sigma(gg \to ZZ \to 4\ell)}{dD_S} \right)_{\mathrm{LO}}$$
$$+ K_{q\bar{q}}^{\mathrm{NNLO}} \left( \frac{d\sigma(q\bar{q} \to ZZ \to 4\ell)}{dD_S} \right)_{\mathrm{LO}} . \tag{6.29}$$

Here the label LO indicates that both the cross sections as well as the ME-based discriminant $D_S$ are calculated at LO in QCD. Clearly, (6.29) only captures part of the higher-order QCD corrections to the $d\sigma/dD_S$ spectra, namely those that are associated to the differential cross sections $d\sigma$, but ignores beyond-LO effects to $dD_S$. To improve upon this approximation one would need to extend the calculation of the ME-based discriminant (6.28) to the NLO in QCD. While achieving NLO accuracy is in principle possible for ME-based discriminants [309–311], the actual calculations are in practice complicated by the fact that they require the use of modified jet algorithms to map resolved and unresolved parton configurations onto the proper MEs — see also [312] for a discussion of this point. Since NLO and NNLO QCD corrections to the shapes of kinematic distributions in $pp \to ZZ \to 4\ell$ are small and often indistinguishable when compared to the associated theoretical uncertainties, it is expected that the LO discriminant $D_S$ as defined in (6.28) maintains its discriminating power beyond the well-defined LO. This renders the procedure (6.29) a pragmatic and simple approach to incorporate higher-order QCD effects.

In the left plot of Figure 6.5 we compare the $D_S$ spectrum for $pp \to ZZ \to 4\ell$ in the SM obtained at LO to the QCD-improved $D_S$ spectrum (6.29). One observes a close

|  | $\sigma_{gg}^{\mathrm{LO}}$ | $\sigma_{gg}^{\mathrm{NLO}}$ | $\sigma_{q\bar{q}}^{\mathrm{LO}}$ | $\sigma_{q\bar{q}}^{\mathrm{NNLO}}$ |
|---|---|---|---|---|
| $K_i^{\mathrm{order}}$ | 1 | 1.83 | 1 | 1.55 |
| $\Delta_i^{\mathrm{scale}}$ | +27.7%<br>−20.5% | +14.8%<br>−13.4% | +5.5%<br>−6.4% | +1.1%<br>−1.2% |

**Table 6.1:** QCD $K$-factors, defined as $K_i^{\mathrm{order}} = \sigma_i^{\mathrm{order}}/\sigma_i^{\mathrm{LO}}$, for the channels $i = gg$, $q\bar{q}$ at different orders in QCD along with the associated relative scale uncertainties $\Delta_i^{\mathrm{scale}}$ for each channel and QCD order. The numbers for the $gg$-initiated channel are obtained utilising results presented in [44], while the results for the $q\bar{q}$-initiated channel are taken from [214]. Consult the main text for further details.

to flat $K$-factor of around 1.6 between the LO and the improved prediction of the $D_S$ spectrum for $pp \to ZZ \to 4\ell$. The uncertainty bands represent the scale uncertainties obtained by applying the numerical values listed in Table 6.1 to the relevant the LO and QCD-improved spectra. We observe that the inclusion of higher-order QCD corrections reduces the scale uncertainties by a factor of about 3 from roughly $(7 - 8)\%$ to about $(2 - 3)\%$, in line with recent precision SM phenomenological studies. However, the fact that the central value of the improved prediction lies well outside the LO uncertainty bands in all bins demonstrates that at LO, scale variations do not provide a reliable way to estimate the size of higher-order QCD effects. In fact, similar issues are known to occur also beyond LO, for example in the case of inclusive ggF Higgs production (see [313–315] for the corresponding state-of-the-art SM calculations) or even for four-lepton production [44], where the loop-induced $gg$ contribution entering at NNLO is unaccounted for by the NLO scale uncertainties. With this in mind and given that the kinematic discriminant $D_S$ is only LO accurate, we wish to take a rather conservative approach and estimate the theoretical uncertainties to be half of the relative difference between the QCD-improved and the LO predictions, which corresponds to a relative uncertainty of about 30%.

On the right-hand side of Figure 6.5 we compare two BSM $D_S$ distributions to the SM prediction, where the scale uncertainties quoted in Table 6.1 and the aforementioned conservative estimate are shown in the lower panel as the solid green and dot-dashed green bands around the SM spectrum, respectively. The depicted spectra have all been obtained using (6.29). In accordance with the general discussion in Section 6.2.2.1, one observes that the BSM spectra deviate most significantly from the SM distribution for $D_S \lesssim -3.5$, while for $D_S \gtrsim -3.5$ the deviations are generically small. In fact, for the two choices of $\bar{c}_6$ shown in the figure the resulting modifications of the $D_S$ spectrum for $D_S \gtrsim -3.5$ lie well within our conservative theoretical uncertainty band. Furthermore, since the deviations for $D_S \lesssim -3.5$ are associated to the modification of the off-shell Higgs production cross section in the region $m_{4\ell} < 2m_h$, they will lead to a detectable change in events for a sufficiently large $|\bar{c}_6|$. For instance, for $\bar{c}_6 = 10$ ($\bar{c}_6 = 15$) the shift in the $pp \to ZZ \to 4\ell$ cross section restricted to $D_S < -3.5$ amounts to around $0.4\,\mathrm{fb}$ ($1.2\,\mathrm{fb}$) compared to the SM. This corresponds to around 1200 (3700) additional $pp \to ZZ \to 4\ell$ events at the HL-LHC. Notice finally that the relative modifications of the $D_S$ spectrum due to insertions of $\mathcal{O}_6$ are much larger than the shifts seen in the $m_{4\ell}$ distribution (*cf.* the right panel in Figure 6.3). The ME-based discriminant (6.28) therefore provides a significantly better sensitivity to BSM models with $\bar{c}_6 \neq 0$ than
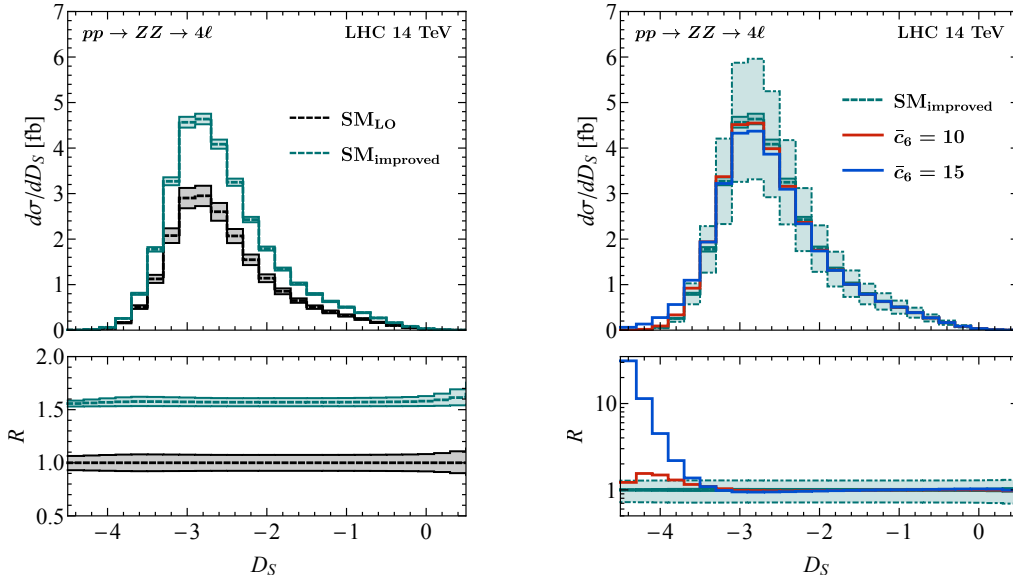
**Figure 6.5:** Left: $D_S$ distributions for the $pp \rightarrow ZZ \rightarrow 4\ell$ process in the SM obtained at LO (dashed black) and the QCD-improved prediction (dashed green). The lower panel shows the ratio to the LO SM prediction and the uncertainty bands been obtained using the scale variations from Table 6.1. Right: $D_S$ spectra for $pp \rightarrow ZZ \rightarrow 4\ell$ production in the SM (dashed green) and for $\bar{c}_6 = 10$ (solid red) and $\bar{c}_6 = 15$ (solid blue). The thin green band corresponds to the scale uncertainties of the QCD-improved SM predictions for $D_S$, while the wide green band represents half of the relative difference between the QCD-improved and the LO SM predictions for ME-based discriminant. The lower panel shows the ratio of the BSM and SM predictions including the aforementioned uncertainty bands. All distributions assume $pp$ collisions at $\sqrt{s} = 14\,\text{TeV}$ and the improved SM as well as the BSM predictions have been obtained by means of (6.29). Additional explanations can be found in the main text.

the $m_{4\ell}$ spectrum.

### 6.2.2.3   Constraints on Wilson coefficients $\bar{c}_6$ and $\bar{c}_H$

Below we determine the constraints on the Wilson coefficients $\bar{c}_6$ and $\bar{c}_H$ that future LHC runs may be able to set. In the case of the constraints arising from off-shell Higgs production, we utilise the QCD-improved $D_S$ predictions obtained by (6.29), assuming a detection efficiency of 99% (95%) for muons (electrons) that satisfy the event selections described at the beginning of Section 6.2.2.1. These efficiencies correspond to those reported in the latest ATLAS analysis of off-shell Higgs production [298]. The statistical uncertainties of the computed $D_S$ distributions are determined per bin assuming Poisson statistics, *i.e.* taking the statistical error to be $\sqrt{N_i}$ with $N_i$ the number of events in a given bin $i$. The largest systematic uncertainties in our analysis arise from the theoretical uncertainties on the $gg \rightarrow h^* \rightarrow ZZ \rightarrow 4\ell$ signal process, the $gg \rightarrow ZZ \rightarrow 4\ell$ and $q\bar{q} \rightarrow ZZ \rightarrow 4\ell$ background processes and the interference between the $gg$-initiated signal and background. For the theoretical uncertainties on the improved $D_S$ prediction (6.29) we take the conservative estimate discussed in Section 6.2.2.2, in which we assume also PDF uncertainties at the level of $\pm 5\%$ are included. In our LHC Run 3 analysis we will thus use a total theoretical uncertainty of $\pm 30\%$ when determining the bounds on $\bar{c}_6$ and $\bar{c}_H$. Anticipating theoretical advances

in the case of the HL-LHC we assume that the theoretical uncertainties due to scale variations and PDFs are reduced to $\pm 15\%$ which does not seem unrealistic. In fact, similar assumptions are made in the HL-LHC studies [294, 295]. Compared to the theoretical uncertainties the experimental uncertainties of systematic origin are close to negligible as they amount to $\mathcal{O}(2\%)$ (see for example [316]). We will thus ignore the experimental systematics in what follows.

The total number of events in bin $i$ depends on the Wilson coefficients $\bar{c}_6$ and $\bar{c}_H$ in the following way

$$N_i(\bar{c}_6, \bar{c}_H) = N_i(\bar{c}_6) - 2\bar{c}_H N_i(0)\,, \tag{6.30}$$

where $N_i(\bar{c}_6)$ denotes the number of events which we calculate using MCFM correcting them by QCD effects (6.29) and lepton efficiencies. Notice that $N_i(0)$ corresponds to the SM expectation of events. The significance $Z_i$ is calculated as a Poisson ratio of likelihoods modified to incorporate systematic uncertainties on the background using the Asimov approximation [317, 318]:

$$Z_i = \left\{ 2 \left[ (s_i + b_i) \ln \left[ \frac{(s_i + b_i)\left(b_i + \sigma_{b_i}^2\right)}{b_i^2 + (s_i + b_i)\,\sigma_{b_i}^2} \right] - \frac{b_i^2}{\sigma_{b_i}^2} \ln \left( 1 + \frac{s_i \sigma_{b_i}^2}{b_i(b_i + \sigma_{b_i}^2)} \right) \right] \right\}^{1/2}\,. \tag{6.31}$$

Here $s_i$ ($b_i$) represents the expected number of signal (background) events in bin $i$ and $\sigma_{b_i}$ denotes the standard deviation that characterises the systematic uncertainties of the associated background. To set bounds on $\bar{c}_6$ and $\bar{c}_H$ we assume that the central values of a future measurements of the $D_S$ distribution will line up with the SM predictions. We hence employ

$$s_i = N_i(\bar{c}_6, \bar{c}_H) - N_i(0,0)\,, \qquad b_i = N_i(0,0)\,, \qquad \sigma_{b_i} = \Delta_i N_i(0,0)\,, \tag{6.32}$$

where $\Delta_i$ denotes the relative total systematic uncertainty in bin $i$. We will employ bin-independent systematic uncertainties of $\Delta_i = 0.3$ and $\Delta_i = 0.15$ at LHC Run 3 and HL-LHC, respectively. The total significance $Z$ is obtained by adding the individual $Z_i$ values in quadrature. Parameter regions with a total significance of $Z > \sqrt{2}\,\mathrm{erf}^{-1}\,(\mathrm{CL})$ are said to be excluded at a given confidence level CL. Here $\mathrm{erf}^{-1}(z)$ denotes the inverse error function. In our numerical analysis, we include 29 bins of equal size of 0.2 that cover the range $-5.1 < D_S < 0.5$.

Before deriving the projected bounds on the Wilson coefficient $\bar{c}_6$ from off-shell Higgs production, we recall that the currently best LHC 95% CL limit reads [289]

$$\bar{c}_6 \in [-3.3, 9.3]\,, \quad (\text{LHC Run 2})\,. \tag{6.33}$$

See also [285, 286]. The bound (6.33) has been obtained from a combination of ten double-Higgs and single-Higgs production measurements performed by the ATLAS collaboration. Assuming $\bar{c}_H = 0$ and employing the fit strategy described above, we find the following 95% CL bounds from future hypothetical measurements of off-shell Higgs production:

$$\bar{c}_6 \in [-8.2, 10.2]\,, \quad (\text{LHC Run 3})\,, \qquad \bar{c}_6 \in [-6.3, 8.4]\,, \quad (\text{HL-LHC})\,. \tag{6.34}$$

The quoted limits for LHC Run 3 (HL-LHC) correspond to a full integrated luminosity $300\,\mathrm{fb}^{-1}$ ($3\,\mathrm{ab}^{-1}$) obtained at $\sqrt{s} = 14\,\mathrm{TeV}$. To illustrate how the sensitivity of our

fit to values of $|\bar{c}_6| = \mathcal{O}(10)$ arises, we show in the upper panel of Figure 6.6 the QCD-improved predictions for the $D_S$ spectrum within the SM and two BSM models. The uncertainty bands around the SM prediction reflect the total uncertainties that are obtained by adding in quadrature the statistical and systematic uncertainties in each bin. From the figure it is evident that for both $\bar{c}_6 = -8$ and $\bar{c}_6 = 11$, the $D_S$ spectrum in enhanced over the SM background within the range $-4.5 \lesssim D_S \lesssim -3.5$. In this range the total uncertainties are largely dominated by the theory uncertainties with the statistically errors playing only a minor role. This feature allows to set limits like (6.34) that are competitive with (6.33) using solely off-shell Higgs production in the ggF channel.

In the lower panel of Figure 6.6 we furthermore show the 68% CL (dashed) and 95% CL (solid) constraints in the $\bar{c}_6$–$\bar{c}_H$ plane that derive from our fit employing LHC Run 3 (blue) and HL-LHC (red) data. One observes that the bounds on $\bar{c}_H$ are essentially independent of the precise value of $\bar{c}_6$ if the latter Wilson coefficient is sufficiently small. In the case of $\bar{c}_6 = 0$, we obtain at 95% CL for instance

$$\bar{c}_H \in [-7.0, 6.4] \cdot 10^{-2}\,, \quad (\text{LHC Run 3})\,, \qquad \bar{c}_H \in [-3.3, 3.1] \cdot 10^{-2}\,, \quad (\text{HL-LHC})\,.$$
$$(6.35)$$

We emphasise that non-zero values of $\bar{c}_H$ do not change the shape of the $D_S$ spectrum but only its normalisation $\big(cf.\ (6.30)\big)$. This feature explains the approximate $\bar{c}_6$-independence of the the exclusion contours in the $\bar{c}_6$–$\bar{c}_H$ plane for small $\bar{c}_6$. Notice finally that the bounds on $\bar{c}_H$ are significantly more stringent than those on $\bar{c}_6$. This is expected because the SMEFT operator $\mathcal{O}_H$ changes the prediction for $pp \to h^* \to ZZ \to 4\ell$ already at LO (i.e. one loop) while the corrections due to $\mathcal{O}_6$ start at NLO (i.e. two loops).
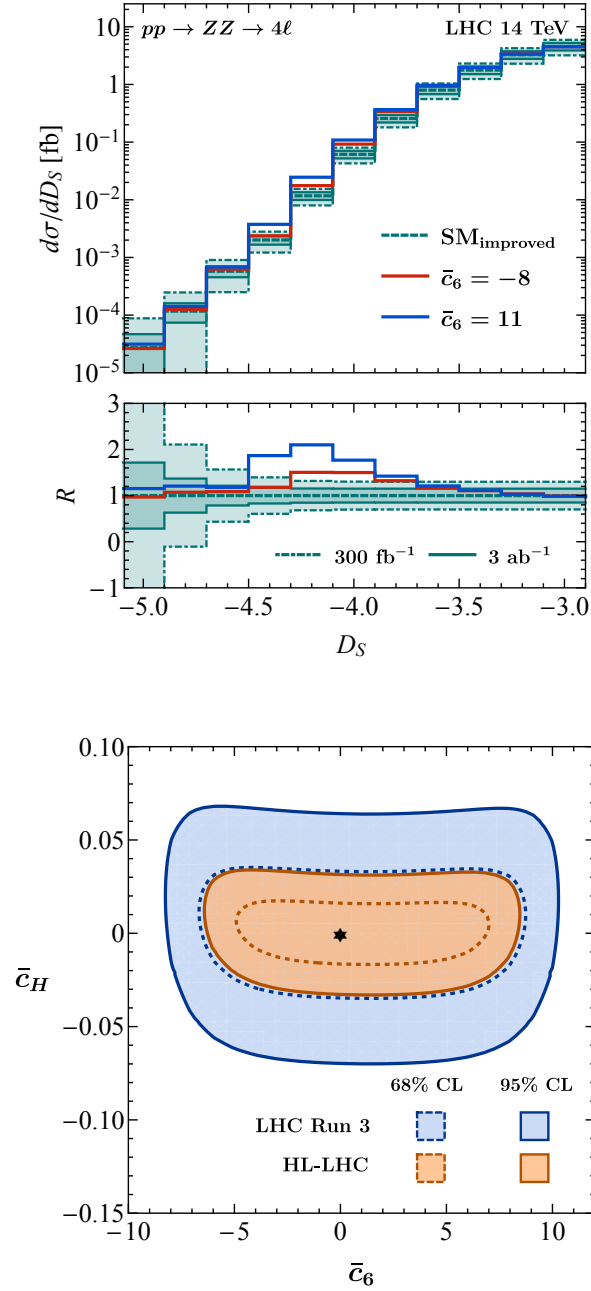
**Figure 6.6:** Upper panels: QCD-improved $D_S$ distributions for $pp \rightarrow ZZ \rightarrow 4\ell$. The SM spectrum (dashed green) and BSM predictions for $\bar{c}_6 = -8$ (solid red) and $\bar{c}_6 = 11$ (solid blue) are shown. The uncertainty bands around the SM spectrum indicate the total uncertainties expected at LHC Run 3 and HL-LHC. Lower panel: Projected 68% and 95% CL constraints in the $\bar{c}_6$–$\bar{c}_H$ plane at LHC Run 3 (dashed and solid blue) and HL-LHC (dashed and solid red). The black star represents the SM prediction. For additional details see main text.

## 6.3  Comparison to bounds from inclusive single-Higgs production

To further demonstrate the benefits of off-shell Higgs production in setting bounds on the Higgs trilinear coupling, we compare the results obtained in the previous section to the projected constraints one expects to obtain from inclusive single-Higgs measurements at future LHC runs. In the inclusive case the $\mathcal{O}(\lambda)$ corrections to the various Higgs production and decay channels can be written in terms of $\bar{c}_6$ and $\bar{c}_H$ as

$$\delta\sigma_i(\bar{c}_6, \bar{c}_H) = \bar{c}_6 \left( N_h(\bar{c}_6 + 2) + C_1^{\sigma_i} \right) - \bar{c}_H\,, \qquad \delta\mathrm{BR}_f(\bar{c}_6) = \frac{\bar{c}_6 \left( C_1^{\Gamma_f} - C_1^{\Gamma_h} \right)}{1 + \bar{c}_6 C_1^{\Gamma_h}}\,, \quad (6.36)$$

where $N_h$ has been defined already in (6.22) and $C_1^{\Gamma_h} = 0.23 \cdot 10^{-2}$ [275, 276, 278]. Notice that the Wilson coefficient $\bar{c}_H$ leads to a universal correction to all Higgs decay channels. Therefore it leaves the Higgs branching ratios unchanged. The calculations needed to obtain the process-dependent factors $C_1^{\sigma_i}$ and $C_1^{\Gamma_f}$ have been performed in [274–279]. In our numerical analysis of the inclusive single-Higgs observables we include ggF, $Wh$, $Zh$, vector-boson fusion (VBF) and $t\bar{t}h$ production and consider the Higgs-boson branching ratios to pairs of photons ($\gamma\gamma$), EW bosons ($W^+W^-, ZZ$), bottom quarks ($b\bar{b}$) and tau leptons ($\tau^+\tau^-$). The associated $C_1^{\sigma_i}$ and $C_1^{\Gamma_f}$ coefficients are collected in Table 6.2.

In terms of (6.36), keeping only terms linear in $\lambda$, the Higgs signal strengths for production in channel $i$ and decay in channel $f$ can be written as

$$\mu_i^f(\bar{c}_6, \bar{c}_H) = 1 + \delta\sigma_i(\bar{c}_6, \bar{c}_H) + \delta\mathrm{BR}_f(\bar{c}_6)\,, \qquad (6.37)$$

which we use to build the following $\chi^2$ function:

$$\chi^2(\bar{c}_6, \bar{c}_H) = \sum_{i,f} \frac{\left( \mu_i^f(\bar{c}_6, \bar{c}_H) - 1 \right)^2}{\left( \Delta_i^f \right)^2}\,. \qquad (6.38)$$

Here we have assumed that the central values of the future measurements of the Higgs signal strengths will coincide with the corresponding SM predictions. The variables $\Delta_i^f$ encode the relative total uncertainties obtained by combining the theoretical and statistical uncertainties associated to $\mu_i^f$. We collect the values of the $\Delta_i^f$ used in our LHC Run 3 and HL-LHC analyses in Table 6.3. Notice that the LHC Run 3 numbers are obtained by combing the current theoretical and the statistical uncertainties in quadrature, while the HL-LHC numbers assume that all theory uncertainties are halved with respect to our current understanding of the relevant signals and backgrounds. The latter assumption corresponds to the scenario S2 in the ATLAS paper [319]. The allowed CL regions are then obtained by minimising (6.38) and determining the solutions to $\Delta\chi^2 = \chi^2 - \chi^2_{\min} < 2Q^{-1}(1/2, 1 - \mathrm{CL})$ with $Q^{-1}(a, z)$ the regularised incomplete gamma function.

In the left (right) panel of Figure 6.7 we show the projected 68% and 95% CL constraints in the $\bar{c}_6$–$\bar{c}_H$ plane for the LHC Run 3 (HL-LHC). One observes that the LHC Run 3 fit to the 15 inclusive single-Higgs observable listed in Table 6.3 shows a pronounced flat direction in the $\bar{c}_6$–$\bar{c}_H$ plane. To understand this feature one first has

|  | ggF | $Wh$ | $Zh$ | VBF | $t\bar{t}h$ |
|---|---|---|---|---|---|
| $C_1^{\sigma_i}$ | $0.66 \cdot 10^{-2}$ | $1.03 \cdot 10^{-2}$ | $1.18 \cdot 10^{-2}$ | $0.64 \cdot 10^{-2}$ | $3.47 \cdot 10^{-2}$ |
|  | $\gamma\gamma$ | $W^+W^-$ | $ZZ$ | $b\bar{b}$ | $\tau^+\tau^-$ |
| $C_1^{\Gamma_f}$ | $0.49 \cdot 10^{-2}$ | $0.73 \cdot 10^{-2}$ | $0.83 \cdot 10^{-2}$ | $0.67 \cdot 10^{-5}$ | $0.33 \cdot 10^{-5}$ |

**Table 6.2:** Values of the process-dependent coefficients $C_1^{\sigma_i}$ and $C_1^{\Gamma_f}$. The numbers are directly taken or obtained from [275, 276, 278] and the coefficients $C_1^{\sigma_i}$ correspond to $pp$ collisions at $\sqrt{s} = 14\,\text{TeV}$.

| production, decay | LHC Run 3 | HL-LHC |
|---|---|---|
| ggF, $h \to \gamma\gamma$ | 0.13 | 0.036 |
| ggF, $h \to W^+W^-$ | 0.13 | 0.044 |
| ggF, $h \to ZZ$ | 0.12 | 0.039 |
| $Wh$, $h \to \gamma\gamma$ | 0.48 | 0.138 |
| $Wh$, $h \to b\bar{b}$ | 0.57 | 0.100 |
| $Zh$, $h \to \gamma\gamma$ | 0.85 | 0.157 |
| $Zh$, $h \to b\bar{b}$ | 0.29 | 0.052 |
| $Vh$, $h \to ZZ$ | 0.35 | 0.182 |
| VBF, $h \to \gamma\gamma$ | 0.47 | 0.089 |
| VBF, $h \to W^+W^-$ | 0.21 | 0.066 |
| VBF, $h \to ZZ$ | 0.36 | 0.118 |
| VBF, $h \to \tau^+\tau^-$ | 0.21 | 0.078 |
| $t\bar{t}h$, $h \to \gamma\gamma$ | 0.38 | 0.074 |
| $t\bar{t}h$, $h \to ZZ$ | 0.49 | 0.193 |

**Table 6.3:** Relative total uncertainties $\Delta_i^f$ on the Higgs signal strengths defined in (6.37). The quoted LHC Run 3 and HL-LHC numbers are taken from [320] and [319], respectively. Further information can be found in the main text.

to realise that only the process-independent coefficients $C_1^{\sigma_i}$ and $C_1^{\Gamma_f}$ are able to break flat directions in the inclusive fit. The relatively large coefficient $C_1^{\sigma_{t\bar{t}h}}$ (*cf.* Table 6.2) plays a particularly important role in this respect. Given the large total uncertainties of $t\bar{t}h, h \to \gamma\gamma, ZZ$ at LHC Run 3, the constraining power of the $t\bar{t}h$ channels and thus the impact of $C_1^{\sigma_{t\bar{t}h}}$ is however limited. As a result, the inclusive LHC Run 3 exclusions are mainly determined by the ggF channels that have a flat direction for $\bar{c}_6$ and $\bar{c}_H$ satisfying $\mu_{\text{ggF}}^f \simeq \delta\sigma_{\text{ggF}}(\bar{c}_6, \bar{c}_H) \simeq 0$. The situation is visibly improved in the inclusive HL-LHC fit, mostly because the total uncertainties of the $t\bar{t}h$ channels are expected to be significantly reduced. From both panels in Figure 6.7 it is however also evident that the flat direction in the inclusive fit is strongly broken by the constraints arising from off-shell Higgs production.

From the above it should be clear that inclusive single-Higgs and off-shell Higgs mea-
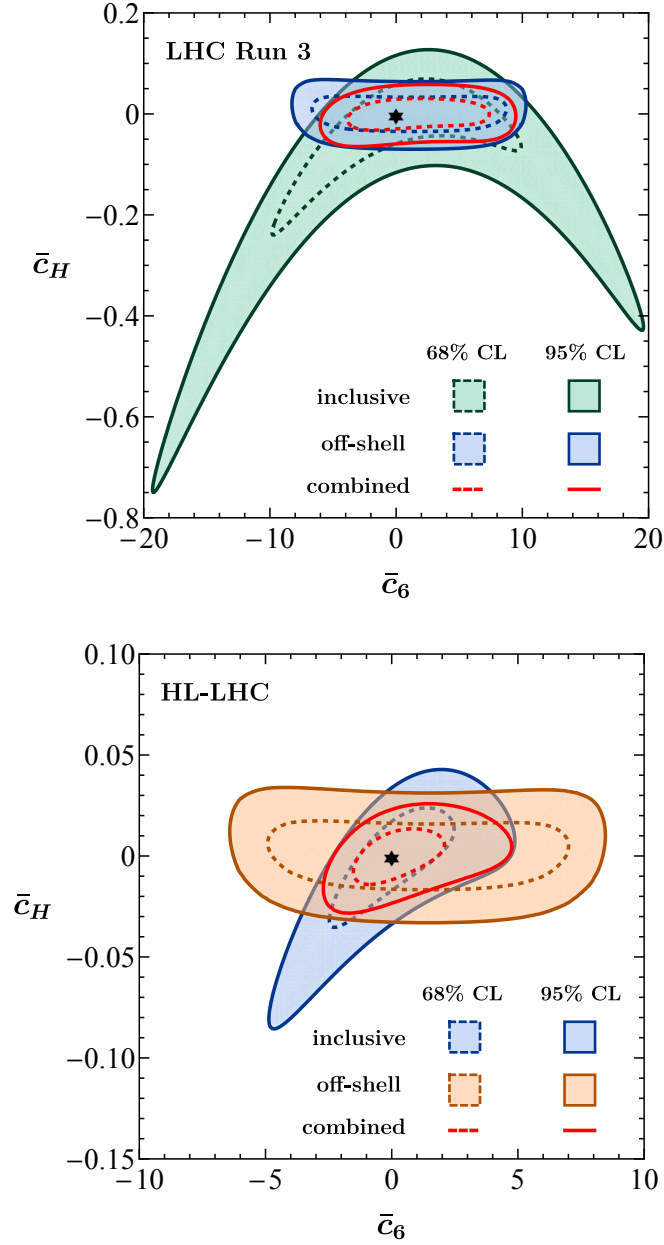
**Figure 6.7:** Projected 68% and 95% CL constraints in the $\bar{c}_6 - \bar{c}_H$ plane for the LHC Run 3 (left) and and HL-LHC (right) assuming integrated luminosities of 300 fb$^{-1}$ and 3 ab$^{-1}$, respectively, and $pp$ collisions at $\sqrt{s} = 14$ TeV. The constraints from inclusive single-Higgs probes (left: green regions, right: blue regions) are compared to the off-shell Higgs constraints (left: blue regions, right: orange regions). The combinations of all constraints are also shown as red contours. The black stars represent the SM point. See main text for further explanations.

surements should therefore be combined if one wants to exploit the full potential of the LHC in constraining the trilinear Higgs coupling through indirect probes. Performing such a combined analysis, we find for $\bar{c}_H = 0$ the following 95% CL limits

$$\bar{c}_6 \in [-5.8, 9.5] \,, \ \ (\text{LHC Run 3}) \,, \qquad \bar{c}_6 \in [-2.3, 4.6] \,, \ \ (\text{HL-LHC}) \,, \tag{6.39}$$

while for $\bar{c}_6 = 0$ we obtain

$$\bar{c}_H \in [-6.0, 5.6] \cdot 10^{-2} \,, \ \ (\text{LHC Run 3}) \,, \qquad \bar{c}_H \in [-2.3, 2.3] \cdot 10^{-2} \,, \ \ (\text{HL-LHC}) \,. \tag{6.40}$$

We add that the bounds (6.39) and (6.40) depend in a non-negligible way on the assumed total uncertainties. In this respect one should remember that in the case of the constraints arising from off-shell Higgs production in ggF production we have assumed total systematic uncertainties of $\pm 30\%$ and $\pm 15\%$ in our LHC Run 3 and HL-LHC fit, respectively. We believe that these are conservative uncertainties — results for two additional more aggressive assumptions about the systematic uncertainties entering the HL-LHC off-shell Higgs analysis can be found in Appendix C. In fact, given the steady progress in the calculation of massive higher-loop corrections to $pp \to ZZ \to 4\ell$ (see [231, 232] for the latest theoretical developments) and in view of the fact that it is theoretically known of how to achieve NLO accuracy for ME-based discriminants [309–311], it should be possible to put our naive estimates of theoretical uncertainties on more solid grounds. As can be seen from the upper panel in Figure 6.6, any improvement of our theoretical understanding of the $D_S$ distribution for $D_S \lesssim -3.5$ will notably increase the sensitive of off-shell Higgs measurements to modifications of the trilinear Higgs coupling.

## 6.4 Summary and outlook

In this chapter, we have studied the constraints on the trilinear Higgs coupling that originate from Higgs production in $pp$ collisions at future LHC runs. To keep the discussion model-independent we have worked in the context of the SMEFT in which the renormalisable SM interactions are augmented by the dimension-six operators $\mathcal{O}_6$ and $\mathcal{O}_H$ $\big(cf.$ (6.8)$\big)$. Our computation of the $\mathcal{O}_6$ contributions to off-shell Higgs production, *i.e.* the $gg \to h^* \to ZZ \to 4\ell$ process, includes two-loop corrections to ggF Higgs production and one-loop corrections to the Higgs propagator as well as the decay $h^* \to ZZ$. The resulting scattering amplitudes have been implemented into MCFM where they can be combined with the SM MEs for $gg \to h^* \to ZZ \to 4\ell$, $gg \to ZZ \to 4\ell$ and $q\bar{q} \to ZZ \to 4\ell$ to obtain differential distributions for the full $pp \to ZZ \to 4\ell$ process, including the corrections due to insertions of the SMEFT operator $\mathcal{O}_6$.

Using our MC implementation, we have then studied the shape differences in the four-lepton invariant mass $m_{4\ell}$ distribution and the ME-based kinematic discriminant $D_S$ defined in (6.28) that are induced by modifications of the trilinear Higgs coupling. We found that the inclusion of BSM effects leads to phenomenologically relevant kinematic features in both spectra. In fact, the discriminant $D_S$ turns out to provide particularly powerful constraints on the Wilson coefficient $\bar{c}_6$ of the pure-Higgs operator $\mathcal{O}_6$. The stringent constraints on $\bar{c}_6$ arise because BSM scenarios with $\bar{c}_6 \neq 0$ can lead to $D_S < -4.5$, which provides a null test since 99% of the $pp \to ZZ \to 4\ell$ events in

the SM fall into the range $-4.5 < D_S < 0.5$. We have also assessed the possible impact of higher-order QCD correction to $D_S$, arguing that (6.28) maintains its discriminating power beyond the well-defined LO.

To demonstrate the benefits of off-shell Higgs production in setting bounds on the Higgs trilinear coupling, we have determined the constraints on the Wilson coefficients $\bar{c}_6$ and $\bar{c}_H$ that the LHC with $300\,\mathrm{fb}^{-1}$ and $3\,\mathrm{ab}^{-1}$ of integrated luminosity at $\sqrt{s} = 14\,\mathrm{TeV}$ may be able to set. We have then compared the obtained LHC Run 3 and HL-LHC bounds to the projected constraints that a combination of inclusive single-Higgs measurements is expected to provide. Our analysis shows that ggF off-shell Higgs production allow to put constraints on the trilinear Higgs coupling that are not only competitive with but also complementary to the exclusion limits obtained from inclusive single-Higgs production. Specifically, we found that future studies of the $D_S$ distribution in $pp \to ZZ \to 4\ell$ production should help to remove flat directions in the $\bar{c}_6$–$\bar{c}_H$ plane that remain unresolved in fits that incorporate only inclusive single-Higgs measurements. By combining all single-Higgs boson measurement we find that at the LHC Run 3 (HL-LHC) it might be possible to constrain modifications of the trilinear Higgs coupling as parameterised by (6.20) to the 95% CL range $c_3 \in [-4.0, 6.1]$ ($c_3 \in [-1.7, 5.7]$). Additional HL-LHC projections that employ two different assumptions about the systematic uncertainties entering our off-shell Higgs analysis can be found in Appendix C.

The studies performed in this chapter can be extended in several ways. First, to strengthen the constraints on the trilinear Higgs coupling derived in our work, one should also include in the projections measurements of double-Higgs production as well as EW precision observables. See [285, 286, 289] for such global analyses based on LHC Run 2 data. Second, the ME-based discriminant $D_S$ might also be a powerful tool to constrain BSM effects in $pp \to ZZ \to 4\ell$ that arise in the context of Higgs portal models [301–303], see Chapter 8. Given the limited direct LHC reach in such models [321, 322], we show in Chapter 8 that investigating the indirect sensitivity that off-shell Higgs production can provide is a worthwhile exercise. Third, since any improvement of our theoretical understanding of the $D_S$ distribution (6.28) will have a tangible impact on the sensitivity of off-shell Higgs measurements to modifications of the trilinear Higgs coupling, we believe that theoretical activity in this direction is important. Since many ingredients (if not all) are already available in the literature on $pp \to ZZ \to 4\ell$ production [44, 79–81, 172, 212, 214, 217, 231, 232, 309–311] achieving such a goal is certainly possible.

# Chapter 7

# Beautiful and charming chromodipole moments

The contributions from the chromoelectric dipole moment (CEDM) and anomalous chromomagnetic dipole moment (CMDM) for a generic quark field $q$ are contained in the following dimension-five effective Lagrangian [323]

$$\mathcal{L} = -\frac{g_s}{2} \left( \tilde{\mu}_q + i\gamma_5 \tilde{d}_q \right) \bar{q}\sigma_{\mu\nu} t^A q \, G^{A,\mu\nu} , \qquad (7.1)$$

where $\tilde{\mu}_q$ and $\tilde{d}_q$ are the CMDM and CEDM, respectively. Furthermore, $g_s$ denotes the QCD coupling, $t^A$ are the $SU(3)$ colour generators, $G^A_{\mu\nu}$ is the gluon field strength tensor and $\sigma_{\mu\nu} = i/2\,(\gamma_\mu\gamma_\nu - \gamma_\nu\gamma_\mu)$ with $\gamma_\mu$ the usual Dirac matrices. The operators in (7.1) are however not gauge invariant under the full SM gauge group, which frustrates their use within linear EFT formalisms such as the SMEFT. The corresponding gauge-invariant chromodipole operators within in the SMEFT include the Higgs field as an active degree of freedom (*i.e.* they are of dimension six). In this chapter, we restrict ourselves to the case of the bottom quarks — sometimes called *beauty* quarks — and charm quarks, for which the dimension-six chromodipole operators within the SMEFT are given by

$$\begin{aligned}
\mathcal{O}_{bG} &= g_s \bar{q}_3 \sigma_{\mu\nu} t^A d_3 \, H \, G^{A,\mu\nu} + \text{h.c.}, \\
\mathcal{O}_{cG} &= g_s \bar{q}_2 \sigma_{\mu\nu} t^A u_2 \, \widetilde{H} \, G^{A,\mu\nu} + \text{h.c.},
\end{aligned} \qquad (7.2)$$

where the symbol $q_f$ denotes left-handed quark doublets of flavour $f$, while $u_f$ and $d_f$ are the right-handed up- and down-type quark singlets, $H$ denotes the SM Higgs doublet and the shorthand notation $\widetilde{H}_i = \epsilon_{ij} \left( H_j \right)^*$ with $\epsilon_{ij}$ totally antisymmetric and $\epsilon_{12} = 1$ has been used. By expanding (7.2), one obtains the following parametrisations for the bottom and charm CMDM and CEDM within the SMEFT

$$\tilde{\mu}_{b(c)} = -\frac{\sqrt{2}v}{\Lambda^2} \, \text{Re}\left(C_{b(c)G}\right), \qquad \tilde{d}_{b(c)} = -\frac{\sqrt{2}v}{\Lambda^2} \, \text{Im}\left(C_{b(c)G}\right), \qquad (7.3)$$

where $\Lambda$ denotes the suppression scale and $C_{bG}$ and $C_{cG}$ are the Wilson coefficients associated to the bottom and charm chromodipole operators, respectively.

The aim of this chapter is to constrain the dipole operators in (7.2) — which are related to the bottom and charm CMDM and CEDM by means of (7.3). First, we

review in Section 7.1 the existing limits obtained from observables that involve the Higgs boson. In Section 7.2, we derive direct and indirect bounds on $\mathcal{O}_{bG}$ and $\mathcal{O}_{cG}$ using a variety of experimental measurements of processes that do not directly involve the Higgs boson. A summary and brief discussion is provided in Section 7.3.

## 7.1 Review of constraints from Higgs physics

The presence of the Higgs field $H$ in the operators in (7.2) induces, upon EWSB, dipole-type interactions involving the physical Higgs boson, such as the ones shown in Figure 7.1. This opens up the possibility of studying their contributions to the CMDM and CEDM of heavy quarks in processes involving a Higgs boson. In this regard, bottom quarks play an important role since $\mathrm{BR}\,(h \to b\bar{b})$ is with around 58% the largest branching ratio of the SM Higgs boson. Due to the large backgrounds from multi-jet production in the dominant ggF Higgs production mode, the most sensitive production channels for detecting $h \to b\bar{b}$ decays are the associated production of a Higgs boson and a $W$ or $Z$ boson $(Vh)$, where the leptonic decay of the vector boson enables efficient triggering. In fact, the $h \to b\bar{b}$ decay mode has been observed by both the ATLAS and the CMS collaborations at LHC Run II [324, 325], and these measurements constrain the $b\bar{b}$ signal strength in $Vh$ production to be SM-like within about 25% at the level of one standard deviation.

BSM physics modifying the bottom-Higgs dynamics is therefore only weakly constrained by existing LHC measurements with even looser limits applying in the charm-Higgs case [326–332]. In the context of the SMEFT the dimension-six mixed-chirality operators that can lead to modifications of the $h \to b\bar{b}$ and $h \to c\bar{c}$ partial decay widths are either of Yukawa or dipole type. While the Yukawa-type operators change the rates at LO in QCD, the chromodipole operators (7.2) start to contribute at the NLO level [333]. Their effect on Higgs observables have been studied in [166, 323, 334]. In this section, we briefly review the resulting constraints.

By generating $pp \to b\bar{b}h$ events for the HL-LHC with $\sqrt{s} = 14$ TeV for different values of $C_{bG}$ and performing a fit to the different MC samples, the authors of [323] obtain the following $C_{bG}$-dependence for the $b\bar{b}h$ signal strength

$$\mu_{b\bar{b}h} = 1 - 9.76 \times 10^{-2} \, \mathrm{Re}\,\big(C_{bG}\big) + 1.49 \times 10^{-1} \, \big|C_{bG}\big|^2 \,, \qquad (7.4)$$

where there is no linear term in $\mathrm{Im}\,\big(C_{bG}\big)$ since odd powers of the CEDM would violate time-reversal symmetry $(T)$[1] and here terms beyond $\mathcal{O}(C_{bG}^2)$ are neglected. Requiring the BSM effects to remain within two standard deviations of the NLO inclusive cross-section $\sigma_{\mathrm{SM}}\,\big(pp \to b\bar{b}h\big) = (5.8 \pm 1.0) \times 10^2$ fb [335] yields for the two benchmark cases where $C_{bG}$ is either purely real or purely imaginary the following limits[2]

$$\mathrm{Re}\,\big(C_{bG}\big) \in [-1.2, 1.9] \,, \qquad \big|\mathrm{Im}\,\big(C_{bG}\big)\big| < 1.5 \,, \qquad (7.5)$$

where $\Lambda = 1$ TeV is assumed. The above limits translate to

$$\frac{\big|\mathrm{Re}\,\big(C_{bG}\big)\big|}{\Lambda^2} < \left(\frac{1}{730\,\mathrm{GeV}}\right)^2 \,, \qquad \frac{\big|\mathrm{Im}\,\big(C_{bG}\big)\big|}{\Lambda^2} < \left(\frac{1}{810\,\mathrm{GeV}}\right)^2 \,. \qquad (7.6)$$

---

[1] $T$-odd interactions are considered for the top-quark case in [323].

[2] We add that at the $1\sigma$ level, one finds $\mathrm{Re}\,\big(C_{bG}\big) \in [-0.8, 1.5]$ and $\big|\mathrm{Im}\,\big(C_{bG}\big)\big| < 1.1$, which translate to the bounds quoted in (16) of [323] upon using (7.3) with a suppression scale of $\Lambda = 3$ TeV.

**Figure 7.1:** Tree-level diagrams generated by the bottom-quark chromodipole operator (7.2), whose insertions are indicated by the red squares, involving a Higgs boson.

We add that significantly stronger bounds on $\mathrm{Im}\left(C_{qG}\right)$ arise in the context of the neutron electric dipole moment, see for instance (7.36) and (7.40). The inclusive approach outlined above is improved in [334], where the sensitivity to the chromodipole operator $\mathcal{O}_{bG}$ is studied for Higgs plus dijet searches in combination with the two-photon decay channel of the Higgs. It is shown that by identifying at least one jet as a bottom quark ($b$-tagging) and applying cuts on the di-photon transverse momentum, the process $pp \rightarrow b\bar{b}h \rightarrow b\bar{b}\gamma\gamma$ furnishes a significantly better bound on $|C_{bG}|$ of

$$\frac{|C_{bG}|}{\Lambda^2} < \left(\frac{1}{2.4\,\mathrm{TeV}}\right)^2 . \tag{7.7}$$

at the end of the HL-LHC (*i.e.* with $\sqrt{s} = 14$ teV and $3\,\mathrm{ab}^{-1}$ of integrated luminosity).

The article [323] furthermore considers inclusive Higgs production as a probe of $C_{cG}$, where they find

$$\sigma\left(pp \rightarrow h\right) = 5.58 - 0.034\,\mathrm{Re}\left(C_{cG}\right) + 0.07\,|C_{cG}|^2\,\mathrm{pb}, \tag{7.8}$$

at 14 TeV. The authors then compare their fit, neglecting the SM contribution of 5.58 pb, directly to the NLO inclusive ggF cross-section $\sigma\left(pp \rightarrow h\right) = 49.97^{+7.3}_{-7.0}$ pb [336]. The resulting bounds at the $2\sigma$ level for $\Lambda = 1$ TeV read[3]

$$\mathrm{Re}\left(C_{cG}\right) \in [-14.2, 14.7], \qquad \left|\mathrm{Im}\left(C_{cG}\right)\right| < 14.4, \tag{7.9}$$

which correspond to

$$\frac{\left|\mathrm{Re}\left(C_{cG}\right)\right|}{\Lambda^2} < \left(\frac{1}{260\,\mathrm{GeV}}\right)^2, \qquad \frac{\left|\mathrm{Im}\left(C_{cG}\right)\right|}{\Lambda^2} < \left(\frac{1}{260\,\mathrm{GeV}}\right)^2 . \tag{7.10}$$

Since the above result for the inclusive ggF Higgs-production cross section is rather outdated, we have repeated the procedure described above employing $\sigma\left(pp \rightarrow h\right) = 49.87^{+0.32\%}_{-2.61\%}$ pb [313] which includes QCD corrections up to the N³LO in the large top-mass limit. This yields an improvement of the bounds shown in (7.9) by about a factor of two. However, clearly the limits originating from inclusive Higgs production are not competitive with $pp \rightarrow b\bar{b}h$, a finding that is also confirmed by [334]. One might find this surprising since earlier studies of the top-quark chromomagnetic dipole using inclusive Higgs production have shown to furnish the most constraining results [334, 337, 338]. However, the suppression coming from the chirality flip needed to obtain a non-zero

---

[3]The bounds quoted in (22) of [323] can be found by applying (7.3) with for $\Lambda = 3$ TeV to the $1\sigma$ constraints $\mathrm{Re}\left(C_{bG}\right) \in [-9.8, 10.5]$ and $\left|\mathrm{Im}\left(C_{bG}\right)\right| < 10.2$.

result in the case of ggF Higgs production proceeding through a quark loop is much more severe in the case of the bottom quark compared to the top-quark case, spoiling much of the sensitivity to insertions of the bottom-quark chromodipole operator.

Finally, we note that more recently, [166] studies the process $pp \to Zh \to b\bar{b}\ell^+\ell^-$ at NNLO QCD within the SMEFT, including up to N³LO corrections due to the operator $\mathcal{O}_{bG}$. It is shown that these corrections enhance the impact of $\mathcal{O}_{bG}$ by about 60% compared to its contributions at the previous order. In particular, the $b\bar{b}$ and $b\bar{b}j$ invariant masses are identified as kinematic distributions that are sensitive to $\mathcal{O}_{bG}$, as well as the transverse momentum of the $Z$ boson and the $b\bar{b}$ pair. While these transverse-momentum observables by themselves are shown to exhibit only a limited constraining power at the LHC, it is noted that an implementation of the aforementioned observables into a multivariate discriminant $\big($a la $(6.28)\big)$ may enhance the overall sensitivity to $\mathcal{O}_{bG}$. A comparison to existing or future differential LHC data is however left for future work.

A summary of the constraints on $C_{qG}$ $(q = b, c)$ discussed here is given in Table 7.2. In the next section, we derive direct in and indirect limits on the bottom and charm chromodipole operators from observables that do not involve a Higgs boson.

## 7.2 Bottom and charm chromodipole operators in non-Higgs observables

In contrast to the SMEFT Yukawa-type operators that can only be constrained by processes involving a Higgs or Higgses both real or virtual, the operators (7.2) can also be bounded by measurements of observables that involve bottom (charm) quarks and possibly other particles but no Higgs boson. The goal of this section is to derive bounds on the Wilson coefficients of the operators $\mathcal{O}_{bG}$ and $\mathcal{O}_{cG}$ using existing measurements of both low- and high-energy observables of the latter type.

### 7.2.1 Constraints from dijet angular distributions

Jet physics has previously been used to put constraints on SMEFT operators [339–344]. In this section we will exploit searches for unflavoured jet pairs to constrain the magnitudes of the Wilson coefficients of the operators introduced in (7.2). For the case of the bottom-quark chromodipole operator $\mathcal{O}_{bG}$, examples of contributing Feynman diagrams are shown in Figure 7.2. The relevant collider searches look either for resonances in the dijet spectrum or analyse the angular distribution of dijet production (see [345–348] for recent LHC results).

The quantity of interest in our case is the jet angular distribution, *i.e.* the differential cross section for a pair of jets with invariant mass $M_{jj}$ produced at an angle $\hat{\theta}$ to the beam direction in the jet-jet centre-of-mass (CM) frame. Compared to resonance searches, the dijet angular distribution has the salient advantage that it also allows to constrain broad $s$-channel resonances or modifications in the spectrum due to the presence of higher-dimensional operators in a rather model-independent fashion. This is due to the fact that the dominant channels in QCD dijet production have the familiar Rutherford scattering behaviour $d\sigma/d\cos\hat{\theta} \propto 1/\sin^4\big(\hat{\theta}/2\big)$ at small angle $\hat{\theta}$, which is characteristic for $t$-channel exchange of a massless spin-one boson. In order to remove
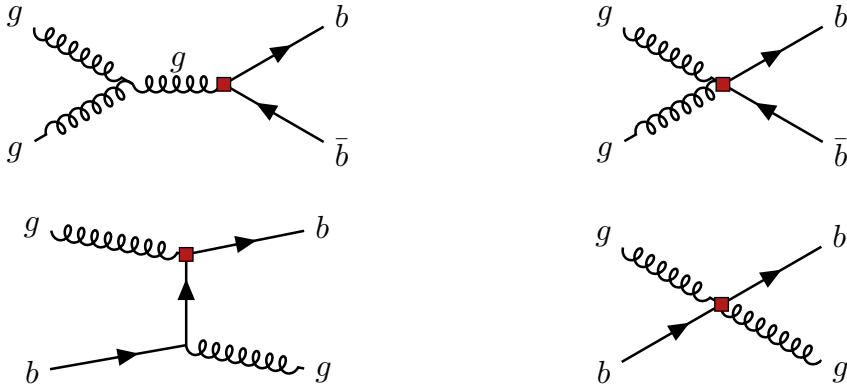
**Figure 7.2:** Tree-level diagrams leading to a correction to dijet production. The red squares denote the insertion of the bottom-quark chromomagnetic dipole moment.

the Rutherford singularity, one usually considers the dijet cross sections differential in

$$\chi = \frac{1 + \cos\hat\theta}{1 - \cos\hat\theta}. \tag{7.11}$$

In the small angle limit, *i.e.* $\chi \to \infty$, the partonic differential QCD cross section then behaves as $d\sigma/d\chi \propto$ const. Relative to the QCD background, the production of a heavy resonance or an effective operator leads to additional hard scattering and hence more jets perpendicular to the beam. In turn one expects a deviation from the QCD prediction in form of an enhanced activity of high-energetic jets in the central region of the detector. If the angular distributions receive contributions from the presence of a heavy degree of freedom or an operator, one should see an excess of events in $d\sigma/d\chi$ for $\chi \to 1$ and large $M_{jj}$ with respect to the (almost) flat QCD spectrum.

By calculating the partonic differential cross section for the interference of the effective operator $\mathcal{O}_{bG}$ with the SM and with itself, we find the following expressions

$$\left(\frac{d\sigma(gg \to b\bar b)}{d\chi}\right)_{bG} = \frac{\pi\alpha_s^2}{2M_{jj}^2}\left[\frac{4 - \chi + 4\chi^2}{3\chi(1+\chi)^2}\frac{v^2}{\Lambda^2}y_b\,\mathrm{Re}\left(C_{bG}\right) + \frac{7M_{jj}^2}{3(1+\chi)^2}\frac{v^2}{\Lambda^4}\left|C_{bG}\right|^2\right],$$

$$\left(\frac{d\sigma(gb \to gb)}{d\chi}\right)_{bG} = \frac{\pi\alpha_s^2}{2M_{jj}^2}\times \tag{7.12}$$

$$\left[\frac{8\left(4 + 9\chi + 9\chi^2\right)}{9\chi(1+\chi)^3}\frac{v^2}{\Lambda^2}y_b\,\mathrm{Re}\left(C_{bG}\right) + \frac{56\,M_{jj}^2}{9(1+\chi)^3}\frac{v^2}{\Lambda^4}\left|C_{bG}\right|^2\right],$$

where $y_b = \sqrt{2}m_b/v$ is the bottom-quark Yukawa coupling with $m_b$ the bottom-quark mass. The result for the differential cross section for the process $g\bar b \to g\bar b$ is identical to the one for $gb \to gb$, and the results for the case of the operator $\mathcal{O}_{cG}$ are simply obtained from the above expressions by replacing $b$ everywhere by $c$. Notice that the first terms in (7.12) which arise from the interference with the SM are suppressed by one power of $y_b$ which provides the chirality flip needed to obtain a non-zero result. The second terms which are due to the interference of the operator $\mathcal{O}_{bG}$ with itself are instead enhanced by two powers of the jet-jet invariant mass $M_{jj}$. As a result
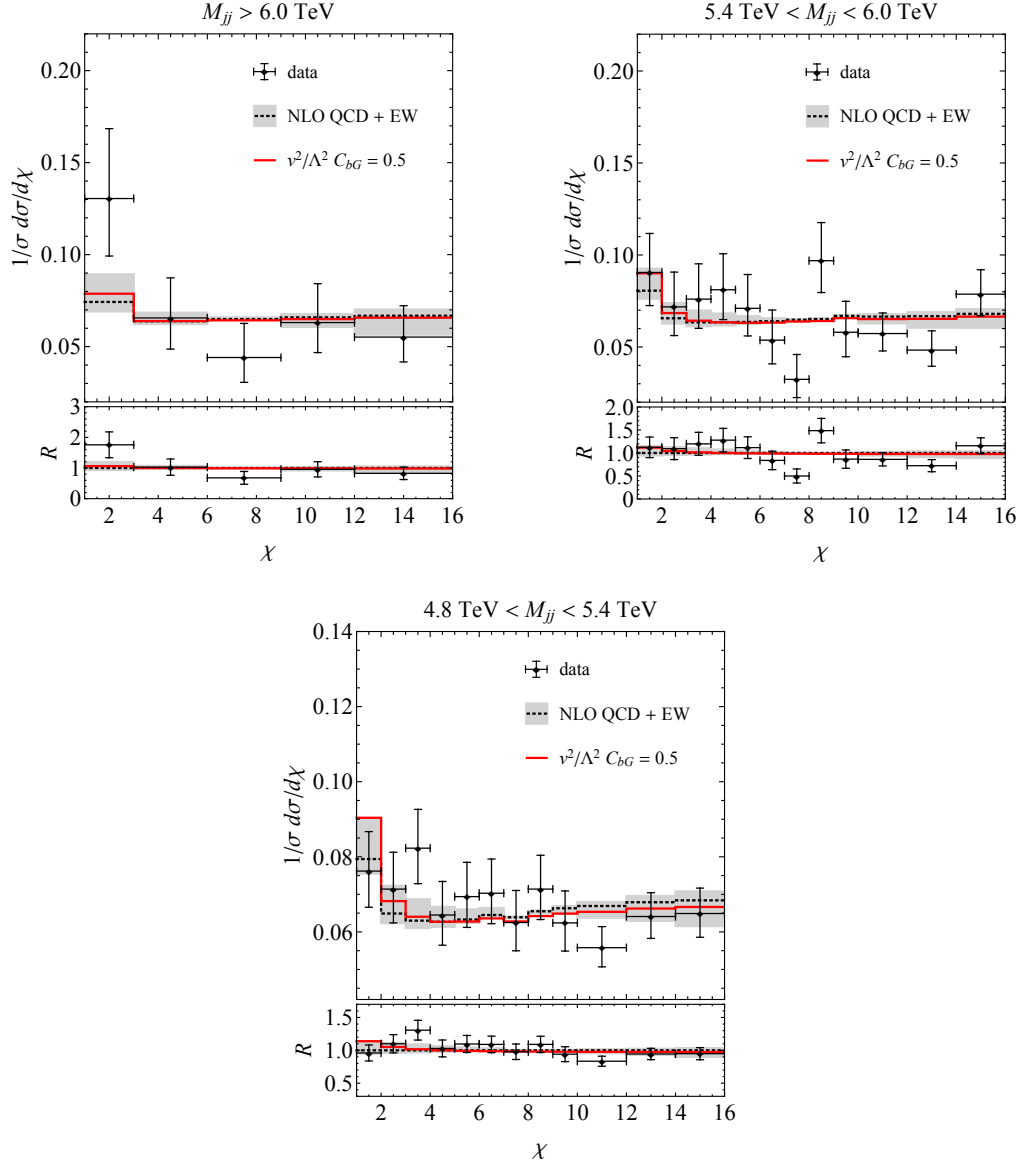
**Figure 7.3:** Normalised $\chi$ distribution in the three highest mass bins studied in the CMS analysis [345]. Unfolded data from [345] are compared to the SM prediction including NLO QCD and EW corrections (black dotted line). The error bars represent statistical and experimental systematic uncertainties combined in quadrature. Theoretical uncertainties are indicated as a grey band. Also shown is the prediction for $v^2/\Lambda^2\,C_{bG} = 0.5$ (red line). The lower panels show the ratio of the unfolded data distributions and the NLO predictions as well as the new-physics distributions. See main text for more details.
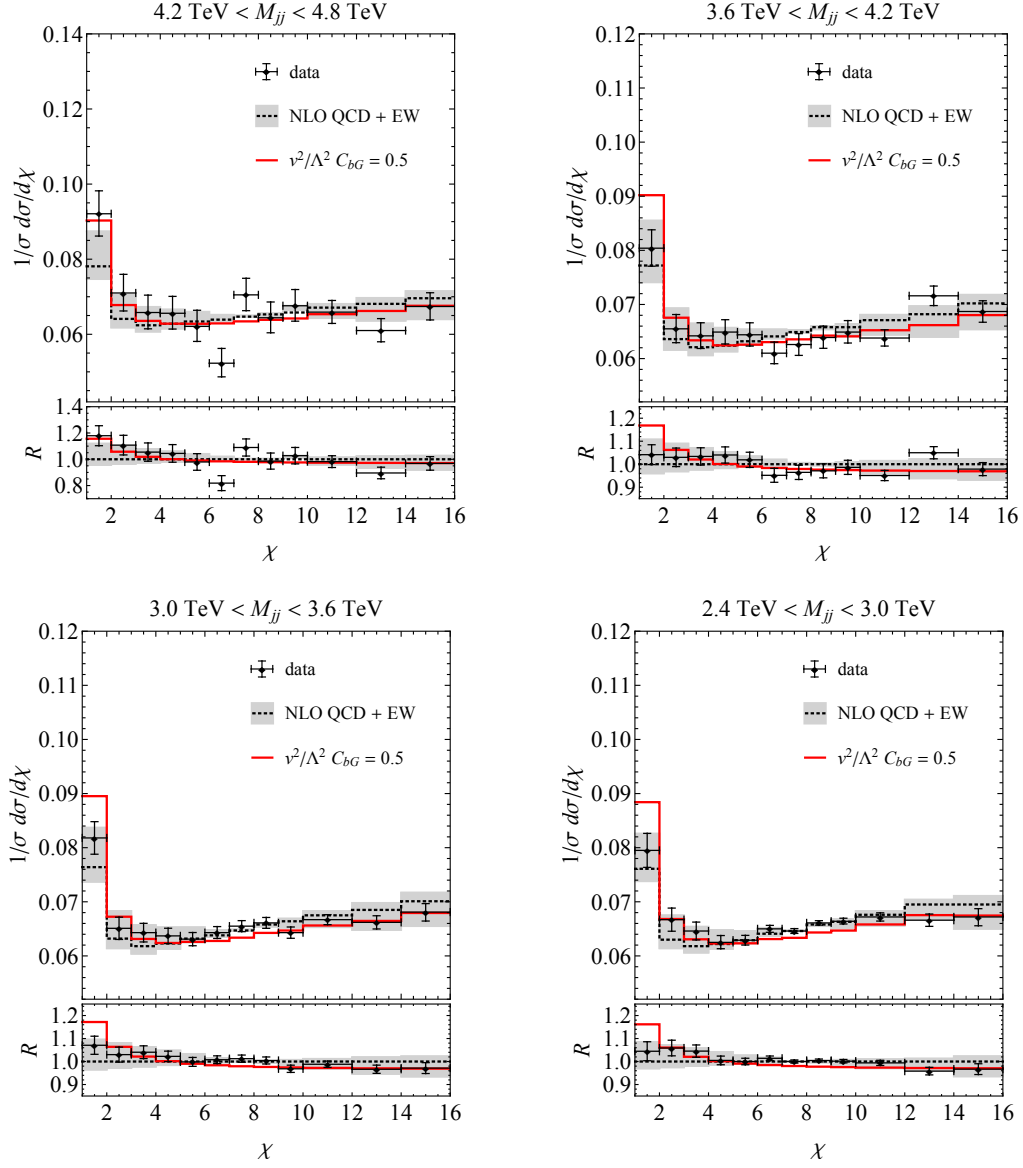
**Figure 7.4:** As Figure 7.3 but for the four lower mass bins considered in the CMS analysis [345].

the quadratic term will in practice always provide the dominant contribution to the dijet spectrum. Given that in addition the gluon-quark initiated channels are strongly suppressed by heavy-quark PDFs this means that the limit that we derive below holds to very good approximation for both $\mathcal{O}_{bG}$ and $\mathcal{O}_{cG}$.

In terms of the partonic differential cross sections (7.12), the contribution to the double differential cross section for a pair of jets with invariant mass $M_{jj}$ produced at $\chi$ that is due to $\mathcal{O}_{bG}$, can be written in the following way

$$\left(\frac{d^2\sigma}{dM_{jj}^2\,d\chi}\right)_{bG} = \frac{M_{jj}^2}{s}\sum_{\{ij\}} f\!f_{ij}\left(M_{jj}^2/s,\mu_F\right)\left(\frac{d\sigma(ij\to f)}{d\chi}\right)_{bG}, \qquad (7.13)$$

where

$$f\!f_{ij}\left(\tau,\mu_F\right) = \frac{1}{s}\frac{2}{1+\delta_{ij}}\int_\tau^1 \frac{dx}{x}\,f_{i/p}(x,\mu_F)\,f_{j/p}(\tau/x,\mu_F), \qquad (7.14)$$

are the so-called parton luminosities, the sum runs over all pairs of incoming partons $\{ij\}$ and $s$ denotes the squared CM energy of the collider. The parton luminosities are obtained from a convolution of the universal non-perturbative PDFs $f_{i/p}(x,\mu_F)$, which describe the probability of finding the parton $i$ in the proton with longitudinal momentum fraction $x$. The variable $\mu_F$ that enters (7.13) and (7.14) denotes the factorisation scale.

In Figures 7.3 and 7.4 the measured normalised $\chi$ distribution for the seven different mass bins unfolded to particle level are compared to the corresponding SM predictions including both QCD and EW corrections at the NLO. The data and the SM predictions are both taken from the CMS analysis [345]. For comparison the normalised $\chi$ distributions assuming $v^2/\Lambda^2\,C_{bG} = 0.5$ are also shown. The new-physics distributions are obtained at LO using `CT14nnlo_as_0118` PDFs [349] with renormalisation and factorisation scale set to $M_{jj}$. These PDFs have also been used in [345] and are accessed through `ManeParse` [350]. The normalised $\chi$ distributions are then multiplied by a bin-wise $K$-factor to obtain a reshaped spectrum that includes effects originating from NLO QCD and EW corrections, additional non-perturbative QCD effects and the detector resolution. The $K$-factor is obtained by calculating the ratio between the central value of the CMS SM prediction and our LO SM prediction. Notice that applying the same rescaling factor to both the QCD and new-physics results is based on the assumption that the effects of the MC shower and the event detection depend only on the invariant mass $M_{jj}$ of the dijet final state, but not on the precise form of the new-physics signal. To determine to which extend this assumption is justified would require to perform a dedicated simulation of including NLO QCD and EW corrections, parton showering and detector effects. However, such an analysis is beyond the scope of this work.

To find the 95% confidence level (CL) limit on the magnitude of the Wilson coefficient of the dipole operator $\mathcal{O}_{bG}$, we perform a $\chi^2$ fit to the normalised angular distribution in all seven dijet invariant mass bins, including both experimental and theoretical uncertainties. Minimising the $\chi^2$ and requiring $\Delta\chi^2 = \chi^2 - \chi^2_{\min} = 3.84$ leads to

$$\frac{|C_{bG}|}{\Lambda^2} < \left(\frac{1}{380\,\mathrm{GeV}}\right)^2. \qquad (7.15)$$

The same bound applies approximately also in the case of $\mathcal{O}_{cG}$. Notice that since the bounds (7.36) and (7.40) are significantly stronger than the latter limit, the exclu-
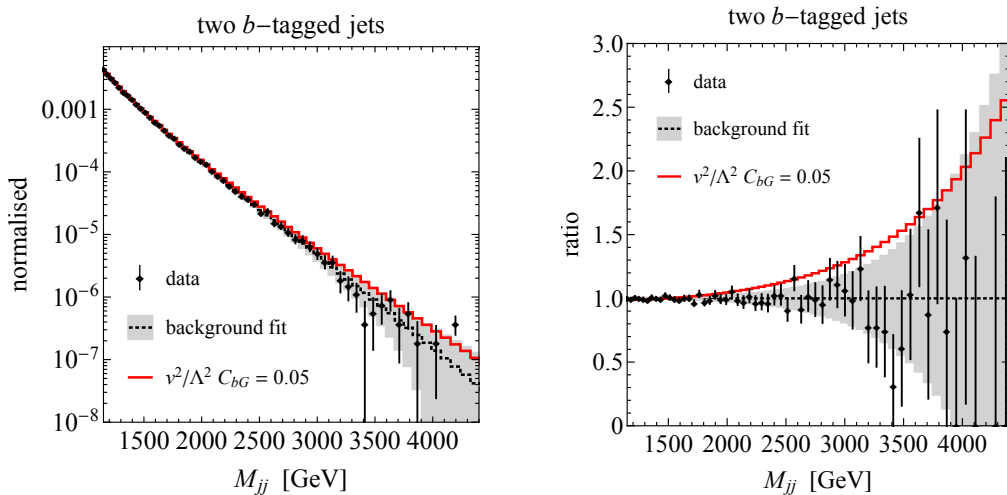
**Figure 7.5:**   Left: Normalised dijet invariant mass distributions for the category with two $b$-jets as measured by ATLAS in [346]. The black dotted line is the central value of the background fit performed by ATLAS, the grey band indicates the associated uncertainties and the red curve shows the new-physics prediction assuming $v^2/\Lambda^2\,C_{bG} = 0.05$. Right: Ratio of the data and the new-physics prediction $v^2/\Lambda^2\,C_{bG} = 0.05$ to the central value of the background fit. The colour coding resembles the one used in the left panel. Consult the main text for further details.

sion (7.15) is in fact a bound on the real part of the Wilson coefficients $C_{bG}$ and $C_{cG}$. We add that non-zero values $v^2/\Lambda^2\,|C_{bG}| \simeq 0.3$ of the Wilson coefficient are, in fact, preferred by the data, and that the most sensitive bins in our $\chi^2$ fit are the three bins of [345] that cover the range $2.4\,\text{TeV} < M_{jj} < 4.2\,\text{TeV}$ of invariant dijet masses. Notice finally that analyses of the jet-jet angular distribution in dijet production can also be used to put constraints on the chromodipole operators involving light quarks. Since the focus of this work lies on deriving constraints on the chromodipole operators involving bottom and charm quarks, we however do not entertain this possibility here.

### 7.2.2   Constraints from searches for $b$-jet pairs

In addition to using data for unflavoured dijet production, one can also exploit the measurements of mass distributions of jet pairs with one or two jets identified as $b$-jets [346, 351–353] to constrain the Wilson coefficient of the operator $\mathcal{O}_{bG}$ — see also [334] for an earlier study.

   To calculate the differential cross sections for the production of $b$-jet pairs we have used a `FeynRules 2` [354] implementation of the operator $\mathcal{O}_{bG}$ in the `UFO` format [355]. The generation and showering of the samples has been performed at LO with MC@NLO [356] and `PYTHIA 8.2` [146], respectively, using `NNPDF31_nlo_as_0118` PDFs [179] and working in the four-flavour scheme. The background distribution was corrected to the NLO prediction using the matrix elements calculated in [357] as implemented in `MCFM` [358]. Hadronic jets are built using the anti-$k_t$ algorithm [128] with a radius parameter of $R = 0.4$, as implemented in `FastJet` [244]. We furthermore rely on `DELPHES 3` [359] as a fast detector simulation and on `CheckMATE 2` [360]. Our event selection follows the ATLAS analysis [346] which is based on $139\,\text{fb}^{-1}$ of dijet data collected at 13 TeV CM energy. We require at least two jets ($j$) with a transverse mo-

mentum $p_T(j)$ satisfying $p_T(j) > 150\,\text{GeV}$ and the azimuthal angle difference $\Delta\phi(j_1 j_2)$ between the two leading jets $j_1$ and $j_2$ must fulfill $|\Delta\phi(j_1 j_2)| > 1.0$. The two leading jets must be $b$-tagged and their pseudorapidities must satisfy $|\eta(j)| < 2.0$. The $b$-tagging algorithm is taken from the ATLAS publication [361], and in accordance with [346] a $b$-tagging working point is chosen that yields a $b$-tagging efficiency of 77%, a $c$-jet rejection of 5 and a light-flavour jet rejection of 110. Furthermore, to suppress the QCD background a selection cut of $|y_*| < 0.8$ is imposed, where $y_* = \big(y(j_1) - y(j_2)\big)/2$ with $y(j_1)$ and $y(j_2)$ the rapidities of the leading and subleading jet, respectively. Both the QCD background and the new-physics samples are generated binned in $p_T(j)$ and the resulting dijet mass distributions are fit to the parametric function

$$f(x) = p_1\,(1 - x)^{p_2}\,x^{p_3 + p_4\ln x}\,,\tag{7.16}$$

where $x = M_{jj}/\sqrt{s}$ and $p_i$ with $i = 1, 2, 3, 4$ are the four fitting parameters. Given the data-driven background estimate, the ATLAS measurement [346] is not a measurement of the absolute cross section of dijet production, making it insensitive to small overall shifts in the $b\bar{b}$ production rates. The ATLAS analysis is however sensitive to the shape of the dijet mass distribution, which can be determined in normalised rates.

In Figure 7.5 we show the results for the normalised invariant dijet mass spectra requiring two $b$-jets. The black dotted line in the left plot denotes the central values of the background fit performed by ATLAS in [346], while the red curve shows our new-physics prediction for $v^2/\Lambda^2\,C_{bG} = 0.05$. The grey band indicates the uncertainties associated to the background prediction as provided in [346]. On the right-hand side the ratio of the data and the new-physics prediction to the central value of the background fit is displayed. One observes that the contributions associated to $\mathcal{O}_{bG}$ lead to an enhancement in the tail of the $M_{jj}$ distribution with respect to the background prediction.

By performing a $\Delta\chi^2$ fit to the normalised spectra over the whole range of invariant dijet masses covered in the ATLAS study [346], *i.e.* $1133\,\text{GeV} < M_{jj} < 4595\,\text{GeV}$, we obtain the following 95% CL limit

$$\frac{\big|C_{bG}\big|}{\Lambda^2} < \left(\frac{1}{1.6\,\text{TeV}}\right)^2\,.\tag{7.17}$$

This bound is by a factor of about 2.5 better than the estimate that has been given in [334] based on the CMS dijet measurement [351]. Let us remark that adding an additional uncertainty of 10% to the background prediction obtained in [346] would lead to a slightly weaker bound than (7.17) of approximately $1/(1.5\,\text{TeV})^2$. Since the unnormalised two $b$-tagged MC distribution and the data are found to agree within around 10% in the mass range $1\,\text{TeV} < M_{jj} < 5\,\text{TeV}$ [352], we believe that the latter bound is very robust. Notice finally that searches for jet pairs with one or two jets identified as $c$-jets could be used to set a bound on the Wilson coefficient $\big|C_{cG}\big|$ similar to (7.17). To our knowledge dijet searches that employ $c$-tagging have however not been performed at the LHC to date.

### 7.2.3 Constraints from $Z$-boson production in association with $b$-jets

Inclusive and differential measurements of $Z$-boson production in association with $b$-jets have been performed at the LHC by both the ATLAS and CMS collaborations [362–
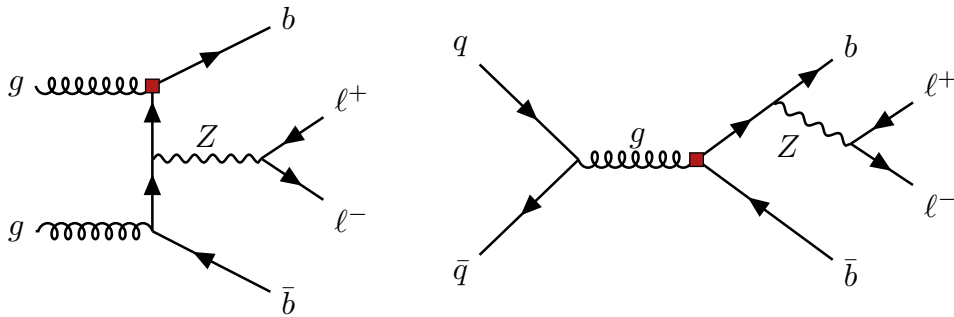
**Figure 7.6:** Examples of Feynman diagrams leading to a $b\bar{b}\ell^+\ell^-$ signature at the LHC. The red squares denote the insertion of the bottom-quark chromomagnetic dipole moment. Graphs with a virtual photon $\gamma^*$ also contribute but are not shown explicitly.

368]. These measurements provide not only an important role in improving our quantitative understanding of perturbative QCD (see e.g. [369]), but can also be exploited to search for BSM physics [370]. In this section we will consider the measurements performed in [367] to set bounds on the Wilson coefficient of the operator $\mathcal{O}_{bG}$.

We calculate the contribution of the operator $\mathcal{O}_{bG}$ to $pp \to b\bar{b}Z/\gamma^* \to b\bar{b}\ell^+\ell^-$ at LO using MC@NLO together with `PYTHIA 8.2` and `NNPDF31_nlo_as_0118` PDFs. The computation is performed in the four-flavour scheme. Relevant Feynman diagrams are shown in Figure 7.6. To be able compare our results to an existing analysis we employ the event selections of the recent ATLAS measurement [367] which is based on $35.6\,\text{fb}^{-1}$ of $13\,\text{TeV}$ LHC data. Electrons must satisfy the tight likelihood requirement [371], and are required to have a transverse momentum and pseudorapidity of $p_T(e) > 27\,\text{GeV}$ and $|\eta(e)| < 2.47$, respectively. Electron candidates in the transition region between the barrel and endcap electromagnetic calorimeters, *i.e.* $1.37 < |\eta(e)| < 1.52$, are excluded. Muons must satisfy medium identification criteria [372] and have to pass the requirements $p_T(\mu) > 27\,\text{GeV}$ and $|\eta(\mu)| < 2.5$. Jets are reconstructed using the anti-$k_t$ algorithm with radius parameter $R = 0.4$, and a $b$-tagging algorithm is applied with a $b$-tagging efficiency of 70% and misidentification rates of 8.3% of 0.26% for $c$-jets and a light-flavour jets, respectively. Events are required to have exactly two same-flavour ($\ell = e, \mu$) opposite-sign leptons with a dilepton invariant mass in the range $76\,\text{GeV} < M_{\ell^+\ell^-} < 106\,\text{GeV}$. To suppress the background from $t\bar{t}$ events with dileptonic decays, events with $p_T(\ell^+\ell^-) < 150\,\text{GeV}$ must also have missing transverse energy of $E_T^{\text{miss}} < 60\,\text{GeV}$. Events passing the above selection are then assigned to two signal regions depending on the number of identified $b$-jets, and we concentrate in the following on the signal region with at least two $b$-jets. The object and event selection used in our analysis are implemented into `CheckMATE 2` which uses `DELPHES 3` as a fast detector simulation.

Several differential observables for the $pp \to b\bar{b}Z/\gamma^* \to b\bar{b}\ell^+\ell^-$ process have been considered in the article [367]. Here we focus on the transverse momentum of the $Z$-boson $\big(p_T(Z)\big)$. In Figure 7.7 we display results for the $p_T(Z)$ spectrum requiring two or more $b$-jets. The black dotted line and the grey band in the left panel are the SM prediction with its uncertainty, while the red curve shows our new-physics prediction assuming $v^2/\Lambda^2 C_{bG} = 0.07$. The used SM numbers correspond to those
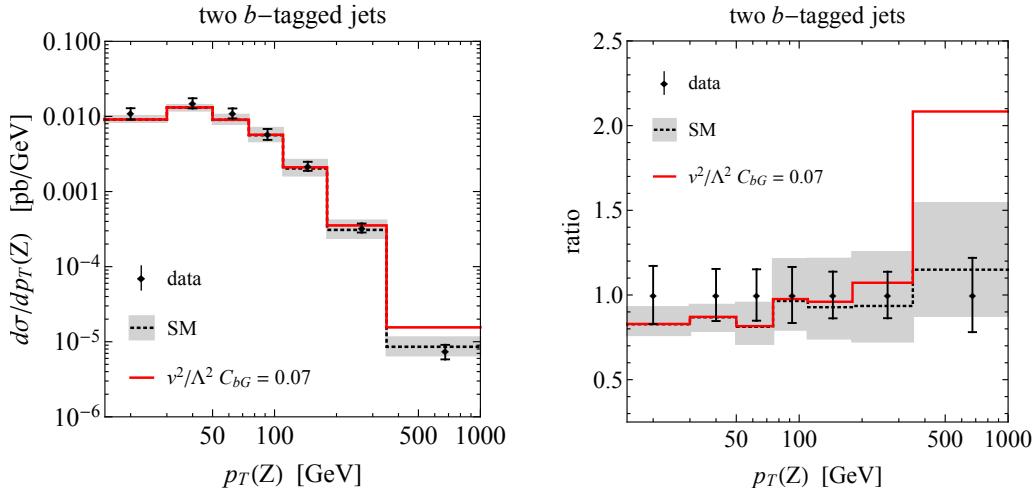
**Figure 7.7:** Left: $p_T(Z)$ distributions for the category with two $b$-jets. The black dotted line is the central value of the SM prediction provided by ATLAS [367], the grey band indicates the associated uncertainties and the red curve shows the new-physics prediction assuming $v^2/\Lambda^2 C_{bG} = 0.07$. Right: Ratio between the SM and the BSM prediction $v^2/\Lambda^2 C_{bG} = 0.07$ and the measurement. The colour coding resembles the one employed on the left-hand side.

referred to as Sherpa 5FNS (NLO) in [367]. They have been obtained by ATLAS using the `Sherpa v2.2.1` generator [373]. From the two panels it is evident that the relative effect of a non-zero contribution due to $\mathcal{O}_{bG}$ grows with transverse momentum and as a result the BSM prediction differs most visibly in the highest bin with $p_T(Z) > 350\,\text{GeV}$.

Considering all seven bins of the ATLAS study [367] in a $\Delta\chi^2$ fit, we obtain

$$\frac{\left|C_{bG}\right|}{\Lambda^2} < \left(\frac{1}{980\,\text{GeV}}\right)^2 , \tag{7.18}$$

at 95% CL. We stress that this bound depends in a notable fashion on the systematic experimental and theoretical uncertainties that plague $pp \to b\bar{b}\,Z/\gamma^* \to b\bar{b}\,\ell^+\ell^-$ at high $p_T(Z)$. In the bin with $p_T(Z) > 350\,\text{GeV}$ the experimental (theoretical) uncertainty used in our analysis amounts to about 20% (35%). Reducing the theoretical uncertainty by a factor of 2 would improve the limit (7.18) to approximately $1/(1.1\,\text{TeV})^2$. In view of the recent progress [369] in the calculation of $Z$-boson production in association with $b$-jets at next-to-next-to-leading order accuracy in QCD including finite heavy-quark mass effects, such a reduction of uncertainties does not seem unreasonable.

## 7.2.4 Constraints from flavour physics

In order to derive a bound on the real part of the Wilson coefficients of the charm-quark dipole operator, let us consider the following effective interaction

$$\mathcal{L}_{\text{eff}} \supset -\tilde{\mu}_c(m_h) \frac{g_s(m_h)}{2} \bar{c}\sigma_{\mu\nu} T^a c\, G^{a,\mu\nu} , \tag{7.19}$$

where the initial condition $\tilde{\mu}_c(m_h)$ of the charm-quark chromomagnetic dipole moment in the terms of the relevant Wilson coefficient multiplying the operators in (7.2) is given

by

$$\tilde{\mu}_c(m_h) = -\frac{\sqrt{2}\,v}{\Lambda^2}\,\mathrm{Re}\left(C_{cG}\right). \tag{7.20}$$

One-loop Feynman diagrams involving a $W$-boson exchange generate the chromomagnetic dipole operator

$$Q_8 = \frac{g_s}{(4\pi)^2}\,m_b\,\bar{s}_L\,\sigma_{\mu\nu}T^a b_R\,G^{a,\mu\nu}\,, \tag{7.21}$$

which appears in the $\Delta B = 1$ Lagrangian $\mathcal{L} = -4G_F/\sqrt{2}V_{ts}^*V_{tb}C_8Q_8$ with $G_F \simeq 1/(\sqrt{2}v^2)$ the Fermi constant and $V_{ij}$ the elements of the Cabibbo-Kobayashi-Maskawa (CKM) matrix. The corresponding matching correction reads [374, 375]

$$\delta C_8(m_h) = \frac{\bar{m}_c(m_h)}{2}\frac{V_{cs}^*V_{cb}}{V_{ts}^*V_{tb}}\,\tilde{\mu}_c(m_h)\,, \tag{7.22}$$

where $\bar{m}_c(m_h)$ denotes the charm-quark $\overline{\mathrm{MS}}$ mass evaluated at the Higgs-boson mass threshold. In terms of the shift $\delta C_8(m_h)$, the ratio between the branching ratio of $B \to X_s\gamma$ and its SM prediction can be written as [376]

$$R_{X_s} = \frac{\mathrm{BR}\left(B \to X_s\gamma\right)}{\mathrm{BR}\left(B \to X_s\gamma\right)_{\mathrm{SM}}} = 1 - 0.59\,\delta C_8(m_h)\,. \tag{7.23}$$

Combining the SM calculation of $B \to X_s\gamma$ with the present world average, one gets [377]

$$R_{X_s} = 0.97 \pm 0.08\,, \tag{7.24}$$

if uncertainties are added in quadrature. Using now that $V_{cs}^*V_{cb} \simeq -V_{ts}^*V_{tb}$ to high accuracy and employing $m_c(m_h) \simeq 0.87\,\mathrm{GeV}$, one obtains from (7.20) to (7.24) the following 95% CL limit

$$\frac{\left|\mathrm{Re}\left(C_{cG}\right)\right|}{\Lambda^2} < \left(\frac{1}{25\,\mathrm{GeV}}\right)^2. \tag{7.25}$$

We add that a bound that is weaker than (7.25) by a factor of around 4 is obtained by confronting the SM prediction $\mathrm{BR}\left(B \to X_s g\right)_{\mathrm{SM}} \simeq 5 \cdot 10^{-3}$ [378, 379], with the corresponding experimental limit that reads $\mathrm{BR}\left(B \to X_s g\right) \lesssim 10\%$ [380]. An even weaker bound follows from the isospin asymmetry in $B \to K^*\gamma$ [381–383]. The above estimate shows clearly that indirect probes of the chromodipole operators through flavour-physics observables cannot compete with the constraints arising from dijets. Notice that this is particularly true for the case of $\mathcal{O}_{bG}$ where a matching correction to $Q_8$ first arises at the two-loop level leading to a further suppression of (7.22) by a factor of the order of $(4\pi)^2$. We finally remark that CP violation in the $\Delta C = 1$ sector — for instance in the form of the difference $\Delta A_{\mathrm{CP}}$ between the two direct CP asymmetries in $D \to K^+K^-$ and $D \to \pi^+\pi^-$ — also does not provide relevant bounds on $\mathrm{Im}\left(C_{bG}\right)$ due to the strong CKM and loop suppression.

### 7.2.5 Constraints from nEDM

Searches for EDMs are known to place stringent constraints on any new-physics scenario with additional sources of CP violation (see [374, 375, 384–405] for reviews and recent discussions). To derive a bound on the imaginary part of the Wilson coefficient of the
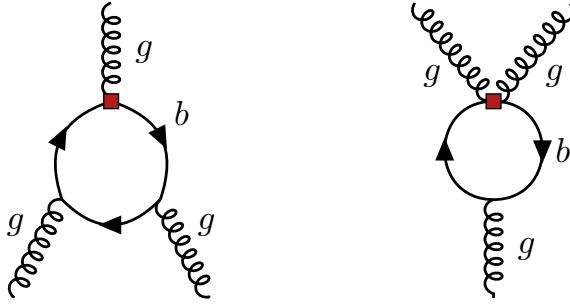
**Figure 7.8:** One-loop diagrams leading to a correction to the Weinberg operator at the bottom-quark threshold. The red squares denote the insertion of the bottom-quark chromoelectric dipole moment.

bottom-quark dipole operator appearing in (7.2), we consider the following effective interactions

$$\mathcal{L}_{\text{eff}} \supset -\tilde{d}_b(m_h) \frac{i g_s(m_h)}{2} \bar{b} \sigma_{\mu\nu} T^a \gamma_5 b \, G^{a,\mu\nu} - w(m_h) \frac{1}{3} f^{abc} G^a_{\mu\sigma} G^{b,\sigma}_\nu \widetilde{G}^{c,\mu\nu} \,, \qquad (7.26)$$

where $\widetilde{G}^{a,\mu\nu} = 1/2 \, \epsilon^{\mu\nu\alpha\beta} G^a_{\alpha\beta}$ is the dual field-strength tensor of QCD with $\epsilon^{\mu\nu\alpha\beta}$ the fully antisymmetric Levi-Civita tensor ($\epsilon^{0123} = 1$).

In the presence of the two dimension-six SMEFT operators (7.2) the initial condition $\tilde{d}_b(m_h)$ of the bottom-quark chromoelectric dipole moment is given by

$$\tilde{d}_b(m_h) = -\frac{\sqrt{2}v}{\Lambda^2} \text{Im}\left(C_{bG}\right) \,, \qquad (7.27)$$

while the initial condition $w(m_h)$ of the Weinberg operator [406] vanishes. The bottom-quark chromoelectric dipole moment has the following QCD running

$$\tilde{d}_b(m_b) = \left(\frac{\alpha_s(m_h)}{\alpha_s(m_b)}\right)^{\frac{\gamma_{\tilde{d}}}{2\gamma_{\alpha_s}}} \tilde{d}_b(m_h) \,, \qquad (7.28)$$

where $\gamma_{\alpha_s}$ denotes the LO anomalous dimension (or beta function) of the strong coupling constant and $\gamma_{\tilde{d}}$ is the LO anomalous dimension of the bottom-quark chromoelectric dipole moment. Explicitly, one has

$$\gamma_{\alpha_s} = 11 - \frac{2}{3} N_f \,, \qquad \gamma_{\tilde{d}} = \frac{4}{3} \,, \qquad (7.29)$$

where the expression for $\gamma_{\alpha_s}$ can be found in any textbook on QCD and the result for $\gamma_{\tilde{d}}$ has first been presented in [407]. Notice that in (7.28) the number of active flavours is $N_f = 5$ and that one could in principle resum large logarithms in the latter equation up to the next-to-next-to-leading logarithmic level because the self-mixing of the dipole operators is known up to the three-loop order [408]. Given the sizeable uncertainties of the hadronic matrix elements of the Weinberg operator and the chromoelectric dipole operators of light quarks $\left(cf.\right.$ the discussion before (7.33)$\left.\right)$ using only the leading-logarithmic (LL) result (7.28) is however fully justified.

At the bottom-quark mass threshold one integrates out the bottom quark. The corresponding Feynman diagrams are shown in Figure 7.8. This gives a finite matching

correction to the Weinberg operator [409–411]

$$\delta w(m_b) = \frac{g_s^3(m_b)}{32\pi^2} \frac{\tilde{d}_b(m_b)}{\bar{m}_b(m_b)} \, . \tag{7.30}$$

Between the bottom-mass scale and the hadronic scale $\mu_H \simeq 1 \, \text{GeV}$ the Weinberg operator mixes into itself and into the chromoelectric and electric dipole operators involving up and down quarks. As it turns out, the contributions from electric dipole operators are numerically very small and we thus neglect it in what follows. The LO anomalous dimensions describing the self-mixing of the Weinberg operator and the mixing of the Weinberg operator in the chromoelectric dipole operators, respectively, are [410, 412, 413]

$$\gamma_w = 3 + 2N_f \, , \qquad \gamma_{w\tilde{d}} = -6 \, . \tag{7.31}$$

Resumming LL corrections in the four- and the three-flavour theory, we obtain

$$w(\mu_H) \simeq 0.71 \, \delta w(m_b) \, , \qquad \tilde{d}_q(\mu_H) \simeq 0.14 \, \bar{m}_q(\mu_H) \, \delta w(m_b) \, , \tag{7.32}$$

where $q = u, d$. The numerical factors in (7.32) correspond to the following values $\alpha_s(m_b) \simeq 0.21$, $\alpha_s(m_c) \simeq 0.32$ and $\alpha_s(\mu_H) \simeq 0.36$ of the QCD coupling constant.

Estimates of the hadronic matrix elements of the Weinberg operator and the chromomagnetic dipole operators of the up and down quark are presently plagued by uncertainties of $50\%$ — see for instance [384, 414–420]. Adopting the QCD sum-rule estimates [414, 418] for the relevant hadronic matrix elements and employing $\bar{m}_u(\mu_H) \simeq 2.5 \cdot 10^{-3} \, \text{GeV}$ and $\bar{m}_d(\mu_H) \simeq 5.4 \cdot 10^{-3} \, \text{GeV}$ [23], the nEDM can be written as

$$\frac{d_n}{e} \simeq \left( -1.77 \, (1 \pm 0.5) + 0.10 \, (1 \pm 0.5) \right) \cdot 10^{-2} \, \text{GeV} \, \delta w(m_b) \, , \tag{7.33}$$

where the first and the second term corresponds to the contribution from the Weinberg operator and the chromomagnetic dipole operators, respectively. Combining the above uncertainties in such a way that our prediction provides a lower absolute limit on the actual size of the $\mathcal{O}_{bG}$ correction to the nEDM, we find

$$\left| \frac{d_n}{e} \right| \simeq 1.5 \cdot 10^{-22} \, \text{cm} \left( \frac{1 \, \text{TeV}}{\Lambda} \right)^2 \left| \text{Im} \left( C_{bG} \right) \right| \, . \tag{7.34}$$

Here we have employed $\alpha_s(m_h) \simeq 0.11$ and $\bar{m}_b(m_b) \simeq 4.2 \, \text{GeV}$ [23] to obtain the numerical result. The current best experimental nEDM result [421] imposes the following $90\%$ CL bound

$$\left| \frac{d_n}{e} \right| < 1.8 \cdot 10^{-26} \, \text{cm} \, . \tag{7.35}$$

From (7.34) and (7.35) it follows that

$$\frac{\left| \text{Im} \left( C_{bG} \right) \right|}{\Lambda^2} < \left( \frac{1}{90 \, \text{TeV}} \right)^2 \, . \tag{7.36}$$

In the case of the charm-quark dipole operator entering (7.2), the derivation of the bound on the imaginary part of $C_{cG}$ follows the steps described above with minor modifications. The first modification is that from the initial scale $m_h$ the charm-quark chromomagnetic dipole moment $\tilde{d}_c$ runs to the charm-quark threshold $m_c$ in the five-

| Observable | Wilson coefficient | 95% CL bound | Scale |
|---|---|---|---|
| Dijet angular distributions | $\left\|C_{bG}\right\|, \left\|C_{cG}\right\|$ | 6.8 | $380\,\text{GeV}$ |
| Two $b$-tagged jets | $\left\|C_{bG}\right\|$ | 0.36 | $1.6\,\text{TeV}$ |
| $Z$-boson production with two $b$-jets | $\left\|C_{bG}\right\|$ | 1.04 | $980\,\text{GeV}$ |
| Inclusive radiative $B$ decay | $\left\|\text{Re}\left(C_{cG}\right)\right\|$ | 1600 | $25\,\text{GeV}$ |
| Searches for nEDM | $\left\|\text{Im}\left(C_{bG}\right)\right\|$ | $1.2 \cdot 10^{-4}$ | $90\,\text{TeV}$ |
| Searches for nEDM | $\left\|\text{Im}\left(C_{cG}\right)\right\|$ | $1.3 \cdot 10^{-5}$ | $275\,\text{TeV}$ |

**Table 7.1:** Summary of the constraints on the Wilson coefficients of the operators $\mathcal{O}_{bG}$ and $\mathcal{O}_{cG}$ derived in this thesis. The given 95% CL bounds correspond to $\Lambda = 1\,\text{TeV}$, while the numbers quoted for the suppression scale assume a purely real or imaginary Wilson coefficient with a magnitude of 1. See text for further explanations.

and four-flavour theory. Second the renormalisation group flow below $m_c$ where the Weinberg operator is generated — see (7.30) — proceeds only in the three-flavour theory, leading to

$$w(\mu_H) \simeq 0.94\,\delta w(m_c)\,, \qquad \tilde{d}_q(\mu_H) \simeq 0.04\,\bar{m}_q(\mu_H)\,\delta w(m_c)\,. \qquad (7.37)$$

Notice that given the smaller scale separation between $m_c$ and $\mu_H$ compared to $m_b$ and $\mu_H$ the renormalisation group effects in (7.37) are notably smaller than those in (7.32). Instead of (7.33) one then finds the following expression

$$\frac{d_n}{e} \simeq \big( -2.34\,(1 \pm 0.5) + 0.03\,(1 \pm 0.5) \big) \cdot 10^{-2}\,\text{GeV}\,\delta w(m_c)\,, \qquad (7.38)$$

which is fully dominated by the contribution from the Weinberg operator. This leads to

$$\left|\frac{d_n}{e}\right| \simeq 1.4 \cdot 10^{-21}\,\text{cm} \left(\frac{1\,\text{TeV}}{\Lambda}\right)^2 \left|\text{Im}\left(C_{cG}\right)\right|\,, \qquad (7.39)$$

where we have used $\bar{m}_c(m_c) \simeq 1.3\,\text{GeV}$ [23]. Combining (7.35) and (7.39) we finally obtain

$$\frac{\left|\text{Im}\left(C_{cG}\right)\right|}{\Lambda^2} < \left(\frac{1}{275\,\text{TeV}}\right)^2\,. \qquad (7.40)$$

## 7.3 Discussion

In Table 7.1 we summarise the limits on the Wilson coefficients of the operators $\mathcal{O}_{bG}$ and $\mathcal{O}_{cG}$ that we have derived in this section, while summarising the existing HL-LHC projected limits from Higgs physics in Table 7.2. Let us first discuss the the former bounds. For what concerns the magnitudes of $C_{bG}$ and $C_{cG}$, one sees that searches for dijets final states provide bounds on the Wilson coefficients of order one assuming a suppression scale $\Lambda$ of $1\,\text{TeV}$. In fact, the nominal strongest limit derives at present from the ATLAS search for $b$-jet pairs performed in [346]. This search probes dijet invariant masses in the range $1133\,\text{GeV} < M_{jj} < 4595\,\text{GeV}$, which pushes the Wilson coefficient to $\left|C_{bG}\right| \gtrsim 4\pi$, if one requires $\Lambda \gtrsim 5\,\text{TeV}$ to cover the whole

| Process | Wilson coefficient | $2\sigma$ bound | Scale |
|---------|--------------------|-----------------|-------|
| $pp \to b\bar{b}h$ [323] | $\mathrm{Re}\left(C_{bG}\right)$ | $[-1.2, 1.9]$ | $810\,\mathrm{GeV}$ |
|  | $\left|\mathrm{Im}\left(C_{bG}\right)\right|$ | $1.5$ | $730\,\mathrm{GeV}$ |
| $pp \to b\bar{b}h \to b\bar{b}\gamma\gamma$ [334] | $\left|C_{bG}\right|$ | $0.17$ | $2.4\,\mathrm{TeV}$ |
| $pp \to h$ [323] | $\mathrm{Re}\left(C_{cG}\right)$ | $[-14.2, 14.7]$ | $260\,\mathrm{GeV}$ |
|  | $\left|\mathrm{Im}\left(C_{cG}\right)\right|$ | $14.4$ | $260\,\mathrm{GeV}$ |

**Table 7.2:** Summary of the constraints on the Wilson coefficients of the operators $\mathcal{O}_{bG}$ and $\mathcal{O}_{cG}$ from Higgs physics at HL-LHC with $\sqrt{s} = 14$ TeV and 3 ab$^{-1}$ of integrated luminosity, derived in [323, 334]. The given $2\sigma$ bounds correspond to $\Lambda = 1$ TeV, while the numbers quoted for the suppression scale assume a Wilson coefficient with a magnitude of 1. See the main text for further details.

range of tested jet-jet invariant masses. Similar statements apply to the constraints following from the CMS measurement of the dijet angular distributions [345]. On general grounds, the limits (7.15) and (7.17) therefore only constrain strongly-coupled UV completions — for related discussions of the applicability of the SMEFT to dijet searches see [339–344]. The situation is better in the case of the bound on $C_{bG}$ that we have derived from the recent ATLAS measurement [367] of $pp \to b\bar{b}\,Z/\gamma^* \to b\bar{b}\,\ell^+\ell^-$, because the energy scales tested by this measurement are all below 1 TeV. Notice that $pp \to b\bar{b}\,Z/\gamma^* \to b\bar{b}\,\ell^+\ell^-$ measurements are systematically limited at the LHC but the prospects of reducing the systematic uncertainties due to an improved theoretical understanding are quite good (*cf.* [369]). These two features taken together make $Z$-boson production in association with $b$-jets in our opinion a key process to search and to constrain the chromomagnetic bottom-quark dipole operator at upcoming LHC runs. Furthermore, as can be learnt from Table 7.1 as well as the discussion at the end of Section 7.2.4, flavour physics does not provide a meaningful bound on either the operator $\mathcal{O}_{bG}$ or the operator $\mathcal{O}_{cG}$.

From Table 7.1 it is also clear that in contrast to $\left|C_{bG}\right|$ and $\left|C_{cG}\right|$, the imaginary parts of both Wilson coefficients are severely constrained by searches for a nEDM. In the case of a purely imaginary Wilson coefficient $C_{bG}$ ($C_{cG}$) of 1, scales as high as $90\,\mathrm{TeV}$ ($275\,\mathrm{TeV}$) are excluded at 90% CL by these indirect searches. Notice that in weakly-coupled UV complete theories the Wilson coefficients of chromodipole operators are typically both Yukawa- and loop-suppressed — see [166] for a more detailed discussion of this point. Assuming that $C_{bG} = y_b/(4\pi)^2$ and $C_{cG} = y_c/(4\pi)^2$ the bounds (7.36) and (7.40) imply $\Lambda > 960\,\mathrm{GeV}$ and $\Lambda > 1.5\,\mathrm{TeV}$, respectively. This numerical example shows that nEDM searches, unlike the studied collider constraints, are able to test weakly-coupled TeV-scale new-physics models. Making effects of bottom-quark and charm-quark chromodipole operators observable at the LHC therefore generically requires a mechanism that suppresses new sources of CP-violation beyond the SM.

A direct comparison of the collider limits shown in Table 7.1 and Table 7.2 is not fully justified since they correspond to different colliders (a 13 TeV machine with 35.6 fb$^{-1}$ of integrated luminosity versus the HL-LHC at 14 TeV with 3 ab$^{-1}$). However, some general remarks are in order. We observe that the best collider constraints are obtained by *pressing the b-tagging button*, where $pp \to b\bar{b}\,Z/\gamma^* \to b\bar{b}\,\ell^+\ell^-$ and $pp \to b\bar{b}h \to b\bar{b}\gamma\gamma$

can play a crucial role in constraining $\mathcal{O}_{bG}$ in the future. This further emphasizes that due to the non-factorisable nature of the corrections involving $\mathcal{O}_{bG}$, exploiting differential LHC data seems a worthwhile exercise, a point which is also made in [166, 334]. In fact, it might also be possible to constrain $\mathcal{O}_{bG}$ at future lepton colliders through an analysis of event-shape variables in $h \to b\bar{b}$ — see for instance [422]. Finally, we add that a generic UV theory will most likely produce a set of higher-dimensional operators, rather than $\mathcal{O}_{bG}$ or $\mathcal{O}_{cG}$ alone. However, the unique kinematic structures in differential observables due to the chromodipole operators would presumably remain unchanged, motivating their further study not only now but also at future LHC runs.

# Chapter 8

# Higgs portals

The discovery of a new fundamental scalar particle [1, 2] has opened up many new avenues in the pursuit of physics beyond the SM, as we have seen for instance in Chapters 6 and 7. There, we parametrised possible BSM effects via effective operators within the framework of the SMEFT, allowing generally for rather model-independent constraints on their associated Wilson coefficients. There are indeed both experimental and theoretical arguments that suggest that the Higgs boson may provide a window into BSM physics. It was already mentioned in Chapter 6 that experimentally the Higgs sector is far less explored and constrained compared to the gauge or fermionic sector of the SM [24, 423]. Theoretically, the SM Higgs doublet $H$ plays a special role not only in BSM searches framed within the SMEFT, but also because it allows to write down relevant and marginal operators of the form $|H|^2 \mathcal{O}$ with $\mathcal{O}$ itself a gauge-invariant operator with a mass dimension of two or lower. Interactions of the latter type, since they provide a unique window into an otherwise hidden sector, are commonly referred to as Higgs portals.

This chapter is structured as follows. After a short motivation in Section 8.1, we investigate in Section 8.2 the sensitivity of future hadron collider measurements of off-shell Higgs production in the $pp \to ZZ \to 4\ell$ channel to Higgs portal interactions of the form mentioned above. In Section 8.3, we compare our main results of Section 8.2 to the limits one expects to obtain from other single- and double-Higgs probes, and provide a short outlook. A discussion of the impact that different assumptions on the systematic uncertainties in our ME-based search strategy have on the projected constraints is relegated to Appendix D, while further details of the relevant loop calculations and their implementation in the MC code for our double-Higgs analysis are given in Appendix E.

## 8.1 Motivation

The simplest and most studied case of an operator of the form $|H|^2 \mathcal{O}$ is the case where $\mathcal{O} = \phi^2$, with $\phi$ begin a real scalar that is a singlet under the SM gauge group but odd under a $\mathbb{Z}_2$ symmetry [424–428]. The corresponding interaction Lagrangian reads

$$\mathcal{L}_{H\phi} = -c_\phi |H|^2 \phi^2 \,. \tag{8.1}$$

Notice that the $\mathbb{Z}_2$ symmetry acts on the real scalar field as $\phi \to -\phi$, which guarantees the stability of $\phi$ making it a suitable dark DM candidate. See for instance [429–431]

for recent reviews of the ensuing DM phenomenology. In particular, under the assumption that $\phi$ is a relic of standard thermal freeze-out production DM direct detection experiments are known to foster stringent constraints on DM portals of the form (8.1) — see for example [431] and references therein. In theories with a non-thermal cosmological history, a real scalar $\phi$ can however be shown to be a viable DM candidate for a wide range of Higgs portal realisations while evading existing experimental limits [432]. This opens up the possibility to probe (8.1) at high-energy colliders.

Another motivation for the existence of sizeable Higgs portal couplings to $|H|^2$ is provided by the hierarchy problem of the Higgs-boson mass. In fact, in models where the hierarchy problem is addressed by the addition of $N_r$ real scalar top partners $\phi_i$ the relevant interaction Lagrangian can be written as [256]

$$\mathcal{L}_{H\phi_i} = -\frac{2N_c}{N_r}\, y_t^2 \, |H|^2 \sum_{i=1}^{N_r} \phi_i^2 \,, \tag{8.2}$$

where $N_c = 3$ is the number of colours in QCD and $y_t = \sqrt{2} m_t/v \simeq 0.94$ is the top-quark Yukawa coupling with $m_t \simeq 163\,\text{GeV}$ the top-quark $\overline{\text{MS}}$ mass. Well-known cases where (8.2) is a proxy for the resulting Higgs portal interactions are stops in the minimal supersymmetric SM (MSSM) and singlet scalar top partners in the hyperbolic Higgs [433] or tripled top model [434], if one assumes that these particles are approximately degenerate in mass. Notice that in such a case the interactions (8.1) and (8.2) are equivalent from the perspective of collider phenomenology if $|c_\phi| = 2N_c/\sqrt{N_r}\, y_t^2$. In the case of the MSSM, the hyperbolic Higgs and the tripled top model where $N_r = 12$, a light Higgs boson is therefore natural if one effectively has a Higgs portal of the form (8.1) with coupling strength $|c_\phi| \leq \sqrt{3}\, y_t^2 \simeq 1.5$.

## 8.2 Higgs portal effects in $gg \to h^* \to ZZ$

The level of difficulty to discover or to exclude Higgs portals of the form (8.1) and (8.2) at high-energy colliders depends mainly on the mass $m_\phi$ of the new states that couple to $|H|^2$. While in the case of $m_\phi < m_h/2 \simeq 62.5\,\text{GeV}$ the decays of the Higgs boson into invisible [435–439] or undetected [423, 431] final states provide stringent constraints on the effective coupling strength of the Higgs portals, obtaining relevant constraints above the kinematic threshold $m_\phi > m_h/2$ turns out to be significantly more challenging. In fact, only two categories of collider measurements are known that provide sensitivity to Higgs portals above the kinematic threshold: firstly, pair-production of the new scalars in off-shell Higgs processes such as the VBF, the $t\bar{t}h$ and the ggF channel [321, 322, 440–450], and secondly, studies of the virtual effects that these particles produce when exchanged in loop diagrams that contribute to processes such as associated $Zh$, double-Higgs and $gg \to h^* \to ZZ$ production [302, 303, 451–455]. The existing analyses have considered a wide range of future high-energy hadron as well as lepton colliders, including the HL-LHC, HE-LHC, FCC, the International Linear Collider (ILC), the Compact Linear Collider (CLIC) and a muon collider.

In this section, we investigate the sensitivity of future hadron collider measurements of off-shell Higgs production in the $pp \to ZZ \to 4\ell$ channel to Higgs portal interactions such as (8.1) and (8.2). Compared to earlier studies of this Higgs production

process [302, 303, 449] that relied on the four-lepton invariant mass ($m_{4\ell}$) spectrum alone to separate signal from background, we instead employ a ME based kinematic discriminant in our work. Being sensitive not only to $m_{4\ell}$ but also to another seven variables such as the invariant masses of the two opposite-sign lepton pairs (for details consult the articles [306–308]), ME-based discriminants fully exploit the event kinematics. As in our recent study [43], we find that the use of a ME method leads to a significantly improved coverage of the BSM parameter space, *i.e.* $c_\phi$ and $m_\phi$ in the case of (8.1), than a shape analysis of the $m_{4\ell}$ distribution. Motivated by this finding, we analyse in detail the HL-LHC, HE-LHC and FCC potential of the proposed method in constraining BSM physics that couples to the operator $|H|^2$. In Section 8.2.1 we briefly discuss the calculation of the loop corrections to $pp \to ZZ \to 4\ell$ production arising from (8.1). The MC implementation and aforementioned ME-based kinematic discriminant are discussed in Section 8.2.2 where we also explain how higher-order QCD corrections are taken into account in our study. The numerical analysis of the HL-LHC reach is performed in Section 8.2.3 and contains a comparison between the sensitivities obtained from a shape analysis of the $m_{4\ell}$ spectrum and the proposed ME method. Finally, in Section 8.2.4 we present our HE-LHC and FCC projections.

### 8.2.1 Description of the calculation

At the one-loop level the $gg \to h^* \to ZZ$ process receives contributions from Feynman graphs such as the one displayed in Figure 8.1 that contains a modified Higgs propagator with insertions of the Higgs portal operator (8.1). The corresponding renormalised contribution to the self-energy of the Higgs takes the form

$$\hat{\Sigma}(\hat{s}) = \Sigma(\hat{s}) + \left(\hat{s} - m_h^2\right)\delta Z_h - \delta m_h^2 \,, \tag{8.3}$$

where the bare Higgs self-energy, the one-loop corrections to the Higgs wave function and the mass counterterm in the on-shell scheme are given by the following expressions

$$\Sigma(\hat{s}) = \frac{1}{(4\pi)^2}\left[c_\phi A_0(m_\phi^2) + 2v^2|c_\phi|^2 B_0\left(\hat{s}, m_\phi^2, m_\phi^2\right)\right],$$

$$\delta Z_h = -\frac{2v^2|c_\phi|^2}{(4\pi)^2}\frac{d}{d\hat{s}}B_0\left(\hat{s}, m_\phi^2, m_\phi^2\right)\bigg|_{\hat{s}=m_h^2}, \tag{8.4}$$

$$\delta m_h^2 = \frac{1}{(4\pi)^2}\left[c_\phi A_0(m_\phi^2) + 2v^2|c_\phi|^2 B_0\left(m_h^2, m_\phi^2, m_\phi^2\right)\right].$$

Here $\hat{s} = p^2$ with $p$ the external four-momentum entering the Higgs propagator and the $A_0$ and $B_0$ functions are one- and two-point Passarino-Veltman scalar integrals defined as in [290, 456]. The expression in (8.4) can be easily generalised to other Higgs portals of the form (8.1). For instance, in the case of $\mathcal{L}_{H\Phi} = -c_\Phi |H|^2|\Phi|^2$ with $\Phi$ a complex scalar field one just has to make the substitutions $c_\phi \to c_\Phi/\sqrt{2}$ and $m_\phi \to m_\Phi$.

Notice that the contribution to the Higgs wave-function renormalisation constant $\delta Z_h$ coming from the propagator corrections exactly cancels against those of the vertices when combined to obtain the full BSM contribution to the off-shell $gg \to h^* \to ZZ$ amplitude. Similarly, the tadpole contribution proportional to $A_0(m_\phi^2)$ also cancels
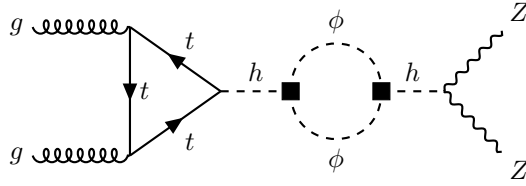
**Figure 8.1:** Example of a one-loop correction to $gg \to h^* \to ZZ$ production with insertions of the Higgs portal operator (8.1) indicated by the black boxes. Also diagrams with tadpoles or counterterms contribute but are not shown explicitly. Consult the main text for further details.

in the difference $\Sigma(\hat{s}) - \delta m_h^2$. In contrast, the Higgs wave-function renormalisation constant $\delta Z_h$ does not drop out in the on-shell Higgs signal strengths $\mu_i^f$ for production in channel $i$ and decay in channel $f$. In terms of the inclusive Higgs production cross sections $\sigma_i$ and the Higgs branching ratios $\mathrm{BR}_f$, these quantities take the form

$$\mu_i^f = \frac{\sigma_i}{\sigma_i^{\mathrm{SM}}} \frac{\mathrm{BR}_f}{\mathrm{BR}_f^{\mathrm{SM}}} = 1 + \delta Z_h \,, \tag{8.5}$$

*i.e.* they receive a universal correction proportional to the Higgs wave-function renormalisation constant as given in (8.4). This feature allows to set indirect constraints on Higgs portal models by precision measurements of Higgs properties [452], which will be discussed in Section 8.3.

### 8.2.2 MC implementation

The Higgs propagator corrections (8.3) and the relevant vertex counterterms have been implemented into version 8.0 of the event generator `MCFM` [291] to obtain kinematic distributions for $pp \to ZZ \to 4\ell$ such as the $m_{4\ell}$ spectrum. In addition, our MC code is also able to calculate the following ME-based kinematic discriminant $\big(cf.\ (6.28)\big)$

$$D_S = \log_{10}\left(\frac{P_h}{P_{gg} + c \cdot P_{q\bar{q}}}\right). \tag{8.6}$$

Here $P_h$ denotes the squared ME for the $gg \to h^* \to ZZ \to 4\ell$ process, $P_{gg}$ is the squared ME for all $gg$-initiated channels (including the Higgs channel, the continuum background and their interference) and $P_{q\bar{q}}$ is the squared ME for the $q\bar{q} \to ZZ \to 4\ell$ process. Like in [293, 296, 298] the constant $c$ is set to 0.1 to balance the $q\bar{q}$- and $gg$-initiated contributions. We stress that in the SM more than 99% of the $pp \to ZZ \to 4\ell$ cross section falls into the range of $-4.5 < D_S < 0.5$ [293]. For BSM models that predict events with $D_S < -4.5$ or $D_S > 0.5$ the variable $D_S$ therefore presents a null test.

Currently, calculations of higher-order QCD corrections to four-lepton production via $q\bar{q}$ annihilation include the full NNLO corrections and top-quark mass effects [79–82]. NLO corrections to the loop-induced $gg$ channel have been computed by now as well [172, 212–214], while for inclusive Higgs production the precision has been pushed to the N³LO in the heavy top-quark limit [313]. As the $gg \to ZZ$ process starts

contributing only at $\mathcal{O}(\alpha_s^2)$, it is part of the NNLO QCD corrections to $ZZ$ production and NLO corrections to this channel formally contribute at N$^3$LO. Lastly, NLO EW corrections could in principle play an important role as well. Within the SM they were combined with NNLO QCD effects for $ZZ$ production in the work [457]. However, it has been shown in the paper [277] that including NLO EW effects in the SM has only a very minor effect on the sensitivity of indirect single-Higgs analyses to modifications of the trilinear Higgs coupling. We expect a similar pattern to arise in the context of the Higgs portal models studied here. A dedicated simulation of four-lepton events including both higher-order QCD as well as EW corrections both in and beyond the SM, consistently matched to a parton shower and including detector effects is clearly beyond the scope of the present article and therefore left for future work.

In order to include higher-order QCD corrections in our $pp \to ZZ \to 4\ell$ analysis, we proceed along the lines of Section 6.2.2.2 — see also [43]. For the two relevant production channels we calculate the so-called $K$-factor defined as the ratio between the fiducial cross section at a given order in QCD and the corresponding LO QCD prediction. In the case of the $gg$-initiated contribution we utilise the results of [44]. The ratio between the NLO and LO ggF predictions turns out to be essentially flat in $m_{4\ell}$ and by averaging we find $K_{gg}^{\mathrm{NLO}} = 1.83$. This number agrees with the $K$-factors reported in [172, 212, 214]. In the case of the $q\bar{q}$-initiated contribution we use the NNLO results obtained in [214]. The relevant $K$-factor again turns out to be basically flat in $m_{4\ell}$ with a central value of $K_{q\bar{q}}^{\mathrm{NNLO}} = 1.55$. This finding is in accordance with [79]. The quoted $K$-factors are then used to obtain a QCD-improved prediction for the $pp \to ZZ \to 4\ell$ cross section differential in the variable $O$ as follows $\big(cf.\ (6.29)\big)$:

$$\frac{d\sigma_{pp}}{dO} = K_{gg}^{\mathrm{NLO}} \left(\frac{d\sigma_{gg}}{dO}\right)_{\mathrm{LO}} + K_{q\bar{q}}^{\mathrm{NNLO}} \left(\frac{d\sigma_{q\bar{q}}}{dO}\right)_{\mathrm{LO}}. \tag{8.7}$$

Notice that (8.7) is accurate in the case of the $m_{4\ell}$ spectrum. For the $D_S$ distribution one observes [43] a close to flat $K$-factor of around 1.6 between the LO and the improved prediction (8.7). It is furthermore found that the inclusion of higher-order QCD corrections reduces the scale uncertainties by a factor of about 3 from $(7-8)\%$ to $(2-3)\%$. The fact that the central value of the improved $D_S$ spectrum lies outside the LO uncertainty bands demonstrates that the scale variations of (8.7) do not provide a reliable way to estimate the size of higher-order QCD effects. In view of this and given that the discriminant $D_S$ as defined in (8.6) is only LO accurate, we will make different assumptions on the systematic uncertainties entering our ME-based search strategy, a point we will discuss in more detail in our numerical analyses presented in Sections 8.2.3 and 8.2.4 as well as in Appendix D. A similar approach is also used in the projections [294, 295] that estimate the HL-LHC reach in constraining off-shell Higgs boson production and the Higgs boson total width in $pp \to ZZ \to 4\ell$.

### 8.2.3 HL-LHC analysis

In our $pp \to ZZ \to 4\ell$ analysis we consider the window $140\,\mathrm{GeV} < m_{4\ell} < 600\,\mathrm{GeV}$ of four-lepton invariant masses. The charged leptons are required to be in the pseudo-rapidity range $|\eta_\ell| < 2.5$ and the lepton with the highest transverse momentum $(p_T)$ must satisfy $p_{T,\ell_1} > 20\,\mathrm{GeV}$ while the second, third and fourth lepton in $p_T$ order is required to obey $p_{T,\ell_2} > 15\,\mathrm{GeV}$, $p_{T,\ell_3} > 10\,\mathrm{GeV}$ and $p_{T,\ell_4} > 6\,\mathrm{GeV}$, respectively. The
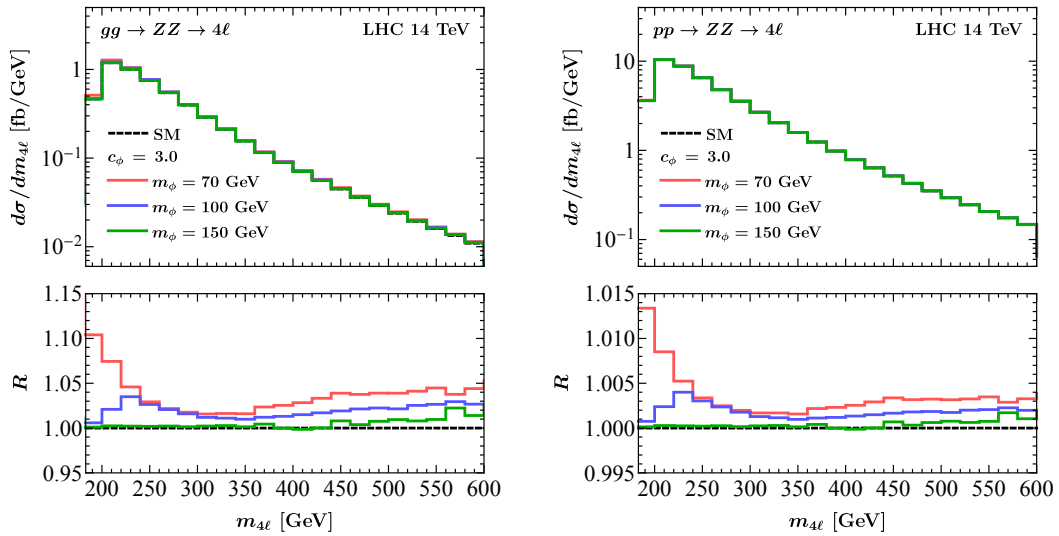
**Figure 8.2:** $m_{4\ell}$ spectra in the SM (dashed black) as well as for three Higgs portal model scenarios (8.1) assuming $c_\phi = 3$ and $m_\phi = 70\,\text{GeV}$ (solid red), $m_\phi = 100\,\text{GeV}$ (solid blue) and $m_\phi = 150\,\text{GeV}$ (solid green). The left (right) plot shows results for $gg \to ZZ \to 4\ell$ ($pp \to ZZ \to 4\ell$) production. All distributions correspond to QCD-improved predictions and LHC collisions at a centre-of-mass energy of $\sqrt{s} = 14\,\text{TeV}$. The lower panels depict the ratios between the BSM distributions and the corresponding SM predictions.

lepton pair with the mass closest to the $Z$-boson mass is referred to as the leading dilepton pair and its invariant mass is required to be within $50\,\text{GeV} < m_{12} < 106\,\text{GeV}$, while the subleading lepton pair must be in the range of $50\,\text{GeV} < m_{34} < 115\,\text{GeV}$. Notice that the ATLAS and CMS analyses [292–298] employ similar cuts. We assume a detection efficiency of 99% (95%) for muons (electrons) that satisfy the event selections. These efficiencies correspond to those reported in the latest ATLAS analysis of off-shell Higgs production [298]. As input parameters we use $G_F = 1/(\sqrt{2}v^2) = 1.16639 \cdot 10^{-5}\,\text{GeV}^{-2}$, $m_Z = 91.1876$ GeV, $m_h = 125\,\text{GeV}$ and $m_t = 173\,\text{GeV}$. We employ `NNPDF40_nlo_as_01180` parton distribution functions (PDFs) [299] with the renormalisation and factorisation scales $\mu_R$ and $\mu_F$ set to $m_{4\ell}$ on an event-by-event basis. Both the different-flavour $e^+e^-\mu^+\mu^-$ and the same-flavour $2e^+2e^-$ and $2\mu^+2\mu^-$ decay channels of the two $Z$ bosons are included throughout our work.

In Figure 8.2 we show our predictions for the $m_{4\ell}$ distributions in the SM (dashed black) and three Higgs portal models (8.1). The displayed BSM benchmarks correspond to scalar masses of $m_\phi = 70\,\text{GeV}$ (solid red), $m_\phi = 100\,\text{GeV}$ (solid blue) and $m_\phi = 150\,\text{GeV}$ (solid green) assuming in all cases a coupling strength of $c_\phi = 3$. Notice that the chosen value of $c_\phi$ is safely below the limit $|c_\phi| < 4\pi$ following from perturbative tree-level unitarity (see for instance [449]). In the left panel the QCD-improved predictions for $gg \to ZZ \to 4\ell$ production including the Higgs signal, the continuum background and their interference are given. Two features of the shown BSM spectra deserve a further discussion. First, one observes peak-like structures in the distributions slightly above the threshold $m_{4\ell} = 2m_\phi$ of two-scalar production. Second, both spectra show an enhancement at large $m_{4\ell}$ because in the limit of partonic centre-of-mass energies $\hat{s} \to \infty$ the correction simplifies to $\Sigma(\hat{s}) - \delta m_h^2 \simeq -v^2|c_\phi|^2/(8\pi^2)\ln\left(\hat{s}/m_h^2\right)$.
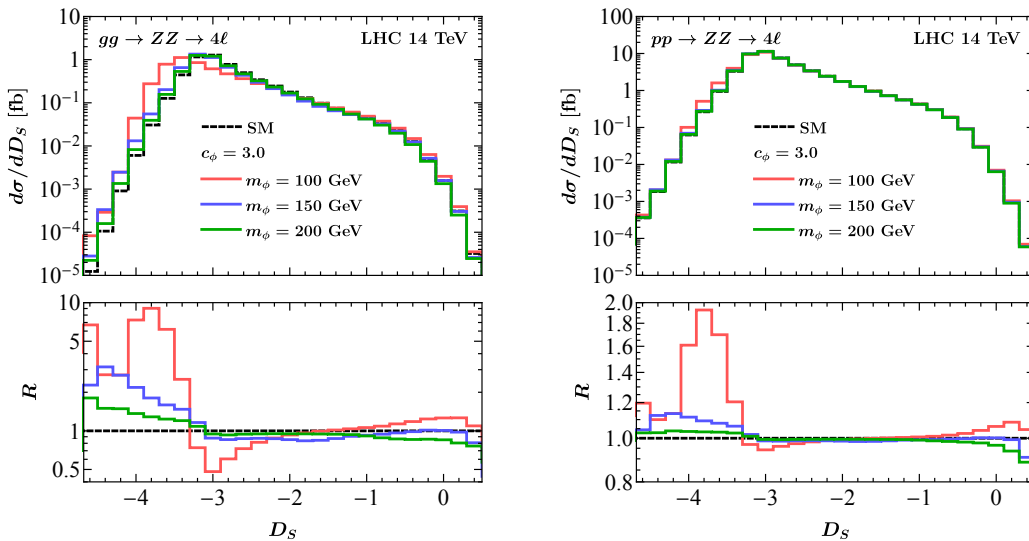
**Figure 8.3:** As Figure 8.2 but for the QCD-improved ME-based discriminant $D_S$ as defined in (8.6) and (8.7). Furthermore, instead of $m_\phi = 70\,\text{GeV}$ a mass of $m_\phi = 200\,\text{GeV}$ is employed. For additional explanations see main text.

This behaviour is easily derived from (8.4). Notice furthermore that the $gg \to h^* \to ZZ \to 4\ell$ amplitudes interfere destructively with the $gg \to ZZ \to 4\ell$ matrix elements so that the overall sign of the correction $\Sigma(\hat{s}) - \delta m_h^2$ is effectively flipped. One also sees that for the three chosen sets of Higgs portal parameters the relative corrections in the spectra amount to less than 15% over the whole range of $m_{4\ell}$ values of interest. The same features are also observed in the right panel of Figure 8.2 which shows the corresponding predictions for $pp \to ZZ \to 4\ell$ production. Notice that in this case the relative modification are smaller by a factor of roughly 10 than for $gg \to ZZ \to 4\ell$ due to the addition of the $q\bar{q} \to ZZ \to 4\ell$ channel which receives no BSM correction.

To illustrate the discriminating power of the ME-based kinematic variable introduced in (8.6) we present in Figure 8.3 the results for the $D_S$ spectra in the SM and beyond. The shown predictions have been obtained by means of (8.7) and the choices for the Higgs portal model parameters are those from before, apart from $m_\phi = 70\,\text{GeV}$ which is replaced by $m_\phi = 200\,\text{GeV}$. One observes that compared to the SM spectrum the BSM distributions are shifted to lower values of $D_S$. This is a simple consequence of the fact that the correction $\Sigma(\hat{s}) - \delta m_h^2$ tends to reduce the $gg \to h^* \to ZZ \to 4\ell$ amplitude and thus $P_h$ in (8.6). As a result of the sharp cut-off of the SM distribution at $D_S \simeq -3.5$, the relative BSM effects in the $D_S$ spectra for $gg \to ZZ \to 4\ell$ turn out to be large, easily exceeding 100% for the chosen benchmark values of $c_\phi$ and $m_\phi$. As illustrated in the right panel of Figure 8.3, adding the $q\bar{q} \to ZZ \to 4\ell$ channel to the predictions for the $D_S$ distributions notably reduces the relative size of the Higgs portal corrections. Still assuming $c_\phi = 3$, the BSM effects reach the level of around 200%, 10% and 5% in the case of $m_\phi = 100\,\text{GeV}$, $m_\phi = 150\,\text{GeV}$ and $m_\phi = 200\,\text{GeV}$, respectively.

By comparing the relative modifications in the right panels of Figures 8.2 and 8.3 it should be already clear that the four-lepton invariant mass $m_{4\ell}$ has a much weaker dis-

criminating power than the variable $D_S$ in constraining interactions of the form (8.1). In order to make this statement quantitative we perform a shape analysis of both the $m_{4\ell}$ and $D_S$ spectrum following the method outlined in Section 6.2.2.3. Specifically, the significance $Z_i$ is calculated as a Poisson ratio of likelihoods modified to incorporate systematic uncertainties on the background using the Asimov approximation [317] $\big(cf.\ (6.31)\big)$:

$$Z_i = \left\{ 2 \left[ (s_i + b_i) \ln \left[ \frac{(s_i + b_i)\left(b_i + \sigma_{b_i}^2\right)}{b_i^2 + (s_i + b_i)\,\sigma_{b_i}^2} \right] - \frac{b_i^2}{\sigma_{b_i}^2} \ln \left( 1 + \frac{s_i \sigma_{b_i}^2}{b_i(b_i + \sigma_{b_i}^2)} \right) \right] \right\}^{1/2} . \quad (8.8)$$

Here $s_i$ $(b_i)$ represents the expected number of signal (background) events in bin $i$ of the $m_{4\ell}$ or $D_S$ spectrum and $\sigma_{b_i}$ denotes the standard deviation that characterises the systematic uncertainties of the associated background in that bin. To set bounds on $c_\phi$ as a function of $m_\phi$ we assume that the central values of a future measurements of the two relevant distributions will line up with the SM predictions. We hence employ

$$s_i = N_i(c_\phi) - N_i(0)\,, \qquad b_i = N_i(0)\,, \qquad \sigma_{b_i} = \Delta_i N_i(0)\,. \quad (8.9)$$

The total significance $Z$ is obtained by adding the individual $Z_i$ values in quadrature. Parameter regions with a total significance of $Z > \sqrt{2}\,\mathrm{erf}^{-1}\,(\mathrm{CL})$ are said to be excluded at a given confidence level CL. Here $\mathrm{erf}^{-1}(z)$ denotes the inverse error function. In our shape analyses, we consider 23 bins of size of $20\,\mathrm{GeV}$ with four-lepton invariant masses in the range $140\,\mathrm{GeV} < m_{4\ell} < 600\,\mathrm{GeV}$ and 27 bins of equal size of 0.2 that cover the range $-4.9 < D_S < 0.5$ in the case of $m_{4\ell}$ and $D_S$, respectively.

A crucial ingredient in our analysis will turn out to be the systematic uncertainties $\sigma_{b_i}$ on the background as parametrised by the parameters $\Delta_i$ in (8.9). In the case of the HL-LHC shape fits, we will employ the two different choices $\Delta_i = \Delta = 8\%$ and $\Delta_i = \Delta = 4\%$ of bin-independent systematic uncertainties. These choices can be motivated by recalling that the systematic uncertainties that ATLAS quotes in the HL-LHC study [319] for the on-shell $gg \to h \to ZZ$ signal strength amount to 5.0% and 3.9% in the baseline scenario S1 and S2 for the expected total systematic uncertainties. The corresponding systematic uncertainties quoted in the CMS work [295] are 7.3% and 4.1%. Since the dominant Higgs portal corrections in $D_S$ are associated to kinematic configurations with $m_{4\ell}$ around $2m_\phi$, we believe that for not too heavy $\phi$, theoretical predictions of the $D_S$ spectra will reach an accuracy that is very similar to the systematics that is expected to be achievable at the HL-LHC in the case of on-shell $gg \to h \to ZZ$ production. Notice that the BSM effects in the $m_{4\ell}$ spectrum also receive important corrections in the region $m_{4\ell} > 2m_t$ as can be seen from the plots in Figure 8.2. Given the limitations $(cf.\ [44, 217, 458])$ of the state-of-the-art SM predictions of $pp \to ZZ$ production for kinematic configurations above the two top-quark threshold, achieving the assumed systematic uncertainties of $\Delta = 8\%$ and $\Delta = 4\%$ is certainly more challenging in the case of the $m_{4\ell}$ distribution. The steady progress of perturbative QCD calculations, in particular the exact evaluations of the two-loop on-shell amplitudes for $gg \to ZZ$ involving top quarks [231, 232] makes us, however, confident that systematic uncertainties in the ballpark of 10% or below are attainable till $3\,\mathrm{ab}^{-1}$ of data are collected at the HL-LHC.

The plot in Figure 8.4 displays the results of our binned-likelihood analysis when applied to the $m_{4\ell}$ (green lines) and the $D_S$ (blue lines) distribution. Given the strong
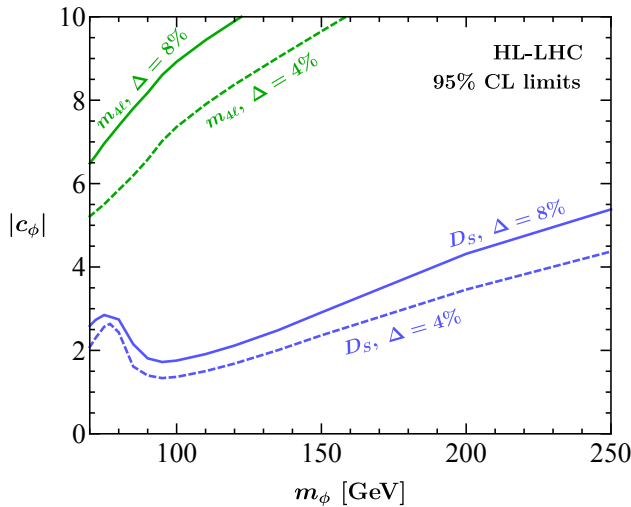
**Figure 8.4:** 95% CL limits on $|c_\phi|$ as a function of $m_\phi$ derived from the binned-likelihood analysis of the $m_{4\ell}$ (green lines) and the $D_S$ (blue lines) spectrum at the HL-LHC. The solid (dashed) curves are obtained assuming a systematic uncertainty of $\Delta = 8\%$ ($\Delta = 4\%$). See main text for additional details.

constraints on $c_\phi$ from on-shell Higgs boson decays into invisible [435–439] or undetected [423, 431] final states, we only consider $m_\phi$ values above the Higgs threshold at $m_h/2$. The shown 95% CL limits correspond to our HL-LHC projections assuming the full expected integrated luminosity of $3\,\mathrm{ab}^{-1}$ at $\sqrt{s} = 14\,\mathrm{TeV}$. The solid (dashed) exclusion lines have been obtained for a systematic uncertainty of $\Delta = 8\%$ ($\Delta = 4\%$). As anticipated, the exclusions that derive from the binned-likelihood analysis of the $m_{4\ell}$ spectrum are significantly weaker than those that follow from the $D_S$ distribution. It is also evident from the figure that the size of the assumed systematic uncertainties plays a non-negligible role in the extraction of the 95% CL limits in the $m_\phi$–$|c_\phi|$ plane, in particular, if the $m_{4\ell}$ spectrum is used to discriminate between the BSM signal and the SM background. We elaborate on this point further in Appendix D. In this context, we also add that our bounds following from the binned-likelihood analysis of the $m_{4\ell}$ distribution agree roughly with the HL-LHC limits presented in [302, 303] if one takes into account that these articles have considered the complex Higgs portal $|H|^2|\Phi|^2$. A thorough comparison with the latter results is however not possible because a discussion of systematic uncertainties is missing in the works [302, 303]. Notice finally that the bounds on $|c_\phi|$ that follow from our $D_S$ likelihood-analysis have a non-trivial behaviour for $m_\phi \lesssim 100\,\mathrm{GeV}$. This feature is related to the interference between the BSM signal and the SM background.

### 8.2.4 HE-LHC and FCC analyses

In the following we repeat the numerical analysis performed at the end of the last section for the HE-LHC and the FCC. In the case of the HE-LHC (FCC) we assume a centre-of-mass energy of $\sqrt{s} = 27\,\mathrm{TeV}$ ($\sqrt{s} = 100\,\mathrm{TeV}$) and an integrated luminosity of $15\,\mathrm{ab}^{-1}$ ($30\,\mathrm{ab}^{-1}$). Apart from the $m_{4\ell}$ window which we enlarge to $1000\,\mathrm{GeV}$ ($1500\,\mathrm{GeV}$) at the HE-LHC (FCC), the selection cuts and detection efficiencies in our
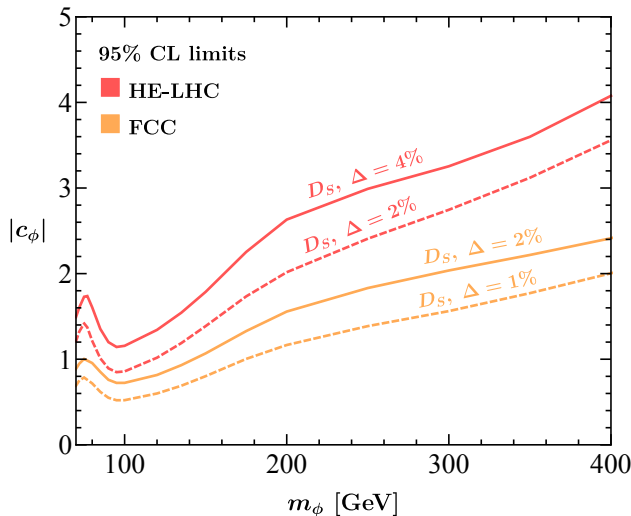
**Figure 8.5:**  95% CL limits on $|c_\phi|$ as a function of $m_\phi$ derived from the binned-likelihood analysis of the ME-based kinematic discriminant $D_S$. The red and orange exclusions illustrate our HE-LHC and FCC projections, respectively. The systematic uncertainties that have been assumed to obtain the different bounds are shown next to the lines and vary between $\Delta = 4\%$ and $\Delta = 1\%$. Further details are given in the main text.

HE-LHC and FCC $pp \to ZZ \to 4\ell$ analyses resemble the ones spelled out at the beginning of Section 8.2.3. Possible reductions of the statistical uncertainties due to improvements in the HE-LHC and FCC detectors such as extended pseudorapidity coverages [459, 460] are not considered in our numerical analysis. We also take the values of the $K$-factors quoted in Section 8.2.2 that have been obtained for LHC collisions to calculate QCD-improved predictions for the kinematic variable $D_S$ a la (8.7). In view of the fact that the assumed systematic uncertainties largely determine the HE-LHC and FCC reach in constraining Higgs portal interactions of the form (8.1), we believe that these simplifications are fully justified. Moreover, since we have seen at the end of the last section that the ME-based kinematic discriminant $D_S$ offers a significantly better sensitivity compared to $m_{4\ell}$, we will below only consider the former observable when determining the disfavoured regions in the $m_\phi - |c_\phi|$ plane.

The HE-LHC and FCC results of our shape fit to the $D_S$ distribution are displayed in Figure 8.5. Like in the case of the HL-LHC we show results assuming different baseline scenarios for the assumed systematic uncertainties. In the case of the HE-LHC we employ $\Delta = 4\%$ and $\Delta = 2\%$, while in our FCC analysis we use $\Delta = 2\%$ and $\Delta = 1\%$. These systematic uncertainties can be motivated by noticing that the systematic uncertainties at the HE-LHC should be at least as small as those expected ultimately at the HL-LHC and that the FCC has a target precision of 1.8% for the $pp \to ZZ \to 4\ell$ channel [461]. Envisaging further theoretical and experimental progress a final systematic uncertainty of 1% at the FCC does therefore not seem inconceivable. From the different curves one again sees that the size of the assumed systematic uncertainties plays a notable role in determining the collider reach. Numerically, we find that halving the systematic uncertainties at the HE-LHC (FCC) leads to improvements of the 95% CL bounds on $|c_\phi|$ of around 25% (30%) at $m_\phi \simeq 100\,\mathrm{GeV}$ and about 20%

(25%) at $m_\phi \simeq 250\,\mathrm{GeV}$. The gain in statistical power of the FCC compared to the HE-LHC is however also visible from the figure with the FCC bound at $m_\phi \simeq 250\,\mathrm{GeV}$ being better by roughly 25% than that of the HE-LHC assuming the same systematic uncertainties of $\Delta = 2\%$. This trend continues at higher values of the real scalar mass reaching up to almost 35% at $m_\phi \simeq 400\,\mathrm{GeV}$.

## 8.3 Discussion

In Figure 8.6 we compare the HL-LHC reach of different search strategies in the $m_\phi-|c_\phi|$ plane. The solid blue exclusion line corresponds to the 95% CL limits that derives from the proposed binned-likelihood analysis of the ME-based kinematic discriminant $D_S$ assuming a systematic uncertainty of $\Delta = 4\%$. The solid green line instead indicates the bound obtained in [321] from a study of off-shell Higgs production in the VBF channel. This analysis assumes a systematic uncertainty of $\Delta = 1\%$. At the HL-LHC, measurements of the global Higgs signal strength $\mu_h$ are expected to reach an accuracy of $\Delta = 2.4\%$ in the baseline scenario S2 for the expected total systematic uncertainties [319]. Utilising the quoted precision together with (8.4) and (8.5) leads at 95% CL to the solid red line. Another process that is sensitive to Higgs portal interactions of the form (8.1) is double-Higgs production as previously demonstrated in [321, 444, 453–455]. The 95% CL bound $\kappa_\lambda \in [0.18, 3.6]$ on the modifications $\kappa_\lambda = \lambda/\lambda_{\mathrm{SM}}$ with $\lambda_{\mathrm{SM}} = m_h^2/(2v^2) \simeq 0.13$ of the trilinear Higgs coupling as found by the CMS projection [272] implies $\mu_{hh} \in [0.7, 1.8]$ on the signal strength in double-Higgs production at the HL-LHC. By implementing the full one-loop corrections due to (8.1) into MCFM and imposing the latter bound we obtain the solid and dashed orange lines. Consult Appendix E for further details. Finally, the dashed black line corresponds to the naturalness bound $|c_\phi| = \sqrt{3}y_t^2 = 1.5$ discussed in Section 8.1.

From Figure 8.6 it is evident that for $m_\phi \lesssim 90\,\mathrm{GeV}$ the VBF and $\mu_h$ projections provide nominally the best constraints at the HL-LHC. In the case of $m_\phi \gtrsim 90\,\mathrm{GeV}$, on the other hand, double-Higgs production at the HL-LHC typically allows to set the most stringent constraints on the parameters appearing in (8.1). Notice also that the $D_S$ constraint provides the best sensitivity for $90\,\mathrm{GeV} \lesssim m_\phi \lesssim 120\,\mathrm{GeV}$ and stronger constraints than VBF and $\mu_h$ for $m_\phi \gtrsim 90\,\mathrm{GeV}$. The fact that the constraints that stem from double-Higgs production are not symmetric under $c_\phi \leftrightarrow -c_\phi$ is readily understood by noting that the Higgs portal corrections to the $gg \to hh$ amplitude involve both terms proportional to $c_\phi^3$ and $c_\phi^2$. In fact, integrating out the real scalar $\phi$ leads to the following one-loop modification of the trilinear Higgs coupling (see for instance [321, 462]):

$$\kappa_\lambda \simeq 1 + \frac{v^2 c_\phi^2}{12\pi^2 m_\phi^2}\left(\frac{v^2 c_\phi}{m_h^2} - \frac{7}{12}\right), \qquad (8.10)$$

where the terms in brackets interfere destructively (constructively) for $c_\phi > 0$ ($c_\phi < 0$). We add that the numerical value of the second term in brackets depends on the definition and the kinematics of the trilinear Higgs vertex and that the value in (8.10) is obtained from the full one-loop form factor (E.2) assuming two on-shell external Higgs bosons. The intricate dependence of the $gg \to hh$ amplitude on $m_\phi$ and $c_\phi$ also leads in the case of $c_\phi > 0$ to the island of disfavoured parameters starting at $m_\phi \simeq$
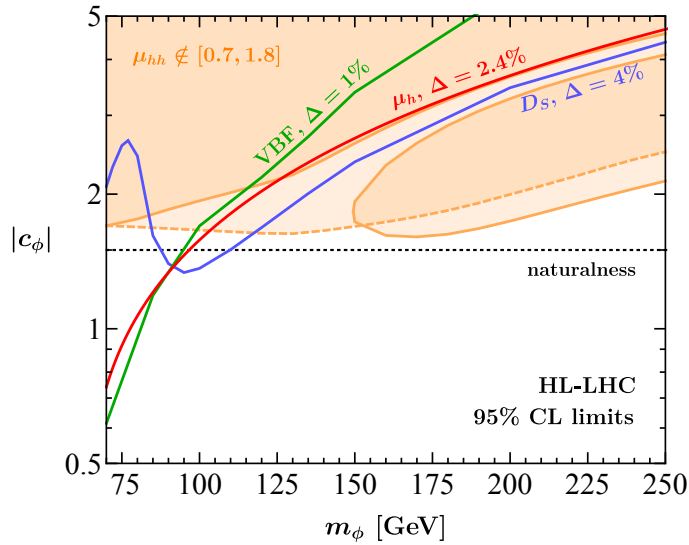
**Figure 8.6:** Comparison of the HL-LHC reach of different search strategies in the $m_\phi - |c_\phi|$ plane. The solid blue, solid green and solid red line correspond to the 95% CL limits that derive from our binned-likelihood analysis of the ME-based kinematic discriminant $D_S$, the VBF analysis performed in [321] and a hypothetical measurement of the global Higgs signal strength $\mu_h$, respectively. If applicable the assumed systematic uncertainties or accuracies are indicated. The parameter spaces above the coloured lines are disfavoured. The region bounded by the solid (dashed) orange line follows from imposing that the signal strength in double-Higgs production obeys $\mu_{hh} \notin [0.7, 1.8]$ for $c_\phi > 0$ ($c_\phi < 0$). The dotted black line corresponds to the bound $|c_\phi| = \sqrt{3}y_t^2 = 1.5$ that derives from naturalness arguments in models of neutral naturalness. For more details see main text.

145 GeV and $c_\phi \simeq 1.7$. This point is discussed in more detail in Appendix E. Notice furthermore that all constraints shown in Figure 8.6 depend in a non-negligible way on the assumed systematic uncertainties or accuracies. Finally, the VBF limit only applies if the new degrees of freedom produced in $h^* \to \phi\phi$ are collider stable and thus lead to a missing transverse energy ($E_T^{\text{miss}}$) signal at the HL-LHC. In view of these caveats one can conclude that to fully exploit the HL-LHC potential in probing Higgs portal interactions of the form (8.1) one should consider all direct and indirect probes displayed in Figure 8.6. But even in such a case one sees that at the HL-LHC only theories compatible with the naturalness bound can be explored if the new particles that cancel the quadratic sensitivity of the Higgs mass are not heavier than $m_\phi \simeq 110$ GeV.

In the case of the HE-LHC and the FCC the sensitivity of the different search strategies to the Higgs portal parameters is shown in the two panels of Figure 8.7. The displayed $D_S$ constraints assume systematic uncertainties of $\Delta = 2\%$ and $\Delta = 1\%$, while the VBF limits taken from [321] include only statistical uncertainties. In the case of the global Higgs signal strength $\mu_h$, we employ $\Delta = 2\%$ and $\Delta = 1\%$ [461]. The 95% CL bounds on modifications of the trilinear Higgs coupling at the HE-LHC and the FCC are expected to be $\kappa_\lambda \in [0.7, 1.3]$ and $\kappa_\lambda \in [0.9, 1.1]$, respectively. See for example [28, 267, 463] for detailed discussions. The corresponding two-sided limits on the signal strength in double-Higgs production are $\mu_{hh} \in [0.80, 1.24]$ and $\mu_{hh} \in [0.93, 1.07]$. In addition, we show in the case of the FCC the exclusion that follows from an extraction of the $Zh$ cross section $\sigma_{Zh}$ with an accuracy of $\Delta = 0.2\%$ as
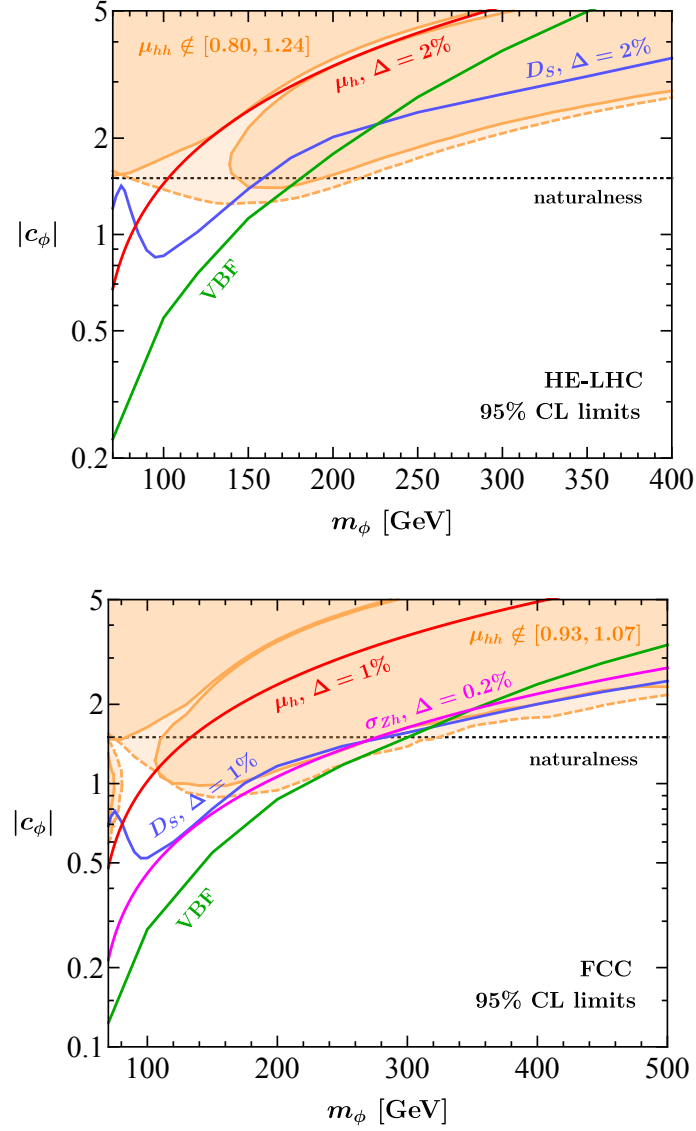
**Figure 8.7:**  Comparison of the HE-LHC (upper panel) and FCC (lower panel) reach of different search strategies in the $m_\phi$–$|c_\phi|$ plane. Besides the constraints shown in Figure 8.6 also the 95% CL limit that follows from a precision measurement of the $Zh$ production cross section $\sigma_{Zh}$ is displayed in the case of the FCC as a solid magenta line. The colour coding and meaning of the other constraints resembles those in the former figure. Consult the main text for additional explanations.

a solid magenta line. Such a precision measurement should be possible at the $e^+e^-$ predecessor of the FCC running at a centre-of-mass energy of $\sqrt{s} = 240\,\text{GeV}$ with an integrated luminosity of $5\,\text{ab}^{-1}$ [464]. The overall picture observed at the HE-LHC is very similar to that seen at the HL-LHC. Nominal the strongest constraint arises for $m_\phi \lesssim 170\,\text{GeV}$ ($m_\phi \gtrsim 170\,\text{GeV}$) from VBF off-shell Higgs (double-Higgs) production, but the $D_S$ constraint also provides complementary sensitivity in particular for higher values of $m_\phi$. In the case of the FCC, one furthermore observes that a high precision measurement of $\sigma_{Zh}$ can provide additional relevant bounds in the $m_\phi$–$|c_\phi|$ plane. The combination of all constraints shown in the panels of Figure 8.7 should allow to probe natural BSM theories of the form (8.2) if the new particles that cancel the quadratic sensitivity of the Higgs mass appear below approximately $m_\phi \simeq 200\,\text{GeV}$ ($m_\phi \simeq 300\,\text{GeV}$) at the HE-LHC (FCC).

We add that the potential of CLIC and a muon collider in constraining Higgs portal interactions of the form (8.1) through VBF off-shell Higgs production has been studied in the article [321]. See also [440–442, 446] for similar analyses concerning the reach of future lepton colliders. While CLIC is not expected to improve the FCC bounds shown in the lower panel of Figure 8.7 even when running at a centre-of-mass energy of $\sqrt{s} = 3\,\text{TeV}$ and collecting $3\,\text{ab}^{-1}$ of data, a muon collider with $\sqrt{s} = 6\,\text{TeV}$ and $6\,\text{ab}^{-1}$ ($\sqrt{s} = 14\,\text{TeV}$ and $14\,\text{ab}^{-1}$) should allow to test natural theories of neutral naturalness up to $m_\phi \simeq 500\,\text{GeV}$ ($m_\phi \simeq 900\,\text{GeV}$) thereby exceeding (significantly) the FCC reach.

# Part III

# Conclusions

# Chapter 9

# Conclusions and outlook

In the absence of unequivocal evidence of physics beyond the SM, either via the discovery of a new state or in the form of a statistically significant global deviation from the SM predictions, there are essentially two broad directions of ongoing exploration at the LHC. On the one hand, precise SM predictions combined with accurate measurements including increasingly more data allow us to test the properties and interactions of the SM particle content with unprecedented scrutiny, thereby further improving the sensitivity to deviations from the SM picture. On the other hand, an EFT paradigm has emerged in which phenomenological studies probe BSM effects indirectly via their low-energy imprints on known collider processes, even in situations where the specific UV completion from which these imprints descent is unknown. It is however evident that the Higgs boson must have a special role in both of these approaches, offering a powerful tool to study manifestations of the SM as well as providing a unique window into possible BSM effects. It will therefore remain one of the cornerstones of the rich physics programme at the LHC. In this thesis, we have presented a number of phenomenological studies, originally published in [42–45], that contribute either directly or indirectly to our understanding of the Higgs sector in and beyond the SM.

In Part I we studied precision Higgs phenomenology within the SM, in particular $ZZ$ production at the LHC in Chapter 4. To this end, we employed the recently developed MiNNLO$_{PS}$ method to match NNLO QCD predictions for the $q\bar{q}$-initiated process to a PS. Using MiNNLO$_{PS}$ has the benefits of being able to include NNLO QCD corrections on-the-fly (*i.e.* without any computationally intensive a-posteriori reweighting), not needing to introduce any merging scale or unphysical boundaries to separate the phase space into different regions corresponding to the number of jets, and furthermore preserves the leading-logarithmic accuracy of the PS when using a $p_T$-ordered shower. In addition, we included the loop-induced $gg$-initiated process, which contributes at $\mathcal{O}(\alpha_s^2)$ and higher, at NLO QCD accuracy matched to PS within the POWHEG-BOX-RES framework (Section 4.1.3). Upon combination, the ensuing nNNLO+PS results constitute the most accurate theoretical predictions for this process to date. Our code is publicly available within the POWHEG-BOX-RES.

We have compared our MiNNLO$_{PS}$ predictions for $ZZ$ production at the theoretical level against both fixed-order and analytically resummed results, finding excellent agreement with fixed-order predictions in phase-space regions where shower effects are expected to be small, in addition to a quite remarkable agreement with the analytically-

resummed NNLO+N$^3$LL $p_{\mathrm{T},4\ell}$ spectrum considering the lower logarithmic accuracy of the PS. In the latter case, fixed-order calculations actually lead to unphysical results in the small-$p_{\mathrm{T},4\ell}$ region due to large logarithmic corrections, which need to be resummed to all orders. In most cases, we observe an overall reduction of the uncertainties due to scale variation by about a factor of three between the NLO+PS accurate MiNLO$'$ results and our MiNNLO$_{\mathrm{PS}}$ results, underlining the importance of including (n)NNLO QCD corrections. In particular, the NLO QCD corrections to the loop-induced $gg$ channel, which are formally part of the N$^3$LO corrections to $ZZ$ production, have a non-negligible impact, especially for small $m_{4\ell}$ and central rapidities. We have furthermore compared our nNNLO+PS results to 13 TeV CMS data [195], finding an agreement on almost all bins within one sigma. In the few bins where the differences are at the two-sigma level we have shown that the inclusion of NLO EW corrections, albeit approximately by means of a multiplicative $K$-factor, removes those differences in most instances.

With the disclaimer that the quoted uncertainties capture merely those associated to missing higher orders, in particular that PDF uncertainties and uncertainties related to missing interference effects in the case of identical leptons in the final state are not included, our final results are accurate at the level of 2% both for inclusive and fiducial cross sections. These are similar in size as the current uncertainties on the experimental side, which will however further improve when new data from LHC Run 3 and the HL-LHC becomes available. We therefore conclude that theoretical predictions with an accuracy comparable to that of the results presented in this work are mandatory to fully exploit $ZZ$ cross-section measurements at the LHC.

Our work can be extended in serval ways. First, an obvious improvement is to combine highest-order QCD and QED corrections consistently in PS simulations. Second, a comprehensive comparison between available NNLO+PS generators is desirable, in particular in light of the small differences between MiNNLO$_{\mathrm{PS}}$ and GENEVA observed in the $p_{\mathrm{T},e^-}$ spectrum. And finally, another interesting direction for future efforts is to implement the amplitudes associated to the subset of SMEFT operators relevant for $ZZ$ production into MiNNLO$_{\mathrm{PS}}$ (and POWHEG for $gg \to ZZ$). In fact, since NLO+PS implementations within the SMEFT for Drell-Yan and EW Higgs production [465, 466] and $WZ$, $WW$ production [467, 468] are already available within the POWHEG-BOX, and even the first NNLO+PS event generators within the SMEFT are starting to emerge [166], it seems worthwhile to further exploit the benefits of the MiNNLO$_{\mathrm{PS}}$ methodology in this direction.

The overarching topic of Part II is Higgs physics beyond the SM. In Chapter 6, we studied the constraints on modifications of the trilinear Higgs coupling that originate from Higgs production in $pp$ collisions at the LHC Run 3 and HL-LHC. To this end, we have augmented the renormalisable SM interactions by the dimension-six operators $\mathcal{O}_6$ and $\mathcal{O}_H$ $\left(cf.\ (6.8)\right)$ within the SMEFT, accompanied by their associated Wilson coefficients $\bar{c}_6$ and $\bar{c}_H$. While the operator $\mathcal{O}_6$ induces non-trivial kinematic shape-changes to the differential $m_{4\ell}$ spectrum through its NLO EW corrections to the process $gg \to h^* \to ZZ \to 4\ell$, the operator $\mathcal{O}_H$ constitutes an overall shift of the cross section as a result of requiring a canonically normalised physical Higgs field $h$. We have made use of a discriminant $D_S$ which turned out to be particularly powerful in constraining BSM scenarios with $\bar{c}_6 \neq 0$ because they can lead to $D_S < -4.5$ while

99 % of the $pp \to ZZ \to 4\ell$ events in the SM fall into the range $-4.5 < D_S < 0.5$, which thus provides a null test. Partially owing to this feature, we have demonstrated our method to be complementary as well as competitive to inclusive single-Higgs probes in constraining the parameter space spanned by $\bar{c}_6$ and $\bar{c}_H$. A combination of our work and inclusive single-Higgs boson probes allowed us to constrain their combination $c_3 = 1 + \bar{c}_6 - 3/2\bar{c}_H$ to the 95% CL range $c_3 \in [-4.0, 6.1]$ ($c_3 \in [-1.7, 5.7]$) at the LHC Run 3 (HL-LHC).

A straightforward way of improving the constraints on the trilinear Higgs coupling derived in our work would be to include also projections of measurements for double-Higgs production as well as EW precision observables, which has for instance been done based on LHC Run 2 data in [285, 286, 289]. Furthermore, we have implemented the aforementioned discriminant $D_S$ in our MC code using LO matrix elements for the $pp \to ZZ \to 4\ell$ process, for which many theoretical improvements [44, 79–81, 172, 212, 214, 217, 231, 232, 309–311] are available in the literature. We hence believe that improving the theoretical understanding of the $D_S$ distribution is certainly possible, which will have a tangible impact on the sensitivity of off-shell Higgs measurements to modifications of the trilinear Higgs coupling.

In Chapter 7, we focussed on potential BSM effects that modify the bottom-Higgs and charm-Higgs dynamics, in the form the chromodipole operators $\mathcal{O}_{bG}$ and $\mathcal{O}_{cG}$ within the SMEFT, *cf.* (7.2). While a short review of the limits on the corresponding Wilson coefficients ($C_{bG}$ and $C_{cG}$) from Higgs physics is provided in Section 7.1 (*cf.* Table 7.2), the effects of $\mathcal{O}_{bG}$ and $\mathcal{O}_{cG}$ can also be studied in processes that do not involve a Higgs boson. The main results of our work are the limits on $C_{bG}$ and $C_{cG}$, derived from non-Higgs observables, presented in Table 7.1. While the nominal strongest collider bound on $|C_{bG}|$ is obtained from an analysis of $M_{jj}$ distributions for two $b$-tagged jets within the experimentally probed region of $1133\,\text{GeV} < M_{jj} < 4595\,\text{GeV}$ [346], requiring its suppression scale $\Lambda$ to be above said range results in a magnitude of $C_{bG}$ larger than $4\pi$, thus constraining only strongly-coupled UV completions.

This leads us to classify the process $pp \to b\bar{b}Z/\gamma^* \to b\bar{b}\ell^+\ell^-$ as the most promising non-Higgs collider probe. Using the $p_{\text{T}}$ spectrum of the $Z$ boson up to 1 TeV, we showed that the production of a $Z$ boson in association with two $b$-jets should be able to exclude effects due to $\mathcal{O}_{bG}$ for $\Lambda < 980$ GeV assuming a Wilson coefficient with a magnitude of one. In fact, since the prospects of reducing the systematic uncertainties due to an improved theoretical understanding are quite good (*cf.* [369]), it is not unlikely that this bound will be pushed above 1 TeV in the future. However, the coefficients $C_{bG}$ and $C_{cG}$ are typically both Yukawa- and loop-suppressed in weakly-coupled TeV-scale new-physics models, in which case we showed that only nEDM searches are able to test such scenarios. Making effects of bottom-quark and charm-quark chromodipole operators observable at the LHC therefore generically requires a mechanism that suppresses new sources of CP-violation beyond the SM.

In the final chapter of Part II, we considered the possibility of a Higgs portal in the form of the operator $|H|^2$, and explored the sensitivity of future hadron-collider measurements of $ZZ \to 4\ell$ production in constraining interactions of the type $c_\phi|H|^2\phi^2$, with $\phi$ a real scalar field and $c_\phi$ parametrising the strength of the Higgs-portal interaction. Using a similar strategy as presented in Chapter 6 by employing the same kinematic discriminant $D_S$, we showed that the reach of the HL-LHC can be signif-

icantly enhanced compared to studies that are based on measurements of the $m_{4\ell}$ spectrum alone (*cf.* Figure 8.4 and Appendix D). We have also analysed the potential of the HE-LHC and the FCC in constraining new physics that couples to $|H|^2$, finding for instance that, using our analysis strategy, it should be able to test models of neutral naturalness that imply a condition $|c_\phi| = \sqrt{3}y_t^2 = 1.5$ that derives from naturalness arguments, up to values for the scalar mass of $m_\phi = 280$ GeV at the FCC with an assumed systematic uncertainty of $1\%$ (*cf.* Figure 8.5). We have compared our HL-LHC, HE-LHC and FCC results to the projected limits that were obtained from off-shell Higgs production in VBF [321], as well as to those that could achieved using inclusive single-Higgs production, double-Higgs production and in the case of the FCC also $Zh$ production at a leptonic predecessor of the FCC. In general, we find that the constraints obtained from our $ZZ \to 4\ell$ analysis turn out to be both competitive with and complementary to the projected limits obtained using other search techniques.

The possible improvement associated to the theoretical understanding of the kinematic discriminant $D_S$ mentioned above will naturally have a similarly beneficial effect here as well. Other interesting avenues for exploring Higgs portals are provided by future lepton colliders (see *e.g.* [440–442, 446]). For instance, a future muon collider with $\sqrt{s} = 6$ TeV and $6\,\text{ab}^{-1}$ ($\sqrt{s} = 14$ TeV and $14\,\text{ab}^{-1}$) should allow to test the aforementioned class of theories of neutral naturalness up to $m_\phi \simeq 500\,\text{GeV}$ ($m_\phi \simeq 900\,\text{GeV}$), thereby exceeding significantly the FCC reach.

# Part IV

# Appendices

# Appendix A

# Fundamentals of QCD

This appendix aims to provide a short description of some of the basic aspects of quantum chromodynamics (QCD), for more detailed and complete treatments of QCD the reader is referred to standard textbooks such as [122, 124, 138, 469–471].

**Definition of the theory** —— QCD is a non-Abelian gauge theory (or Yang–Mills theory) with gauge group $SU(3)$. The bare Lagrangian density $\mathcal{L}_{\mathrm{QCD}}^0$ that defines the theory is given by

$$\mathcal{L}_{\mathrm{QCD}}^0 = \bar{\psi}_a^0 \left( i \slashed{D} - m_\psi^0 \right)_{ab} \psi_b^0 - \frac{1}{4} \left( G_{\mu\nu}^{0A} \right)^2 + \mathcal{L}_{\text{gauge-fixing}} + \mathcal{L}_{\text{ghost}} \,, \qquad \text{(A.1)}$$

where spinor and flavour indices are not written explicitly, and the superscript 0 is used to indicate bare quantities. The Dirac fields $\psi_a$ with color index $a = 1, 2, 3$ denote the quark fields, while the gauge fields $G_\mu^A$ with color index $A = 1, \ldots, 8$ are called gluon fields. The covariant derivative and gluon field strength appearing in the gauge-invariant part of (A.1) are defined as follows

$$\begin{aligned} D_\mu \psi_0 &\equiv \left( \partial_\mu + i g_s^0 t^A G_\mu^{0A} \right) \psi_0 \,, \\ G_{\mu\nu}^{0A} &\equiv \partial_\mu G_\nu^{0A} - \partial_\nu G_\mu^{0A} - g_s^0 f_{ABC} G_\mu^{0B} G_\nu^{0C} \,, \end{aligned} \qquad \text{(A.2)}$$

with $g_s$ the strong coupling constant, $t^A$ the $SU(3)$ generators and the fully antisymmetric structure constants $f_{ABC}$ defined via the relation $[t_A, t_B] = i f_{ABC} t_C$. The Casimir operators $C_\mathrm{F}$ and $C_\mathrm{A}$ and normalisation $T_\mathrm{R}$ that appear often in computations performed in $SU(3)$ are given by

$$\sum_A t_{ab}^A t_{bc}^A = C_\mathrm{F} \delta_{ac} \quad \Rightarrow \quad C_\mathrm{F} = \frac{N_\mathrm{c}^2 - 1}{2 N_\mathrm{c}} = \frac{4}{3} \,, \qquad \text{(A.3)}$$

$$\sum_{A,B} f^{ABC} f^{ABD} = C_\mathrm{A} \delta^{CD} \quad \Rightarrow \quad C_\mathrm{A} = N_\mathrm{c} = 3 \,, \qquad \text{(A.4)}$$

$$\mathrm{Tr} \left[ t_A, t_B \right] = T_\mathrm{R} \delta_{AB} \quad \Rightarrow \quad T_\mathrm{R} = \frac{1}{2} \,. \qquad \text{(A.5)}$$

When quantising QCD, choosing a covariant gauge with gauge parameter $\xi$ as follows

$$\mathcal{L}_{\text{gauge-fixing}} = -\frac{1}{2\xi^0} \left( \partial^\mu G_\mu^{0A} \right)^2 \,, \qquad \text{(A.6)}$$

solves the issue of defining a Feynman propagator for the gluon field. However, for non-Abelian theories one also has to add the following terms

$$\mathcal{L}_{\text{ghost}} = \partial_\mu \bar{\eta}_A^0 \partial^\mu \eta_A^0 + g_s^0 \partial^\mu \bar{\eta}_B^0 f_{ABC} G_\mu^{0A} \eta_C^0 \,, \tag{A.7}$$

which contain the Faddeev-Poppov [472] ghost fields $\eta_A$ in order to cancel the unphysical longitudinal degrees of freedom that would otherwise propagate when using a covariant gauge-fixing procedure. The above considerations allow one to write down the basic QCD Feynman rules, listed in Figure A.1, that follow from (A.1).

**Renormalisation** —— As is the case for most relativistic quantum field theories, UV divergencies appear also in QCD when considering interactions beyond tree level. However, as the Lagrangian for a non-Abelian gauge theory contains no terms with a mass dimension higher than four, QCD is renormalisable, meaning its UV divergencies can be removed by adding a finite number of counterterms. In the counterterm approach, the renormalised QCD Lagrangian $\mathcal{L}_{\text{QCD}}$ can written as the sum of three parts corresponding to the free theory, the (possibly divergent) interactions and a counterterm Lagrangian

$$\mathcal{L}_{\text{QCD}} = \mathcal{L}_{\text{QCD}}^{\text{free}} + \mathcal{L}_{\text{QCD}}^{\text{int}} + \mathcal{L}_{\text{QCD}}^{\text{ct}} \,, \tag{A.8}$$

where, suppressing the colour labels of the quark fields, the three individual parts are given by the following expressions

$$\mathcal{L}_{\text{QCD}}^{\text{free}} = \bar{\psi} \left( i \slashed{\partial} - m_\psi \right) \psi - \frac{1}{4} \left( \partial_\mu G_\nu^A - \partial_\nu G_\mu^A \right)^2 - \frac{1}{2\xi} \left( \partial^\mu G_\mu^A \right)^2 + \partial_\mu \bar{\eta}_A \partial^\mu \eta_A \,,$$

$$\mathcal{L}_{\text{QCD}}^{\text{int}} = -g_s \mu^\epsilon \bar{\psi} t^A \slashed{G}^A \psi + g_s \mu^\epsilon f_{ABC} G^{B\mu} G^{C\nu} \partial_\mu G_\nu^A - \frac{g_s^2 \mu^{2\epsilon}}{4} \left( f_{ABC} G_\mu^B G_\nu^C \right)^2$$
$$+ g_s \mu^\epsilon \partial^\mu \bar{\eta}_B f_{ABC} G_\mu^A \eta_C \,,$$

$$\mathcal{L}_{\text{QCD}}^{\text{ct}} = (Z_2 - 1) \bar{\psi} i \slashed{\partial} \psi + (Z_2 Z_m - 1) \bar{\psi} m_\psi \psi - g_s \mu^\epsilon \left( Z_g Z_2 Z_3^{1/2} - 1 \right) \bar{\psi} t^A \slashed{G}^A \psi$$
$$+ g_s \mu^\epsilon \left( Z_3^{3/2} Z_g - 1 \right) f_{ABC} G^{B\mu} G^{C\nu} \partial_\mu G_\nu^A - \frac{g_s^2 \mu^{2\epsilon}}{4} \left( Z_3^2 Z_g^2 - 1 \right) \left( f_{ABC} G_\mu^B G_\nu^C \right)^2$$
$$+ \left( \bar{Z} - 1 \right) \partial_\mu \bar{\eta}_A \partial^\mu \eta_A + g_s \mu^\epsilon \left( \bar{Z} Z_3^{1/2} Z_g - 1 \right) \partial^\mu \bar{\eta}_B f_{ABC} G_\mu^A \eta_C \,. \tag{A.9}$$

Here, we introduced the renormalisation scale $\mu$, which is the unit of mass for dimensional regularisation, in order to keep $g_s$ dimensionless for all $\epsilon$. We used the freedom to not only renormalise the strong coupling $g_s^0$ and quark masses $m_\psi^0$, but also the (wave functions of) the fields in the theory and the gauge parameter $\xi^0$. The renormalisation constants used in the above expressions are given by

$$G_\mu^{0A} = Z_3^{1/2} G_\mu^A \,, \qquad \psi_a^0 = Z_2^{1/2} \psi_a \,, \qquad \eta_A^0 = \bar{Z}^{1/2} \eta_A \,, \tag{A.10}$$
$$g_s^0 = Z_g g_s \mu^\epsilon \,, \qquad \xi^0 = Z_3 \xi \,, \qquad m_\psi^0 = Z_m m_\psi \,. \tag{A.11}$$

The counterterm Lagrangian in (A.9) has its own associated Feynman rules. The three- and four-point counterterm vertices can be read off from Figure A.1, and making the
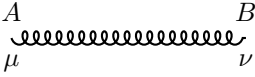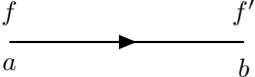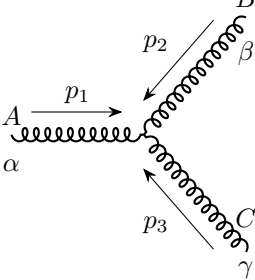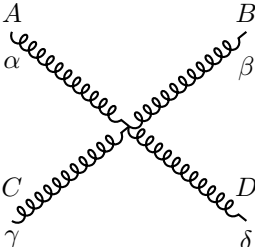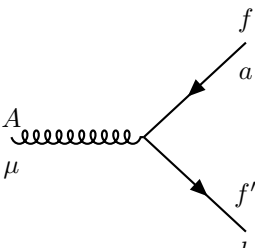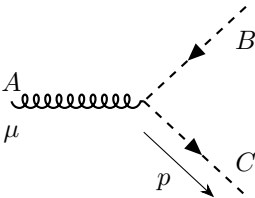
Gluon propagator

$$\left(-g_{\mu\nu} + (1-\xi)\frac{p_\mu p_\nu}{p^2 + i\epsilon}\right)\frac{-i\delta^{AB}}{p^2 + i\epsilon}$$

Quark propagator

$$\frac{i(\not{p} + m_f)_{ab}\delta_{ff'}}{p^2 - m_f^2 + i\epsilon}$$

Ghost propagator

$$\frac{i\delta^{AB}}{p^2 + i\epsilon}$$

Three-gluon vertex

$$-g_s^0 f_{ABC}\Big[g^{\alpha\beta}(p_1 - p_2)^\gamma$$
$$+ g^{\beta\gamma}(p_2 - p_3)^\alpha + g^{\gamma\alpha}(p_3 - p_1)^\beta\Big]$$

Four-gluon vertex

$$-i(g_s^0)^2\Big[f_{ABE}f_{CDE}(g^{\alpha\gamma}g^{\beta\delta} - g^{\alpha\delta}g^{\beta\gamma})$$
$$+ f_{ACE}f_{BDE}(g^{\alpha\beta}g^{\gamma\delta} - g^{\alpha\delta}g^{\gamma\beta})$$
$$+ f_{ADE}f_{BCE}(g^{\alpha\beta}g^{\delta\gamma} - g^{\alpha\gamma}g^{\delta\beta})\Big]$$

Quark-gluon vertex

$$-ig_s^0\,(\gamma^\mu)_{ff'}\,\big(t^A\big)_{ab}$$

Ghost-gluon vertex

$$g_s^0 f_{ABC}p^\mu$$

**Figure A.1:** Basic QCD Feynman rules.
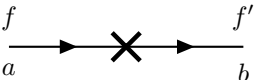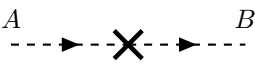
| | | |
|---|---|---|
| Gluon propagator | | $i\left(Z_3 - 1\right)\left(-g_{\mu\nu}p^2 + p_\mu p_\nu\right)\delta^{AB}$ |
| Quark propagator | | $i\left(\not{p}\left(Z_2 - 1\right) - \left(Z_2 Z_m - 1\right)m_\psi\right)_{ab}\delta_{ff'}$ |
| Ghost propagator | | $i\left(\bar{Z} - 1\right)p^2\delta^{AB}$ |

**Figure A.2:** Feynman rules for the two-point counterterms in QCD.

following substitutions

$$
\begin{aligned}
\text{Three-gluon vertex:} &\quad g_s^0 \to g_s^0 Z_3^{3/2} Z_g - g_s\mu^\epsilon\,, \\
\text{Four-gluon vertex:} &\quad (g_s^0)^2 \to (g_s^0)^2 Z_3^2 Z_g^2 - g_s^2\mu^{2\epsilon}\,, \\
\text{Quark-gluon vertex:} &\quad g_s^0 \to g_s^0 Z_2 Z_3^{1/2} Z_g - g_s\mu^\epsilon\,, \\
\text{Ghost-gluon vertex:} &\quad g_s^0 \to g_s^0 \bar{Z} Z_3^{1/2} Z_g - g_s\mu^\epsilon\,.
\end{aligned}
\tag{A.12}
$$

The two-point counterterm vertices are given in Figure A.2. Finally, we add that (A.9) holds to all orders in perturbation theory, but in practice one determines the renormalisation constants order-by-order, i.e. expanding $Z_i = 1 + \delta_i + \ldots$, and requiring the Green functions to be finite at the given order. Explicit expressions at one loop are for instance derived in [124, 469].

**The $\beta$ function and asymptotic freedom** —— The renormalised QCD coupling, defined via the relation $g_s^0 = g_s\mu^\epsilon Z_g$, deserves a further discussion since it is intimately related to the renormalisation-group (RG) invariance and asymptotic freedom of the theory. In fact, RG invariance means nothing more than that the complete theory should not depend on the renormalisation scale $\mu$. The value of $\mu$ can be freely chosen, as long as the values of the renormalised parameters in theory are changed in such a way that the complete theory remains invariant. One obtains the $\mu$-dependence of the renormalised coupling $g_s$ by requiring

$$
\frac{dg_s^0}{d\ln\mu} = \epsilon\alpha_s + \beta\left(\alpha_s\right) + 2\frac{\alpha_s}{Z_g}\frac{dZ_g}{d\alpha_s}\beta\left(\alpha_s\right) = 0\,,
\tag{A.13}
$$

where we have introduced $\alpha_s = g_s^2/(4\pi)$ and the QCD $\beta$ function, defined as

$$
\beta\left(\alpha_s\right) \equiv \frac{d\alpha_s}{d\ln\mu^2} = \frac{g_s}{4\pi}\frac{dg_s}{d\ln\mu}\,.
\tag{A.14}
$$

The explicit expression for the renormalisation constant $Z_g$ at one loop is

$$
Z_g = 1 - \frac{\alpha_s S_\epsilon}{4\pi\epsilon}\left(\frac{11}{6}C_{\mathrm{A}} - \frac{2}{3}T_{\mathrm{R}}n_f\right) + \mathcal{O}(\alpha_s^2)\,,
\tag{A.15}
$$

where $n_f$ is the number of quark flavours and the symbol $S_\epsilon$ is a subtraction-scheme dependent factor, which for instance in the $\overline{\mathrm{MS}}$ scheme is defined as $S_\epsilon = (4\pi)^\epsilon/\Gamma(1-\epsilon)$

with $\Gamma$ the gamma function. We will set $S_\epsilon$ to 1 (minimal subtraction) for notational clarity hereafter. Solving (A.13) for $\beta(\alpha_s)$ using (A.15) and expanding in powers of $\alpha_s$, we find at the physical space-time dimension ($\epsilon = 0$) the following expression for the $\beta$ function

$$\beta(\alpha_s) = -\left(11 - \frac{2}{3}n_f\right)\frac{\alpha_s^2}{4\pi} + \mathcal{O}(\alpha_s^3) = -\beta_0\alpha_s^2 + \mathcal{O}(\alpha_s^3).\tag{A.16}$$

Here one observes that $\beta_0$ is positive for $n_f \leq 16$, so that (A.16) and (A.14) can be combined to obtain the scale-dependence (or running) of $\alpha_s$

$$\alpha_s(\mu^2) = \frac{1}{\beta_0 \ln(\mu^2/\Lambda^2)},\tag{A.17}$$

where the integration constant $\Lambda$, which has receives mass dimension of one via dimensional transmutation, is around 200 MeV for QCD [23]. Below said value one enters the non-perturbative regime. For any observable that depends on an energy scale $Q$, one could show that

$$\alpha_s(Q^2) = \frac{\alpha_s(\mu^2)}{1 + \beta_0 \ln(Q^2/\mu^2)\,\alpha_s(\mu^2)},\tag{A.18}$$

where, since $\beta_0$ is positive (for $n_f \leq 16$), the coupling tends to zero as the energy is increased. QCD is therefore asymptotically free, which is a crucial feature of the theory as it makes QCD susceptible to perturbative methods at sufficiently high energies.

For completeness, we report the $\beta$ function and the coefficients $\beta_0$, $\beta_1$ and $\beta_2$ in the conventions of [34], given by

$$\beta(\alpha_s) = -\beta_0\alpha_s^2 - \beta_1\alpha_s^3 - \beta_2\alpha_s^4 + \mathcal{O}(\alpha_s^5),\tag{A.19}$$

where

$$\begin{aligned}
\beta_0 &= \frac{11C_A - 2n_f}{12\pi}, \\
\beta_1 &= \frac{17C_A^2 - 5C_A n_f - 3C_F n_f}{24\pi^2}, \\
\beta_2 &= \frac{2857C_A^3 + \left(54C_F^2 - 615C_A C_F - 1415C_A^2\right)n_f + (66C_F + 79C_A)n_f^2}{3456\pi^3}.
\end{aligned}\tag{A.20}$$

# Appendix B

# Higgs width effects

In this appendix we illustrates how rescalings of the form

$$g_{hXX}^{\rm SM} \to \xi^{1/4}\, g_{hXX}^{\rm SM}\,, \qquad \Gamma_h^{\rm SM} \to \xi\, \Gamma_h^{\rm SM}\,, \tag{B.1}$$

with $g_{hXX}^{\rm SM}$ and $\Gamma_h^{\rm SM}$ denoting the couplings and total decay width of the SM Higgs boson, respectively, modify the kinematic distributions in off-shell ggF Higgs production. Notice that (B.1) leaves the total Higgs production cross sections in all channels unchanged compared to their SM values. This is however not true for the off-shell Higgs cross sections that are essentially independent of $\Gamma_h^{\rm SM}$ and are thus modified if the Higgs couplings $g_{hXX}^{\rm SM}$ are rescaled as in (B.1). By measuring the total number of off-shell Higgs events one can therefore place indirect limits on the total width of the Higgs boson [168, 169, 292–298, 305].

In Figure B.1 we show our results for the $m_{4\ell}$ distributions in the $gg \to ZZ \to 4\ell$ channel (left) and the $D_S$ spectrum of $pp \to ZZ \to 4\ell$ (right) for two different rescalings (B.1). The choice $\xi = 3$ and $\xi = 1.5$ thereby corresponds approximately to the present LHC Run 2 [296, 297] and the projected HL-LHC [294, 295] sensitivity, respectively. From the left plot one sees that compared to the SM the BSM predictions have larger off-shell Higgs cross sections with the relative difference between the spectra growing roughly linearly with $m_{4\ell}$. Notice that the observed shape changes are qualitatively different from the relative modifications that occur in the case of the $\mathcal{O}(\lambda)$ corrections associated to insertions of the operator $\mathcal{O}_6$ as shown on the right-hand side in Figure 6.3. From the right plot in Figure B.1 one furthermore observes that compared to the SM the BSM distributions of the ME-based discriminant are enhanced for $D_S \gtrsim -1$. Since they do not feature the enhancements for $D_S \lesssim -3.5$, the shown $D_S$ spectra are hence distinct from the distributions that are displayed on the right in Figure 6.5, which correspond to the spectra resulting from insertions of the SMEFT operator $\mathcal{O}_6$. Notice that in contrast to the $\mathcal{O}(\lambda)$ corrections, the effects of (B.1) lead solely to enhancements in the tail of the $m_{4\ell}$ distribution. In this case extra care is required in estimating the systematic uncertainties, because the NLO QCD corrections to the $gg$-induced channel included approximately by means of (6.29) implicitly assume an asymptotic expansion in the top-quark mass (*cf.* [44, 217]) of the relevant two-loop $gg \to ZZ$ amplitudes. This expansion fails above the top-quark threshold, *i.e.* for four-lepton invariant masses $m_{4\ell} > 2m_t$, which introduces compared to the case discussed in Section 6.2.2.2 an additional systematic uncertainty. To account for this issue, we
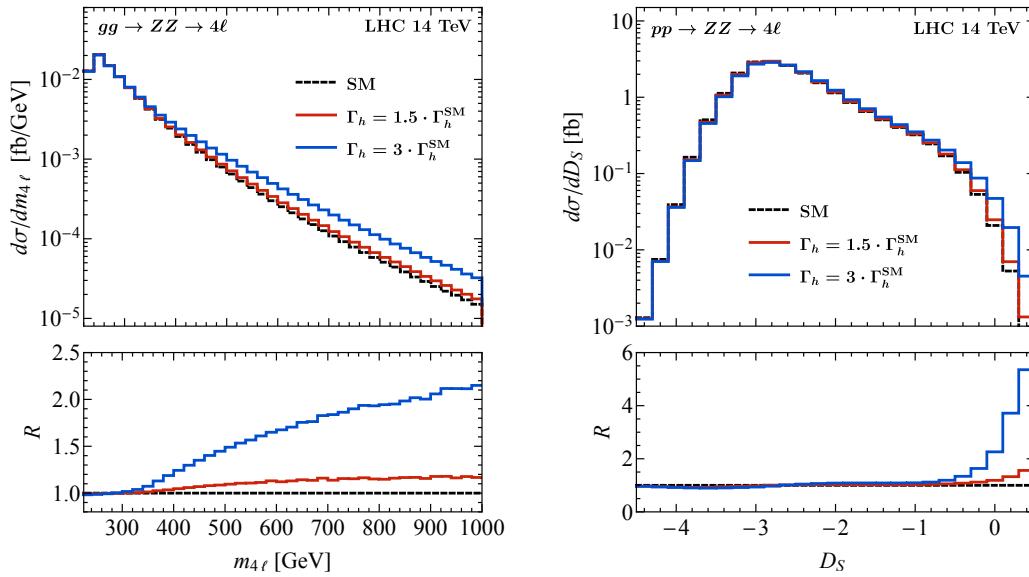
**Figure B.1:** Left: $m_{4\ell}$ distributions for the $gg$-initiated contributions in the SM (dashed black), for $\Gamma_h = 1.5 \cdot \Gamma_h^{\text{SM}}$ (solid red) and for $\Gamma_h = 3 \cdot \Gamma_h^{\text{SM}}$ (solid blue). Right: $D_S$ distributions for the $pp \to ZZ \to 4\ell$ process in the SM (dashed black), for $\Gamma_h = 1.5 \cdot \Gamma_h^{\text{SM}}$ (solid red) and for $\Gamma_h = 3 \cdot \Gamma_h^{\text{SM}}$ (solid blue). All distributions are obtained using (B.1), are LO QCD accurate and assume $pp$ collisions at $\sqrt{s} = 14\,\text{TeV}$. The lower panels show the ratios between the BSM and SM predictions.

instead of $\pm 15\%$ assume an enlarged total theoretical uncertainty of $\pm 25\%$. Employing this uncertainty estimate and performing a shape-fit to the $D_S$ spectrum following the procedure outlined in Section 6.2.2.3, we obtain for $3\,\text{ab}^{-1}$ of HL-LHC data the 95% CL bound $\Gamma_h < 1.49 \cdot \Gamma_h^{\text{SM}}$. This finding is in line with the limits reported in [294, 295] which validates the used fitting approach.

# Appendix C

# Additional HL-LHC projections

A crucial ingredient in the shape fit to the $D_S$ distribution described in Section 6.2.2.3 are the systematic uncertainties $\sigma_{b_i}$ on the background as parametrised by the parameters $\Delta_i$ in (8.9). In this appendix we present results for two additional more aggressive assumptions about the systematic uncertainties entering the HL-LHC off-shell Higgs analysis. Specifically, we will employ the two different choices $\Delta_i = 0.08$ and $\Delta_i = 0.04$ of bin-independent systematic uncertainties. These choices can be motivated by recalling that the systematic uncertainties that ATLAS quotes in the HL-LHC study [319] for the on-shell $gg \to h \to ZZ$ signal strength amount to 5.0% and 3.9% in the baseline scenario S1 and S2 for the expected total systematic uncertainties. The corresponding systematic uncertainties quoted in the CMS work [295] are 7.3% and 4.1%. Since the $\mathcal{O}(\lambda)$ corrections to $D_S$ considered in this work are associated to kinematic configurations with $m_{4\ell}$ not far above $2m_Z$, it seems not unreasonable that theoretical predictions of the $D_S$ spectra can reach an accuracy that is very similar to the systematics that is expected to be achievable at the HL-LHC in the case of on-shell $gg \to h \to ZZ$ production.

In the left (right) panel of Figure C.1 we show the projected 68% and 95% CL HL-LHC constraints in the $\bar{c}_6$–$\bar{c}_H$ plane assuming $\Delta_i = 0.08$ ($\Delta_i = 0.04$). The constraints from inclusive single-Higgs probes (blue regions) are compared to the off-shell Higgs constraints (orange regions). Their combinations (red contours) are also displayed. From a combined analysis of inclusive single-Higgs and off-shell Higgs probes, we find for $\bar{c}_H = 0$ the following 95% CL limits

$$\bar{c}_6 \in [-2.3, 4.5] \,, \quad (\text{HL-LHC}, \, \Delta_i = 0.08) \,,$$
$$\bar{c}_6 \in [-2.2, 4.3] \,, \quad (\text{HL-LHC}, \, \Delta_i = 0.04) \,,$$
(C.1)

while for $\bar{c}_6 = 0$ we obtain

$$\bar{c}_H \in [-1.6, 1.6] \cdot 10^{-2} \,, \quad (\text{HL-LHC}, \, \Delta_i = 0.08) \,,$$
$$\bar{c}_H \in [-1.0, 1.0] \cdot 10^{-2} \,, \quad (\text{HL-LHC}, \Delta_i = 0.04) \,.$$
(C.2)

By comparing the HL-LHC limits given in (6.39) and (6.40) to the above results, one observes that a reduction of systematic uncertainties has only a minor impact in the case of $\bar{c}_6$, while it has a noticeable impact on the resulting bounds on $\bar{c}_H$. The limits (C.1) and (C.2) can also be translated into constraints on the modifications of the trilinear
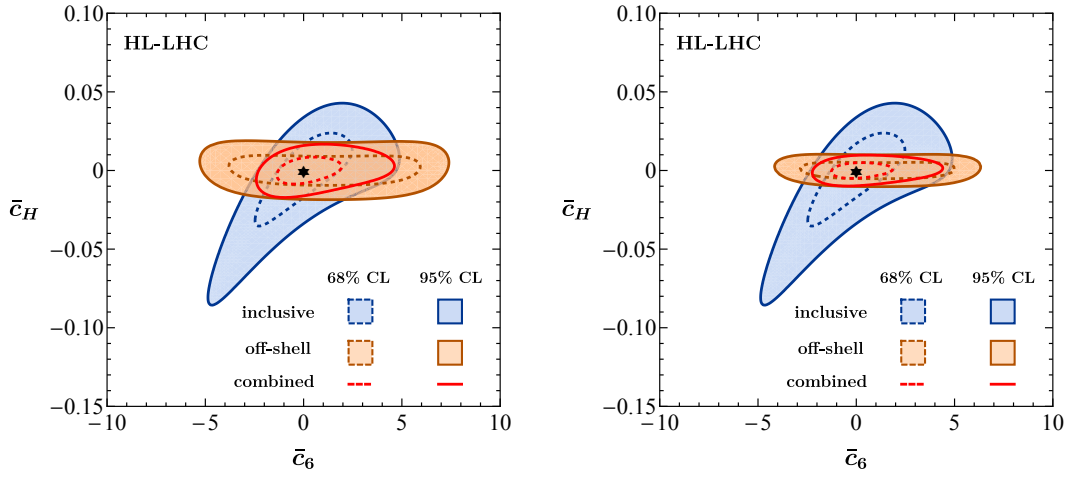
**Figure C.1:** Projected 68% and 95% CL constraints in the $\bar{c}_6-\bar{c}_H$ plane for the HL-LHC assuming $3\,\mathrm{ab}^{-1}$ of data collected at $\sqrt{s} = 14\,\mathrm{TeV}$. The constraints from inclusive single-Higgs probes (blue regions) are compared to the off-shell Higgs constraints (orange regions). The left (right) off-shell Higgs constraints employ a bin-independent systematic uncertainty of $\Delta_i = 0.08$ ($\Delta_i = 0.04$) in the shape fit to the $D_S$ distribution. The combinations of all constraints are also shown as red contours. The black stars represent the SM point. For additional details see the main text.

Higgs coupling as parameterised by (6.20). The corresponding 95% CL ranges read $c_3 \in [-1.4, 5.6]$ and $c_3 \in [-1.2, 5.4]$, respectively, which again represent only minor improvements compared to the HL-LHC bound derived in Section 6.3.

# Appendix D

# Systematic uncertainties in the $m_{4\ell}$ and $D_S$ analyses

In this appendix we discuss in more detail the prospects of the in Section 8.2 proposed binned-likelihood analyses of the $m_{4\ell}$ and $D_S$ spectra for the HL-LHC, the HE-LHC and the FCC. In particular, we examine how different assumptions on the systematic uncertainties affect the resulting constraints on the parameter space of the Higgs portal model (8.1).

In Table D.1, we report the 95% CL limits on $|c_\phi|$ derived from the binned-likelihood analysis of the $m_{4\ell}$ spectra in the case of the HL-LHC, HE-LHC and FCC, for three benchmark values $m_\phi = 100\,\text{GeV}$, $m_\phi = 150\,\text{GeV}$ and $m_\phi = 200\,\text{GeV}$ of the scalar mass. Different assumed values for the systematic uncertainty $\Delta$ are indicated, except in cases where the ensuing 95% CL limit exceeds the bound $|c_\phi| < 4\pi$ following from perturbative tree-level unitarity [449]. First of all, from Table D.1 it is evident that the assumed systematic uncertainty plays a crucial role in determining the sensitivity with which one can probe $|c_\phi|$, with an improvement on the 95% CL limit of about a

| $\Delta$ | HL-LHC | | | HE-LHC | | | FCC | | |
|---|---|---|---|---|---|---|---|---|---|
| | $m_\phi =$ 100 GeV | $m_\phi =$ 150 GeV | $m_\phi =$ 200 GeV | $m_\phi =$ 100 GeV | $m_\phi =$ 150 GeV | $m_\phi =$ 200 GeV | $m_\phi =$ 100 GeV | $m_\phi =$ 150 GeV | $m_\phi =$ 200 GeV |
| 50 % | - | - | - | - | - | - | 11.5 | - | - |
| 20 % | 12.0 | - | - | 10.0 | - | - | 8.5 | 10.3 | - |
| 8 % | 8.9 | 11.3 | - | 7.4 | 9.3 | 11.4 | 6.2 | 7.9 | 9.7 |
| 4 % | 7.4 | 9.7 | 11.7 | 5.9 | 7.7 | 9.5 | 4.8 | 6.4 | 8.1 |
| 2 % | 6.1 | 8.7 | 11.1 | 4.7 | 6.4 | 8.3 | 3.6 | 5.1 | 6.7 |
| 1 % | 5.2 | 8.3 | 10.8 | 3.7 | 5.6 | 7.6 | 2.8 | 4.0 | 5.4 |

**Table D.1:** 95% CL limits on $|c_\phi|$ derived from the binned-likelihood analysis of the $m_{4\ell}$ spectra in the case of the HL-LHC, HE-LHC and FCC. The limits are displayed for different values of the assumed systematic uncertainty, $\Delta = \{0.5, 0.2, 0.1, 0.08, 0.04, 0.02, 0.01\}$, and for three benchmark values $m_\phi = 100\,\text{GeV}$, $m_\phi = 150\,\text{GeV}$ and $m_\phi = 200\,\text{GeV}$ of the scalar mass. Values for the 95% CL limits that exceed the bound $|c_\phi| < 4\pi$ following from perturbative tree-level unitarity [449] are omitted.
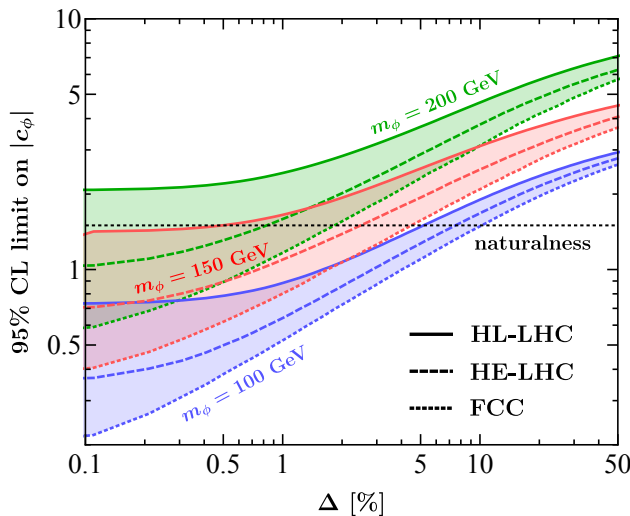
**Figure D.1:** 95% CL limits on $|c_\phi|$ derived from the binned-likelihood analysis of the $D_S$ spectra as a function of the assumed systematic uncertainty $\Delta$. The bounds for the HL-LHC (solid lines), the HE-LHC (dashed lines) and the FCC (dotted lines) are displayed for the three benchmark values $m_\phi = 100\,\mathrm{GeV}$ (blue), $m_\phi = 150\,\mathrm{GeV}$ (red) and $m_\phi = 200\,\mathrm{GeV}$ (green) of the scalar mass. The dotted black line corresponds to the condition $|c_\phi| = \sqrt{3}y_t^2 = 1.5$ that derives from naturalness arguments in models of neutral naturalness. See main text for additional details.

factor of four between an assumed $\Delta$ of 50% and 1% at FCC and $m_\phi = 100$ GeV. Still, we observe that even at the FCC, assuming a systematic uncertainty of a mere 1%, it is not possible to exclude the neutral-naturalness models discussed in Section 8.1, *i.e.* that lead to the condition condition $|c_\phi| = \sqrt{3}y_t^2 = 1.5$, using only the four-lepton invariant mass.

In Figure D.1, we show the projected 95% CL limits on $|c_\phi|$ derived from our $D_S$ analysis as a function of the assumed systematic uncertainty $\Delta$ for the three afore-mentioned colliders. The presented limits are obtained using the benchmark numerical values for the scalar masses indicated in the figure that vary between $100\,\mathrm{GeV} \leq m_\phi \leq 200\,\mathrm{GeV}$. Figure D.1 further illustrates the point already made in Sections 8.2.3 and 8.2.4, that the assumptions on the systematic uncertainties $\Delta$ play a crucial role in constraining the $m_\phi$–$|c_\phi|$ parameter space by using the $D_S$ distribution as a kinematic discriminant. In particular, one observes that the enhanced statistical power provided by the HE-LHC and the FCC, which results from the increased centre-of-mass energy and integrated luminosity of these machines compared to the HL-LHC, can only be fully exploited if systematic uncertainties are under control. For instance, in the case of $m_\phi = 100\,\mathrm{GeV}$ the sensitivity gain between the HL-LHC and the FCC is around 17% for $\Delta = 20\%$, while for $\Delta = 1\%$ the improvement amounts to about 41%. Similar numbers of approximately 26% and 51% are found for $m_\phi = 150\,\mathrm{GeV}$ and $m_\phi = 200\,\mathrm{GeV}$, implying that the gain in sensitivity between different colliders is to first approximation mass-independent for the low values of $m_\phi$ considered in the figure.

# Appendix E

# Details of the double-Higgs calculation

At the one-loop level the $gg \rightarrow hh$ process receives contributions from virtual $\phi$ exchange in propagator and vertex diagrams as well as counterterm contributions associated to wave-function, mass and tadpole renormalisation. Corresponding Feynman diagrams are shown in Figures E.1 and E.2, respectively — consult for instance [453, 455] for further details.

In the on-shell scheme the combined corrections involving the Wilson coefficient $c_\phi$
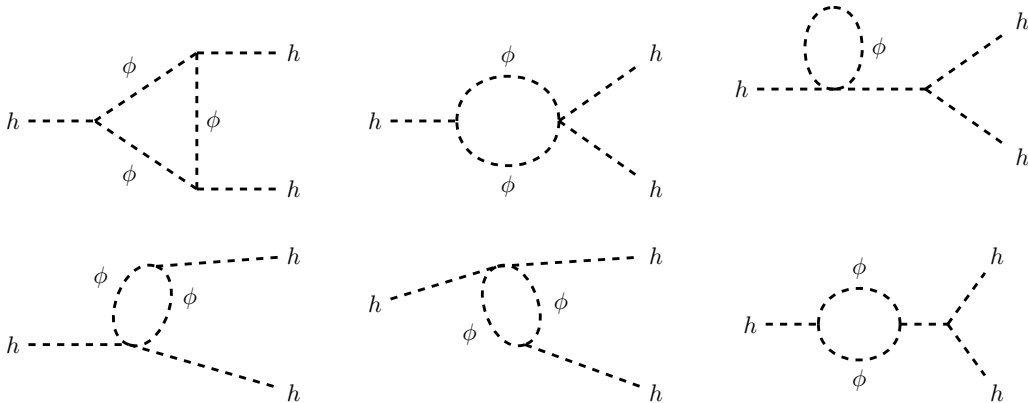


**Figure E.1:**  Diagrams representing a one-loop correction to the $hhh$ vertex and Higgs propagator involving $\phi$, which contribute to the $gg \rightarrow hh$ process at NLO.



**Figure E.2:**  Counter-term diagrams contributing to the $gg \rightarrow hh$ process at NLO, corresponding to wave-function, mass and tadpole renormalisation.
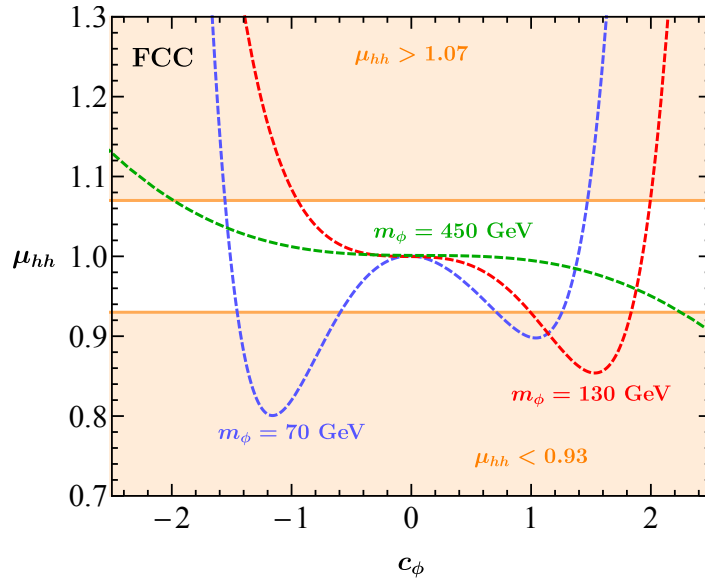
**Figure E.3:** The signal strength for double-Higgs production ($\mu_{hh}$) at the FCC as a function of the Wilson coefficient $c_\phi$ for three values of the scalar mass: $m_\phi = 70\,\text{GeV}$ (dashed blue), $m_\phi = 130\,\text{GeV}$ (dashed red) and $m_\phi = 450\,\text{GeV}$ (dashed green). The regions excluded by the projected experimental constraint $\mu_{hh} \in [0.93, 1.07]$ are shown in orange. For further explanations see main text.

can be written as a finite shift:

$$\lambda \to \lambda \left[ 1 + \delta(\hat{s}) \right]. \tag{E.1}$$

Here $\lambda = m_h^2/(2v^2)$ is the tree-level expression for the trilinear Higgs coupling in the SM and the $\hat{s}$-dependent form factor is given by

$$
\begin{aligned}
\delta(\hat{s}) = & -\frac{v^2 c_\phi^2}{24\pi^2 m_h^2} \left( 1 + \frac{3m_h^2}{\hat{s} - m_h^2} \right) \left[ B_0\big(\hat{s}, m_\phi^2, m_\phi^2\big) - B_0\big(m_h^2, m_\phi^2, m_\phi^2\big) \right] \\
& - \frac{v^4 c_\phi^3}{6\pi^2 m_h^2} C_0\big(m_h^2, m_h^2, \hat{s}, m_\phi^2, m_\phi^2, m_\phi^2\big) - \frac{v^2 c_\phi^2}{8\pi^2} \frac{d}{d\hat{s}} B_0\big(\hat{s}, m_\phi^2, m_\phi^2\big)\Big|_{\hat{s}=m_h^2},
\end{aligned}
\tag{E.2}
$$

with the $A_0$, $B_0$ and $C_0$ functions are one-, two-, and three-point Passarino-Veltman scalar integrals defined as in [290, 456]. Our result (E.2) agrees with [453, 455], after fixing a sign error in (12) of [455]. Notice that after integrating out the scalar field $\phi$ by expanding the on-shell form factor $\delta(2m_h^2)$ up to the first power in $m_h^2/m_\phi^2$, one recovers the approximate correction for $\kappa_\lambda$ as given in (8.10).

To obtain predictions for double-Higgs production we have implemented the analytic results (E.2) at the amplitude level into MCFM. We then perform sensitivity scans in the parameters $c_\phi$ and $m_\phi$, using the setup discussed at the beginning of Section 8.2.3, but fixing the renormalisation and factorisation scales $\mu_R$ and $\mu_F$ to the value $2m_h$. In Figure E.3 we show results for the signal strength $\mu_{hh}$ in double-Higgs production for three different values of $m_\phi$ as a function of $c_\phi$. The displayed curves correspond to the results obtained at the FCC. Two feature of the shown predictions deserve some

comments. First, due to the $c_\phi^3$ and $c_\phi^2$ dependence of (E.2) the signal strengths $\mu_{hh}$ are not symmetric under $c_\phi \leftrightarrow -c_\phi$. Second, the functional form of $\mu_{hh}$ depends also sensitively on the mass $m_\phi$. For low $\phi$ masses as illustrated by the choice $m_\phi = 70\,\mathrm{GeV}$ in the figure, the signal strength $\mu_{hh}$ has two minima, one at around $c_\phi \simeq -1.1$ and another one at $c_\phi \simeq 1.0$. This feature leads to the orange exclusions in the lower plot in Figure 8.7 at $|c_\phi| \simeq 1$. For larger values of $m_\phi$ the signal strengths $\mu_{hh}$ have instead only a single minimum at positive values of $c_\phi$. Notice that if the value of $\mu_{hh}$ at this minimum is incompatible with the experimental allowed range, such as happens to be the case for example for $m_\phi = 130\,\mathrm{GeV}$ at the FCC, increasing/decreasing the value of $c_\phi$ will always result in $\mu_{hh}$ values that are consistent with experiment. This feature leads to the orange exclusions shown in the plots of Figures 8.6 and 8.7 that are relevant for $c_\phi > 0$ and separated by a funnel of viable solutions.

# Acknowledgements

# Bibliography

[1] ATLAS collaboration, G. Aad et al., *Observation of a new particle in the search for the Standard Model Higgs boson with the ATLAS detector at the LHC*, *Phys. Lett. B* **716** (2012) 1–29, [1207.7214].

[2] CMS collaboration, S. Chatrchyan et al., *Observation of a New Boson at a Mass of 125 GeV with the CMS Experiment at the LHC*, *Phys. Lett. B* **716** (2012) 30–61, [1207.7235].

[3] J. Bardeen, L. N. Cooper and J. R. Schrieffer, *Theory of superconductivity*, *Phys. Rev.* **108** (1957) 1175–1204.

[4] Y. Nambu, *Quasiparticles and Gauge Invariance in the Theory of Superconductivity*, *Phys. Rev.* **117** (1960) 648–663.

[5] P. W. Anderson, *Plasmons, Gauge Invariance, and Mass*, *Phys. Rev.* **130** (1963) 439–442.

[6] Y. Nambu, *Axial vector current conservation in weak interactions*, *Phys. Rev. Lett.* **4** (1960) 380–382.

[7] J. Goldstone, *Field Theories with Superconductor Solutions*, *Nuovo Cim.* **19** (1961) 154–164.

[8] J. Goldstone, A. Salam and S. Weinberg, *Broken Symmetries*, *Phys. Rev.* **127** (1962) 965–970.

[9] F. Englert and R. Brout, *Broken Symmetry and the Mass of Gauge Vector Mesons*, *Phys. Rev. Lett.* **13** (1964) 321–323.

[10] P. W. Higgs, *Broken symmetries, massless particles and gauge fields*, *Phys. Lett.* **12** (1964) 132–133.

[11] P. W. Higgs, *Broken Symmetries and the Masses of Gauge Bosons*, *Phys. Rev. Lett.* **13** (1964) 508–509.

[12] G. S. Guralnik, C. R. Hagen and T. W. B. Kibble, *Global Conservation Laws and Massless Particles*, *Phys. Rev. Lett.* **13** (1964) 585–587.

[13] S. L. Glashow, *Partial Symmetries of Weak Interactions*, *Nucl. Phys.* **22** (1961) 579–588.

[14] S. Weinberg, *A Model of Leptons*, *Phys. Rev. Lett.* **19** (1967) 1264–1266.

[15] A. Salam, *Weak and Electromagnetic Interactions*, *Conf. Proc. C* **680519** (1968) 367–377.

[16] G. 't Hooft, *Renormalizable Lagrangians for Massive Yang-Mills Fields*, *Nucl. Phys. B* **35** (1971) 167–188.

[17] G. 't Hooft and M. J. G. Veltman, *Regularization and Renormalization of Gauge Fields*, *Nucl. Phys. B* **44** (1972) 189–213.

[18] M. Gell-Mann, *A Schematic Model of Baryons and Mesons*, *Phys. Lett.* **8** (1964) 214–215.

[19] G. Zweig, *An SU(3) model for strong interaction symmetry and its breaking. Version 1*, .

[20] H. Fritzsch, M. Gell-Mann and H. Leutwyler, *Advantages of the Color Octet Gluon Picture*, *Phys. Lett. B* **47** (1973) 365–368.

[21] D. J. Gross and F. Wilczek, *Ultraviolet Behavior of Nonabelian Gauge Theories*, *Phys. Rev. Lett.* **30** (1973) 1343–1346.

[22] H. D. Politzer, *Reliable Perturbative Results for Strong Interactions?*, *Phys. Rev. Lett.* **30** (1973) 1346–1349.

[23] Particle Data Group collaboration, P. A. Zyla et al., *Review of Particle Physics*, *PTEP* **2020** (2020) 083C01.

[24] CMS collaboration, *Combined Higgs boson production and decay measurements with up to* $137\,\text{fb}^{-1}$ *of proton-proton collision data at* $\sqrt{s} = 13\,\text{TeV}$, tech. rep., CERN, Geneva, 2020.

[25] ATLAS collaboration, *Combined measurements of Higgs boson production and decay using up to* $139\,fb^{-1}$ *of proton-proton collision data at* $\sqrt{s} = 13\,TeV$ *collected with the ATLAS experiment*, .

[26] G. P. Salam, L.-T. Wang and G. Zanderighi, *The Higgs boson turns ten*, *Nature* **607** (2022) 41–47, [2207.00478].

[27] CMS collaboration, A. M. Sirunyan et al., *Evidence for Higgs boson decay to a pair of muons*, *JHEP* **01** (2021) 148, [2009.04363].

[28] M. Cepeda et al., *Report from Working Group 2: Higgs Physics at the HL-LHC and HE-LHC*, *CERN Yellow Rep. Monogr.* **7** (2019) 221–584, [1902.00134].

[29] ATLAS collaboration, *A detailed map of Higgs boson interactions by the ATLAS experiment ten years after the discovery*, *Nature* **607** (2022) 52–59, [2207.00092].

[30] CMS collaboration, *A portrait of the Higgs boson by the CMS experiment ten years after the discovery*, *Nature* **607** (2022) 60–68, [2207.00043].

[31] M. Kado, "The Discovery of the Higgs Boson: a 30 year-long experimental enterprise." Tea Break Special Edition: Happy Birthday Higgs Boson, GGI Firenze (Italy), 6-7-2022, 2022.

[32] P. Nason, *A New method for combining NLO QCD with shower Monte Carlo algorithms*, *JHEP* **11** (2004) 040, [hep-ph/0409146].

[33] S. Frixione, P. Nason and C. Oleari, *Matching NLO QCD computations with Parton Shower simulations: the POWHEG method*, *JHEP* **11** (2007) 070, [0709.2092].

[34] P. F. Monni, P. Nason, E. Re, M. Wiesemann and G. Zanderighi, *MiNNLO$_{PS}$: a new method to match NNLO QCD to parton showers*, *JHEP* **05** (2020) 143, [1908.06987].

[35] P. F. Monni, E. Re and M. Wiesemann, *MiNNLO$_{PS}$: optimizing* $2 \to 1$ *hadronic processes*, *Eur. Phys. J. C* **80** (2020) 1075, [2006.04133].

[36] ALEPH, CDF, D0, DELPHI, L3, OPAL, SLD, LEP Electroweak Working Group, Tevatron Electroweak Working Group, SLD Electroweak, Heavy Flavour Groups collaboration, *Precision Electroweak Measurements and Constraints on the Standard Model*, 1012.2367.

[37] Super-Kamiokande collaboration, Y. Fukuda et al., *Evidence for oscillation of atmospheric neutrinos*, *Phys. Rev. Lett.* **81** (1998) 1562–1567, [hep-ex/9807003].

[38] SNO collaboration, Q. R. Ahmad et al., *Direct evidence for neutrino flavor transformation from neutral current interactions in the Sudbury Neutrino Observatory*, *Phys. Rev. Lett.* **89** (2002) 011301, [nucl-ex/0204008].

[39] Planck collaboration, N. Aghanim et al., *Planck 2018 results. VI. Cosmological parameters*, *Astron. Astrophys.* **641** (2020) A6, [1807.06209].

[40] M. Kobayashi and T. Maskawa, *CP Violation in the Renormalizable Theory of Weak Interaction*, *Prog. Theor. Phys.* **49** (1973) 652–657.

[41] J. Alison et al., *Higgs boson potential at colliders: Status and perspectives*, *Rev. Phys.* **5** (2020) 100045, [1910.00012].

[42] U. Haisch and G. Koole, *Probing Higgs portals with matrix-element based kinematic discriminants in* $ZZ \to 4\ell$ *production*, *JHEP* **04** (2022) 166, [2201.09711].

[43] U. Haisch and G. Koole, *Off-shell Higgs production at the LHC as a probe of the trilinear Higgs coupling*, *JHEP* **02** (2022) 030, [2111.12589].

[44] L. Buonocore, G. Koole, D. Lombardi, L. Rottoli, M. Wiesemann and G. Zanderighi, *ZZ production at nNNLO+PS with MiNNLO$_{PS}$*, *JHEP* **01** (2022) 072, [2108.05337].

[45] U. Haisch and G. Koole, *Beautiful and charming chromodipole moments*, *JHEP* **09** (2021) 133, [2106.01289].

[46] L. Buonocore et al., *NNLO+PS with MiNNLO_PS: status and prospects*, 3, 2022. 2203.07240.

[47] R. Fleischer, R. Jaarsma and G. Koole, *Testing Lepton Flavour Universality with (Semi)-Leptonic $D_{(s)}$ Decays*, *Eur. Phys. J. C* **80** (2020) 153, [1912.08641].

[48] V. N. Gribov and L. N. Lipatov, *Deep inelastic e p scattering in perturbation theory*, *Sov. J. Nucl. Phys.* **15** (1972) 438–450.

[49] G. Altarelli and G. Parisi, *Asymptotic Freedom in Parton Language*, *Nucl. Phys.* **B126** (1977) 298–318.

[50] Y. L. Dokshitzer, *Calculation of the Structure Functions for Deep Inelastic Scattering and e+ e- Annihilation by Perturbation Theory in Quantum Chromodynamics.*, *Sov. Phys. JETP* **46** (1977) 641–653.

[51] S. Moch, J. A. M. Vermaseren and A. Vogt, *The Three loop splitting functions in QCD: The Nonsinglet case*, *Nucl. Phys. B* **688** (2004) 101–134, [hep-ph/0403192].

[52] A. Vogt, S. Moch and J. A. M. Vermaseren, *The Three-loop splitting functions in QCD: The Singlet case*, *Nucl. Phys. B* **691** (2004) 129–181, [hep-ph/0404111].

[53] S. Höche, *Introduction to parton-shower event generators*, in *Theoretical Advanced Study Institute in Elementary Particle Physics: Journeys Through the Precision Frontier: Amplitudes for Colliders*, pp. 235–295, 2015. 1411.4085. DOI.

[54] S. Frixione and B. R. Webber, *Matching NLO QCD computations and parton shower simulations*, *JHEP* **06** (2002) 029, [hep-ph/0204244].

[55] S. Frixione, P. Nason and B. R. Webber, *Matching NLO QCD and parton showers in heavy flavor production*, *JHEP* **08** (2003) 007, [hep-ph/0305252].

[56] S. Frixione and B. R. Webber, *The MC@NLO 2.0 event generator*, hep-ph/0307146.

[57] K. Hamilton, P. Nason and G. Zanderighi, *MINLO: Multi-Scale Improved NLO*, *JHEP* **10** (2012) 155, [1206.3572].

[58] K. Hamilton, P. Nason, C. Oleari and G. Zanderighi, *Merging H/W/Z + 0 and 1 jet at NLO with no merging scale: a path to parton shower + NNLO matching*, *JHEP* **05** (2013) 082, [1212.4504].

[59] K. Hamilton, P. Nason, E. Re and G. Zanderighi, *NNLOPS simulation of Higgs boson production*, *JHEP* **10** (2013) 222, [1309.0017].

[60] G. Ferrera, M. Grazzini and F. Tramontano, *Associated WH production at hadron colliders: a fully exclusive QCD calculation at NNLO*, *Phys. Rev. Lett.* **107** (2011) 152003, [1107.1164].

[61] G. Ferrera, M. Grazzini and F. Tramontano, *Associated ZH production at hadron colliders: the fully differential NNLO QCD calculation*, *Phys. Lett.* **B740** (2015) 51–55, [1407.4747].

[62] G. Ferrera, G. Somogyi and F. Tramontano, *Associated production of a Higgs boson decaying into bottom quarks at the LHC in full NNLO QCD*, *Phys. Lett.* **B780** (2018) 346–351, [1705.10304].

[63] J. M. Campbell, R. K. Ellis and C. Williams, *Associated production of a Higgs boson at NNLO*, *JHEP* **06** (2016) 179, [1601.00658].

[64] R. V. Harlander and W. B. Kilgore, *Higgs boson production in bottom quark fusion at next-to-next-to leading order*, *Phys. Rev.* **D68** (2003) 013001, [hep-ph/0304035].

[65] R. V. Harlander, K. J. Ozeren and M. Wiesemann, *Higgs plus jet production in bottom quark annihilation at next-to-leading order*, *Phys. Lett.* **B693** (2010) 269–273, [1007.5411].

[66] R. Harlander and M. Wiesemann, *Jet-veto in bottom-quark induced Higgs production at next-to-next-to-leading order*, *JHEP* **04** (2012) 066, [1111.2182].

[67] S. Bühler, F. Herzog, A. Lazopoulos and R. Müller, *The fully differential hadronic production of a Higgs boson via bottom quark fusion at NNLO*, *JHEP* **07** (2012) 115, [1204.4415].

[68] S. Marzani, R. D. Ball, V. Del Duca, S. Forte and A. Vicini, *Higgs production via gluon-gluon fusion with finite top mass beyond next-to-leading order*, *Nucl. Phys.* **B800** (2008) 127–145, [0801.2544].

[69] R. V. Harlander and K. J. Ozeren, *Finite top mass effects for hadronic Higgs production at next-to-next-to-leading order*, *JHEP* **11** (2009) 088, [0909.3420].

[70] R. V. Harlander, H. Mantler, S. Marzani and K. J. Ozeren, *Higgs production in gluon fusion at next-to-next-to-leading order QCD for finite top mass*, *Eur. Phys. J.* **C66** (2010) 359–372, [0912.2104].

[71] A. Pak, M. Rogal and M. Steinhauser, *Finite top quark mass effects in NNLO Higgs boson production at LHC*, *JHEP* **02** (2010) 025, [0911.4662].

[72] T. Neumann and M. Wiesemann, *Finite top-mass effects in gluon-induced Higgs production with a jet-veto at NNLO*, *JHEP* **11** (2014) 150, [1408.6836].

[73] S. Catani, L. Cieri, D. de Florian, G. Ferrera and M. Grazzini, *Diphoton production at hadron colliders: a fully-differential QCD calculation at NNLO*, *Phys. Rev. Lett.* **108** (2012) 072001, [1110.2375].

[74] J. M. Campbell, R. K. Ellis, Y. Li and C. Williams, *Predictions for diphoton production at the LHC through NNLO in QCD*, *JHEP* **07** (2016) 148, [1603.02663].

[75] M. Grazzini, S. Kallweit, D. Rathlev and A. Torre, *$Z\gamma$ production at hadron colliders in NNLO QCD*, *Phys. Lett.* **B731** (2014) 204–207, [1309.7000].

[76] M. Grazzini, S. Kallweit and D. Rathlev, *$W\gamma$ and $Z\gamma$ production at the LHC in NNLO QCD*, *JHEP* **07** (2015) 085, [1504.01330].

[77] J. M. Campbell, T. Neumann and C. Williams, *$Z\gamma$ Production at NNLO Including Anomalous Couplings*, *JHEP* **11** (2017) 150, [1708.02925].

[78] T. Gehrmann, N. Glover, A. Huss and J. Whitehead, *Scale and isolation sensitivity of diphoton distributions at the LHC*, *JHEP* **01** (2021) 108, [2009.11310].

[79] F. Cascioli, T. Gehrmann, M. Grazzini, S. Kallweit, P. Maierhöfer, A. von Manteuffel, S. Pozzorini, D. Rathlev, L. Tancredi and E. Weihs, *ZZ production at hadron colliders in NNLO QCD*, *Phys. Lett. B* **735** (2014) 311–313, [1405.2219].

[80] M. Grazzini, S. Kallweit and D. Rathlev, *ZZ production at the LHC: fiducial cross sections and distributions in NNLO QCD*, *Phys. Lett. B* **750** (2015) 407–410, [1507.06257].

[81] G. Heinrich, S. Jahn, S. P. Jones, M. Kerner and J. Pires, *NNLO predictions for Z-boson pair production at the LHC*, *JHEP* **03** (2018) 142, [1710.06294].

[82] S. Kallweit and M. Wiesemann, *ZZ production at the LHC: NNLO predictions for $2\ell2\nu$ and $4\ell$ signatures*, *Phys. Lett. B* **786** (2018) 382–389, [1806.05941].

[83] T. Gehrmann, M. Grazzini, S. Kallweit, P. Maierhöfer, A. von Manteuffel, S. Pozzorini, D. Rathlev and L. Tancredi, *$W^+W^-$ Production at Hadron Colliders in Next to Next to Leading Order QCD*, *Phys. Rev. Lett.* **113** (2014) 212001, [1408.5243].

[84] M. Grazzini, S. Kallweit, S. Pozzorini, D. Rathlev and M. Wiesemann, *$W^+W^-$ production at the LHC: fiducial cross sections and distributions in NNLO QCD*, *JHEP* **08** (2016) 140, [1605.02716].

[85] M. Grazzini, S. Kallweit, D. Rathlev and M. Wiesemann, *$W^\pm Z$ production at hadron colliders in NNLO QCD*, *Phys. Lett.* **B761** (2016) 179–183, [1604.08576].

[86] M. Grazzini, S. Kallweit, D. Rathlev and M. Wiesemann, *$W^\pm Z$ production at the LHC: fiducial cross sections and distributions in NNLO QCD*, *JHEP* **05** (2017) 139, [1703.09065].

[87] D. de Florian and J. Mazzitelli, *Higgs Boson Pair Production at Next-to-Next-to-Leading Order in QCD*, *Phys. Rev. Lett.* **111** (2013) 201801, [1309.6594].

[88] D. de Florian, M. Grazzini, C. Hanga, S. Kallweit, J. M. Lindert, P. Maierhöfer, J. Mazzitelli and D. Rathlev, *Differential Higgs Boson Pair Production at Next-to-Next-to-Leading Order in QCD*, *JHEP* **09** (2016) 151, [1606.09519].

[89] M. Grazzini, G. Heinrich, S. Jones, S. Kallweit, M. Kerner, J. M. Lindert and J. Mazzitelli, *Higgs boson pair production at NNLO with top quark mass effects*, *JHEP* **05** (2018) 059, [1803.02463].

[90] J. Baglio, A. Djouadi, R. Gröber, M. Mühlleitner, J. Quevillon and M. Spira, *The measurement of the Higgs self-coupling at the LHC: theoretical status*, *JHEP* **04** (2013) 151, [1212.5581].

[91] H. T. Li and J. Wang, *Fully Differential Higgs Pair Production in Association With a W Boson at Next-to-Next-to-Leading Order in QCD*, *Phys. Lett. B* **765** (2017) 265–271, [1607.06382].

[92] D. de Florian, I. Fabre and J. Mazzitelli, *Triple Higgs production at hadron colliders at NNLO in QCD*, *JHEP* **03** (2020) 155, [1912.02760].

[93] M. Czakon, R. V. Harlander, J. Klappert and M. Niggetiedt, *Exact Top-Quark Mass Dependence in Hadronic Higgs Production*, *Phys. Rev. Lett.* **127** (2021) 162002, [2105.04436].

[94] G. Heinrich, *Collider Physics at the Precision Frontier*, *Phys. Rept.* **922** (2021) 1–69, [2009.00516].

[95] H. A. Chawdhry, M. L. Czakon, A. Mitov and R. Poncelet, *NNLO QCD corrections to three-photon production at the LHC*, *JHEP* **02** (2020) 057, [1911.00479].

[96] S. Kallweit, V. Sotnikov and M. Wiesemann, *Triphoton production at hadron colliders in NNLO QCD*, *Phys. Lett. B* **812** (2021) 136013, [2010.04681].

[97] M. Czakon, A. Mitov and R. Poncelet, *Tour de force in Quantum Chromodynamics: A first next-to-next-to-leading order study of three-jet production at the LHC*, 2106.05331.

[98] H. A. Chawdhry, M. Czakon, A. Mitov and R. Poncelet, *NNLO QCD corrections to diphoton production with an additional jet at the LHC*, 2105.06940.

[99] A. Karlberg, E. Re and G. Zanderighi, *NNLOPS accurate Drell-Yan production*, *JHEP* **09** (2014) 134, [1407.2940].

[100] W. Astill, W. Bizon, E. Re and G. Zanderighi, *NNLOPS accurate associated HW production*, *JHEP* **06** (2016) 154, [1603.01620].

[101] W. Astill, W. Bizoń, E. Re and G. Zanderighi, *NNLOPS accurate associated HZ production with H → b$\bar{b}$ decay at NLO*, *JHEP* **11** (2018) 157, [1804.08141].

[102] E. Re, M. Wiesemann and G. Zanderighi, *NNLOPS accurate predictions for $W^+W^-$ production*, *JHEP* **12** (2018) 121, [1805.09857].

[103] S. Höche, Y. Li and S. Prestel, *Higgs-boson production through gluon fusion at NNLO QCD with parton showers*, *Phys. Rev.* **D90** (2014) 054011, [1407.3773].

[104] S. Höche, Y. Li and S. Prestel, *Drell-Yan lepton pair production at NNLO QCD with parton showers*, *Phys. Rev.* **D91** (2015) 074015, [1405.3607].

[105] S. Alioli, C. W. Bauer, C. J. Berggren, A. Hornig, F. J. Tackmann, C. K. Vermilion, J. R. Walsh and S. Zuberi, *Combining Higher-Order Resummation with Multiple NLO Calculations and Parton Showers in GENEVA*, *JHEP* **09** (2013) 120, [1211.7049].

[106] S. Alioli, C. W. Bauer, C. Berggren, F. J. Tackmann, J. R. Walsh and S. Zuberi, *Matching Fully Differential NNLO Calculations and Parton Showers*, *JHEP* **06** (2014) 089, [1311.0286].

[107] S. Alioli, C. W. Bauer, C. Berggren, F. J. Tackmann and J. R. Walsh, *Drell-Yan production at NNLL'+NNLO matched to parton showers*, *Phys. Rev.* **D92** (2015) 094020, [1508.01475].

[108] S. Alioli, A. Broggio, S. Kallweit, M. A. Lim and L. Rottoli, *Higgsstrahlung at NNLL'+NNLO matched to parton showers in GENEVA*, *Phys. Rev.* **D100** (2019) 096016, [1909.02026].

[109] S. Alioli, A. Broggio, A. Gavardi, S. Kallweit, M. A. Lim, R. Nagar, D. Napoletano and L. Rottoli, *Precise predictions for photon pair production matched to parton showers in GENEVA*, 2010.10498.

[110] S. Alioli, A. Broggio, A. Gavardi, S. Kallweit, M. A. Lim, R. Nagar, D. Napoletano and L. Rottoli, *Resummed predictions for hadronic Higgs boson decays*, 2009.13533.

[111] S. Alioli, A. Broggio, A. Gavardi, S. Kallweit, M. A. Lim, R. Nagar and D. Napoletano, *Next-to-next-to-leading order event generation for Z boson pair production matched to parton shower*, *Phys. Lett. B* **818** (2021) 136380, [2103.01214].

[112] T. Cridge, M. A. Lim and R. Nagar, *Wγ production at NNLO+PS accuracy in GENEVA*, 2105.13214.

[113] S. Alioli, A. Broggio, A. Gavardi, S. Kallweit, M. A. Lim, R. Nagar, D. Napoletano, C. W. Bauer and L. Rottoli, *Matching NNLO to parton shower using $N^3LL$ colour-singlet transverse momentum resummation in GENEVA*, 2102.08390.

[114] D. Lombardi, M. Wiesemann and G. Zanderighi, *Advancing MiNNLO$_{PS}$ to diboson processes: Zγ production at NNLO+PS*, 2010.10478.

[115] D. Lombardi, M. Wiesemann and G. Zanderighi, *$W^+W^-$ production at NNLO+PS with MiNNLO$_{PS}$*, 2103.12077.

[116] J. Mazzitelli, P. F. Monni, P. Nason, E. Re, M. Wiesemann and G. Zanderighi, *Next-to-next-to-leading order event generation for top-quark pair production*, 2012.14267.

[117] J. C. Collins, D. E. Soper and G. F. Sterman, *Factorization of Hard Processes in QCD*, *Adv. Ser. Direct. High Energy Phys.* **5** (1989) 1–91, [hep-ph/0409313].

[118] T. Kinoshita, *Mass singularities of Feynman amplitudes*, *J. Math. Phys.* **3** (1962) 650–677.

[119] T. D. Lee and M. Nauenberg, *Degenerate Systems and Mass Singularities*, *Phys. Rev.* **133** (1964) B1549–B1562.

[120] F. Bloch and A. Nordsieck, *Note on the Radiation Field of the electron*, *Phys. Rev.* **52** (1937) 54–59.

[121] G. Luisoni and S. Marzani, *QCD resummation for hadronic final states*, *J. Phys. G* **42** (2015) 103101, [1505.04084].

[122] R. K. Ellis, W. J. Stirling and B. R. Webber, *QCD and collider physics*, vol. 8. Cambridge University Press, 2, 2011, 10.1017/CBO9780511628788.

[123] A. Gehrmann-De Ridder, T. Gehrmann, E. W. N. Glover and G. Heinrich, *NNLO corrections to event shapes in e+ e- annihilation*, *JHEP* **12** (2007) 094, [0711.4711].

[124] M. E. Peskin and D. V. Schroeder, *An Introduction to quantum field theory*. Addison-Wesley, Reading, USA, 1995.

[125] G. F. Sterman and S. Weinberg, *Jets from Quantum Chromodynamics*, *Phys. Rev. Lett.* **39** (1977) 1436.

[126] S. D. Ellis and D. E. Soper, *Successive combination jet algorithm for hadron collisions*, *Phys. Rev. D* **48** (1993) 3160–3166, [hep-ph/9305266].

[127] S. Catani, Y. L. Dokshitzer, M. H. Seymour and B. R. Webber, *Longitudinally invariant $K_t$ clustering algorithms for hadron hadron collisions*, *Nucl. Phys. B* **406** (1993) 187–224.

[128] M. Cacciari, G. P. Salam and G. Soyez, *The anti-$k_t$ jet clustering algorithm*, *JHEP* **04** (2008) 063, [0802.1189].

[129] G. Curci, W. Furmanski and R. Petronzio, *Evolution of Parton Densities Beyond Leading Order: The Nonsinglet Case*, *Nucl. Phys. B* **175** (1980) 27–92.

[130] W. Furmanski and R. Petronzio, *Singlet Parton Densities Beyond Leading Order*, *Phys. Lett. B* **97** (1980) 437–442.

[131] T. Gehrmann and N. Greiner, *Photon Radiation with MadDipole*, *JHEP* **12** (2010) 050, [1011.0321].

[132] V. V. Sudakov, *Vertex parts at very high-energies in quantum electrodynamics*, *Sov. Phys. JETP* **3** (1956) 65–71.

[133] G. Parisi and R. Petronzio, *Small Transverse Momentum Distributions in Hard Processes*, *Nucl. Phys. B* **154** (1979) 427–440.

[134] J. C. Collins, D. E. Soper and G. F. Sterman, *Transverse Momentum Distribution in Drell-Yan Pair and W and Z Boson Production*, *Nucl. Phys. B* **250** (1985) 199–224.

[135] R. K. Ellis, D. A. Ross and S. Veseli, *Vector boson production in hadronic collisions*, *Nucl. Phys. B* **503** (1997) 309–338, [hep-ph/9704239].

[136] R. K. Ellis and S. Veseli, *W and Z transverse momentum distributions: Resummation in $q_T$ space*, *Nucl. Phys. B* **511** (1998) 649–669, [hep-ph/9706526].

[137] A. Kulesza and W. J. Stirling, *Sudakov logarithm resummation in transverse momentum space for electroweak boson production at hadron colliders*, *Nucl. Phys. B* **555** (1999) 279–305, [hep-ph/9902234].

[138] J. Campbell, J. Huston and F. Krauss, *The Black Book of Quantum Chromodynamics: A Primer for the LHC Era*. Oxford University Press, 12, 2017.

[139] D. de Florian and M. Grazzini, *Next-to-next-to-leading logarithmic corrections at small transverse momentum in hadronic collisions*, *Phys. Rev. Lett.* **85** (2000) 4678–4681, [hep-ph/0008152].

[140] D. de Florian and M. Grazzini, *The Structure of large logarithmic corrections at small transverse momentum in hadronic collisions*, *Nucl. Phys.* **B616** (2001) 247–285, [hep-ph/0108273].

[141] P. F. Monni, E. Re and P. Torrielli, *Higgs Transverse-Momentum Resummation in Direct Space*, *Phys. Rev. Lett.* **116** (2016) 242001, [1604.02191].

[142] W. Bizon, P. F. Monni, E. Re, L. Rottoli and P. Torrielli, *Momentum-space resummation for transverse observables and the Higgs $p_\perp$ at $N^3LL+NNLO$*, 1705.09127.

[143] G. Bozzi, S. Catani, D. de Florian and M. Grazzini, *Transverse-momentum resummation and the spectrum of the Higgs boson at the LHC*, *Nucl. Phys.* **B737** (2006) 73–120, [hep-ph/0508068].

[144] A. Banfi, P. F. Monni, G. P. Salam and G. Zanderighi, *Higgs and Z-boson production with a jet veto*, *Phys. Rev. Lett.* **109** (2012) 202001, [1206.4998].

[145] T. Sjostrand, S. Mrenna and P. Z. Skands, *PYTHIA 6.4 Physics and Manual*, *JHEP* **0605** (2006) 026, [hep-ph/0603175].

[146] T. Sjöstrand, S. Ask, J. R. Christiansen, R. Corke, N. Desai, P. Ilten, S. Mrenna, S. Prestel, C. O. Rasmussen and P. Z. Skands, *An introduction to PYTHIA 8.2*, *Comput. Phys. Commun.* **191** (2015) 159–177, [1410.3012].

[147] G. Corcella, I. G. Knowles, G. Marchesini, S. Moretti, K. Odagiri, P. Richardson, M. H. Seymour and B. R. Webber, *HERWIG 6: An Event generator for hadron emission reactions with interfering gluons (including supersymmetric processes)*, *JHEP* **01** (2001) 010, [hep-ph/0011363].

[148] J. Bellm et al., *Herwig 7.0/Herwig++ 3.0 release note*, *Eur. Phys. J. C* **76** (2016) 196, [1512.01178].

[149] T. Gleisberg, S. Hoeche, F. Krauss, M. Schonherr, S. Schumann, F. Siegert and J. Winter, *Event generation with SHERPA 1.1*, *JHEP* **02** (2009) 007, [0811.4622].

[150] Sherpa collaboration, E. Bothmann et al., *Event Generation with Sherpa 2.2*, *SciPost Phys.* **7** (2019) 034, [1905.09127].

[151] M. H. Seymour, *Matrix element corrections to parton shower algorithms*, *Comput. Phys. Commun.* **90** (1995) 95–101, [hep-ph/9410414].

[152] C. Bierlich et al., *A comprehensive guide to the physics and usage of PYTHIA 8.3*, 2203.11601.

[153] S. Catani, B. R. Webber and G. Marchesini, *QCD coherent branching and semiinclusive processes at large x*, *Nucl. Phys. B* **349** (1991) 635–654.

[154] S. Catani, F. Krauss, R. Kuhn and B. R. Webber, *QCD matrix elements + parton showers*, *JHEP* **11** (2001) 063, [hep-ph/0109231].

[155] J. Alwall et al., *Comparative study of various algorithms for the merging of parton showers and matrix elements in hadronic collisions*, *Eur. Phys. J. C* **53** (2008) 473–500, [0706.2569].

[156] ATLAS collaboration, *Standard Model Summary Plots February 2022*, .

[157] L. Lönnblad and S. Prestel, *Merging Multi-leg NLO Matrix Elements with Parton Showers*, *JHEP* **03** (2013) 166, [1211.7278].

[158] S. Höche, Y. Li and S. Prestel, *Drell-Yan lepton pair production at NNLO QCD with parton showers*, *Phys. Rev. D* **91** (2015) 074015, [1405.3607].

[159] S. Frixione, Z. Kunszt and A. Signer, *Three jet cross-sections to next-to-leading order*, *Nucl. Phys.* **B467** (1996) 399–442, [hep-ph/9512328].

[160] S. Frixione, *A General approach to jet cross-sections in QCD*, *Nucl. Phys.* **B507** (1997) 295–314, [hep-ph/9706545].

[161] S. Catani and M. Seymour, *A General algorithm for calculating jet cross-sections in NLO QCD*, *Nucl. Phys.* **B485** (1997) 291–419, [hep-ph/9605323].

[162] K. Hamilton, T. Melia, P. F. Monni, E. Re and G. Zanderighi, *Merging WW and WW+jet with MINLO*, *JHEP* **09** (2016) 057, [1606.07062].

[163] R. Frederix and K. Hamilton, *Extending the MINLO method*, *JHEP* **05** (2016) 042, [1512.02663].

[164] D. Lombardi, M. Wiesemann and G. Zanderighi, *Anomalous couplings in $Z\gamma$ events at NNLO+PS and improving $\nu\nu\,\bar{}\gamma$ backgrounds in dark-matter searches*, *Phys. Lett. B* **824** (2022) 136846, [2108.11315].

[165] S. Zanoli, M. Chiesa, E. Re, M. Wiesemann and G. Zanderighi, *Next-to-next-to-leading order event generation for $VH$ production with $H \to b\bar{b}$ decay*, 2112.04168.

[166] U. Haisch, D. J. Scott, M. Wiesemann, G. Zanderighi and S. Zanoli, *NNLO event generation for $pp \to Zh \to \ell^+\ell^- b\bar{b}$ production in the SM effective field theory*, 2204.00663.

[167] J. Mazzitelli, P. F. Monni, P. Nason, E. Re, M. Wiesemann and G. Zanderighi, *Top-pair production at the LHC with MINNLO_PS*, *JHEP* **04** (2022) 079, [2112.12135].

[168] F. Caola and K. Melnikov, *Constraining the Higgs boson width with ZZ production at the LHC*, *Phys. Rev. D* **88** (2013) 054024, [1307.4935].

[169] J. M. Campbell, R. K. Ellis and C. Williams, *Bounding the Higgs Width at the LHC Using Full Analytic Results for $gg \to e^-e^+\mu^-\mu^+$*, *JHEP* **04** (2014) 060, [1311.3589].

[170] J. M. Campbell, R. K. Ellis and C. Williams, *Bounding the Higgs width at the LHC: Complementary results from $H \to WW$*, *Phys. Rev.* **D89** (2014) 053011, [1312.1628].

[171] J. M. Campbell, R. K. Ellis and C. Williams, *Bounding the Higgs Width at the LHC*, *PoS* **LL2014** (2014) 008, [1408.1723].

[172] M. Grazzini, S. Kallweit, M. Wiesemann and J. Y. Yook, *Four lepton production in gluon fusion: Off-shell Higgs effects in NLO QCD*, *Phys. Lett. B* **819** (2021) 136465, [2102.08344].

[173] CMS collaboration, V. Khachatryan et al., *Constraints on the Higgs boson width from off-shell production and decay to Z-boson pairs*, *Phys. Lett. B* **736** (2014) 64–85, [1405.3455].

[174] ATLAS collaboration, G. Aad et al., *Constraints on the off-shell Higgs boson signal strength in the high-mass ZZ and WW final states with the ATLAS detector*, *Eur. Phys. J.* **C75** (2015) 335, [1503.01060].

[175] CMS collaboration, V. Khachatryan et al., *Limits on the Higgs boson lifetime and width from its decay to four charged leptons*, *Phys. Rev. D* **92** (2015) 072010, [1507.06656].

[176] CMS collaboration, V. Khachatryan et al., *Search for Higgs boson off-shell production in proton-proton collisions at 7 and 8 TeV and derivation of constraints on its total decay width*, *JHEP* **09** (2016) 051, [1605.02329].

[177] ATLAS collaboration, M. Aaboud et al., *Constraints on off-shell Higgs boson production and the Higgs boson total width in $ZZ \to 4\ell$ and $ZZ \to 2\ell2\nu$ final states with the ATLAS detector*, *Phys. Lett.* **B786** (2018) 223–244, [1808.01191].

[178] CMS collaboration, A. M. Sirunyan et al., *Measurements of the Higgs boson width and anomalous HVV couplings from on-shell and off-shell production in the four-lepton final state*, *Phys. Rev. D* **99** (2019) 112003, [1901.00174].

[179] NNPDF collaboration, R. D. Ball et al., *Parton distributions from high-precision collider data*, *Eur. Phys. J. C* **77** (2017) 663, [1706.00428].

[180] CMS collaboration, A. Tumasyan et al., *Measurements of the electroweak diboson production cross sections in proton-proton collisions at $\sqrt{s} = 5.02$ TeV using leptonic decays*, 2107.01137.

[181] ATLAS collaboration, G. Aad et al., *Measurement of the ZZ production cross section and limits on anomalous neutral triple gauge couplings in proton-proton collisions at $\sqrt{s} = 7$ TeV with the ATLAS detector*, *Phys. Rev. Lett.* **108** (2012) 041804, [1110.5016].

[182] ATLAS collaboration, G. Aad et al., *Measurement of ZZ production in pp collisions at $\sqrt{s} = 7$ TeV and limits on anomalous ZZZ and ZZ$\gamma$ couplings with the ATLAS detector*, *JHEP* **03** (2013) 128, [1211.6096].

[183] CMS collaboration, S. Chatrchyan et al., *Measurement of the ZZ Production Cross Section and Search for Anomalous Couplings in 2 l2l ' Final States in pp Collisions at $\sqrt{s} = 7$ TeV*, *JHEP* **01** (2013) 063, [1211.4890].

[184] CMS collaboration, V. Khachatryan et al., *Measurements of the Z Z production cross sections in the 2l2$\nu$ channel in proton–proton collisions at $\sqrt{s} = 7$ and 8 TeV and combined constraints on triple gauge couplings*, *Eur. Phys. J. C* **75** (2015) 511, [1503.05467].

[185] CMS collaboration, V. Khachatryan et al., *Measurements of the Z Z production cross sections in the 2l2$\nu$ channel in proton–proton collisions at $\sqrt{s} = 7$ and 8 TeV and combined constraints on triple gauge couplings*, *Eur. Phys. J.* **C75** (2015) 511, [1503.05467].

[186] CMS collaboration, S. Chatrchyan et al., *Measurement of $W^+W^-$ and ZZ Production Cross Sections in pp Collisions at $\sqrt{s} = 8 TeV$*, *Phys. Lett. B* **721** (2013) 190–211, [1301.4698].

[187] CMS collaboration, V. Khachatryan et al., *Measurement of the pp $\rightarrow$ ZZ production cross section and constraints on anomalous triple gauge couplings in four-lepton final states at $\sqrt{s} = 8$ TeV*, *Phys. Lett.* **B740** (2015) 250–272, [1406.0113].

[188] ATLAS collaboration, G. Aad et al., *Measurements of four-lepton production in pp collisions at $\sqrt{s} = 8$ TeV with the ATLAS detector*, *Phys. Lett. B* **753** (2016) 552–572, [1509.07844].

[189] ATLAS collaboration, M. Aaboud et al., *Measurement of the ZZ production cross section in proton-proton collisions at $\sqrt{s} = 8$ TeV using the $ZZ \rightarrow \ell^-\ell^+\ell'^-\ell'^+$ and $ZZ \rightarrow \ell^-\ell^+\nu\bar{\nu}$ channels with the ATLAS detector*, *JHEP* **01** (2017) 099, [1610.07585].

[190] CMS collaboration, A. M. Sirunyan et al., *Measurement of differential cross sections for Z boson pair production in association with jets at $\sqrt{s} = 8$ and 13 TeV*, *Phys. Lett. B* **789** (2019) 19–44, [1806.11073].

[191] CMS collaboration, V. Khachatryan et al., *Measurement of the ZZ production cross section and $Z \rightarrow \ell^+\ell^-\ell'^+\ell'^-$ branching fraction in pp collisions at $\sqrt{s}=13$ TeV*, *Phys. Lett. B* **763** (2016) 280–303, [1607.08834].

[192] ATLAS collaboration, M. Aaboud et al., *$ZZ \rightarrow \ell^+\ell^-\ell'^+\ell'^-$ cross-section measurements and search for anomalous triple gauge couplings in 13 TeV pp collisions with the ATLAS detector*, *Phys. Rev.* **D97** (2018) 032005, [1709.07703].

[193] CMS collaboration, A. M. Sirunyan et al., *Measurements of the pp $\rightarrow$ ZZ production cross section and the $Z \rightarrow 4\ell$ branching fraction, and constraints on anomalous triple gauge couplings at $\sqrt{s} = 13$ TeV*, *Eur. Phys. J. C* **78** (2018) 165, [1709.08601].

[194] ATLAS collaboration, M. Aaboud et al., *Measurement of ZZ production in the $\ell\ell\nu\nu$ final state with the ATLAS detector in pp collisions at $\sqrt{s} = 13$ TeV*, *JHEP* **10** (2019) 127, [1905.07163].

[195] CMS collaboration, A. M. Sirunyan et al., *Measurements of pp $\rightarrow$ ZZ production cross sections and constraints on anomalous triple gauge couplings at $\sqrt{s} = 13$ TeV*, *Eur. Phys. J. C* **81** (2021) 200, [2009.01186].

[196] B. Mele, P. Nason and G. Ridolfi, *QCD radiative corrections to Z boson pair production in hadronic collisions*, *Nucl. Phys.* **B357** (1991) 409–438.

[197] J. Ohnemus and J. Owens, *An Order $\alpha_s$ calculation of hadronic ZZ production*, *Phys. Rev.* **D43** (1991) 3626–3639.

[198] J. Ohnemus, *Hadronic ZZ, $W^-W^+$, and $W^{\pm}Z$ production with QCD corrections and leptonic decays*, *Phys. Rev.* **D50** (1994) 1931–1945, [hep-ph/9403331].

[199] L. J. Dixon, Z. Kunszt and A. Signer, *Helicity amplitudes for O(alpha-s) production of $W^+W^-$, $W^\pm Z$, $ZZ$, $W^\pm\gamma$, or $Z\gamma$ pairs at hadron colliders*, *Nucl. Phys. B* **531** (1998) 3–23, [hep-ph/9803250].

[200] J. M. Campbell and R. K. Ellis, *An Update on vector boson pair production at hadron colliders*, *Phys. Rev.* **D60** (1999) 113006, [hep-ph/9905386].

[201] T. Melia, P. Nason, R. Röntsch and G. Zanderighi, *W+W-, WZ and ZZ production in the POWHEG BOX*, *JHEP* **11** (2011) 078, [1107.5051].

[202] P. Nason and G. Zanderighi, *$W^+W^-$ , WZ and ZZ production in the POWHEG-BOX-V2*, *Eur. Phys. J.* **C74** (2014) 2702, [1311.1365].

[203] R. Frederix, S. Frixione, V. Hirschi, F. Maltoni, R. Pittau and P. Torrielli, *Four-lepton production at hadron colliders: aMC@NLO predictions with theoretical uncertainties*, *JHEP* **02** (2012) 099, [1110.4738].

[204] A. Bierweiler, T. Kasprzik and J. H. Kühn, *Vector-boson pair production at the LHC to $\mathcal{O}(\alpha^3)$ accuracy*, *JHEP* **1312** (2013) 071, [1305.5402].

[205] J. Baglio, L. D. Ninh and M. M. Weber, *Massive gauge boson pair production at the LHC: a next-to-leading order story*, *Phys. Rev.* **D88** (2013) 113005, [1307.4331].

[206] B. Biedermann, A. Denner, S. Dittmaier, L. Hofer and B. Jäger, *Electroweak corrections to $pp \to \mu^+\mu^-e^+e^- + X$ at the LHC: a Higgs background study*, *Phys. Rev. Lett.* **116** (2016) 161803, [1601.07787].

[207] B. Biedermann, A. Denner, S. Dittmaier, L. Hofer and B. Jäger, *Next-to-leading-order electroweak corrections to the production of four charged leptons at the LHC*, *JHEP* **01** (2017) 033, [1611.05338].

[208] M. Chiesa, A. Denner and J.-N. Lang, *Anomalous triple-gauge-boson interactions in vector-boson pair production with RECOLA2*, *Eur. Phys. J. C* **78** (2018) 467, [1804.01477].

[209] M. Chiesa, C. Oleari and E. Re, *NLO QCD+NLO EW corrections to diboson production matched to parton shower*, *Eur. Phys. J. C* **80** (2020) 849, [2005.12146].

[210] A. Denner and G. Pelliccioli, *NLO EW and QCD corrections to polarized ZZ production in the four-charged-lepton channel at the LHC*, 2107.06579.

[211] M. Grazzini, S. Kallweit, J. M. Lindert, S. Pozzorini and M. Wiesemann, *NNLO QCD + NLO EW with Matrix+OpenLoops: precise predictions for vector-boson pair production*, *JHEP* **02** (2020) 087, [1912.00068].

[212] F. Caola, K. Melnikov, R. Röntsch and L. Tancredi, *QCD corrections to ZZ production in gluon fusion at the LHC*, *Phys. Rev. D* **92** (2015) 094028, [1509.06734].

[213] F. Caola, M. Dowling, K. Melnikov, R. Röntsch and L. Tancredi, *QCD corrections to vector boson pair production in gluon fusion including interference effects with off-shell Higgs at the LHC*, *JHEP* **07** (2016) 087, [1605.04610].

[214] M. Grazzini, S. Kallweit, M. Wiesemann and J. Y. Yook, *ZZ production at the LHC: NLO QCD corrections to the loop-induced gluon fusion channel*, *JHEP* **03** (2019) 070, [1811.09593].

[215] T. Binoth, N. Kauer and P. Mertsch, *Gluon-induced QCD corrections to $pp \to ZZ \to l\bar{l}l'\bar{l}'$*, *Proceedings* **DIS 2008** (2008) 142, [0807.0024].

[216] S. Alioli, F. Caola, G. Luisoni and R. Röntsch, *ZZ production in gluon fusion at NLO matched to parton-shower*, *Phys. Rev.* **D95** (2017) 034042, [1609.09719].

[217] S. Alioli, S. Ferrario Ravasio, J. M. Lindert and R. Röntsch, *Four-lepton production in gluon fusion at NLO matched to parton showers*, *Eur. Phys. J. C* **81** (2021) 687, [2102.07783].

[218] S. Alioli, P. Nason, C. Oleari and E. Re, *A general framework for implementing NLO calculations in shower Monte Carlo programs: the POWHEG BOX*, *JHEP* **06** (2010) 043, [1002.2581].

[219] T. Ježo and P. Nason, *On the Treatment of Resonances in Next-to-Leading Order Calculations Matched to a Parton Shower*, *JHEP* **12** (2015) 065, [1509.09071].

[220] F. Cascioli, P. Maierhöfer and S. Pozzorini, *Scattering Amplitudes with Open Loops*, *Phys. Rev. Lett.* **108** (2012) 111601, [1111.5206].

[221] F. Buccioni, S. Pozzorini and M. Zoller, *On-the-fly reduction of open loops*, *Eur. Phys. J.* **C78** (2018) 70, [1710.11452].

[222] F. Buccioni, J.-N. Lang, J. M. Lindert, P. Maierhöfer, S. Pozzorini, H. Zhang and M. F. Zoller, *OpenLoops 2*, *Eur. Phys. J. C* **79** (2019) 866, [1907.13071].

[223] M. Grazzini, S. Kallweit and M. Wiesemann, *Fully differential NNLO computations with MATRIX*, *Eur. Phys. J. C* **78** (2018) 537, [1711.06631].

[224] The VVAMP project, by T. Gehrmann, A. von Manteuffel, and L. Tancredi, is publicly available at http://vvamp.hepforge.org.

[225] T. Gehrmann, A. von Manteuffel and L. Tancredi, *The two-loop helicity amplitudes for $q\bar{q}' \to V_1 V_2 \to 4$ leptons*, *JHEP* **09** (2015) 128, [1503.04812].

[226] G. P. Salam and J. Rojo, *A Higher Order Perturbative Parton Evolution Toolkit (HOPPET)*, *Comput. Phys. Commun.* **180** (2009) 120–156, [0804.3755].

[227] T. Gehrmann and E. Remiddi, *Numerical evaluation of harmonic polylogarithms*, *Comput. Phys. Commun.* **141** (2001) 296–312, [hep-ph/0107173].

[228] P. Nason and C. Oleari, *Generation cuts and Born suppression in POWHEG*, 1303.3922.

[229] T. Ježo, J. M. Lindert, P. Nason, C. Oleari and S. Pozzorini, *An NLO+PS generator for $t\bar{t}$ and Wt production and decay including non-resonant and interference effects*, *Eur. Phys. J. C* **76** (2016) 691, [1607.04538].

[230] A. von Manteuffel and L. Tancredi, *The two-loop helicity amplitudes for $gg \to V_1 V_2 \to 4$ leptons*, *JHEP* **1506** (2015) 197, [1503.08835].

[231] B. Agarwal, S. P. Jones and A. von Manteuffel, *Two-loop helicity amplitudes for $gg \to ZZ$ with full top-quark mass effects*, *JHEP* **05** (2021) 256, [2011.15113].

[232] C. Brønnum-Hansen and C.-Y. Wang, *Top quark contribution to two-loop helicity amplitudes for Z boson pair production in gluon fusion*, *JHEP* **05** (2021) 244, [2101.12095].

[233] *ATLAS Pythia 8 tunes to 7 TeV datas*, *ATL-PHYS-PUB-2014-021*, 11, 2014.

[234] F. Cascioli, S. Höche, F. Krauss, P. Maierhöfer, S. Pozzorini and F. Siegert, *Precise Higgs-background predictions: merging NLO QCD and squared quark-loop corrections to four-lepton + 0,1 jet production*, *JHEP* **01** (2014) 046, [1309.0500].

[235] J. M. Campbell, R. K. Ellis, E. Furlan and R. Röntsch, *Interference effects for Higgs boson mediated Z-pair plus jet production*, *Phys. Rev. D* **90** (2014) 093008, [1409.1897].

[236] C. Li, Y. An, C. Charlot, R. Covarelli, Z. Guan and Q. Li, *Loop-induced ZZ production at the LHC: An improved description by matrix-element matching*, *Phys. Rev. D* **102** (2020) 116003, [2006.12860].

[237] A. Denner, S. Dittmaier, M. Roth and D. Wackeroth, *Predictions for all processes e+ e- —> 4 fermions + gamma*, *Nucl. Phys. B* **560** (1999) 33–65, [hep-ph/9904472].

[238] A. Buckley, J. Ferrando, S. Lloyd, K. Nordström, B. Page, M. Rüfenacht, M. Schönherr and G. Watt, *LHAPDF6: parton density access in the LHC precision era*, *Eur. Phys. J.* **C75** (2015) 132, [1412.7420].

[239] A. Manohar, P. Nason, G. P. Salam and G. Zanderighi, *How bright is the proton? A precise determination of the photon parton distribution function*, *Phys. Rev. Lett.* **117** (2016) 242002, [1607.04266].

[240] A. V. Manohar, P. Nason, G. P. Salam and G. Zanderighi, *The Photon Content of the Proton*, *JHEP* **12** (2017) 046, [1708.01256].

[241] NNPDF collaboration, V. Bertone, S. Carrazza, N. P. Hartland and J. Rojo, *Illuminating the photon content of the proton within a global PDF analysis*, *SciPost Phys.* **5** (2018) 008, [1712.07053].

[242] M. Czakon, D. Heymes and A. Mitov, *Dynamical scales for multi-TeV top-pair production at the LHC*, *JHEP* **04** (2017) 071, [1606.03350].

[243] F. Caola, F. A. Dreyer, R. W. McDonald and G. P. Salam, *Framing energetic top-quark pair production at the LHC*, *JHEP* **07** (2021) 040, [2101.06068].

[244] M. Cacciari, G. P. Salam and G. Soyez, *FastJet User Manual*, *Eur. Phys. J. C* **72** (2012) 1896, [1111.6097].

[245] S. Kallweit, E. Re, L. Rottoli and M. Wiesemann, *Accurate single- and double-differential resummation of colour-singlet processes with MATRIX+RADISH: $W^+W^-$ production at the LHC*, *JHEP* **12** (2020) 147, [2004.07720].

[246] S. Bräuer, A. Denner, M. Pellen, M. Schönherr and S. Schumann, *Fixed-order and merged parton-shower predictions for WW and WWj production at the LHC including NLO QCD and EW corrections*, *JHEP* **10** (2020) 159, [2005.12128].

[247] T. Appelquist and J. Carazzone, *Infrared Singularities and Massive Fields*, *Phys. Rev. D* **11** (1975) 2856.

[248] W. Buchmüller and D. Wyler, *Effective Lagrangian Analysis of New Interactions and Flavor Conservation*, *Nucl. Phys.* **B268** (1986) 621–653.

[249] B. Grzadkowski, M. Iskrzynski, M. Misiak and J. Rosiek, *Dimension-Six Terms in the Standard Model Lagrangian*, *JHEP* **10** (2010) 085, [1008.4884].

[250] I. Brivio and M. Trott, *The Standard Model as an Effective Field Theory*, *Phys. Rept.* **793** (2019) 1–98, [1706.08945].

[251] S. Weinberg, *Baryon and Lepton Nonconserving Processes*, *Phys. Rev. Lett.* **43** (1979) 1566–1570.

[252] J. Ellis, C. W. Murphy, V. Sanz and T. You, *Updated Global SMEFT Fit to Higgs, Diboson and Electroweak Data*, *JHEP* **06** (2018) 146, [1803.03252].

[253] SMEFiT collaboration, J. J. Ethier, G. Magni, F. Maltoni, L. Mantani, E. R. Nocera, J. Rojo, E. Slade, E. Vryonidou and C. Zhang, *Combined SMEFT interpretation of Higgs, diboson, and top quark data from the LHC*, *JHEP* **11** (2021) 089, [2105.00006].

[254] G. Panico and A. Wulzer, *The Composite Nambu-Goldstone Higgs*, vol. 913. Springer, 2016, 10.1007/978-3-319-22617-0.

[255] A. Djouadi, *The Anatomy of electro-weak symmetry breaking. II. The Higgs bosons in the minimal supersymmetric model*, *Phys. Rept.* **459** (2008) 1–241, [hep-ph/0503173].

[256] D. Curtin and P. Saraswat, *Towards a No-Lose Theorem for Naturalness*, *Phys. Rev. D* **93** (2016) 055044, [1509.04284].

[257] U. Haisch, *Yukawas and trilinear Higgs terms from loops*, in *52nd Rencontres de Moriond on EW Interactions and Unified Theories*, pp. 9–16, 2017. 1706.09730.

[258] G. F. Giudice, C. Grojean, A. Pomarol and R. Rattazzi, *The Strongly-Interacting Light Higgs*, *JHEP* **06** (2007) 045, [hep-ph/0703164].

[259] J. Elias-Miró, C. Grojean, R. S. Gupta and D. Marzocca, *Scaling and tuning of EW and Higgs observables*, *JHEP* **05** (2014) 019, [1312.2928].

[260] T. Plehn, *Lectures on LHC Physics*, *Lect. Notes Phys.* **844** (2012) 1–193, [0910.4182].

[261] A. Papaefstathiou and K. Sakurai, *Triple Higgs boson production at a 100 TeV proton-proton collider*, *JHEP* **02** (2016) 006, [1508.06524].

[262] C.-Y. Chen, Q.-S. Yan, X. Zhao, Y.-M. Zhong and Z. Zhao, *Probing triple-Higgs productions via 4b2γ decay channel at a 100 TeV hadron collider*, *Phys. Rev. D* **93** (2016) 013007, [1510.04013].

[263] B. Fuks, J. H. Kim and S. J. Lee, *Probing Higgs self-interactions in proton-proton collisions at a center-of-mass energy of 100 TeV*, *Phys. Rev. D* **93** (2016) 035026, [1510.07697].

[264] W. Kilian, S. Sun, Q.-S. Yan, X. Zhao and Z. Zhao, *New Physics in multi-Higgs boson final states*, *JHEP* **06** (2017) 145, [1702.03554].

[265] B. Fuks, J. H. Kim and S. J. Lee, *Scrutinizing the Higgs quartic coupling at a future 100 TeV proton–proton collider with taus and b-jets*, *Phys. Lett. B* **771** (2017) 354–358, [1704.04298].

[266] T. Liu, K.-F. Lyu, J. Ren and H. X. Zhu, *Probing the quartic Higgs boson self-interaction*, *Phys. Rev. D* **98** (2018) 093004, [1803.04359].

[267] W. Bizoń, U. Haisch and L. Rottoli, *Constraints on the quartic Higgs self-coupling from double-Higgs production at future hadron colliders*, *JHEP* **10** (2019) 267, [1810.04665].

[268] S. Borowka, C. Duhr, F. Maltoni, D. Pagani, A. Shivaji and X. Zhao, *Probing the scalar potential via double Higgs boson production at hadron colliders*, *JHEP* **04** (2019) 016, [1811.12366].

[269] A. Papaefstathiou, G. Tetlalmatzi-Xolocotzi and M. Zaro, *Triple Higgs boson production to six b-jets at a 100 TeV proton collider*, *Eur. Phys. J. C* **79** (2019) 947, [1909.09166].

[270] M. Chiesa, F. Maltoni, L. Mantani, B. Mele, F. Piccinini and X. Zhao, *Measuring the quartic Higgs self-coupling at a multi-TeV muon collider*, *JHEP* **09** (2020) 098, [2003.13628].

[271] ATLAS collaboration, *Measurement prospects of the pair production and self-coupling of the Higgs boson with the ATLAS experiment at the HL-LHC*, tech. rep., CERN, Geneva, Dec, 2018.

[272] CMS collaboration, *Prospects for HH measurements at the HL-LHC*, tech. rep., CERN, Geneva, 2018.

[273] M. McCullough, *An Indirect Model-Dependent Probe of the Higgs Self-Coupling*, *Phys. Rev. D* **90** (2014) 015001, [1312.3322].

[274] M. Gorbahn and U. Haisch, *Indirect probes of the trilinear Higgs coupling: $gg \to h$ and $h \to \gamma\gamma$*, *JHEP* **10** (2016) 094, [1607.03773].

[275] G. Degrassi, P. P. Giardino, F. Maltoni and D. Pagani, *Probing the Higgs self coupling via single Higgs production at the LHC*, *JHEP* **12** (2016) 080, [1607.04251].

[276] W. Bizon, M. Gorbahn, U. Haisch and G. Zanderighi, *Constraints on the trilinear Higgs coupling from vector boson fusion and associated Higgs production at the LHC*, *JHEP* **07** (2017) 083, [1610.05771].

[277] F. Maltoni, D. Pagani, A. Shivaji and X. Zhao, *Trilinear Higgs coupling determination via single-Higgs differential measurements at the LHC*, *Eur. Phys. J. C* **77** (2017) 887, [1709.08649].

[278] M. Gorbahn and U. Haisch, *Two-loop amplitudes for Higgs plus jet production involving a modified trilinear Higgs coupling*, *JHEP* **04** (2019) 062, [1902.05480].

[279] G. Degrassi and M. Vitti, *The effect of an anomalous Higgs trilinear self-coupling on the $h \to \gamma Z$ decay*, *Eur. Phys. J. C* **80** (2020) 307, [1912.06429].

[280] S. Di Vita, G. Durieux, C. Grojean, J. Gu, Z. Liu, G. Panico, M. Riembau and T. Vantalon, *A global view on the Higgs self-coupling at lepton colliders*, *JHEP* **02** (2018) 178, [1711.03978].

[281] F. Maltoni, D. Pagani and X. Zhao, *Constraining the Higgs self-couplings at $e^+e^-$ colliders*, *JHEP* **07** (2018) 087, [1802.07616].

[282] G. Degrassi, M. Fedele and P. P. Giardino, *Constraints on the trilinear Higgs self coupling from precision observables*, *JHEP* **04** (2017) 155, [1702.01737].

[283] G. D. Kribs, A. Maier, H. Rzehak, M. Spannowsky and P. Waite, *Electroweak oblique parameters as a probe of the trilinear Higgs boson self-interaction*, *Phys. Rev. D* **95** (2017) 093004, [1702.07678].

[284] S. Di Vita, C. Grojean, G. Panico, M. Riembau and T. Vantalon, *A global view on the Higgs self-coupling*, *JHEP* **09** (2017) 069, [1704.01953].

[285] E. Rossi, *Measurement of Higgs-boson self-coupling with single-Higgs and double-Higgs production channels*, 2010.05252.

[286] G. Degrassi, B. Di Micco, P. P. Giardino and E. Rossi, *Higgs boson self-coupling constraints from single Higgs, double Higgs and Electroweak measurements*, *Phys. Lett. B* **817** (2021) 136307, [2102.07651].

[287] CMS collaboration, *Constraints on the Higgs boson self-coupling from $t\bar{t}H + tH$, $H \to \gamma\gamma$ differential measurements at the HL-LHC*, tech. rep., CERN, Geneva, 2018.

[288] ATLAS collaboration, *Constraint of the Higgs boson self-coupling from Higgs boson differential production and decay measurements*, tech. rep., CERN, Geneva, Mar, 2019.

[289] ATLAS collaboration, *Constraints on the Higgs boson self-coupling from the combination of single-Higgs and double-Higgs production analyses performed with the ATLAS experiment*, tech. rep., CERN, Geneva, Oct, 2019.

[290] T. Hahn and M. Perez-Victoria, *Automatized one loop calculations in four-dimensions and D-dimensions*, *Comput. Phys. Commun.* **118** (1999) 153–165, [hep-ph/9807565].

[291] R. Boughezal, J. M. Campbell, R. K. Ellis, C. Focke, W. Giele, X. Liu, F. Petriello and C. Williams, *Color singlet production at NNLO in MCFM*, *Eur. Phys. J. C* **77** (2017) 7, [1605.08011].

[292] CMS collaboration, V. Khachatryan et al., *Constraints on the Higgs boson width from off-shell production and decay to Z-boson pairs*, *Phys. Lett. B* **736** (2014) 64–85, [1405.3455].

[293] ATLAS collaboration, G. Aad et al., *Constraints on the off-shell Higgs boson signal strength in the high-mass ZZ and WW final states with the ATLAS detector*, *Eur. Phys. J. C* **75** (2015) 335, [1503.01060].

[294] ATLAS collaboration, *Off-shell Higgs boson couplings measurement using H → ZZ → 4l events at High Luminosity LHC*, tech. rep., CERN, Geneva, 2015.

[295] CMS collaboration, *Sensitivity projections for Higgs boson properties measurements at the HL-LHC*, tech. rep., CERN, Geneva, 2018.

[296] ATLAS collaboration, M. Aaboud et al., *Constraints on off-shell Higgs boson production and the Higgs boson total width in ZZ → 4ℓ and ZZ → 2ℓ2ν final states with the ATLAS detector*, *Phys. Lett. B* **786** (2018) 223–244, [1808.01191].

[297] CMS collaboration, A. M. Sirunyan et al., *Measurements of the Higgs boson width and anomalous HVV couplings from on-shell and off-shell production in the four-lepton final state*, *Phys. Rev. D* **99** (2019) 112003, [1901.00174].

[298] ATLAS collaboration, M. Aaboud et al., *Measurement of the four-lepton invariant mass spectrum in 13 TeV proton-proton collisions with the ATLAS detector*, *JHEP* **04** (2019) 048, [1902.05892].

[299] R. D. Ball et al., *The Path to Proton Structure at One-Percent Accuracy*, 2109.02653.

[300] C. Englert and M. Spannowsky, *Limitations and Opportunities of Off-Shell Coupling Measurements*, *Phys. Rev. D* **90** (2014) 053003, [1405.0285].

[301] C. Englert, Y. Soreq and M. Spannowsky, *Off-Shell Higgs Coupling Measurements in BSM scenarios*, *JHEP* **05** (2015) 145, [1410.5440].

[302] D. Goncalves, T. Han and S. Mukhopadhyay, *Off-Shell Higgs Probe of Naturalness*, *Phys. Rev. Lett.* **120** (2018) 111801, [1710.02149].

[303] D. Gonçalves, T. Han and S. Mukhopadhyay, *Higgs Couplings at High Scales*, *Phys. Rev. D* **98** (2018) 015023, [1803.09751].

[304] J. S. Gainer, J. Lykken, K. T. Matchev, S. Mrenna and M. Park, *Beyond Geolocating: Constraining Higher Dimensional Operators in H → 4ℓ with Off-Shell Production and More*, *Phys. Rev. D* **91** (2015) 035011, [1403.4951].

[305] N. Kauer and G. Passarino, *Inadequacy of zero-width approximation for a light Higgs boson signal*, *JHEP* **08** (2012) 116, [1206.4803].

[306] Y. Gao, A. V. Gritsan, Z. Guo, K. Melnikov, M. Schulze and N. V. Tran, *Spin Determination of Single-Produced Resonances at Hadron Colliders*, *Phys. Rev. D* **81** (2010) 075022, [1001.3396].

[307] S. Bolognesi, Y. Gao, A. V. Gritsan, K. Melnikov, M. Schulze, N. V. Tran and A. Whitbeck, *On the spin and parity of a single-produced resonance at the LHC*, *Phys. Rev. D* **86** (2012) 095031, [1208.4018].

[308] I. Anderson et al., *Constraining Anomalous HVV Interactions at Proton and Lepton Colliders*, *Phys. Rev. D* **89** (2014) 035007, [1309.4819].

[309] J. Alwall, A. Freitas and O. Mattelaer, *The Matrix Element Method and QCD Radiation*, *Phys. Rev. D* **83** (2011) 074010, [`1010.2263`].

[310] J. M. Campbell, W. T. Giele and C. Williams, *The Matrix Element Method at Next-to-Leading Order*, *JHEP* **11** (2012) 043, [`1204.4424`].

[311] T. Martini and P. Uwer, *Extending the Matrix Element Method beyond the Born approximation: Calculating event weights at next-to-leading order accuracy*, *JHEP* **09** (2015) 083, [`1506.08798`].

[312] A. V. Gritsan, R. Röntsch, M. Schulze and M. Xiao, *Constraining anomalous Higgs boson couplings to the heavy flavor fermions using matrix element techniques*, *Phys. Rev. D* **94** (2016) 055023, [`1606.03107`].

[313] C. Anastasiou, C. Duhr, F. Dulat, F. Herzog and B. Mistlberger, *Higgs Boson Gluon-Fusion Production in QCD at Three Loops*, *Phys. Rev. Lett.* **114** (2015) 212001, [`1503.06056`].

[314] C. Anastasiou, C. Duhr, F. Dulat, E. Furlan, T. Gehrmann, F. Herzog, A. Lazopoulos and B. Mistlberger, *High precision determination of the gluon fusion Higgs boson cross-section at the LHC*, *JHEP* **05** (2016) 058, [`1602.00695`].

[315] B. Mistlberger, *Higgs boson production at hadron colliders at $N^3LO$ in QCD*, *JHEP* **05** (2018) 028, [`1802.00833`].

[316] ATLAS collaboration, G. Aad et al., *Measurements of Higgs boson production and couplings in the four-lepton channel in pp collisions at center-of-mass energies of 7 and 8 TeV with the ATLAS detector*, *Phys. Rev. D* **91** (2015) 012006, [`1408.5191`].

[317] G. Cowan, K. Cranmer, E. Gross and O. Vitells, *Asymptotic formulae for likelihood-based tests of new physics*, *Eur. Phys. J. C* **71** (2011) 1554, [`1007.1727`].

[318] G. Cowan, *Discovery sensitivity for a counting experiment with background uncertainty*, tech. rep., 2012.

[319] ATLAS collaboration, *Projections for measurements of Higgs boson cross sections, branching ratios, coupling parameters and mass with the ATLAS detector at the HL-LHC*, tech. rep., CERN, Geneva, 2018.

[320] ATLAS collaboration, *Projections for measurements of Higgs boson signal strengths and coupling parameters with the ATLAS detector at a HL-LHC*, tech. rep., CERN, Geneva, Oct, 2014.

[321] M. Ruhdorfer, E. Salvioni and A. Weiler, *A Global View of the Off-Shell Higgs Portal*, *SciPost Phys.* **8** (2020) 027, [`1910.04170`].

[322] U. Haisch, G. Polesello and S. Schulte, *Searching for pseudo Nambu-Goldstone boson dark matter production in association with top quarks*, *JHEP* **09** (2021) 206, [`2107.12389`].

[323] A. Hayreter and G. Valencia, *Constraints on anomalous color dipole operators from Higgs boson production at the LHC*, *Phys. Rev. D* **88** (2013) 034033, [`1304.6976`].

[324] ATLAS collaboration, M. Aaboud et al., *Observation of $H \to b\bar{b}$ decays and $VH$ production with the ATLAS detector*, *Phys. Lett.* **B786** (2018) 59–86, [`1808.08238`].

[325] CMS collaboration, A. M. Sirunyan et al., *Observation of Higgs boson decay to bottom quarks*, *Phys. Rev. Lett.* **121** (2018) 121801, [`1808.08242`].

[326] F. Bishara, U. Haisch, P. F. Monni and E. Re, *Constraining Light-Quark Yukawa Couplings from Higgs Distributions*, *Phys. Rev. Lett.* **118** (2017) 121801, [`1606.09253`].

[327] Y. Soreq, H. X. Zhu and J. Zupan, *Light quark Yukawa couplings from Higgs kinematics*, *JHEP* **12** (2016) 045, [`1606.09621`].

[328] ATLAS collaboration, M. Aaboud et al., *Search for the Decay of the Higgs Boson to Charm Quarks with the ATLAS Experiment*, *Phys. Rev. Lett.* **120** (2018) 211802, [`1802.04329`].

[329] CMS collaboration, A. M. Sirunyan et al., *Measurement and interpretation of differential cross sections for Higgs boson production at $\sqrt{s} = 13$ TeV*, *Phys. Lett.* **B792** (2019) 369–396, [`1812.06504`].

[330] CMS collaboration, A. M. Sirunyan et al., *A search for the standard model Higgs boson decaying to charm quarks*, *JHEP* **03** (2020) 131, [1912.01662].

[331] ATLAS collaboration, *Measurements and interpretations of Higgs-boson fiducial cross sections in the diphoton decay channel using 139 fb$^{-1}$ of pp collision data at $\sqrt{s} = 13$ TeV with the ATLAS detector*, Tech. Rep. ATLAS-CONF-2019-029, CERN, Geneva, Jul, 2019.

[332] ATLAS collaboration, G. Aad et al., *Measurements of the Higgs boson inclusive and differential fiducial cross sections in the 4ℓ decay channel at $\sqrt{s} = 13$ TeV*, *Eur. Phys. J. C* **80** (2020) 942, [2004.03969].

[333] R. Gauld, B. D. Pecjak and D. J. Scott, *QCD radiative corrections for $h \to b\bar{b}$ in the Standard Model Dimension-6 EFT*, *Phys. Rev. D* **94** (2016) 074045, [1607.06354].

[334] J. Bramante, A. Delgado, L. Lehman and A. Martin, *Boosted Higgses from chromomagnetic b's: $b\bar{b}h$ at high luminosity*, *Phys. Rev. D* **93** (2016) 053001, [1410.3484].

[335] S. Dittmaier, M. Krämer and M. Spira, *Higgs radiation off bottom quarks at the Tevatron and the CERN LHC*, *Phys. Rev. D* **70** (2004) 074010, [hep-ph/0309204].

[336] LHC HIGGS CROSS SECTION WORKING GROUP collaboration, S. Dittmaier et al., *Handbook of LHC Higgs Cross Sections: 1. Inclusive Observables*, 1101.0593.

[337] C. Degrande, J. M. Gerard, C. Grojean, F. Maltoni and G. Servant, *Probing Top-Higgs Non-Standard Interactions at the LHC*, *JHEP* **07** (2012) 036, [1205.1065].

[338] J. Bramante, A. Delgado and A. Martin, *Cornering a hyper Higgs boson: Angular kinematics for boosted Higgs bosons with top pairs*, *Phys. Rev. D* **89** (2014) 093006, [1402.5985].

[339] F. Krauss, S. Kuttimalai and T. Plehn, *LHC multijet events as a probe for anomalous dimension-six gluon interactions*, *Phys. Rev. D* **95** (2017) 035024, [1611.00767].

[340] S. Alioli, M. Farina, D. Pappadopulo and J. T. Ruderman, *Precision Probes of QCD at High Energies*, *JHEP* **07** (2017) 097, [1706.03068].

[341] S. Alte, M. König and W. Shepherd, *Consistent Searches for SMEFT Effects in Non-Resonant Dijet Events*, *JHEP* **01** (2018) 094, [1711.07484].

[342] V. Hirschi, F. Maltoni, I. Tsinikos and E. Vryonidou, *Constraining anomalous gluon self-interactions at the LHC: a reappraisal*, *JHEP* **07** (2018) 093, [1806.04696].

[343] E. Keilmann and W. Shepherd, *Dijets at Tevatron Cannot Constrain SMEFT Four-Quark Operators*, *JHEP* **09** (2019) 086, [1907.13160].

[344] R. Goldouzian and M. D. Hildreth, *LHC dijet angular distributions as a probe for the dimension-six triple gluon vertex*, *Phys. Lett. B* **811** (2020) 135889, [2001.02736].

[345] CMS collaboration, A. M. Sirunyan et al., *Search for new physics in dijet angular distributions using proton–proton collisions at $\sqrt{s} = 13$ TeV and constraints on dark matter and other models*, *Eur. Phys. J. C* **78** (2018) 789, [1803.08030].

[346] ATLAS collaboration, G. Aad et al., *Search for new resonances in mass distributions of jet pairs using 139 fb$^{-1}$ of pp collisions at $\sqrt{s} = 13$ TeV with the ATLAS detector*, *JHEP* **03** (2020) 145, [1910.08447].

[347] CMS collaboration, A. M. Sirunyan et al., *Search for high mass dijet resonances with a new background prediction method in proton-proton collisions at $\sqrt{s} = 13$ TeV*, *JHEP* **05** (2020) 033, [1911.03947].

[348] ATLAS collaboration, G. Aad et al., *Dijet resonance search with weak supervision using $\sqrt{s} = 13$ TeV pp collisions in the ATLAS detector*, *Phys. Rev. Lett.* **125** (2020) 131801, [2005.02983].

[349] S. Dulat, T.-J. Hou, J. Gao, M. Guzzi, J. Huston, P. Nadolsky, J. Pumplin, C. Schmidt, D. Stump and C. P. Yuan, *New parton distribution functions from a global analysis of quantum chromodynamics*, *Phys. Rev. D* **93** (2016) 033006, [1506.07443].

[350] D. B. Clark, E. Godat and F. I. Olness, *ManeParse : A Mathematica reader for Parton Distribution Functions*, *Comput. Phys. Commun.* **216** (2017) 126–137, [1605.08012].

[351] CMS collaboration, *Search for Heavy Resonances Decaying into bb and bg Final States in pp Collisions at $\sqrt{s} = 8$ TeV*, Tech. Rep. CMS-PAS-EXO-12-023, CERN, Geneva, 2013.

[352] ATLAS collaboration, M. Aaboud et al., *Search for resonances in the mass distribution of jet pairs with one or two jets identified as b-jets in proton-proton collisions at $\sqrt{s} = 13$ TeV with the ATLAS detector*, Phys. Rev. D **98** (2018) 032016, [1805.09299].

[353] CMS collaboration, A. M. Sirunyan et al., *Search for low-mass resonances decaying into bottom quark-antiquark pairs in proton-proton collisions at $\sqrt{s} = 13$ TeV*, Phys. Rev. D **99** (2019) 012005, [1810.11822].

[354] A. Alloul, N. D. Christensen, C. Degrande, C. Duhr and B. Fuks, *FeynRules 2.0 - A complete toolbox for tree-level phenomenology*, Comput. Phys. Commun. **185** (2014) 2250–2300, [1310.1921].

[355] C. Degrande, C. Duhr, B. Fuks, D. Grellscheid, O. Mattelaer and T. Reiter, *UFO - The Universal FeynRules Output*, Comput. Phys. Commun. **183** (2012) 1201–1214, [1108.2040].

[356] J. Alwall, R. Frederix, S. Frixione, V. Hirschi, F. Maltoni, O. Mattelaer, H. S. Shao, T. Stelzer, P. Torrielli and M. Zaro, *The automated computation of tree-level and next-to-leading order differential cross sections, and their matching to parton shower simulations*, JHEP **07** (2014) 079, [1405.0301].

[357] P. Nason, S. Dawson and R. K. Ellis, *The Total Cross-Section for the Production of Heavy Quarks in Hadronic Collisions*, Nucl. Phys. B **303** (1988) 607–633.

[358] J. Campbell and T. Neumann, *Precision Phenomenology with MCFM*, JHEP **12** (2019) 034, [1909.09117].

[359] DELPHES 3 collaboration, J. de Favereau, C. Delaere, P. Demin, A. Giammanco, V. Lemaître, A. Mertens and M. Selvaggi, *DELPHES 3, A modular framework for fast simulation of a generic collider experiment*, JHEP **02** (2014) 057, [1307.6346].

[360] D. Dercks, N. Desai, J. S. Kim, K. Rolbiecki, J. Tattersall and T. Weber, *CheckMATE 2: From the model to the limit*, Comput. Phys. Commun. **221** (2017) 383–418, [1611.09856].

[361] ATLAS collaboration, G. Aad et al., *ATLAS b-jet identification performance and efficiency measurement with $t\bar{t}$ events in pp collisions at $\sqrt{s} = 13$ TeV*, Eur. Phys. J. C **79** (2019) 970, [1907.05120].

[362] CMS collaboration, S. Chatrchyan et al., *Measurement of the Cross Section and Angular Correlations for Associated Production of a Z Boson with b Hadrons in pp Collisions at $\sqrt{s} = 7$ TeV*, JHEP **12** (2013) 039, [1310.1349].

[363] CMS collaboration, S. Chatrchyan et al., *Measurement of the production cross sections for a Z boson and one or more b jets in pp collisions at sqrt(s) = 7 TeV*, JHEP **06** (2014) 120, [1402.1521].

[364] ATLAS collaboration, G. Aad et al., *Measurement of differential production cross-sections for a Z boson in association with b-jets in 7 TeV proton-proton collisions with the ATLAS detector*, JHEP **10** (2014) 141, [1407.3643].

[365] CMS collaboration, V. Khachatryan et al., *Measurements of the associated production of a Z boson and b jets in pp collisions at $\sqrt{s} = 8$ TeV*, Eur. Phys. J. C **77** (2017) 751, [1611.06507].

[366] CMS collaboration, A. M. Sirunyan et al., *Measurement of the associated production of a Z boson with charm or bottom quark jets in proton-proton collisions at $\sqrt{s}=13$ TeV*, Phys. Rev. D **102** (2020) 032007, [2001.06899].

[367] ATLAS collaboration, G. Aad et al., *Measurements of the production cross-section for a Z boson in association with b-jets in proton-proton collisions at $\sqrt{s} = 13$ TeV with the ATLAS detector*, JHEP **07** (2020) 044, [2003.11960].

[368] ATLAS collaboration, *Search for new phenomena in final states with two leptons and one or no b-tagged jets at $\sqrt{s} = 13$ TeV using the ATLAS detector*, tech. rep., CERN, Geneva, Mar, 2021.

[369] R. Gauld, A. Gehrmann-De Ridder, E. W. N. Glover, A. Huss and I. Majer, *Predictions for Z*

*-Boson Production in Association with a b-Jet at* $\mathcal{O}(\alpha_s^3)$, *Phys. Rev. Lett.* **125** (2020) 222002, [2005.03016].

[370] Y. Afik, S. Bar-Shalom, J. Cohen and Y. Rozen, *Searching for New Physics with* $b\bar{b}\ell^+\ell^-$ *contact interactions*, *Phys. Lett. B* **807** (2020) 135541, [1912.00425].

[371] ATLAS collaboration, M. Aaboud et al., *Electron reconstruction and identification in the ATLAS experiment using the 2015 and 2016 LHC proton-proton collision data at* $\sqrt{s} = 13$ *TeV*, *Eur. Phys. J. C* **79** (2019) 639, [1902.04655].

[372] ATLAS collaboration, G. Aad et al., *Muon reconstruction performance of the ATLAS detector in proton–proton collision data at* $\sqrt{s}$ =13 *TeV*, *Eur. Phys. J. C* **76** (2016) 292, [1603.05598].

[373] SHERPA collaboration, E. Bothmann et al., *Event Generation with Sherpa 2.2*, *SciPost Phys.* **7** (2019) 034, [1905.09127].

[374] F. Sala, *A bound on the charm chromo-EDM and its implications*, *JHEP* **03** (2014) 061, [1312.2589].

[375] M. Gorbahn and U. Haisch, *Searching for* $t \to c(u)h$ *with dipole moments*, *JHEP* **06** (2014) 033, [1404.4873].

[376] M. Misiak et al., *Updated NNLO QCD predictions for the weak radiative B-meson decays*, *Phys. Rev. Lett.* **114** (2015) 221801, [1503.01789].

[377] M. Misiak and M. Steinhauser, *Weak radiative decays of the B meson and bounds on* $M_{H^\pm}$ *in the Two-Higgs-Doublet Model*, *Eur. Phys. J. C* **77** (2017) 201, [1702.04571].

[378] C. Greub and P. Liniger, *The Rare decay* $b \to s$ *gluon beyond leading logarithms*, *Phys. Lett. B* **494** (2000) 237–247, [hep-ph/0008071].

[379] C. Greub and P. Liniger, *Calculation of next-to-leading QCD corrections to* $b \to sg$, *Phys. Rev. D* **63** (2001) 054025, [hep-ph/0009144].

[380] A. Kagan, *The Phenomenology of enhanced* $b \to sg$, in *2nd International Conference on B Physics and CP Violation (BCONF 97)*, 7, 1997. hep-ph/9806266. DOI.

[381] M. Dimou, J. Lyon and R. Zwicky, *Exclusive Chromomagnetism in heavy-to-light FCNCs*, *Phys. Rev. D* **87** (2013) 074008, [1212.2242].

[382] J. Lyon and R. Zwicky, *Isospin asymmetries in* $B \to (K^*, \rho)\gamma/l^+l^-$ *and* $B \to Kl^+l^-$ *in and beyond the standard model*, *Phys. Rev. D* **88** (2013) 094004, [1305.4797].

[383] HFLAV collaboration, Y. S. Amhis et al., *Averages of b-hadron, c-hadron, and* $\tau$-*lepton properties as of 2018*, *Eur. Phys. J. C* **81** (2021) 226, [1909.12524].

[384] M. Pospelov and A. Ritz, *Electric dipole moments as probes of new physics*, *Annals Phys.* **318** (2005) 119–169, [hep-ph/0504231].

[385] Y. Li, S. Profumo and M. Ramsey-Musolf, *A Comprehensive Analysis of Electric Dipole Moment Constraints on CP-violating Phases in the MSSM*, *JHEP* **08** (2010) 062, [1006.1440].

[386] J. F. Kamenik, M. Papucci and A. Weiler, *Constraining the dipole moments of the top quark*, *Phys. Rev. D* **85** (2012) 071501, [1107.3143].

[387] D. McKeen, M. Pospelov and A. Ritz, *Modified Higgs branching ratios versus CP and lepton flavor violation*, *Phys. Rev. D* **86** (2012) 113004, [1208.4597].

[388] W.-F. Chang, W.-P. Pan and F. Xu, *Effective gauge-Higgs operators analysis of new physics associated with the Higgs boson*, *Phys. Rev. D* **88** (2013) 033004, [1303.7035].

[389] J. Engel, M. J. Ramsey-Musolf and U. van Kolck, *Electric Dipole Moments of Nucleons, Nuclei, and Atoms: The Standard Model and Beyond*, *Prog. Part. Nucl. Phys.* **71** (2013) 21–74, [1303.2371].

[390] M. Jung and A. Pich, *Electric Dipole Moments in Two-Higgs-Doublet Models*, *JHEP* **04** (2014) 076, [1308.6283].

[391] B. Gripaios and D. Sutherland, *Searches for CP-violating dimension-6 electroweak gauge boson operators*, *Phys. Rev. D* **89** (2014) 076004, [1309.7822].

[392] J. Brod, U. Haisch and J. Zupan, *Constraints on CP-violating Higgs couplings to the third generation*, *JHEP* **11** (2013) 180, [1310.1385].

[393] S. Inoue, M. J. Ramsey-Musolf and Y. Zhang, *CP-violating phenomenology of flavor conserving two Higgs doublet models*, *Phys. Rev. D* **89** (2014) 115023, [1403.4257].

[394] W. Altmannshofer, J. Brod and M. Schmaltz, *Experimental constraints on the coupling of the Higgs boson to electrons*, *JHEP* **05** (2015) 125, [1503.04830].

[395] S. Dwivedi, D. K. Ghosh, B. Mukhopadhyaya and A. Shivaji, *Constraints on CP-violating gauge-Higgs operators*, *Phys. Rev. D* **92** (2015) 095015, [1505.05844].

[396] Y. T. Chien, V. Cirigliano, W. Dekens, J. de Vries and E. Mereghetti, *Direct and indirect constraints on CP-violating Higgs-quark and Higgs-gluon interactions*, *JHEP* **02** (2016) 011, [1510.00725].

[397] V. Cirigliano, W. Dekens, J. de Vries and E. Mereghetti, *Is there room for CP violation in the top-Higgs sector?*, *Phys. Rev. D* **94** (2016) 016002, [1603.03049].

[398] V. Cirigliano, W. Dekens, J. de Vries and E. Mereghetti, *Constraining the top-Higgs sector of the Standard Model Effective Field Theory*, *Phys. Rev. D* **94** (2016) 034031, [1605.04311].

[399] W. Dekens, J. de Vries, M. Jung and K. K. Vos, *The phenomenology of electric dipole moments in models of scalar leptoquarks*, *JHEP* **01** (2019) 069, [1809.09114].

[400] C. Cesarotti, Q. Lu, Y. Nakai, A. Parikh and M. Reece, *Interpreting the Electron EDM Constraint*, *JHEP* **05** (2019) 059, [1810.07736].

[401] G. Panico, A. Pomarol and M. Riembau, *EFT approach to the electron Electric Dipole Moment at the two-loop level*, *JHEP* **04** (2019) 090, [1810.09413].

[402] J. Brod and E. Stamou, *Electric dipole moment constraints on CP-violating heavy-quark Yukawas at next-to-leading order*, 1810.12303.

[403] J. Brod and D. Skodras, *Electric dipole moment constraints on CP-violating light-quark Yukawas*, *JHEP* **01** (2019) 233, [1811.05480].

[404] V. Cirigliano, A. Crivellin, W. Dekens, J. de Vries, M. Hoferichter and E. Mereghetti, **CP** *violation in Higgs-gauge interactions: from tabletop experiments to the LHC*, *Phys. Rev. Lett.* **123** (2019) 051801, [1903.03625].

[405] U. Haisch and A. Hala, *Bounds on CP-violating Higgs-gluon interactions: the case of vanishing light-quark Yukawa couplings*, *JHEP* **11** (2019) 117, [1909.09373].

[406] S. Weinberg, *Larger Higgs Exchange Terms in the Neutron Electric Dipole Moment*, *Phys. Rev. Lett.* **63** (1989) 2333.

[407] M. A. Shifman, A. I. Vainshtein and V. I. Zakharov, *On the Weak Radiative Decays (Effects of Strong Interactions at Short Distances)*, *Phys. Rev. D* **18** (1978) 2583–2599.

[408] M. Gorbahn, U. Haisch and M. Misiak, *Three-loop mixing of dipole operators*, *Phys. Rev. Lett.* **95** (2005) 102004, [hep-ph/0504194].

[409] G. Boyd, A. K. Gupta, S. P. Trivedi and M. B. Wise, *Effective Hamiltonian for the Electric Dipole Moment of the Neutron*, *Phys. Lett. B* **241** (1990) 584–588.

[410] E. Braaten, C.-S. Li and T.-C. Yuan, *The Evolution of Weinberg's Gluonic CP Violation Operator*, *Phys. Rev. Lett.* **64** (1990) 1709.

[411] D. Chang, W.-Y. Keung, C. S. Li and T. C. Yuan, *{QCD} Corrections to {CP} Violation From Color Electric Dipole Moment of b Quark*, *Phys. Lett. B* **241** (1990) 589–592.

[412] E. Braaten, C. S. Li and T. C. Yuan, *The Gluon Color - Electric Dipole Moment and Its Anomalous Dimension*, *Phys. Rev. D* **42** (1990) 276–278.

[413] J. de Vries, G. Falcioni, F. Herzog and B. Ruijl, *Two- and three-loop anomalous dimensions of Weinberg's dimension-six CP-odd gluonic operator*, 1907.04923.

[414] M. Pospelov and A. Ritz, *Neutron EDM from electric and chromoelectric dipole moments of quarks*, *Phys. Rev. D* **63** (2001) 073015, [hep-ph/0010037].

[415] D. A. Demir, M. Pospelov and A. Ritz, *Hadronic EDMs, the Weinberg operator, and light gluinos*, *Phys. Rev. D* **67** (2003) 015007, [hep-ph/0208257].

[416] O. Lebedev, K. A. Olive, M. Pospelov and A. Ritz, *Probing CP violation with the deuteron electric dipole moment*, *Phys. Rev. D* **70** (2004) 016003, [hep-ph/0402023].

[417] J. Hisano, J. Y. Lee, N. Nagata and Y. Shimizu, *Reevaluation of Neutron Electric Dipole Moment with QCD Sum Rules*, *Phys. Rev. D* **85** (2012) 114044, [1204.2653].

[418] U. Haisch and A. Hala, *Sum rules for CP-violating operators of Weinberg type*, *JHEP* **11** (2019) 154, [1909.08955].

[419] N. Yamanaka and E. Hiyama, *Weinberg operator contribution to the nucleon electric dipole moment in the quark model*, *Phys. Rev. D* **103** (2021) 035023, [2011.02531].

[420] Y. Hatta, *Nucleon electric dipole moment from polarized deep inelastic scattering*, *Phys. Lett. B* **814** (2021) 136126, [2012.01865].

[421] C. Abel et al., *Measurement of the Permanent Electric Dipole Moment of the Neutron*, *Phys. Rev. Lett.* **124** (2020) 081803, [2001.11966].

[422] G. Coloretti, A. Gehrmann-De Ridder and C. T. Preuss, *QCD predictions for event-shape distributions in hadronic Higgs decays*, *JHEP* **06** (2022) 009, [2202.07333].

[423] ATLAS collaboration, *A combination of measurements of Higgs boson production and decay using up to* $139\,\text{fb}^{-1}$ *of proton-proton collision data at* $\sqrt{s} = 13\,\text{TeV}$ *collected with the ATLAS experiment*, tech. rep., CERN, Geneva, 2020.

[424] V. Silveira and A. Zee, *SCALAR PHANTOMS*, *Phys. Lett. B* **161** (1985) 136–140.

[425] J. McDonald, *Gauge singlet scalars as cold dark matter*, *Phys. Rev. D* **50** (1994) 3637–3649, [hep-ph/0702143].

[426] C. P. Burgess, M. Pospelov and T. ter Veldhuis, *The Minimal model of nonbaryonic dark matter: A Singlet scalar*, *Nucl. Phys. B* **619** (2001) 709–728, [hep-ph/0011335].

[427] B. Patt and F. Wilczek, *Higgs-field portal into hidden sectors*, hep-ph/0605188.

[428] V. Barger, P. Langacker, M. McCaskey, M. J. Ramsey-Musolf and G. Shaughnessy, *LHC Phenomenology of an Extended Standard Model with a Real Scalar Singlet*, *Phys. Rev. D* **77** (2008) 035005, [0706.4311].

[429] G. Arcadi, A. Djouadi and M. Raidal, *Dark Matter through the Higgs portal*, *Phys. Rept.* **842** (2020) 1–180, [1903.03616].

[430] O. Lebedev, *The Higgs portal to cosmology*, *Prog. Part. Nucl. Phys.* **120** (2021) 103881, [2104.03342].

[431] S. Argyropoulos, O. Brandt and U. Haisch, *Collider Searches for Dark Matter through the Higgs Lens*, *Symmetry* **2021** (9, 2021) 13, [2109.13597].

[432] E. Hardy, *Higgs portal dark matter in non-standard cosmological histories*, *JHEP* **06** (2018) 043, [1804.06783].

[433] T. Cohen, N. Craig, G. F. Giudice and M. McCullough, *The Hyperbolic Higgs*, *JHEP* **05** (2018) 091, [1803.03647].

[434] H.-C. Cheng, L. Li, E. Salvioni and C. B. Verhaaren, *Singlet Scalar Top Partners from Accidental Supersymmetry*, *JHEP* **05** (2018) 057, [1803.03651].

[435] A. Djouadi, O. Lebedev, Y. Mambrini and J. Quevillon, *Implications of LHC searches for Higgs–portal dark matter*, *Phys. Lett. B* **709** (2012) 65–69, [1112.3299].

[436] Y. Mambrini, *Higgs searches and singlet scalar dark matter: Combined constraints from XENON 100 and the LHC*, *Phys. Rev. D* **84** (2011) 115017, [1108.0671].

[437] A. Djouadi, A. Falkowski, Y. Mambrini and J. Quevillon, *Direct Detection of Higgs-Portal Dark Matter at the LHC*, *Eur. Phys. J. C* **73** (2013) 2455, [1205.3169].

[438] CMS collaboration, A. M. Sirunyan et al., *Search for invisible decays of a Higgs boson produced through vector boson fusion in proton-proton collisions at* $\sqrt{s} = 13\ TeV$, *Phys. Lett. B* **793** (2019) 520–551, [1809.05937].

[439] ATLAS collaboration, *Combination of searches for invisible Higgs boson decays with the ATLAS experiment*, tech. rep., CERN, Geneva, 2020.

[440] S. Matsumoto, K. Fujii, T. Honda, S. Kanemura, T. Nabeshima, N. Okada, Y. Takubo and H. Yamamoto, *Observing the Coupling between Dark Matter and Higgs Boson at the ILC*, in *International Linear Collider Workshop*, 6, 2010. 1006.5268.

[441] S. Kanemura, S. Matsumoto, T. Nabeshima and H. Taniguchi, *Testing Higgs portal dark matter via Z fusion at a linear collider*, *Phys. Lett. B* **701** (2011) 591–596, [1102.5147].

[442] Z. Chacko, Y. Cui and S. Hong, *Exploring a Dark Sector Through the Higgs Portal at a Lepton Collider*, *Phys. Lett. B* **732** (2014) 75–80, [1311.3306].

[443] M. Endo and Y. Takaesu, *Heavy WIMP through Higgs portal at the LHC*, *Phys. Lett. B* **743** (2015) 228–234, [1407.6882].

[444] D. Curtin, P. Meade and C.-T. Yu, *Testing Electroweak Baryogenesis with Future Colliders*, *JHEP* **11** (2014) 127, [1409.0005].

[445] N. Craig, H. K. Lou, M. McCullough and A. Thalapillil, *The Higgs Portal Above Threshold*, *JHEP* **02** (2016) 127, [1412.0258].

[446] P. Ko and H. Yokoya, *Search for Higgs portal DM at the ILC*, *JHEP* **08** (2016) 109, [1603.04737].

[447] D. Buttazzo, D. Redigolo, F. Sala and A. Tesi, *Fusing Vectors into Scalars at High Energy Lepton Colliders*, *JHEP* **11** (2018) 144, [1807.04743].

[448] J. Heisig, M. Krämer, E. Madge and A. Mück, *Probing Higgs-portal dark matter with vector-boson fusion*, *JHEP* **03** (2020) 183, [1912.08472].

[449] C. Englert, J. Jaeckel, M. Spannowsky and P. Stylianou, *Power meets Precision to explore the Symmetric Higgs Portal*, *Phys. Lett. B* **806** (2020) 135526, [2002.07823].

[450] A. Garcia-Abenza and J. M. No, *Shining light through the Higgs portal with $\gamma\gamma$ colliders*, 2011.03551.

[451] C. Englert and M. McCullough, *Modified Higgs Sectors and NLO Associated Production*, *JHEP* **07** (2013) 168, [1303.1526].

[452] N. Craig, C. Englert and M. McCullough, *New Probe of Naturalness*, *Phys. Rev. Lett.* **111** (2013) 121803, [1305.5251].

[453] S.-P. He and S.-h. Zhu, *One-loop radiative correction to the triple Higgs coupling in the Higgs singlet model*, *Phys. Lett. B* **764** (2017) 31–37, [1607.04497].

[454] S. Kanemura, M. Kikuchi and K. Yagyu, *One-loop corrections to the Higgs self-couplings in the singlet extension*, *Nucl. Phys. B* **917** (2017) 154–177, [1608.01582].

[455] C. Englert and J. Jaeckel, *Probing the Symmetric Higgs Portal with Di-Higgs Boson Production*, *Phys. Rev. D* **100** (2019) 095017, [1908.10615].

[456] T. Hahn, S. Paßehr and C. Schappacher, *FormCalc 9 and Extensions*, *PoS* **LL2016** (2016) 068, [1604.04611].

[457] M. Grazzini, S. Kallweit, J. M. Lindert, S. Pozzorini and M. Wiesemann, *NNLO QCD + NLO EW with Matrix+OpenLoops: precise predictions for vector-boson pair production*, *JHEP* **02** (2020) 087, [1912.00068].

[458] S. Amoroso et al., *Les Houches 2019: Physics at TeV Colliders: Standard Model Working Group Report*, in *11th Les Houches Workshop on Physics at TeV Colliders: PhysTeV Les Houches*, 3, 2020. 2003.01700.

[459] F. Zimmermann, M. Benedikt, M. Capeans Garrido, F. Cerutti, B. Goddard, J. Gutleber, J. M. Jimenez, M. Mangano, V. Mertens, J. A. Osborne, T. Otto et al., *HE-LHC: The High-Energy Large Hadron Collider: Future Circular Collider Conceptual Design Report Volume 4. Future Circular Collider*, tech. rep., CERN, Geneva, 2018. 10.1140/epjst/e2019-900088-6.

[460] M. Benedikt, M. Capeans Garrido, F. Cerutti, B. Goddard, J. Gutleber, J. M. Jimenez, M. Mangano, V. Mertens, J. A. Osborne, T. Otto, J. Poole et al., *FCC-hh: The Hadron*

*Collider: Future Circular Collider Conceptual Design Report Volume 3. Future Circular Collider*, tech. rep., CERN, Geneva, 2018. 10.1140/epjst/e2019-900087-0.

[461] FCC collaboration, A. Abada et al., *FCC Physics Opportunities: Future Circular Collider Conceptual Design Report Volume 1*, *Eur. Phys. J. C* **79** (2019) 474.

[462] U. Haisch, M. Ruhdorfer, E. Salvioni, E. Venturini and A. Weiler, *Singlet night in Feynman-ville: one-loop matching of a real scalar*, *JHEP* **04** (2020) 164, [2003.05936].

[463] D. Gonçalves, T. Han, F. Kling, T. Plehn and M. Takeuchi, *Higgs boson pair production at future hadron colliders: From kinematics to dynamics*, *Phys. Rev. D* **97** (2018) 113004, [1802.04319].

[464] J. de Blas et al., *Higgs Boson Studies at Future Particle Colliders*, *JHEP* **01** (2020) 139, [1905.03764].

[465] K. Mimasu, V. Sanz and C. Williams, *Higher Order QCD predictions for Associated Higgs production with anomalous couplings to gauge bosons*, *JHEP* **08** (2016) 039, [1512.02572].

[466] S. Alioli, W. Dekens, M. Girard and E. Mereghetti, *NLO QCD corrections to SM-EFT dilepton and electroweak Higgs boson production, matched to parton shower in POWHEG*, *JHEP* **08** (2018) 205, [1804.07407].

[467] J. Baglio, S. Dawson and I. M. Lewis, *NLO effects in EFT fits to $W^+W^-$ production at the LHC*, *Phys. Rev. D* **99** (2019) 035029, [1812.00214].

[468] J. Baglio, S. Dawson and S. Homiller, *QCD corrections in Standard Model EFT fits to $WZ$ and $WW$ production*, *Phys. Rev. D* **100** (2019) 113010, [1909.11576].

[469] J. Collins, *Foundations of perturbative QCD*, vol. 32. Cambridge University Press, 11, 2013.

[470] M. D. Schwartz, *Quantum Field Theory and the Standard Model*. Cambridge University Press, 3, 2014.

[471] J. F. Donoghue, E. Golowich and B. R. Holstein, *Dynamics of the standard model*, vol. 2. Cambridge University Press, 2014, 10.1017/CBO9780511524370.

[472] L. D. Faddeev and V. N. Popov, *Feynman Diagrams for the Yang-Mills Field*, *Phys. Lett. B* **25** (1967) 29–30.